DOCTORAL THESIS

Adaptation of Local Droplet Etching for InGaAs/InAlAs Quantum Dot Fabrication Towards Telecom C-Band Emission

Author:
Dennis DEUTSCH

Supervisor:
Prof. Dr. Dirk REUTER

A thesis submitted in fulfillment of the requirements for the degree of Dr. rer. nat.

February 23, 2026

Declaration of Authorship

I, Dennis DEUTSCH, declare that this thesis titled, "Adaptation of Local Droplet Etching for InGaAs/InAlAs Quantum Dot Fabrication Towards Telecom C-Band Emission" and the work presented in it are my own. I confirm that:

- This work was done wholly or mainly while in candidature for a research degree at this University.
- No part of this thesis has previously been submitted for a degree or any other qualification at this University or any other institution.
- Where I have consulted the published work of others, this is always clearly attributed.
- Where I have quoted from the work of others, the source is always given. With the exception of such quotations, this thesis is entirely my own work.
- I have acknowledged all main sources of help.
- Where the thesis is based on work done by myself jointly with others, I have made clear exactly what was done by others and what I have contributed myself.

Signed:

Date:

Declaration on the use of AI

I hereby declare that this thesis was written with limited assistance from the artificial intelligence (AI) tool ChatGPT (Version 5.0). The AI was used solely for language refinement, including grammatical correction and improvement of readability. It was not employed to generate data, analyses, or original scientific content, and no citations were provided by the AI.

I have carefully reviewed all text edited with AI assistance and take full responsibility for the correctness, originality, and completeness of the entire work.

Deutsche Kurzfassung

Adaptation of Local Droplet Etching for InGaAs/InAlAs Quantum Dot Fabrication Towards Telecom C-Band Emission

von Dennis DEUTSCH

Halbleiter-Quantenpunkte haben sich als eine vielversprechende Plattform für deterministische Photonenquellen erwiesen. Besonders GaAs/$Al_xGa_{1-x}As$-Quantenpunkte, die epitaktisch mittels der Lokalen Tröpfchen-Ätzen-Methode hergestellt werden, gelten derzeit als der Goldstandard für die Erzeugung von polarisationsverschränkten Photonenpaaren. Hierbei werden nanometergroße Löcher in Halbleiterschichten durch Tröpfchenätzung generiert, die anschließend gefüllt und überwachsen werden, sodass spannungsfreie Quantenpunkte mit ausgezeichneter Symmetrie und geringer Feinstrukturaufspaltung entstehen. In dieser Arbeit wurde diese Methode auf das InP/$In_xAl_{1-x}As$/$In_yGa_{1-y}As$ Materialsystem übertragen, um die Emission der Quantenpunkte in die optischen Telekom-Bänder zu verschieben. Die Proben wurden mittels Molekularstrahlepitaxie hergestellt und mit Rasterkraftmikroskopie, Rasterelektronenmikroskopie, hochauflösender Röntgenbeugung und Photolumineszenz-Spektroskopie charakterisiert. Die Lochbildung auf InP-gitterangepassten $In_{0.52}Al_{0.48}As$-Schichten wurde optimiert, indem der Einfluss von Temperatur, Arsenfluss, Materialfluss, Abscheidungsmenge, Ätzzeit und Tropfenzusammensetzung untersucht wurde. Die Löcher wurden anschließend mit $In_yGa_{1-y}As$ gefüllt und mit $In_{0.52}Al_{0.48}As$ überwachsen, sodass Quantenpunkte mit bis zu 1.55 µm Emission entstanden. Abschließend wurde der Prozess zudem auf $In_xAl_{1-x}As$-Schichten, die auf $In_yGa_{1-y}As$/GaAs-metamorphen Pufferschichten gewachsen wurden, ausgeweitet.

Abstract

Adaptation of Local Droplet Etching for InGaAs/InAlAs Quantum Dot Fabrication Towards Telecom C-Band Emission

by Dennis DEUTSCH

Semiconductor quantum dots have emerged as a highly promising platform for on-demand photon sources. In particular, GaAs/$Al_xGa_{1-x}As$ quantum dots, grown epitaxially via the local droplet etching method, have emerged as the current gold standard for polarization-entangled photon pair generation. In this method, group-III droplets etch nanometer-sized holes into semiconductor layers, which are subsequently infilled and overgrown to form nominally strain-free quantum dots with excellent in-plane symmetry, exhibiting very low excitonic fine-structure splitting. In this work, the method was adapted to the InP/$In_xAl_{1-x}As$/$In_yGa_{1-y}As$ material platform to extend quantum dot emission into the optical telecom bands. Samples were grown by molecular beam epitaxy and characterized using atomic force microscopy, scanning electron microscopy, high-resolution X-ray diffraction, and photoluminescence spectroscopy. Nanohole formation on $In_{0.52}Al_{0.48}As$ layers lattice-matched to InP was systematically optimized by investigating the influence of temperature, arsenic flux, droplet material flux, droplet material amount, etching time, and droplet composition. The nanoholes were then infilled with $In_yGa_{1-y}As$ and overgrown with $In_{0.52}Al_{0.48}As$, to produce quantum dots whose emission could be tuned to 1.55 µm. To assess compatibility with GaAs-based platforms, the process was further transferred to $In_xAl_{1-x}As$ layers grown on $In_yGa_{1-y}As$/GaAs metamorphic buffer structures.

Acknowledgements

Scientific research is rarely the work of a single individual. Although I spent countless hours, evenings, and weekends in the laboratory conducting the experiments for this dissertation, none of it would have been possible without the help and support of many people to whom I am deeply grateful.

My foremost thanks go to **Prof. Dr. Dirk Reuter**, who made this work possible. He acquired the necessary funding and gave me the opportunity to grow semiconductors in his MBE system. While he always provided excellent input and valuable suggestions for the direction of my research, he also granted me the freedom to pursue my own ideas - to make mistakes, learn from them, and grow as a physicist.

I am very grateful to **Prof. Dr. Klaus Jöns** and his students **Christopher Buchholz** and **Juan Nicolás Claro Rodríguez** for their collaboration, sample processing, and μPL measurements. I also thank **Dr. Michael Jetter** and **Ponraj Vijayan** from the University of Stuttgart for their collaboration, for providing the metamorphic buffer layer samples used in this work and μPL measurements.

Furthermore, I want to thank **Prof. Dr. Donat J. As** for his valuable scientific input. His extensive expertise in epitaxy and X-ray diffraction has been of great help to this work.

My special thanks go to **Timo Langer** for showing me the ropes, introducing me to the MBE system, and teaching me the fundamentals of epitaxial growth on InP. I sincerely thank **Bastian Aisenbrey** for always being there when something broke and for organizing the yearly MBE opening - without him, we would truly be lost. I also thank **Dr. Tobias Henksmeier** for his continuous help in the lab and, beyond that, for teaching me how to ski during the MBE conference in France. Further thanks go to **Dr. Viktoriya Zolatanosha** for her assistance in the lab, her help with wet chemical etching, and for performing many SEM measurements on my samples.

I want to thank my fellow PhD colleagues in Prof. Reuter's group - **Pascal Mahler**, **Normen Auler**, and **Binamra Shrestha** - for their support and the many insightful discussions we shared. I will never forget a single MBE opening with you; we were truly a great team. My gratitude also goes to my Master's students **Marvin Böing** and **Ali Anvari** for their dedicated work and valuable contributions to this research.

Finally, I want to thank my friends and family for being there for me when I needed them the most and their unwavering support all the way throughout this journey.

"Per aspera ad astra."

Contents

Declaration of Authorship **iii**

Declaration on the use of AI **v**

Deutsche Kurzfassung **vii**

Abstract **ix**

Acknowledgements **xi**

Contents **xv**

1 Introduction **1**
1.1 Motivation 1
1.2 Overview 3

2 Polarization entangled photons from quantum dots **5**
2.1 Photon pair entanglement 5
2.2 Low dimensional semiconductors 8
2.3 Semiconductor quantum dots 13
2.4 The biexciton-exciton cascade 15

3 Epitaxy **21**
3.1 Molecular beam epitaxy 21
3.2 Growth kinetics 24
3.3 Growth modes 26
3.4 Material and structural considerations in III–V epitaxy 27
3.5 Local droplet etching 28

4 Experimental methods for sample characterization **33**
4.1 Atomic force microscopy 33
4.2 Scanning electron microscopy 38
4.3 High resolution X-ray diffractometry 39
4.3.1 Reciprocal space maps 43
4.3.2 ω-2θ-scans 47
4.3.3 Rocking curve 49
4.4 Photoluminescence spectroscopy 49

5 Local droplet etching on $In_{0.52}Al_{0.48}As$ 53
5.1 Film growth on InP (100) . . . 54
5.2 Influence of etching parameters . . . 58
5.2.1 Nanohole degradation under As_2 flux . . . 60
5.2.2 Etching temperature . . . 64
5.2.3 $In_{0.52}Al_{0.48}As$ overgrowth . . . 67
5.2.4 As flux and etching material amount . . . 69
5.2.5 Droplet material type and etching temperature . . . 74
5.2.6 Etching material deposition rate . . . 79
5.2.7 Etching time . . . 85
5.2.8 Droplet etching with Ga . . . 90
5.3 Local droplet etching on $In_{0.53}Ga_{0.47}As$ . . . 92
5.4 Infilling of droplet etched nanoholes . . . 96
5.5 Quantum dot fabrication and spectroscopy . . . 100

6 Local droplet etching on metamorphic buffer layers 105
6.1 Characterization of MBLs . . . 106
6.2 $In_xAl_{1-x}As$ layer growth on MBLs . . . 109
6.3 Droplet etching on $In_xAl_{1-x}As$ layers grown on MBLs . . . 111
6.4 Nanohole infilling and overgrowth . . . 114

7 Summary and Outlook 117

A Sample number reference catalog 121

Scientific contributions 125

Bibliography 127

List of Abbreviations

AFM	**A**tomic **F**orce **M**icroscopy
Al	**Al**uminium
As	**A**r**s**enic
BEP	**B**eam **E**quivalent **P**ressure
DBR	**D**istributed **B**ragg **R**eflector
DE	**D**roplet **E**pitaxy
FSS	**F**ine **S**tructure **S**plitting
FvdM	**F**rank-**v**an **d**er **M**erwe
Ga	**Ga**llium
GaAs	**Ga**llium **A**r**s**enide
HRXRD	**H**igh **R**esolution **X**-**R**ay **D**iffraction
In	**In**dium
InAl	**In**0.52**Al**0.48 (droplet material composition)
InAs	**In**dium **A**r**s**enide
InP	**In**dium **P**hosphide
LDE	**L**ocal **D**roplet **E**tching
MBE	**M**olecular **B**eam **E**pitaxy
MBL	**M**etamorphic **B**uffer **L**ayer
ML	**M**ono **L**ayer
MOVPE	**M**etal**O**rganic **V**apor-**P**hase **E**pitaxy
P	**P**hosphorus
PL	**P**hoto**L**uminescence
QDs	**Q**uantum **D**ot**s**
QKD	**Q**uantum **K**ey **D**istribution
SEM	**S**canning **E**lectron **M**icroscopy
SK	**S**transki-**K**rastanov
UHV	**U**ltra **H**igh **V**acuum
VACS	**V**alved **A**rsenic **C**racker **S**ource
VM	**V**olmer-**W**eber

Chapter 1

Introduction

1.1 Motivation

Quantum mechanics is fundamentally counterintuitive. It describes nature on a microscopic scale and introduces concepts that have no counterpart in classical physics. Two of its most striking features are superposition, the ability of a quantum system to exist in multiple states simultaneously, and entanglement, where distinct quantum entities become correlated so that their states cannot be described independently. These effects now form the foundation for an emerging class of information technologies.

Quantum computers exploit superposition and entanglement to perform computations that are infeasible for classical hardware. For certain problems, such as large integer factorization through Shor's alogrithm [1] or Boson sampling [2], quantum computers promise to be much faster than classical computers, a regime referred to as quantum supremacy [3, 4].

However, the same capabilities that make quantum computers powerful also pose a long-term threat to classical data security. Modern public-key encryption schemes, such as RSA [5], rely on the computational difficulty of factoring very large integers. Quantum algorithms for efficient factorization would render such encryption methods insecure once sufficiently powerful quantum computers become available [6].

At the same time, quantum mechanics also provides a solution to this challenge. Quantum key distribution (QKD) [7, 8] allows two parties to share encryption keys with theoretically unbreakable security. By encoding information in quantum states and exploiting the no-cloning theorem [9], which forbids perfect duplication of an unknown quantum state, QKD ensures that any eavesdropping attempt leaves detectable traces.

Combining QKD with entanglement swapping based quantum repeater schemes to overcome fiber transmission losses could ultimately enable quantum communication on a global scale [10]. Realizing such an infrastructure, however, requires reliable, efficient, and high-quality photon sources.

Early demonstrations of quantum photonic applications relied on spontaneous parametric down-conversion [11] and four-wave mixing [12] for the generation of

single and entangled photons. While these sources provide high entanglement fidelity and photon indistinguishability, their intrinsically probabilistic nature limits the achievable source brightness, as maintaining high fidelity and indistinguishability requires operation at low generation rates [13].

Semiconductor quantum dots (QDs) have emerged as a powerful alternative, acting as deterministic single-photon and entangled-photon sources. QDs combined with optimized device design can emit photons on demand with high brightness [13, 14], purity [13, 14, 15], indistinguishability [13, 14, 16, 17], and repetition rates [17]. Additionaly, their compatibility with established semiconductor fabrication processes and their small footprint make them ideal for scalable device integration and on-chip photonics [18].

Among the existing QD systems, local droplet etched (LDE) GaAs QDs currently represent one of the most promising material platforms for entangled photon pair generation. These structures are fabricated in molecular beam epitaxy (MBE) via the LDE technique, in which group-III metals are deposited under a strongly reduced arsenic flux on a III-As semiconductor surface. The group-III atoms aggregate into liquid droplets in a Volmer-Weber-like growth mode and – driven by an arsenic concentration gradient between the metallic droplet and the substrate – arsenic diffuses into the droplet, locally liquefying the interface and causing the droplet to etch nanometer-sized holes into the surface. Subsequent infilling and overgrowth of these nanoholes yields GaAs quantum dots embedded within a lattice-matched $Al_xGa_{1-x}As$ matrix [19].

The key advantages of these LDE QDs are their nominally strain-free nature and their highly symmetric shape. These properties suppress the fine-structure splitting (FSS) of exciton states, which is essential for generating high-fidelity polarization-entangled photon pairs from a single QD through the biexciton-exciton cascade [20, 21].

Indeed, GaAs/$Al_xGa_{1-x}As$ LDE QDs have been demonstrated to exhibit FSS values below the homogeneous linewidth [22], resulting in polarization-entangled photon-pair emission with fidelities of 0.94 ± 0.01 via the biexciton-exciton cascade, without requiring external tuning [20].

Additionally, these QDs can be embedded in diode heterostructures – typically p-i-n or n-i-p configurations – which allow the QD charge state to be locked by Coulomb blockade while suppressing charge noise and spectral wandering [23, 24]. This architecture also enables in-situ tuning of the emission wavelength via an applied gate voltage [25]. When grown in such electrically controlled structures using optimized conditions that yield ultra-clean, low-defect materials, GaAs LDE QDs have demonstrated two-photon (Hong-Ou-Mandel) interference with a visibility of $(93.0 \pm 0.8)\%$ and an entanglement fidelity of $(85.0 \pm 1.0)\%$ for two spatially separated GaAs LDE QDs, located in independent cryostats [23].

Further improvements can be achieved by integrating LDE QDs into photonic

nanostructures, such as circular Bragg gratings (CBG). These structures can be tailored to reduce the lifetime of the biexciton via Purcell enhancement [26], a requirement for achieving near unity indistinguishability from cascaded emission processes and to realize quantum repeater schemes based on photon entanglement [27]. CBG devices have demonstrated enhanced indistinguishability while significantly increasing photon-pair collection probability [13].

However, one remaining challenge for LDE QDs lies in their emission wavelength. $GaAs/Al_xGa_{1-x}As$ QDs typically emit around 750–800 nm [23], far from the telecom C-band at 1530–1565 nm, which offers the lowest attenuation for fiber-based long-distance optical transmission.

A straightforward approach to achieving telecom-wavelength emission would be to transfer the LDE process to other material systems. One of those is the indium phosphide (InP) platform, where the lattice-matched ternary alloys $In_{0.52}Al_{0.48}As$ and $In_{0.53}Ga_{0.47}As$ offer suitable band gap energies for QD emission in the 1.3–1.55 μm range of the optical telecom bands. This adaptation would promise to combine the symmetry and optical quality of LDE-fabricated QDs with the ability to generate photons at wavelengths compatible with existing fiber communication networks.

Consequently, the central goal of this work was the extension of the local droplet etching technique to this material platform and to establish the foundation for symmetric, strain-free QD emitters operating at telecom wavelengths.

1.2 Overview

The previous section has outlined the motivation and background for the present work. The following chapters introduce the theoretical framework, experimental methods, and original research results that form the core of this dissertation.

Chapter 2 introduces the fundamental physical principles of semiconductor quantum dots (QDs) and outlines their unique properties as quantum light sources.

Chapter 3 describes the growth of semiconductor materials by molecular beam epitaxy (MBE) and discusses the epitaxial concepts relevant to this thesis. The chapter concludes with an overview of the local droplet etching (LDE) method.

Chapter 4 presents the main characterization techniques employed during this research, i.e., atomic force microscopy (AFM), scanning electron microscopy (SEM), high-resolution x-ray diffraction (HRXRD), and photoluminescence (PL) spectroscopy. The principles and practical implementation of each method are briefly summarized together with their relevance to the studied nanostructures.

Chapters 5 and 6 contain the main results and original contributions of this dissertation. Chapter 5 discusses in detail the adaptation of the LDE process to $In_{0.52}Al_{0.48}As$ layers grown lattice matched on InP substrates. The chapter begins with the growth of lattice matched layers on InP (100) and continues with a systematic investigation of the parameters governing the LDE process, focusing on

their optimization for creating well-defined nanohole templates suitable for quantum dot fabrication. Subsequent sections cover the controlled infilling of the etched nanoholes, overgrowth to form quantum dots, and optical analysis of the resulting structures.

Chapter 6 extends the LDE approach to $In_xAl_{1-x}As$ layers grown on InGaAs/GaAs metamorphic buffer systems.

Finally, Chapter 7 provides a concise summary of the results, highlights the main conclusions of this work, and outlines possible directions for future research.

Chapter 2

Polarization entangled photons from quantum dots

This chapter provides an introduction to the physics of polarization entanglement and semiconductor quantum dots (QDs) and outlines how a QD can function as a source of polarization-entangled photons. The chapter begins with an overview of quantum-mechanical entanglement, illustrated through the example of polarization-entangled photon pairs. Such photon pairs can be generated by QDs; however, understanding the underlying mechanisms requires knowledge of the formation of discrete energy states within the semiconductor band structure. After discussing the relevant physics of low-dimensional semiconductors, the formation of energy states in a QD is examined, followed by an explanation of how single photons and entangled photon pairs can be emitted.

2.1 Photon pair entanglement

Entanglement is a fundamental quantum mechanical phenomenon that is central to the ongoing 2nd quantum revolution [28]. First proposed by Einstein, Podolsky, and Rosen in 1935 [29], a two-particle state is considered entangled when its wavefunction is *not separable* [30]. Considering a pair of polarized photons: if the photons are not entangled in polarization, the polarization state of each photon can be described independently. In contrast, for an entangled state, both photons share a single joint wavefunction, and a complete description of the polarization requires inclusion of both particle states. Consequently, for an entangled photon pair, a polarization measurement performed on one photon instantaneously influences the state of the other, regardless of the spatial separation between them [21].

The study of entanglement is of fundamental importance for advancing the understanding of quantum mechanics. Its counterintuitive properties lie at the core of quantum mechanics, and deeper insights into entanglement may contribute to a more comprehensive conceptual understanding of microscopic physics. Although entanglement cannot be used to transmit information faster than the speed of light, as this would violate causality, it remains essential for several quantum-technology applications. One prominent example is quantum key distribution. Protocols such

as E91 [8] or BBM92 [31] employ entangled photon pairs to establish an encryption key between two parties. Such quantum key exchange schemes promise security against all forms of eavesdropping, as the quantum no-cloning theorem [9] forbids perfect copying of arbitrary quantum states and any attempt by a third party to extract information from the photon stream would lead to detection via the error rate in the key-generation process [32].

For a clearer understanding of entanglement and its measurement, the underlying quantum mechanical description must be considered. Two particles (or subsystems) A and B are assumed to occupy the Hilbert space $\mathcal{H} = \mathcal{H}_A \otimes \mathcal{H}_B$, with the corresponding state vectors $|a\rangle$ and $|b\rangle$. If the composite state Ψ of both subsystems can be written as a product state,

$$|\Psi\rangle = |a\rangle \otimes |b\rangle\,, \tag{2.1}$$

the state is separable and therefore *not entangled* [33]. However, because quantum mechanics allows for superpositions, not all composite states are separable. If particles A and B form a superposition of the states $|a_1\rangle \otimes |b_1\rangle$ and $|a_2\rangle \otimes |b_2\rangle$, the resulting state can be written as

$$|\Psi\rangle = \frac{1}{N}\left(|a_1\rangle \otimes |b_1\rangle + |a_2\rangle \otimes |b_2\rangle\right), \tag{2.2}$$

where N is a normalization factor satisfying $\langle\Psi|\Psi\rangle = 1$. Such a state cannot be expressed as a product state and is therefore regarded as entangled [33], and until it interacts with a measuring device, this type of state exhibits quantum correlations that have no classical counterpart [21].

To determine whether any pure or mixed state is entangled, it is useful to consider the density operator

$$\hat{\rho} = \sum_K P_K \,|\Psi_K\rangle\,\langle\Psi_K|\,, \tag{2.3}$$

where P_K denotes the probability of occupying the state $|\Psi_K\rangle$ and satisfies $\sum_K P_K = 1$. The density operator $\hat{\rho}$ offers full information over a quantum state, as it allows for calculating the expectation value of every operator [21]. $\hat{\rho}$ can be obtained through quantum state tomography. Experimentally, this procedure is implemented by directing each photon into a separate detection arm. Wave plates and polarizers placed before each detector select the projection state in any chosen linear or circular basis. The detection events are time-correlated, enabling measurement of polarization-dependent cross-correlation functions. For a two-photon state, the full two-photon density matrix can then be reconstructed by recording coincidence counts for 16 different sets of measurements [34].

Figure 2.1 illustrates exemplary density matrices for polarization states of photon pairs, expressed in the basis set $|HH\rangle$, $|HV\rangle$, $|VH\rangle$, and $|VV\rangle$, where H and V denote horizontal and vertical linear polarizations, respectively. In Figure 2.1 a), the

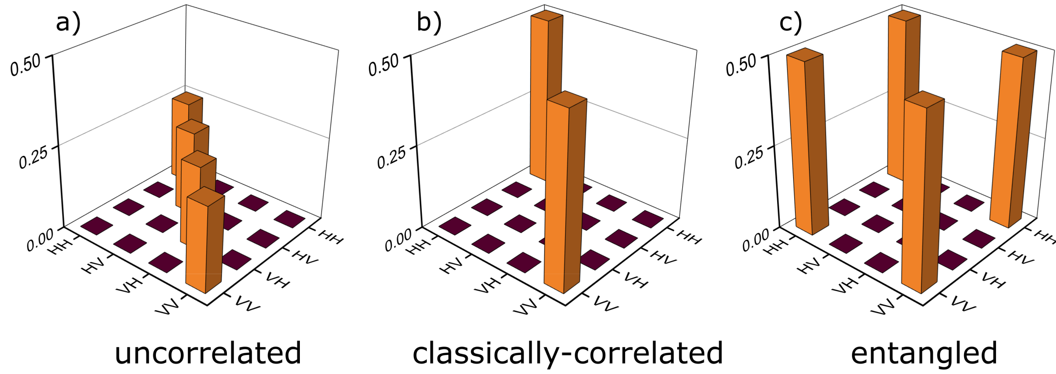

FIGURE 2.1: Exemplary density matrices for two photon polarization states. Adapted from [21]

matrix corresponds to an uncorrelated state, in which only the diagonal elements are nonzero. Such a state can be written directly as a product state of the form given in Eq. 2.1. In the case of a classically correlated state, shown in Figure 2.1 b), only two diagonal elements, also referred to as populations, are present. Although measurements would reveal that both photons exhibit the same polarization, this state remains separable, as it can be represented as a statistical mixture of $|\Psi_1\rangle = |HH\rangle$ and $|\Psi_2\rangle = |VV\rangle$ [21].

For an entangled state, the density matrix takes the form sketched in Figure 2.1 c), where the off-diagonal elements $|HH\rangle\langle VV|$ and $|VV\rangle\langle HH|$, referred to as coherences, are nonzero. This entangled state, a Bell state, can be written as

$$\Psi = \frac{1}{\sqrt{2}}\left(|HH\rangle + |VV\rangle\right), \tag{2.4}$$

which cannot be expressed as a product state and has the same structure as the entangled state in Eq. 2.2.

In real experiments the resulting density matrices generally deviate from these idealized cases. Imperfections in the sample or measurement setup can degrade the entanglement, yielding experimentally reconstructed density matrices that differ from those in Figures 2.1 a-c) [35]. This gives rise to the need for entanglement quantification, which characterizes the degree of entanglement present in the reconstructed density matrix. Two commonly used measures are concurrence and negativity, which map the density matrix to a function whose output quantifies the entanglement [36, 37]. For photon pairs, both concurrence and negativity take values between 0 and 1, where 0 corresponds to an uncorrelated or classically correlated state and 1 indicates maximal entanglement. These quantities therefore provide a means to compare entanglement performance between different photon pair sources, by calculating them from their density matrices [21].

Another frequently reported quantity in the context of entangled photon pairs

is the fidelity [38]. Fidelity measures the closeness between two states and represents the probability that one state will be identified as another. It ranges from 0 to 1, with 0.5 corresponding to a classically correlated state and 1 indicating maximal entanglement. An important advantage of fidelity is its reduced experimental complexity, only requiring six cross-correlation measurements to calculate the fidelity of a two-photon state [21, 38].

2.2 Low dimensional semiconductors

A prominent source of polarization-entangled photon pairs are semiconductor quantum dot (QDs). These are three-dimensional semiconductor nanostructures with dimensions of only a few nanometers, where electrons and holes are spatially confined by potential barriers formed by surrounding semiconductor material. When the characteristic dimensions of a semiconductor structure become comparable to the de Broglie wavelength of the charge carriers, spatial confinement imposes additional boundary conditions on the electronic wave functions, leading to a quantized and discrete energy spectrum [21].

The discrete energy spectrum of a QD is therefore not a fundamental property of the constituent atoms, but an emergent consequence of carrier confinement within a crystalline semiconductor. To make this connection explicit, a microscopic description of the electronic structure of bulk semiconductors is first introduced, and the modifications arising from reduced dimensionality are subsequently discussed.

For a crystalline solid consisting of N atoms, each with atomic number Z_I and one valence electron per atom, a microscopic description is obtained by solving the many-electron Schrödinger equation. Within the Born-Oppenheimer approximation, the dynamics of the electrons and the nuclei are separated due to their mass difference, such that the electronic motion is determined for static nuclei located at the lattice positions R_I [21]. Neglecting the spin degree of freedom the resulting electronic Hamiltonian H is given by

$$\mathcal{H} = \sum_{i=1}^{n} \left(\frac{-\hbar^2 \nabla_i^2}{2m_e} - \sum_I \frac{e^2 Z_I}{\left| \vec{r}_i - \vec{R}_I \right|} \right) + \frac{1}{2} \sum_{i \neq j}^{N} \frac{e^2}{\left| \vec{r}_i - \vec{r}_j \right|}, \tag{2.5}$$

Here, the first term represents the kinetic energy of the electrons, the second term describes the Coulomb attraction between electrons at positions r_i and the nuclei located at lattice sites R_I, and the final term accounts for the Coulomb repulsion between electrons. The quantity $\hbar$ denotes the reduced Planck constant, e the elementary charge, and m_e the electron rest mass. The operator ∇_i acts on the spatial coordinate of the ith electron [39].

The final term in the Hamiltonian couples the degrees of freedom of different electrons, rendering the Schrödinger equation difficult to solve. In practice, this complexity is commonly reduced by replacing the full many-body Hamiltonian with an effective independent-particle Hamiltonian, in which each electron is assumed to move in an average potential generated by the nuclei and the other electrons. The corresponding effective Hamiltonian can be written as

$$\mathcal{H} = \sum_{i=1}^{n} \left(\frac{-\hbar^2 \nabla_i^2}{2m_e} + v_{\text{eff}}(\vec{r}_i) \right), \tag{2.6}$$

where the effects of the electron-electron and electron-nucleus interactions are incorporated into an effective potential $v_{\text{eff}}(\vec{r})$ [39].

In a crystal $v_{\text{eff}}(\vec{r})$ can be modeled by the periodic potential V of the crystalline lattice, such that

$$v_{\text{eff}}(\vec{r}) = V(\vec{r}) = V(\vec{r} + \vec{t}), \tag{2.7}$$

where $\vec{t} = t_1\vec{a}_1 + t_2\vec{a}_2 + t_3\vec{a}_3$ represents the translation between lattice sites, with the basis vectors $\vec{a}_i$ [21].

The discrete translational symmetry of the crystal lattice allows the eigenstates of the single-particle Hamiltonian to be chosen in the form of Bloch functions. According to Bloch's theorem, the electronic wave functions can be written as

$$\psi_{n\vec{k}}(\vec{r}) = e^{i\vec{k}\cdot\vec{r}} u_{n\vec{k}}(\vec{r}), \tag{2.8}$$

where $u_{n\vec{k}}(\vec{r})$ has the periodicity of the lattice, n denotes the band index, and $\vec{k}$ is the crystal momentum, which may be restricted to the first Brillouin zone [39].

As a starting point, the one-dimensional empty-lattice model is considered. In this approximation, a lattice constant a is defined, while the periodic potential is set to zero. The resulting energy eigenvalues correspond to those of free electrons,

$$\epsilon_k = \frac{\hbar^2 k^2}{2m}, \tag{2.9}$$

and are shown in Figure 2.2 a) using the extended-zone scheme [39].

A more realistic description is obtained by introducing a weak periodic potential within the independent-particle approximation. The presence of the periodic potential leads to Bragg reflection at the Brillouin-zone boundaries, which lifts the degeneracy of states and results in the opening of energy gaps between adjacent bands [40]. The resulting dispersion relations are commonly represented in the reduced-zone

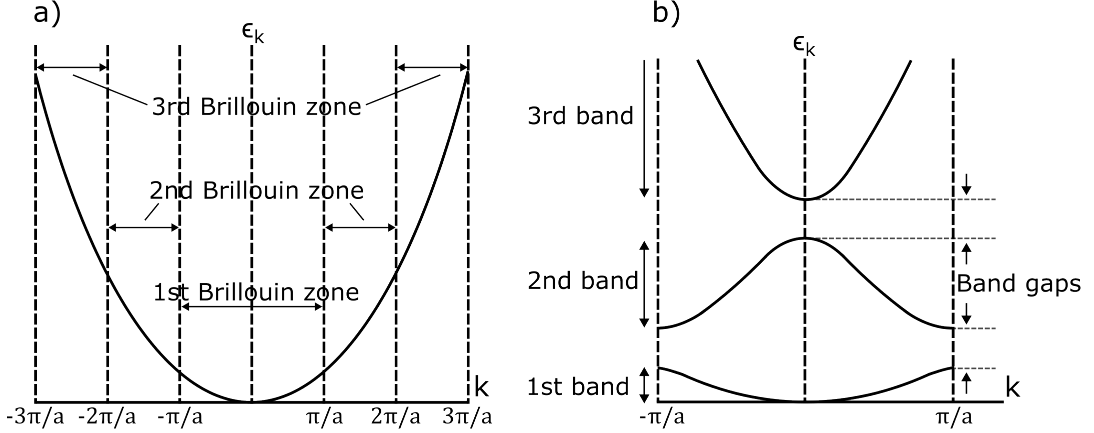

FIGURE 2.2: a) Electron dispersion for the one-dimensional empty-lattice model shown in the extended-zone scheme. b) Electron dispersion in the reduced-zone scheme for a weak one-dimensional periodic potential, illustrating the opening of energy gaps at the Brillouin-zone boundaries. Adapted from [39].

scheme, where all wave vectors are folded back into the first Brillouin zone, as illustrated in Figure 2.2 b). The sequence of allowed energy bands separated by forbidden energy regions constitutes the electronic band structure of the crystal [39]. In a three-dimensional crystal containing a macroscopic number of unit cells, the allowed crystal momenta $\vec{k}$ form a dense set of values within the Brillouin zone. As a consequence, each energy band consists of a very large number of closely spaced eigenstates, giving rise to a quasi-continuous energy spectrum in the bulk limit [21].

In semiconductors, the highest occupied electronic band at zero temperature is referred to as the valence band, while the lowest unoccupied band is known as the conduction band [40]. The two bands are separated by a finite energy gap. Excitation of an electron from the valence band into the conduction band leaves behind an unoccupied electronic state in the valence band. This absence of an electron is described as a hole. Rather than representing a single particle, the hole is understood as a collective excitation of the remaining $N-1$ valence-band electrons and behaves as a quasiparticle carrying a positive elementary charge $+e$ [21, 40].

The motion of electrons and holes in a crystal is strongly influenced by the periodic potential of the lattice. The complex interaction between charge carriers and the crystal environment can be simplified within the effective mass approximation, which allows the dynamics of individual carriers to be treated in terms of quasi-free particles whose inertial response differs from that of free electrons in vacuum.

Within this framework, the effective mass tensor is defined by the local curvature of the electronic band dispersion $\epsilon(\vec{k})$ in reciprocal space [41],

$$\left(\frac{1}{m^*}\right)_{ij} = \frac{1}{\hbar^2}\frac{\partial^2 \epsilon(\vec{k})}{\partial k_i \, \partial k_j}. \tag{2.10}$$

For typical direct-gap group III-V zincblende semiconductors, the extrema of the

conduction and valence bands are located near the center of the first Brillouin zone at $\vec{k} \approx 0$. In this region, the energy dispersion is approximately isotropic and can be well described by a parabolic form. As a consequence, the effective mass becomes a scalar constant, and the carrier energy can be written as

$$E = \frac{\hbar^2 \vec{k}^2}{2m^*_{e,h}} = \frac{\hbar^2}{2}\left(\frac{k_x^2}{m^*_{e,h}} + \frac{k_y^2}{m^*_{e,h}} + \frac{k_z^2}{m^*_{e,h}}\right), \tag{2.11}$$

where $m^*_{e,h}$ is the effective mass for electrons in the conduction band or holes in the valence band [42].

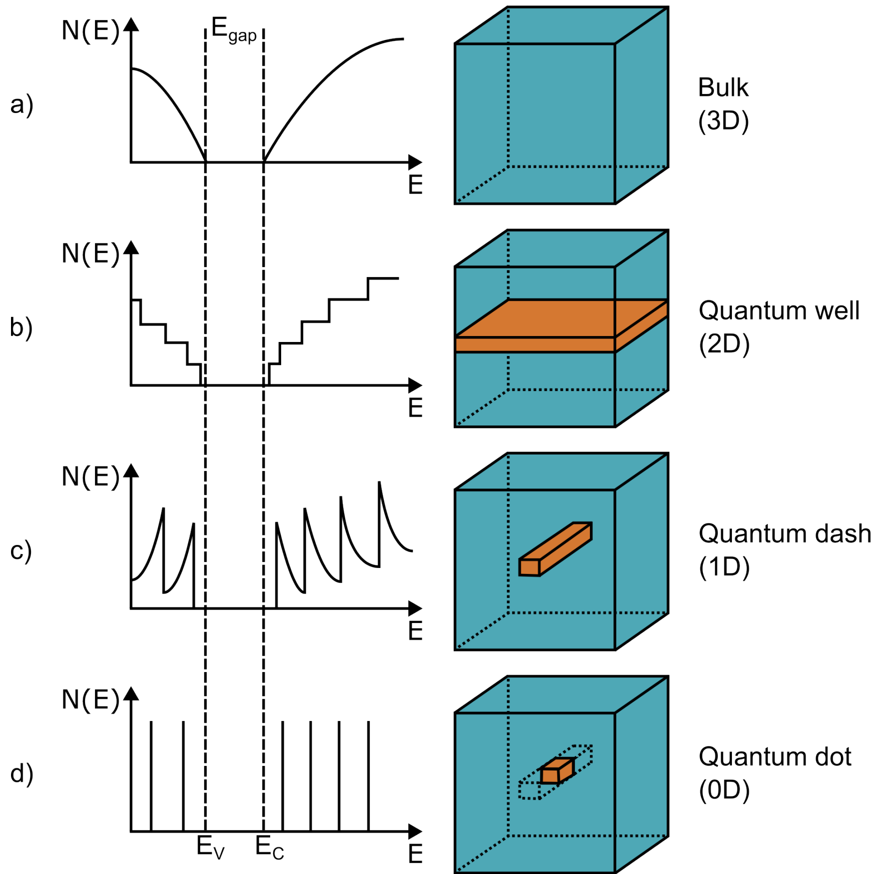

FIGURE 2.3: Density of states for a) a bulk semiconductor, b) a quantum well (2D), c) a quantum wire or quantum dash (1D), and d) a quantum dot (0D). E_V and E_C mark the valence band edge and conduction band edge, respectively. Adapted from [21].

The electronic density of states (DOS) describes the number of available electronic states per unit energy and unit volume. For a bulk three-dimensional semiconductor with a parabolic band dispersion, the density of states is $N_{3D}(E) \propto \sqrt{E}$, as illustrated in Figure 2.3 a) [43].

By combining semiconductor materials with different band gaps, heterostructures can be formed in which the motion of electrons and holes is restricted by potential barriers in one, two, or all three spatial directions. Significant modifications

of the carrier eigenstates and the density of states occur when the characteristic confinement length becomes comparable to or smaller than the carrier de Broglie wavelength,

$$\lambda_{e,h}^{\text{De Broglie}} = \frac{2\pi\hbar}{\sqrt{3m_{e,h}^{*}k_B T}}, \tag{2.12}$$

where k_B denotes the Boltzmann constant and T the temperature [21].

When carrier motion is confined in one spatial direction, for example along the z axis over a length L_z, a two-dimensional system is obtained. In this case, the motion in the x,y-plane remains free and separable from the confined direction. The in-plane energy contribution is given by

$$E_{x,y} = \frac{\hbar^2 k_x^2}{2m_{e,h}^{*}} + \frac{\hbar^2 k_y^2}{2m_{e,h}^{*}}, \tag{2.13}$$

while quantization in the confinement direction, under the assumption of infinitely high potential barriers, leads to the eigenvalues

$$E_{z,n} = \frac{\hbar^2}{2m_{e,h}^{*}}\left(\frac{n\pi}{L_z}\right)^2, \qquad n = 1, 2, 3, \ldots, \tag{2.14}$$

which correspond to the solutions of the particle-in-a-box problem. The total energy is obtained as $E = E_{x,y} + E_{z,n}$ and the band structure along k_x and k_y therefore consists of a series of parabolic subbands indexed by n. For such a system, the density of states exhibits a characteristic step-like behavior, as shown in Figure 2.3 b), with each subband contributing a constant density of states and the stair positions are given by $E_{z,n}$ [43].

If confinement is imposed in two spatial directions, for instance along y and z, the system becomes effectively one-dimensional. In this case, the energies associated with the confined directions are quantized, while free motion remains along the x-axis. The corresponding energy eigenvalues are given by

$$E = \frac{\hbar^2 k_x^2}{2m_{e,h}^{*}} + E_{l,n} = \frac{\hbar^2 k_x^2}{2m_{e,h}^{*}} + \frac{\hbar^2}{2m_{e,h}^{*}}\left(\frac{l\pi}{L_y}\right)^2 + \frac{\hbar^2}{2m_{e,h}^{*}}\left(\frac{n\pi}{L_z}\right)^2. \tag{2.15}$$

In the one dimensional case the density of states follows an inverse energy relationship $N_{1\text{D}}(E) \propto \sum_{l,n} (E - E_{l,n})^{-1/2}$, as depicted in Figure 2.3 c) [43].

Finally, confinement in all three spatial directions results in a zero-dimensional system. In this case, the carrier energies are fully quantized and given by

$$E = E_{j,l,n} = \frac{\hbar^2}{2m^*_{e,h}} \left[\left(\frac{j\pi}{L_x} \right)^2 + \left(\frac{l\pi}{L_y} \right)^2 + \left(\frac{n\pi}{L_z} \right)^2 \right]. \tag{2.16}$$

As a consequence, the density of states consists of a discrete set of delta-like peaks, expressed by the Dirac delta function $N_{0D}(E) \propto \sum_{j,l,n} \delta(E - E_{j,l,n})$. This fully discrete density of states, shown schematically in Figure 2.3 d), underlies the atom-like optical properties of semiconductor quantum dots [43].

2.3 Semiconductor quantum dots

In epitaxially grown semiconductor heterostructures, quantum dots (QDs) are typically formed through self-assembly processes such as Stranski-Krastanov growth, local droplet etching, or droplet epitaxy. Depending on the growth technique and material system, the resulting QDs can exhibit a wide range of shapes, sizes, and symmetries, giving rise to different effective confinement potentials for electrons and holes [21].

For QDs with complex geometries and material compositions, the electronic structure generally has to be determined using numerical methods. For analytical calculations of QD eigenenergies, a commonly used approach is based on a parabolic confinement potential. This description is applicable to single-particle states in QDs with a lens-shaped geometry and strong confinement along the growth direction and is known as the Fock-Darwin model [44, 45].

The strong confinement in the growth (z-) direction allows for an approximate separation of variables in the Schrödinger equation using the adiabatic approximation [46]. The QD wavefunction is factorized as

$$\Psi(x, y, z) = \Phi_n(z)\, \chi(x, y), \tag{2.17}$$

which separates motion along the strongly confined direction from motion in the weakly confined lateral plane. This reduces the three-dimensional problem to a one-dimensional equation in the z direction and a two-dimensional equation in the xy-plane. The approximation assumes negligible coupling between the lateral and vertical carrier dynamics, a condition that is well satisfied for QDs with a sufficiently large aspect ratio [47].

In large and weakly confined QDs the confinement along the growth direction can be insufficient to enforce a clear separation of vertical and lateral energy scales. As a result, the adiabatic separation of the wavefunction in Equation 2.17 becomes only approximate and the electronic structure might be more appropriately described using a full three-dimensional approach [47].

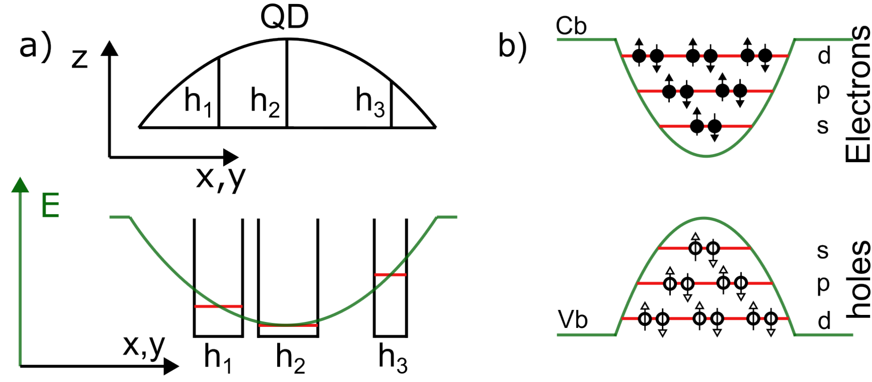

FIGURE 2.4: a) Sketch of the adiabatic approximation for a QD. Strong confinement in the z direction gives rise to an effective harmonic confinement potential in the xy-plane. Adapted from [48]. b) Discrete energy states in a harmonic potential. Their occupation is limited by the Pauli exclusion principle. Labeling follows the conventional atomic-shell notation. Adapted from [21].

The adiabatic approximation for a lens shaped QD is sketched in Figure 2.4 a). The one-dimensional confinement problem along z is determined by the QD thickness at lateral distance r from the dot center. Solving this yields the lowest confined state $\Phi_1(z)$ and an associated energy $E_{1D}(r)$, which acts as an effective potential for the two-dimensional Schrödinger equation [49]. Because of the strong confinement and finite potential height due to the band offset between QD and barrier material, typically, only the lowest state is considered [21]. For lens-shaped QDs, this effective lateral confinement is well approximated by a harmonic potential,

$$V_{\text{eff}}(r) = \frac{1}{2} m^* \,\omega_0^2 r^2, \tag{2.18}$$

which has been solved under the assumption of an optional magnetic field $\vec{B}$ applied along the z-direction [44, 45]. The resulting eigenenergies of the single carrier states are

$$E_{n,l} = (2n + |l| + 1)\,\hbar\sqrt{\omega_0^2 + \frac{1}{4}\omega_c^2} \pm \frac{1}{2} l\hbar\omega_c, \tag{2.19}$$

where $n = 0, 1, 2, \ldots$ denotes the radial quantum number, $l = 0, \pm1, \pm2, \ldots$ the angular momentum quantum number and $\omega_c = eB/m^*$ the cyclotron frequency, with the magnetic strength B [50]. Without the magnetic field the energies become a series of equidistant states,

$$E_{n,l} = (2n + |l| + 1)\,\hbar\omega_0. \tag{2.20}$$

Due to Pauli's exclusion principle each state can only be occupied by a limited number of carriers which is given by the degeneracy

$$d = 2(2n + |l| + 1) = 2, 4, 6, \ldots, \quad (2.21)$$

where the factor of 2 accounts for spin degeneracy. In analogy to atoms these shells are conventionally labeled as *s*-, *p*-, *d*-shells, as shown in Figure 2.4 b) [21].

QDs fabricated by infilling of local droplet-etched (LDE) nanoholes deviate from the idealized lens-shaped geometry commonly assumed in the Fock-Darwin model. As a result of the nanohole geometry and the infilling process, such structures are more accurately described by a cone-shell morphology, in which the base of the cone is slightly indented at its center [51].

Despite these geometric differences, numerical calculations have demonstrated that, for a representative GaAs/AlGaAs LDE quantum dot with a height of 19 nm and a radius of 35 nm, the calculated single-particle eigenenergies are in very good agreement with the predictions of the Fock-Darwin model in the absence of an external electric field [50]. Small deviations from the ideal Fock-Darwin spectrum are observed, however, in the form of an energy offset that increases with $|l|$, leading to a departure from the strictly equidistant level spacing predicted for $B = 0$, as described in Equation 2.20. Nevertheless, the overall level structure remains well captured, supporting the use of the Fock-Darwin model as a first-order description of single-particle states in droplet-etched QD geometries [50].

2.4 The biexciton-exciton cascade

The electronic states introduced in the previous section describe single electrons and holes confined in a quantum-dot potential. When multiple charge carriers are present in a QD, Coulomb interactions between electrons and holes give rise to multiparticle states, collectively referred to as excitons.

The simplest excitation configuration in a QD is the neutral exciton (X), which consists of one electron occupying the lowest conduction-band state and one hole occupying the highest valence-band state.

In III-V zincblende semiconductors, the conduction-band edge is formed from *s*-like atomic orbitals with angular momentum $L = 0$. As a result, the electron states are characterized by a total angular momentum $j_e = \frac{1}{2}$ with angular momentum projections $m_e = \pm\frac{1}{2}$. On the other hand, the valence band states hybridize from p-type orbitals and carry an angular momentum of $L = 1$ at the Brillouin-zone center $(\vec{k} = 0)$. The valence band is thus split by spin-orbit interaction into a fourfold-degenerate heavy-hole and light-hole band with total angular momentum $j_h = \frac{3}{2}$ and projections $m_{hh} = \pm\frac{3}{2}$ (heavy-hole) and $m_{lh} = \pm\frac{1}{2}$ (light-hole), as well as a lower-lying split-off band with $j_{so} = \frac{1}{2}$ and $m_{so} = \pm\frac{1}{2}$ [41].

In a quantum-dot confinement potential, the degeneracy between light-hole and heavy-hole states is lifted due to their different effective masses (see Equation 2.16).

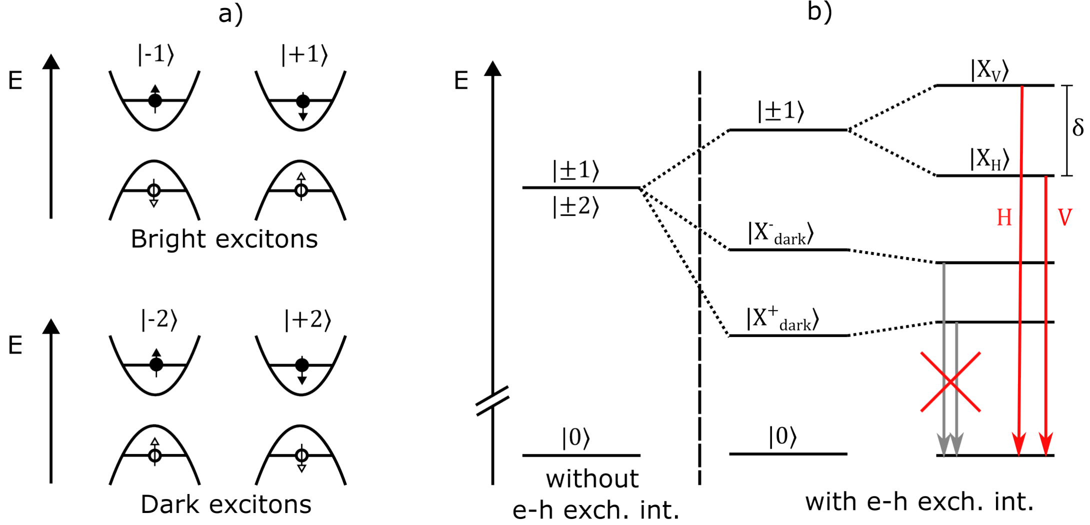

FIGURE 2.5: a) Neutral exciton states in a QD. The ground states are occupied by one electron-hole pair, giving rise to four spin configurations. b) Energetic splitting of exciton states due to the electron-hole exchange interaction. The exchange first separates bright and dark excitons and lifts the degeneracy of the dark states. In QDs with in-plane asymmetry, the bright states are further split by the fine-structure splitting δ. Adapted from [21].

As a consequence, the heavy-hole states form the highest-energy valence-band states and dominate the hole ground state [21]. Additional energetic separation can be introduced by strain effects: compressive strain enhances the heavy-hole-light-hole splitting, while tensile strain can reduce or even invert the ordering [52]. Even in nominally strain-free QDs, the valence-band ground state remains predominantly heavy-hole in character [21].

Assuming a predominantly heavy-hole like valence band, the total angular momentum projection of the neutral exciton becomes

$$M = m_e + m_{hh} = \pm 1, \pm 2. \tag{2.22}$$

The states with $M = \pm 2$ are forbidden in electric-dipole transitions because a photon cannot carry angular momentum ± 2. These states are therefore non-radiative and are referred to as dark excitons [53]. The states with $M = \pm 1$, shown in Figure 2.5 a), are optically active and radiatively decay by emitting right- ($|+1\rangle$) or left-circularly ($|-1\rangle$) polarized photons [21].

In the single-particle picture, the bright and dark exciton states are degenerate. However, the exchange interaction between electron and hole lifts this degeneracy, resulting in an energy splitting. The electron-hole exchange can be separated into short-range and long-range contributions. The short-range contribution comes from the part of the electron-hole exchange integral where electron and hole wavefunctions overlap at the same unit cell and is very sensitive to the symmetry of the crystal lattice. In zincblende semiconductors, this interaction separates the bright and dark

excitons and also lifts the degeneracy between the two dark states [54].

The long-range exchange interaction arises from the nonlocal part of the exchange integral and contributes to the bright and dark exciton splitting. Additionally, it affects the bright exciton states if the in-plane rotational symmetry of the QD is broken. This lifts the degeneracy between the two bright states and produces the fine-structure splitting (FSS), denoted by δ [54].

The resulting new eigenstates of the bright states are superpositions of the original state

$$|X_{H,V}\rangle = \frac{1}{\sqrt{2}} \left(|+1\rangle \pm |-1\rangle \right), \tag{2.23}$$

corresponding to two orthogonally oriented transition dipoles in the QD plane and are typically found along the main crystalline axis. Their radiative decay produces linearly polarized photons, labeled horizontal (H) and vertical (V), with an energy difference equal to the FSS. Nearly all self-assembled QDs exhibit a finite FSS because perfect in-plane symmetry is rarely achieved during growth. However, it is possible to tune the FSS using external perturbations such as strain, electric fields, or magnetic fields [21].

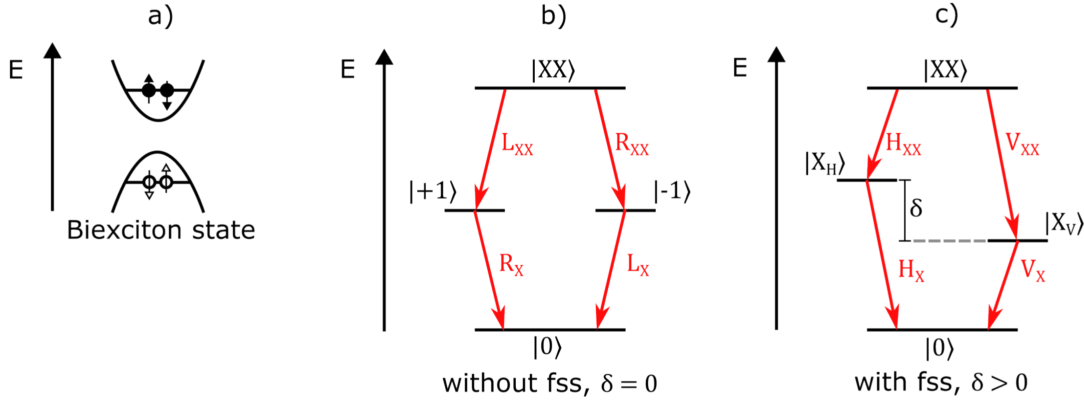

FIGURE 2.6: a) Sketch of the biexciton state. b) The biexciton-exciton cascade for an ideal QD without FSS. c) The biexciton-exciton cascade in a QD with finite FSS. Adapted from [21].

The neutral biexciton state (XX) consists of two electrons in the lowest conduction-band state and two holes in the highest valence-band state, with both electron and hole pairs occupying antiparallel spin configurations, as illustrated in Figure 2.6 a). The direct radiative recombination of the biexciton to the ground state is dipole forbidden. Instead, the biexciton decays through an intermediate exciton state before reaching the ground state. This sequential decay constitutes the biexciton-exciton cascade and enables the generation of polarization-entangled photon pairs [55].

For a QD with vanishing FSS, the exciton eigenstates $|\pm1\rangle$ are degenerate. As shown in Figure 2.6 b), the biexciton can decay through two indistinguishable paths: (1) emission of a left-circularly polarized photon (L) followed by a right-circularly

polarized photon (R), or (2) emission of an R-polarized photon followed by an L-polarized photon. Unless the photons polarisation states are measured these paths are indistinguishable and the two-photon state is the coherent superposition

$$\left|\Psi^{+}\right\rangle = \frac{1}{\sqrt{2}}\left(\left|L_{XX}R_{X}\right\rangle + \left|R_{XX}L_{X}\right\rangle\right), \tag{2.24}$$

which is a maximally entangled Bell state [56] of the same form as Eq. 2.2. In the circular basis, measurement of one photon yields L or R with equal probability, while the second photon is always found in the opposite polarization, resulting in perfect anticorrelation.

By transforming the circular polarization states, the Bell state can also be expressed in the rectilinear (H/V) and diagonal (D/A) bases:

$$\left|\Psi^{+}\right\rangle = \frac{1}{\sqrt{2}}\left(\left|H_{XX}H_{X}\right\rangle + \left|V_{XX}V_{X}\right\rangle\right), \tag{2.25}$$

$$\left|\Psi^{+}\right\rangle = \frac{1}{\sqrt{2}}\left(\left|D_{XX}D_{X}\right\rangle + \left|A_{XX}A_{X}\right\rangle\right). \tag{2.26}$$

Thus, the photon pair appears entangled in all three polarization bases [57].

For QDs with nonzero FSS ($\delta > 0$), the bright exciton eigenstates are linearly polarized $|X_H\rangle$, $|X_V\rangle$ states, which are superpositions of the $|\pm 1\rangle$ states [57]. After a residence time time t_{XX} in the biexciton (XX) state, the biexciton radiatively decays by emitting either an H-polarized or V-polarized photon, depending on whether the system transitions into $|X_H\rangle$ or $|X_V\rangle$ (Figure 2.6 c)). Consequently, the system is projected into the symmetric superposition of the $|H_{XX}H_X\rangle$ and $|V_{XX}V_X\rangle$ states [58].

The system remains in this superposition for a time delay τ, before the second radiative transition emits the exciton photon (H_X or V_X) [58]. Due to the energetic splitting δ between the two exciton states, the two components of the exciton state will develop a relative phase difference $\Phi = \delta\tau/\hbar$ over the time τ [59].

With the relative phase factor $e^{i\Phi}$ between the two paths the two-photon state then becomes

$$|\Psi\rangle = \frac{1}{\sqrt{2}}\left(\left|H_{XX}H_{X}\right\rangle + e^{i\delta\tau/\hbar}\left|V_{XX}V_{X}\right\rangle\right), \tag{2.27}$$

i.e., a time-evolving Bell state, similar in form to the state expected from a QD without FSS, but with the additional phase term [21, 58, 59].

Consequently, the state corresponds to the $|\Psi^{+}\rangle$ state in Equation 2.25 only for $\tau = 2\pi N\hbar/\delta$ (N is an integer) and the fidelity f^{+} between the two will generally exhibit an oscillatory behavior as a function of τ [58, 60].

In time-integrated measurements, coincidences are accumulated over photon pairs with all possible time delays τ, such that the phase factor $e^{i\delta\tau/\hbar}$ is effectively

averaged over many values [21]. For sufficiently large FSS and/or exciton lifetimes, the off-diagonal elements of the two-photon density matrix are strongly reduced and the measured polarization state approaches one with predominantly classical correlations [60, 61].

However, entanglement in time-integrated measurements can be preserved if δ is smaller than the exciton homogeneous linewidth Γ, such that the phase evolution is slow on the relevant coherence time scale and the phase relationship remains well defined [21]. In the energy picture, this corresponds to overlapping spectral lines within the homogeneous linewidth, such that the decay paths are not distinguishable by photon energy and no which-path information is available, thereby preserving entanglement [21, 58].

The effect of FSS can also be mitigated by spectral [62] or temporal [58] post-selection (time-gating), to select only photon pairs with high fidelity [60]. However, these post-selection schemes introduce photon pair losses and limits on-demand generation and in particular temporal filtering increases the experimental complexity [21, 60]. As such, a more favorable strategy is to eliminate the FSS itself, for example via the growth of symmetric QDs [60].

Chapter 3

Epitaxy

Epitaxy describes the growth of ordered atomic layers on a substrate, in which the deposited material inherits the lattice orientation of the underlying crystal. Among the available growth techniques, molecular beam epitaxy (MBE) is particularly well suited for investigating epitaxial processes, as it allows for monolayer-resolved film deposition with sharp interfaces and precise control of material fluxes and growth parameters. This chapter first introduces the MBE method, followed by the principles of epitaxial growth kinetics. The fundamental growth modes are then discussed, together with general considerations in III-V epitaxy, i.e., lattice constants and band gap energies in ternary alloys as well as the temperature dependence of the band gap. The chapter concludes with an introduction to the local droplet etching (LDE) technique, which is central to this dissertation.

3.1 Molecular beam epitaxy

Molecular Beam Epitaxy (MBE) is one of the most versatile and precise growth techniques for semiconductors. Developed in the early 1970s by Arthur and Cho [63, 64], MBE employs beams of atoms or molecules directed onto a heated crystalline substrate under ultra-high vacuum to epitaxially grow semiconductor films. The growth environment in MBE provides a high degree of control over material composition, film thickness and minimizes impurity incorporation. Owing to this level of control, MBE has become a widely used method in semiconductor research.

While different configurations of MBE systems exist, the following discussion focuses on solid-source III-V MBE, which is directly relevant to the work of this dissertation. A sketch of such a system can be seen in Figure 3.1. In a typical system, Knudsen-type effusion cells serve as sources of the elemental group-III and group-V species [63, 64]. The cells consist of high-purity crucibles, often made of pyrolytic boron nitride or graphite, containing the constituent elements, which are typically solid at room temperature. The crucibles are resistively heated, usually by tungsten or tantalum filaments, to evaporate or sublimate the material at controlled rates [65].

Other approaches to provide beams of evaporated material are also in use, such as electron-beam evaporation or laser heating of the source, though these are less common in III-V MBE. For group-V sources, special variants known as *cracker cells*

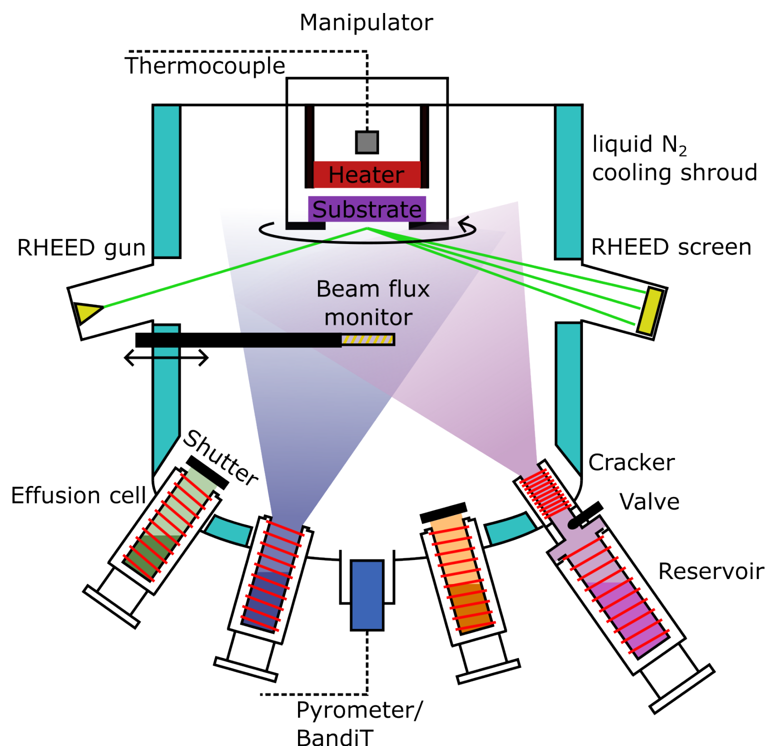

FIGURE 3.1: Schematic of a solid-source MBE growth chamber. The system consists of Knudsen-type effusion cells equipped with shutters, directed towards a substrate holder with heater and rotation stage. Growth takes place under ultra-high vacuum, maintained by cryogenic shrouds and dedicated pumps (not shown for clarity). Beam equivalent pressure can be measured by a flux gauge and in-situ growth monitoring is provided by a RHEED gun and screen.

are employed [65]. These devices add a high-temperature zone downstream of the crucible, which dissociates tetramer molecules such as As_4 or P_4 into dimers (As_2, P_2). Modern valved cracker cells additionally incorporate a fast mechanical valve, enabling group-V flux control without requiring thermal cycling of the cell temperature.

In addition to group-III and group-V sources, dedicated cells are installed for doping. For n-type doping in GaAs, silicon is typically used, since at usual growth conditions it incorporates preferentially on the group-V (As) sublattice. For p-type doping, beryllium or carbon are commonly employed. Carbon in particular is attractive because it is non-toxic and exhibits low diffusivity in GaAs, making it well-suited for sharp doping profiles [66].

The material evaporated from the source cells forms molecular beams that propagate line-of-sight across the UHV chamber toward the substrate. During growth, the cells are maintained at their operating temperatures, while the flux can be modulated abruptly by fast-acting mechanical shutters placed in front of each cell. This shutter control, combined with the slow growth rates ranging typically from a few $0.01\,\mathrm{ML\,s^{-1}}$ to $\sim 1\,\mathrm{ML\,s^{-1}}$, enables the precise fabrication of atomically sharp heterointerfaces and low-dimensional structures, such as quantum wells, quantum wires, and quantum dots. Absolute fluxes are monitored and routinely calibrated via beam

equivalent pressure (BEP) measurements using ion gauges.

The MBE growth chamber operates at base pressures on the order of 10^{-10} mbar [64]. At such ultra-high vacuum (UHV) conditions, the mean free path of residual gas molecules greatly exceeds the typical chamber dimensions, ensuring ballistic transport of the molecular beams without collisions [42]. The extremely low pressure also suppresses background impurities, enabling the growth of semiconductor layers with high optical and electronic quality.

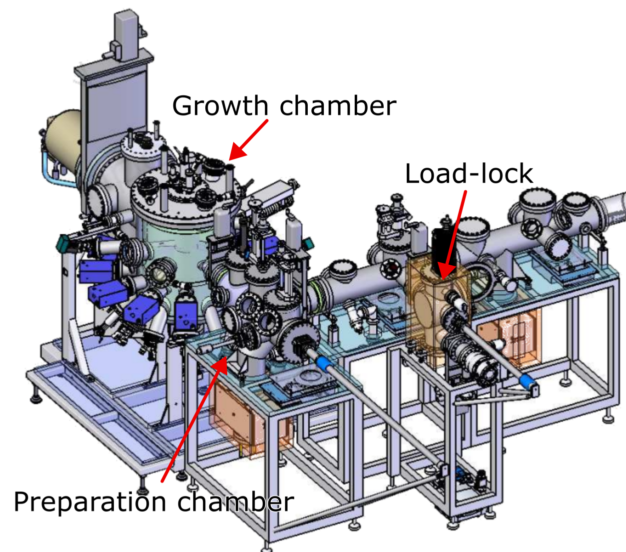

FIGURE 3.2: Skematic of the Octoplus 500 MBE system by Dr. Eberl MBE-Komponenten GmbH, employed by Prof. Dr. Dirk Reuters group in Paderborn University [67].

A complete MBE system typically consists of interconnected chambers, such as load-lock and preparation chambers, which are separated from the growth chamber by vacuum valves. In the system used during this work (see Figure 3.2), wafers are first loaded into the load-lock, where the chamber is then heated to 120 °C for 8 h. Afterwards each wafer is further degassed at 200–300 °C before transfer into the MBE chamber. This deliberate degassing of substrates in combination with the architecture permits substrate transfers without breaking vacuum and ensures that the growth chamber retains its cleanliness.

The UHV environment is maintained by a combination of pumping technologies, including turbomolecular pumps, ion-getter pumps, and cryogenic pumps, supported by liquid-nitrogen-cooled cryopanels. These cryogenic shrouds improve chamber purity by condensing residual gases such as water vapor and hydrocarbons, and simultaneously protect viewports and internal surfaces from unwanted deposition [65].

The substrate stage is a central component of any MBE system, as it defines the conditions under which impinging atoms and molecules are incorporated into crystalline layers. In the system used here, substrates are mounted into a manipulator

and oriented facing downwards toward the effusion cells. During growth the manipulator can be rotated, averaging out geometric flux variations from the sources and thereby ensuring uniformity of the deposited layer across the wafer surface.

Accurate substrate temperature control is essential in MBE, since surface adatom mobility, desorption rates, and incorporation pathways are strongly temperature dependent. In this system, the manipulator incorporates a radiative heater allowing for the controlled substrate heating depending on material system and growth process. The heater temperature is monitored by a thermocouple, however, this does not directly reflect the temperature of the substrate itself, as the thermocouple is not in contact with the wafer. For precise calibration, additional methods such as blackbody pyrometry and band-edge thermometry (BandiT) are employed, which enable accurate substrate temperature determination during growth.

3.2 Growth kinetics

A complete formal description of epitaxial growth involves both the thermodynamics, which describe the direction a system tends to reach and the conditions near the thermodynamic equilibrium, and the atomistic kinetics of surface processes. A detailed, quantitative treatment of epitaxial growth is beyond the scope of this dissertation and can be found in standard references [42, 65]. In the following, only the concepts relevant to the growth of $In_xAl_{1-x}As$ and $In_yGa_{1-y}As$ layers and to the process of local droplet etching (LDE) are introduced.

Thermodynamics provides the general framework for understanding equilibrium properties such as surface energies, island shapes, or nucleation thresholds, as will be discussed in Section 3.3. However, the short-time and nanoscale dynamics of film formation are governed primarily by kinetic effects, which describe how individual atoms attach, diffuse, or detach on a crystal surface.

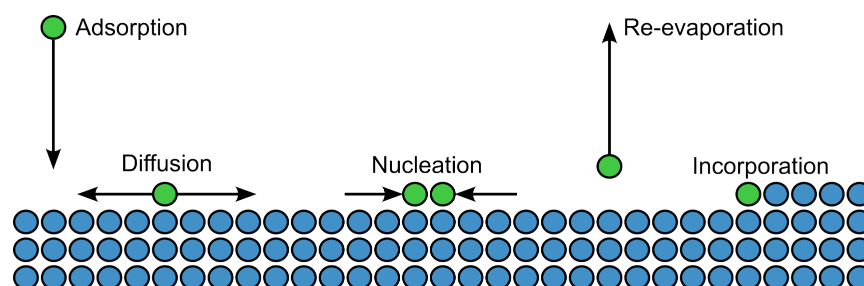

FIGURE 3.3: Schematic illustration of elementary adatom processes during epitaxial growth. After adsorption onto the substrate surface, adatoms (green) may diffuse across the surface, nucleate into clusters with other adatoms, incorporate into existing steps or islands, or desorb by re-evaporation. Detachment from unstable nuclei, not depicted here, can also occur.

After their arrival on the substrate surface, impinging atoms – referred to as *adatoms* once adsorbed – initially bind weakly to the substrate via van der Waals interactions. These adatoms can then migrate across the surface until one of several

competing processes occurs, as illustrated schematically in Figure 3.3. They may encounter one another and form a stable nucleus (*nucleation*), attach to existing islands or steps (*incorporation*), or desorb from the surface by thermal re-evaporation. In addition, atoms incorporated in small, unstable clusters can detach again, particularly at elevated substrate temperatures.

The kinetics of these processes are often treated as activated phenomena that follow Arrhenius-type rate expressions. Assuming fixed lattice sites on the substrate, the general temperature dependence of any rate $\nu(T)$ can be written as

$$\nu(T) = \nu_0 \exp\left(-\frac{E}{k_\mathrm{B}T}\right), \tag{3.1}$$

where ν_0 is the attempt frequency, E the activation energy of the process, T the substrate temperature, and k_B the Boltzmann constant [65].

Surface migration can be described by a nearest-neighbor hopping process, where the rate of jumps between adjacent lattice sites ν_d follows

$$\nu_d = \nu_{d,0} \exp\left(-\frac{E_d}{k_\mathrm{B}T}\right), \tag{3.2}$$

with E_d denoting the surface diffusion barrier. Elevated substrate temperatures increase the probability of overcoming this barrier, thereby enhancing adatom mobility. The adatom performs a random walk on the surface, with its mean square displacement after time t given by

$$\langle \lambda^2 \rangle = \nu_d a^2 t, \tag{3.3}$$

where a is the mean jump distance, typically corresponding to the distance of two lattice sites on the surface. From this relation, a temperature-dependent diffusion coefficient (or diffusivity) D can be defined as

$$D = \frac{\langle \lambda^2 \rangle}{\eta t} = \left(\frac{a^2}{\eta}\nu_{d,0}\right) \exp\left(-\frac{E_d}{k_\mathrm{B}T}\right) \tag{3.4}$$

$$= D_0 \exp\left(-\frac{E_d}{k_\mathrm{B}T}\right), \tag{3.5}$$

where η is the number of equivalent neighboring sites accessible for a single jump and $D_0 = (a^2/\eta)\nu_{d,0}$ represents a temperature-independent prefactor.

Because desorption places an upper limit on the residence time of adatoms, the average surface lifetime τ depends on the desorption barrier E_{des} as $\tau \propto \exp(E_{des}/k_\mathrm{B}T)$. However, E_{des} is generally smaller than E_d and exceeds several times $k_\mathrm{B}T$ at typical

growth temperatures. Consequently, the diffusion length $\lambda = \sqrt{D\tau}$ is largely governed by the diffusivity D [42]. The diffusion coefficient constitutes a critical parameter for layer growth and especially droplet nucleation during the LDE process.

3.3 Growth modes

The interplay of adsorption, diffusion, incorporation, desorption, and detachment processes ultimately governs the morphology that emerges during epitaxial film growth. Which growth regime materializes in practice is determined not only by these kinetic factors but also by the balance of interface energies as well as by strain in the growing layer. These considerations lead to the classification of the fundamental epitaxial growth modes.

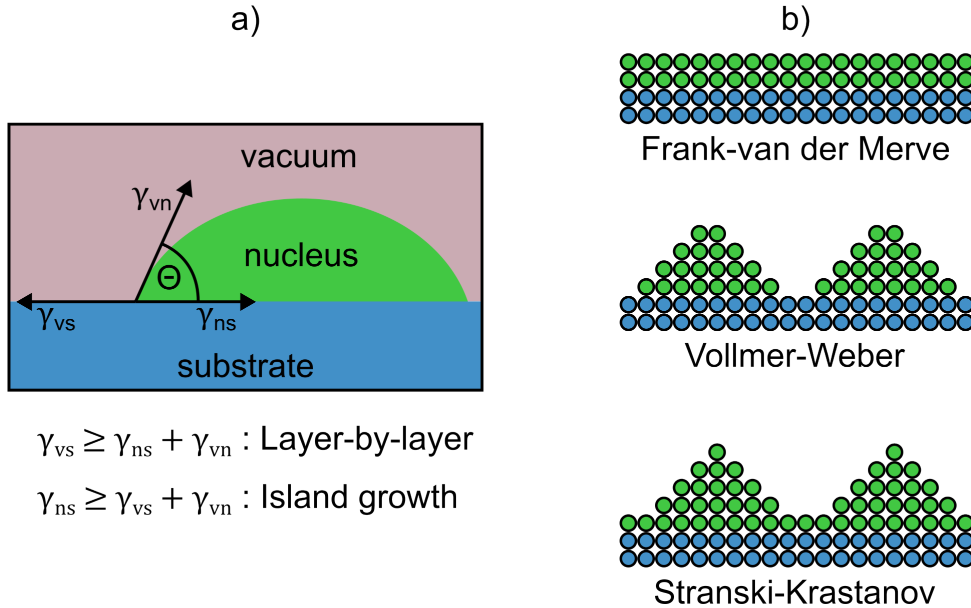

FIGURE 3.4: (a) Young's construction of the contact angle Θ for a nucleus on a substrate, determined by the balance of interface energies γ_{ij}. (b) The three principal epitaxial growth modes: Frank-van der Merwe (layer-by-layer), Volmer-Weber (island growth), and Stranski-Krastanov (layer-plus-island). Adapted from [42]

From a macroscopic perspective, epitaxial layer growth on a surface is governed by the balance of interface energies γ_{ij}. For nucleation on a substrate in a vacuum environment, as illustrated in Figure 3.4 a), the relevant interface energies are the vacuum-substrate energy γ_{vs}, the nucleus-substrate energy γ_{ns}, and the vacuum-nucleus energy γ_{vn}. The equilibrium shape of a nucleus on the substrate is determined by the balance of these energies and is described by Young's relation [42]:

$$\cos\Theta = \frac{\gamma_{vs} - \gamma_{ns}}{\gamma_{vn}}. \tag{3.6}$$

Here, Θ denotes the contact angle of the nucleus on the substrate and can range from 0°, corresponding to complete wetting, to 180°, corresponding to no wetting.

Complete wetting ($\Theta = 0$) implies that the deposited material spreads uniformly across the substrate surface. This situation occurs when the energy of the vacuum-substrate interface is greater than or equal to the sum of the nucleus-substrate and vacuum-nucleus interfacial energies, i.e., $\gamma_{vs} \geq \gamma_{ns} + \gamma_{vn}$. Under this condition, the deposited atoms exhibit a stronger affinity for the substrate than for each other, resulting in the formation of atomically flat layers. This growth mode is referred to as the Frank-van der Merwe (FvdM) or layer-by-layer growth mode [42].

Reversing this, so that the atoms of the nucleus are more strongly bound to each other the condition changes to $\gamma_{ns} \geq \gamma_{vs} + \gamma_{vn}$. This results in the spontaneous nucleation of islands directly on the bare substrate and is is known as the Volmer-Weber (VW) growth mode [42].

Between these limiting cases lies the Stranski-Krastanov (SK) growth mode. Here, a film initially wets the substrate, forming a pseudomorphic two-dimensional wetting layer. However, once this exceeds a critical thickness elastic strain relaxation leads to the formation of three-dimensional islands, partially relaxing strain at the expense of increased surface energy [68]. This SK transition underlies the self-assembly of InAs/GaAs quantum dots and many other heteroepitaxial nanostructures [42].

The source of strain is the lattice mismatch

$$f = \frac{a_{film} - a_{sub}}{a_{sub}}, \tag{3.7}$$

where a_{film} and a_{sub} are the lattice constants of film and substrate. Films below the critical thickness [68] remain coherent and elastically strained. When this thickness is exceeded, strain relaxation may occur either via the formation of misfit dislocations or by transition into the SK growth mode. Whereas controlled strain-driven islanding can be harnessed for quantum dot self-assembly, uncontrolled relaxation via defects reduces optical and electrical quality, highlighting the importance of lattice matching when defect-free films are required [42].

3.4 Material and structural considerations in III–V epitaxy

While binary III-V semiconductors such as GaAs or InP possess fixed lattice constants and band gap energies at a given temperature, ternary alloys, for example $In_xAl_{1-x}As$, allow these material parameters to be tuned through the alloy composition, which plays a crucial role in heterostructure design and epitaxial growth.

Lattice constant: Vegard's law

For the lattice constant, the empirical Vegard's law provides a useful approximation by assuming a linear interpolation between the lattice constants of the binary constituents. For a ternary alloy $A_xB_{1-x}C$, formed from the materials AC and BC

with lattice constants a_{AC} and a_{BC} and sharing the same crystal structure, the lattice constant of the alloy is given by [42]

$$a_{\mathrm{alloy}}(x) = x\, a_{\mathrm{AC}} + (1-x)\, a_{\mathrm{BC}}. \tag{3.8}$$

Lattice-matched growth of $\mathrm{In}_x\mathrm{Al}_{1-x}\mathrm{As}$ on InP, which has a room-temperature lattice constant of $a_{\mathrm{InP}} = 5.8697$ Å, requires a composition of approximately $x \approx 0.52$, corresponding to 52% InAs ($a_{\mathrm{InAs}} = 6.0583$ Å) and 48% AlAs ($a_{\mathrm{AlAs}} = 5.6611$ Å). The difference in thermal expansion among these materials is small: $\mathrm{In}_{0.52}\mathrm{Al}_{0.48}\mathrm{As}$ layers remain lattice matched to InP both at typical growth temperatures (505 °C, mismatch $f_{800K} = 0.035\,\%$) and at cryogenic temperatures ($f_{4K} = 0.036\,\%$) [69].

Band gap energy and bowing

In contrast to the lattice constant, the band gap energy $E_{g,\mathrm{alloy}}$ of a ternary alloy does not generally follow a simple linear dependence on composition. For a ternary alloy $\mathrm{A}_x\mathrm{B}_{1-x}\mathrm{C}$ with band gap energies $E_{g,\mathrm{AC}}$ and $E_{g,\mathrm{BC}}$ of its binary constituents, the band gap energy of the alloy is given by

$$E_{g,\mathrm{alloy}}(x) = x\, E_{g,\mathrm{AC}} + (1-x)\, E_{g,\mathrm{BC}} - b\, x(1-x), \tag{3.9}$$

where b denotes the bowing parameter, which depends on the specific material system and accounts for deviations from linear interpolation [42].

Temperature dependence of the band gap

In addition to composition, temperature has a strong effect on the band gap of semiconductors. The decrease of E_g with increasing temperature arises from both lattice expansion (changing the average bond distance) and electron-phonon interactions. This dependence is commonly described by the Varshni formula

$$E_g(T) = E_g(0) - \frac{\alpha T^2}{T+\beta}, \tag{3.10}$$

where $E_g(0)$ is the band gap at $T = 0\,\mathrm{K}$, and α and β are empirical material parameters obtained from experiment [42].

3.5 Local droplet etching

Local droplet etching (LDE) is a self-organized nanostructuring technique performed in a molecular beam epitaxy (MBE) environment, in which nanoscale holes are generated through the interaction of metallic droplets with a semiconductor surface.

The process exploits the energetics and kinetics of droplet formation, localized material removal, and subsequent surface reorganization, enabling the fabrication of well-defined nanostructures without the need for lithographic patterning.

LDE is closely related to droplet epitaxy (DE), which was introduced in 1991 [70]. In DE, liquid droplets first form on semiconductor surfaces from deposited metallic group-III material following a Volmer-Weber-type growth mode and are subsequently crystallized under an arsenic overpressure [70, 71]. In 2005, the group of Gregory Salamo at the University of Arkansas first introduced LDE, which emerged from studies of DE [72], showing that the group-III droplets can locally remove material from III-V semiconductor layers. The method was later systematically investigated and refined by Christian Heyn and co-workers at the University of Hamburg [73], who were also the first to demonstrate LDE-based QD fabrication by infilling and overgrowth of the etched nanoholes [19].

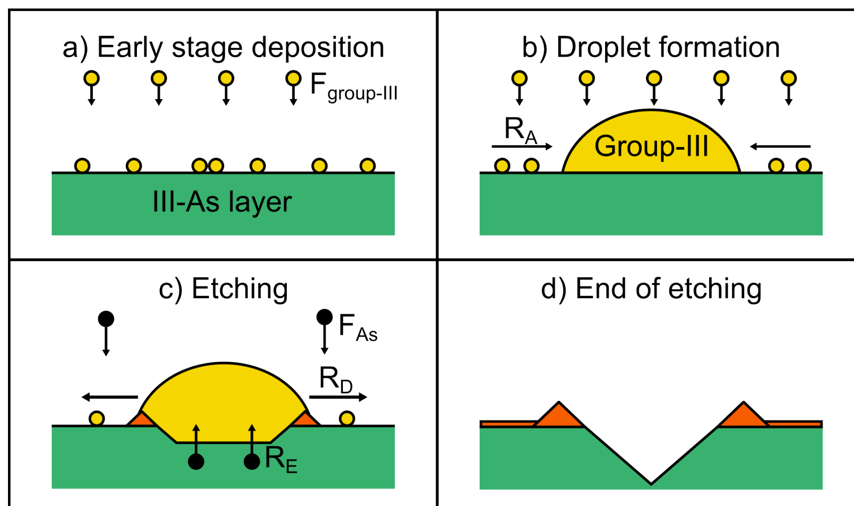

FIGURE 3.5: Schematic illustration of the LDE process, adapted from [74].

Figure 3.5 depicts the LDE process, which can be understood as a sequence of two main steps. In the first step, shown in Figure 3.5 a) and b), group-III material is deposited at low arsenic flux onto a group-III-arsenide surface, typically $Al_xGa_{1-x}As$. The arsenic flux is usually reduced by a factor of 10 to 100 compared to standard layer growth conditions, and typical deposition amounts of group-III material correspond to a few ML of layer-equivalent material deposited over a few seconds. The deposited group-III atoms (Ga, Al, In, or a combination thereof) adsorb onto the surface and – driven by surface energy minimization of the droplet material – aggregate to form liquid droplets in a Volmer-Weber-like growth mode [74].

In contrast to Stranski-Krastanov growth, where additional measures are often required to reduce the areal density of QDs, LDE intrinsically yields comparatively low droplet densities over the entire wafer, which can be tuned over several orders of magnitude by adjusting the process parameters. As such LDE provides straightforward and reproducible control of droplet density on a wafer scale without the need for elaborate growth protocols.

The overall droplet density n is determined by the total material deposited θ, material flux F, and substrate temperature T, and can be described by the classical nucleation model developed by J.A. Venables

$$n \propto F^p \cdot \theta^{1-z} \exp\left[\frac{E_n}{k_B T}\right], \tag{3.11}$$

where E_n is the nucleation-related activation energy, p the nucleation scaling exponent and z the coverage parameter [42, 75, 76].

E_n is a parameter which provides a compact measure of the temperature sensitivity of droplet nucleation and depends in the complete condensation 3D island nucleation regime on the critical nucleus size i, the binding energy of the critical nucleus E_i and the surface diffusion barrier energy E_d [75]

$$E_n = \frac{E_i + iE_d}{i + 2.5}. \tag{3.12}$$

The material deposition rate F and total deposited amount θ are related by the deposition time t,

$$\theta = F \cdot t. \tag{3.13}$$

The droplet density n and average droplet volume V are linked and can be expressed as

$$V = (\theta - \theta_w) \frac{N_0}{n} \frac{V_m}{N_A}, \tag{3.14}$$

where N_0 is the surface site density of the substrate, V_m the molar volume of the droplet material, N_A Avogadro's constant, and θ_w the critical material amount required for droplet formation. Droplet formation begins only after θ_w has been deposited, as this amount is consumed by surface reconstruction changes [77].

In the second step of the LDE process, depicted in Figure 3.5 c) and d), the liquid droplets locally etch into the semiconductor layer. This process is driven by the arsenic concentration gradient between the liquid droplet and the surrounding III-As substrate. Arsenic atoms diffuse from the substrate into the droplet, partially liquefying the interface and allowing the droplet to sink into the layer. The etching rate R_E can be approximated by

$$R_E = (x_{\mathrm{As,max}} - x_{\mathrm{As}})\, \nu \exp\left[-\frac{E_E}{k_B T}\right] \text{ for } x_{\mathrm{As}} < x_{\mathrm{As,max}}, \tag{3.15}$$

where x_{As} is the arsenic concentration in the liquid droplet, $x_{As,\mathrm{max}}$ the maximum solubility of arsenic in the droplet material, and E_E the activation energy [78]. The LDE process can be performed at a constant or variable temperature, allowing T to be adjusted between the droplet formation and etching steps to provide an additional control parameter.

Equation 3.15 shows that the etching rate becomes zero when $x_{\mathrm{As}} = x_{\mathrm{As,max}}$, i.e., when the droplet is saturated with arsenic. For $x_{\mathrm{As}} < x_{\mathrm{As,max}}$, etching proceeds, while for $x_{\mathrm{As}} \geq x_{\mathrm{As,max}}$, $R_E = 0$. In the case of Ga, the maximum solubility of As is limited to $x_{\mathrm{As,max}} \approx 5 \times 10^{-4}$ at a typical etching temperature of 550 °C for Ga droplets on $\mathrm{Al}_x\mathrm{Ga}_{1-x}\mathrm{As}$ layers [79]. Consequently, material transport would quickly halt without a mechanism that removes arsenic from the liquid droplet.

Such a removal mechanism is provided by the formation of a solid wall around the droplet, as illustrated in Figure 3.5 c). It is hypothesized that group-III atoms detach from the droplet surface and diffuse outward onto the surrounding layer, locally increasing the arsenic concentration x_{As}. When x_{As} exceeds $x_{\mathrm{As,max}}$, the droplet material crystallizes at the triple line at the droplet perimeter, forming a ring surrounding the droplet [74]. This process transfers arsenic from the substrate into the ring, consistent with observations showing that the volume of material removed from the hole equals the volume accumulated in the surrounding ring [80].

As mentioned previously, group-III material detaches during etching and diffuses across the surface. This surface diffusion is critical for the overall evolution of the structure and explains why a small residual arsenic flux is required during the etching step. In the absence of arsenic flux, diffusion of atoms from the droplet to the surface and vice versa would balance, preventing droplet consumption and thus inhibiting nanohole formation. The presence of arsenic flux breaks this equilibrium by inducing crystallization of diffused material on the surface, effectively capturing it and preventing its return to the droplet. Under these conditions, the droplet eventually vanishes, leaving behind a nanohole surrounded by a crystallized ring. The ring consists primarily of droplet material, while a thin crystallized layer of the same material covers the surface near the ring, its width determined by the diffusion length of the material [74].

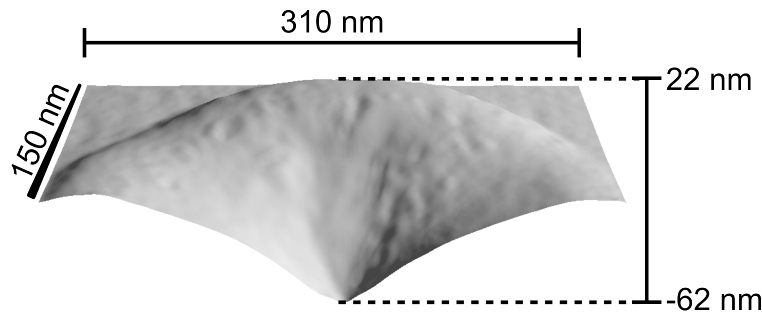

FIGURE 3.6: Chross-sectional AFM image of a nanohole with surrounding ring structure under a 30° viewing angle, etched into $\mathrm{In}_{0.52}\mathrm{Al}_{0.48}\mathrm{As}$ layers by depositing Al for 4 s at an As_2 flux of $p_{\mathrm{As2}} = 2 \times 10^{-7}$ mbar and deposition and etching temperature of $T_{\mathrm{etch}} = 435$ °C.

The diameter of the nanohole opening is correlated with the size of the initial droplet [77, 78]. The average etch depth h of the nanoholes is controlled by the etching rate and duration t_{etch} of the etching step, which can be terminated by increasing the arsenic flux to standard layer-growth conditions. If not terminated beforehand, the etching process stops when the droplet is fully consumed, and the achievable maximum depth h_{max} depends on

$$h_{\text{max}} \propto V \exp\left[-\frac{E_s}{k_B T}\right], \tag{3.16}$$

where V is the droplet volume, representing the available etching material, and activation energy E_s [77, 78]. However, it has been shown that for longer etching times, the droplet depth slightly decreases from h_{max} due to material diffusion from the surface layer back into the nanohole [81].

From Equations 3.11, 3.14, 3.15, and 3.16, the following critical process parameters for LDE can be identified:

- Substrate temperature T,
- Material deposition rate F,
- Material deposition amount θ,
- Choice of droplet and substrate materials, related to activation energies E and vibration frequency ν,
- Etching time t, and
- Residual arsenic flux.

To produce QDs, the nanoholes are infilled and overgrown in subsequent epitaxy steps, generating, for example, GaAs/$Al_xGa_{1-x}As$ QDs. Infilling is typically performed by pulsed deposition, where the group-III shutters are opened for short intervals (typically 1 s) followed by longer growth interruptions of 30–60 s. This sequence increases adatom diffusion length so that atoms diffuse into the nanoholes, infilling them from the bottom upward [19]. The infilled holes are subsequently capped, producing strain-free QDs that adopt the shape of the original nanohole.

Since the in-plane symmetry and size of the QDs strongly influences their optical properties, optimization of the nanohole base morphology is crucial. Consequently, the impact of the above process parameters on nanohole morphology has been the subject of extensive investigation in the GaAs/$Al_xGa_{1-x}As$ system [74, 81, 82, 83, 84].

Chapter 4

Experimental methods for sample characterization

This chapter provides an overview of the experimental techniques employed for the characterization of the samples grown during research on this work. It begins with a detailed discussion of atomic force microscopy (AFM), followed by an examination of scanning electron microscopy (SEM). Subsequently, the principles and applications of high-resolution X-ray diffraction (HRXRD) are presented. Finally, the chapter concludes with an analysis of photoluminescence (PL) spectroscopy, which was used to investigate the optical properties of the samples.

4.1 Atomic force microscopy

Atomic force microscopy (AFM) is a powerful technique that allows the measurement of surface topography with nanometer-scale resolution. Developed in 1986 by Binnig, Quate, and Gerber [85], an AFM maps the sample surface using a sharp probe attached to a cantilever. The advantage of the AFM is that the height data of a single measurement can be used to create a three-dimensional reconstruction of the surface with proper analysis software. This enables the straightforward quantitative analysis of feature sizes in such an AFM image [86].

For this work two different AFMs were used: The *Nanosurf Mobile S* from NanoAndMore GmbH and the *DIMENSION icon XR* from Bruker Corporation.

The basic AFM measurement principle is roughly sketched in Figure 4.1. The sample is placed on an X-Y positioning stage, which allows for positioning under the cantilever (probe). This is supported by an optical camera setup, enabling the finding of larger features on the sample before starting the AFM measurement. A piezoelectric actuator allows for precise control over the x,y and z positioning of the cantilever. The approach of the cantilever towards the sample surface is performed by the combination of stepper motor for coarse and the piezoelectric actuator for precise movement. During measurement the cantilevers displacement is monitored by a laser reflected of the back of the tip of the cantilever onto a segmented photodiode. The position of the laser on the segmented photodiode is fed back into a PID controller, which controls the piezoelectric actuator on the z-axis to adjust the

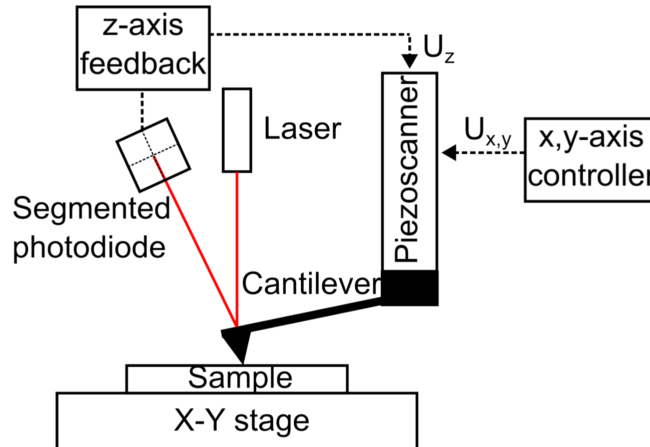

FIGURE 4.1: Schematic of the atomic force microscopy principle. A laser beam is reflected from the back of a cantilever onto a segmented photodetector. The cantilever deflection is converted into a feedback signal to control the piezoelectric scanner in the *z*-axis, keeping tip-surface interactions constant during scanning. The sample is positioned on an *X*-*Y* stage, and the surface is raster-scanned to generate a topographic map.

height of the cantilever according to the selected operation mode. During the measurement x- and y-movement are done by decoupled piezoelectric actuators that are controlled by separate electronic control circuits [86].

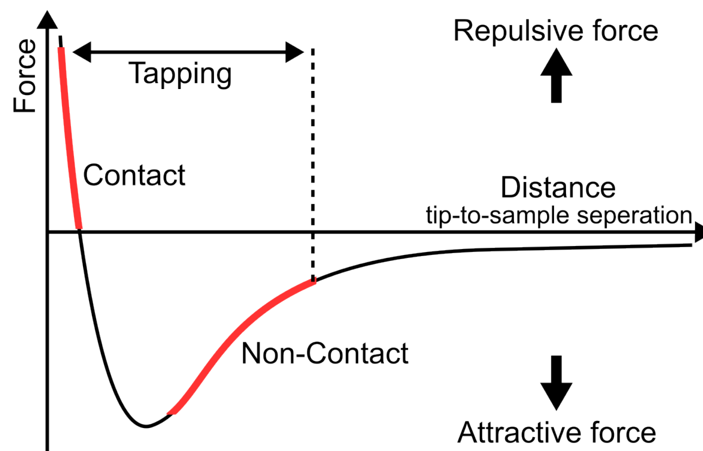

FIGURE 4.2: Schematic force curve for the tip-sample interaction during AFM. Adapted from [87]

AFM can be operated in several distinct modes, most commonly contact, non-contact, and intermittent-contact (or tapping) mode, as illustrated by the force curve in Figure 4.2 [87]. In contact mode, the tip of the cantilever remains in continuous physical contact with the sample surface. The tip is held only a few angstroms from the surface, operating in the repulsive-force regime. A feedback loop regulates the cantilever deflection along the z-axis to maintain either a constant force or a constant height between the tip and the surface, thereby mapping the surface topography [86]. In non-contact mode, the cantilever oscillates tens to hundreds of angstroms away from the surface and is typically operated in the attractive-force

regime. Here, the feedback maintains a constant oscillation amplitude, and variations in this amplitude are used to reconstruct the surface topography [86]. Tapping mode represents an intermediate approach that combines aspects of both contact and non-contact operation. The oscillating tip is brought close enough to the sample that it intermittently touches, or "taps," the surface at the end of each oscillation cycle. The image is obtained by monitoring and controlling changes in the oscillation amplitude [86]. During the experiments described in this work, both contact and tapping modes were employed; however, tapping mode was primarily used. For the nanostructures produced by local droplet etching, tapping mode offered the significant benefit of reduced tip wear compared to contact mode, while comparative measurements revealed no discernible differences in the resulting topography for the same samples.

All AFM measurements required proper setup beforehand. After fixing each sample on the X-Y stage via a vacuum chuck and mounting the cantilever onto the sensor head, the optics were aligned via the built-in optical microscope. The laser was adjusted towards the center of the cantilevers back to maximize the detected signal and then the deflected signal was centered on the receiving optics. Tapping mode required additionally the selection of the operating frequency, which was generally done via an automatic routine and slightly adjusted after the fact. While the actual operation frequency is at the maximum of the amplitude, it is usually better to slightly offset the amplitude to the low frequency side of the maximum. This is done to account for the frequency shift that occurs when the cantilever approaches the surface, due to interactions with attractive van der Waal forces [86].

After these steps the sample surface was first approached by hand via the coarse stepper motor of the z-axis. This was stopped at a distance when the manual approach was no longer deemed safe and depends on the system and user experience. At this point the much slower automatic approach was started, which utilizes both the stepper motor and the more precise piezoelectric actuator. When the surface is approached the cantilever begins scanning the surface and at this point the user adjusts the feedback parameters to optimize the measurement results. The *DIMENSION icon XR* allowed for measurements of up to $90 \times 90\,\mu\text{m}^2$ with a maximal resolution of 4096×4096 pixels.

Atomic force microscopy is not only valuable for characterizing nanoscale surface structures but also provides a powerful means to analyze the surface morphology and crystal quality of epitaxial layers. In this context, the surface roughness is a central parameter: epitaxial films grown by island growth or with a high defect density exhibit rougher surfaces than atomically flat, defect-free films. A commonly used quantitative measure is the root-mean-square (RMS) roughness, defined as

$$\sigma_{\text{RMS}} = \sqrt{\frac{1}{N}\sum_{i}^{N}(z_i - \bar{z})^2}, \tag{4.1}$$

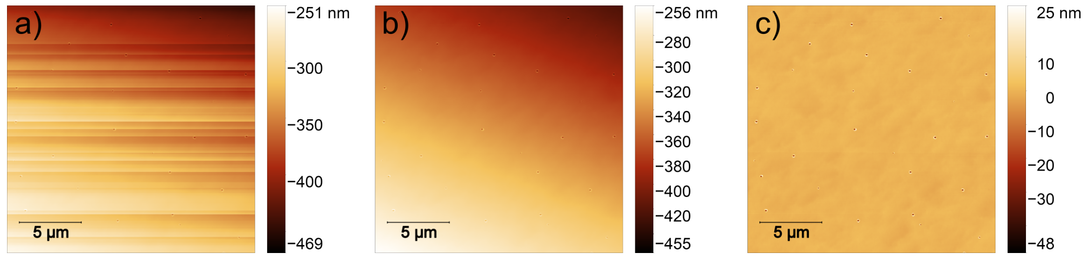

FIGURE 4.3: AFM image processing steps on a $20 \times 20\,\mu m^2$ $In_{0.52}Al_{0.48}As$ sample after local droplet etching. (a) Raw image shows a gradient across the scan and line artifacts. (b) After row alignment using the median-of-differences method (software: Gwyddion). (c) After subsequent 1st-order polynomial background subtraction. The processed image appears flat, centered at zero height, and the nanoholes become clearly visible.

where N is the total number of sampled pixels, z_i the measured height value of pixel i, and $\bar{z}$ the average height.

It is important to note that σ_{RMS} is sensitive to the specific data processing steps applied. For meaningful comparison between samples, image processing should therefore be limited to the minimal universally required corrections.

In general, large-scale background distortions in AFM data are caused by macroscopic effects outside the operator's control, such as sample tilt, scanner nonlinearities, and z-drift due to piezoelectric thermal expansion [86]. Figure 4.3 a) shows an exemplary $20 \times 20\,\mu m^2$ AFM scan before any data processing. Here local droplet etching has been performed on a flat $In_{0.52}Al_{0.48}As$ surface, however the image shows a height gradient starting at the bottom left and going to the top right. Additionally, the image displays horizontal line noise.

Analysis and processing of the produced AFM data was done with the open source software *Gwyddion*. Aligning the rows can be performed by a variety of different methods, where the correct choice depends on the type of measured sample. In this work Gwyddions *median of differences* row aligning method produced the best results for samples with nanohole structures, the result for this image is displayed in Figure 4.3 b). However, the gradient is still present and requires leveling via removal of the background by polynomial fitting. Here the data is flattened by subtracting a fitted polynomial function from each scan line, resulting in a flattening of the lines and a shift such that it centers on zero height. For flat samples a first order correction is usually sufficient, while a second order is required if bowing caused by the scanner head is present [86]. Figure 4.3 c) shows the sample after row alignment and 1st order polynomial fitting. The image appears flat, the surface is centered at zero height and all nanoholes are clearly visible.

The substrates used in this work were either GaAs (100) or InP (100) 3 inch wafers. Figure 4.4 sketches the flat orientation for both of these wafer types, with the big flat corresponding to the $(0\bar{1}\bar{1})$ surface and the small flat corresponding to the $(0\bar{1}1)$ surface. All measurements were taken along either of the two high symmetry directions, i.e. [011] or $[0\bar{1}1]$.

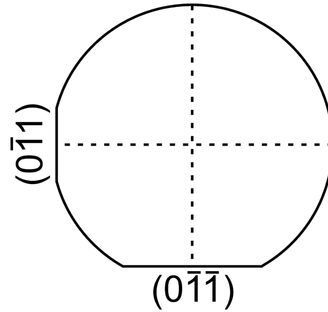

FIGURE 4.4: Sketch showing the orientation of in-plane crystallographic directions for the GaAs (100) and InP (100) wafers used in this work. The 3 inch wafers were cleaved before growth into quarters along the dashed lines.

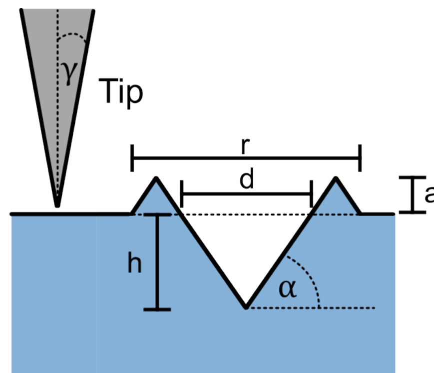

FIGURE 4.5: Sketch of the parameters measured on individual nanoholes for statistical analysis: nanohole depth h, nanohole diameter d, ring height a, and ring-hole diameter r. The angles α and γ illustrate the sidewall and cantilever half-cone angles, respectively, as discussed in the main text.

Figure 4.5 illustrates the geometric parameters extracted from individual nanoholes for statistical analysis. For the evaluation of a given sample, the measured nanohole depths, nanohole diameters, ring heights, and ring-hole diameters were averaged. For each parameter, the uncertainty of the statistical mean is quantified by the corresponding standard deviation.

AFM measurements performed with the Nanosurf Mobile S system were carried out in contact mode using *PPP-CONTR* cantilevers (Nanosensors), which feature a nominal tip radius of 7 nm and a half-cone angle γ in the range of 25–30°. Measurements conducted with the Dimension Icon XR system were predominantly performed in tapping mode using *TESPA-V2* cantilevers (Bruker), which also provide a nominal tip radius of 7 nm and a half-cone angle γ between 17.5 and 25°.

The steepest sidewall angles α observed for nanoholes etched into $In_xAl_{1-x}As$ were typically on the order of $\sim 45°$. Consequently, the employed cantilevers were well suited to resolve the relevant nanostructure geometries.

4.2 Scanning electron microscopy

First realized by Max von Ardenne in the 1930s [88], scanning electron microscopy (SEM) provides high-resolution imaging of surfaces by raster-scanning a focused electron beam across a sample. Its central advantage compared to conventional optical microscopy lies in the use of electrons rather than photons: the much smaller de Broglie wavelength of accelerated electrons allows resolutions far beneath the diffraction limit of light. Modern SEM systems can magnify objects up to one million times and achieve spatial resolutions in the order of a few nanometers [89].

The electron beam is generated in an electron gun and focused onto the sample using electromagnetic lenses and apertures. In this work, a *Pioneer Raith-150* system (Raith GmbH) was employed, which allows for acceleration voltages between 2 and 30 keV. The scanning of the beam over the sample area is performed by electromagnetic deflection coils, moving the beam point by point across the surface. The time the beam dwells on each location is defined by the scan speed, which is set by the operator: slower scans improve signal-to-noise ratio but require longer acquisition times.

Upon interacting with the sample, the incident electrons undergo a combination of elastic and inelastic scattering events, penetrating into the material to a depth determined by the acceleration voltage. These interactions give rise to a variety of signals, including backscattered electrons, secondary electrons, characteristic X-rays, and Auger electrons, which can be collected by different detectors to provide complementary information. In this thesis, SEM was primarily used to produce two-dimensional images of surface morphology using the secondary and backscattered electron detectors integrated in the Pioneer Raith-150 system.

Backscattered electrons are a fraction of the primary beam that is elastically scattered to angles larger than 90°. The probability for high angle elastic scattering increases with the size of the atoms, as those have stronger positive charge. Since backscattered electrons retain a large fraction of the incident electron energy, they contain information from deeper within the interaction volume. Secondary electrons, in contrast, are low-energy electrons (10 eV to 50 eV) ejected from the outer shells of atoms during inelastic scattering. Due to their low mean free path, secondary electrons can only escape from the top few nanometers of the surface, making them highly surface-sensitive. Consequently, images recorded with secondary electron detection usually exhibit better surface resolution and contrast of fine features, whereas backscattered electron images are often more sensitive to compositional contrast [89].

SEM provides two-dimensional projections of sample surfaces. Figure 4.6 a) shows an SEM image of droplet-etched nanoholes in an $In_{0.52}Al_{0.48}As$ layer at a magnification of $\times 10$ k, and b) a close-up view of one of these nanoholes at $\times 150$ k magnification. While it is generally possible to extract height information from SEM

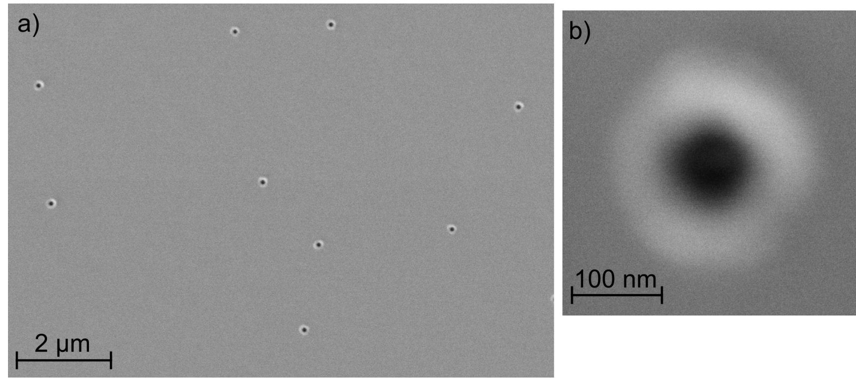

FIGURE 4.6: SEM images of droplet etched nanoholes in an $In_{0.52}Al_{0.48}As$ layer at a) ×10 k and b) ×150 k k magnification, both taken with the secondary electron detector at an acceleration voltage of 5 kV. Measurements were done by Dr. Viktroyia Zolatanosha.

data, doing so requires additional steps such as preparing cross-sections or employing extra detectors [90]. AFM is therefore better suited for precise topographical measurements. Nevertheless, SEM offers much faster scan speeds, making it invaluable for rapid, large-scale overview imaging. In this thesis, SEM was mainly used to determine the nanohole density over large surface areas, since hundreds of holes can be recorded in a single overview scan, whereas AFM was used for detailed depth and shape analysis.

4.3 High resolution X-ray diffractometry

While AFM and SEM provide essential information about the surface morphology of semiconductor structures, high-resolution X-ray diffractometry (HRXRD) is one of the most important non-destructive techniques for analyzing their crystallographic structure and material quality. HRXRD utilizes the diffraction phenomena that occur when electromagnetic radiation impinges on periodic lattice structures of crystals, where the wavelength of the radiation is comparable to the lattice spacing. By recording the intensity of the diffracted X-ray beam while varying the incidence angle quantitative information about lattice constants, strain, epitaxial layer thicknesses, layer tilt and material composition can be obtained [91].

Central to this is the order and periodicity in a crystalline film. For GaAs, AlAs, InAs, InP and their alloys the atomic arrangement follows the zincblende structure, sketched in Figure 4.7 a). The crystal periodicity can be described by families of parallel lattice planes, identified by their Miller indices (hkl). These are defined by the intercepts of the plane with the crystallographic axes in units of the lattice constant a. For zincblende, examples of the (100), (111), and (011) planes are shown in Figure 4.7 b). The interplanar spacing d_{hkl} depends on a and the Miller indices, and can be derived geometrically as [91]

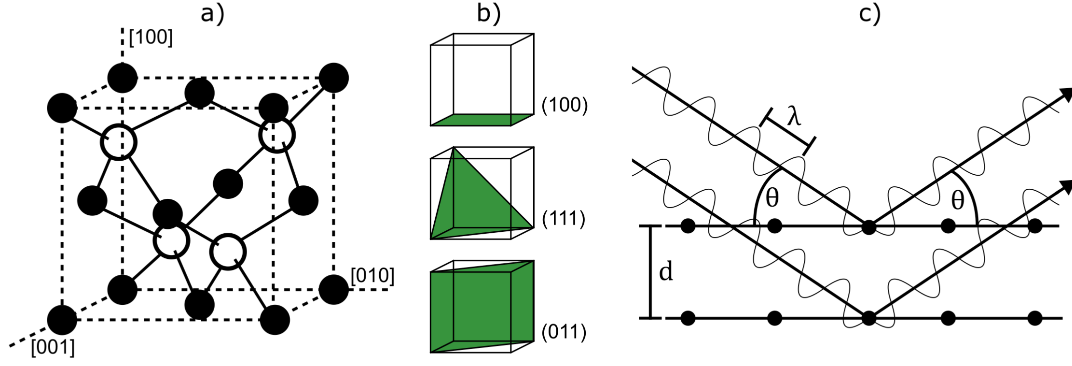

FIGURE 4.7: a) Zincblende crystal structure with b) the (100), (111), and (011) planes. c) Illustration of Bragg's law: constructive interference occurs when the path difference of scattered waves from adjacent lattice planes fulfills $2d \sin\theta = n\lambda$. Adapted from [42]

$$d_{hkl} = \frac{a}{\sqrt{h^2 + k^2 + l^2}}. \tag{4.2}$$

When X-rays impinge on such a periodic arrangement of lattice planes, constructive interference occurs if the path-length difference between waves reflected from adjacent planes equals an integer multiple of the wavelength. This gives rise to Bragg's law, proposed in 1913 by W.H. Bragg and W.L. Bragg [92],

$$2d_{hkl} \sin\theta_B = n\lambda, \tag{4.3}$$

where θ_B is the Bragg angle, λ is the X-ray wavelength, and n is the diffraction order. The geometric origin of this condition, based purely on interplanar interference, is sketched in Figure 4.7 c).

A complementary and more general description is obtained by viewing the crystal as a three-dimensional periodic array of atoms. In this perspective, the scattering process is described by the change in wavevector

$$\vec{Q} = \vec{k}_{\text{out}} - \vec{k}_{\text{in}}, \tag{4.4}$$

where $\vec{k}_{\text{in}}$ and $\vec{k}_{\text{out}}$ denote the incident and diffracted wavevectors, respectively, with $|\vec{k}| = 2\pi/\lambda$ [42].

The periodicity of the crystal is then represented in reciprocal space, which is defined by the reciprocal lattice basis vectors $\vec{g}_1$, $\vec{g}_2$, and $\vec{g}_3$. These vectors are generated from the basis vectors of the crystal in real space $\vec{a}_1$, $\vec{a}_2$, and $\vec{a}_3$ via

$$\vec{g}_1 = 2\pi \frac{\vec{a}_2 \times \vec{a}_3}{\vec{a}_1 \cdot (\vec{a}_2 \times \vec{a}_3)}, \tag{4.5}$$

with $\vec{g}_2$ and $\vec{g}_3$ obtained by cyclic permutation of the indices in the numerator [42]. Diffraction occurs when the scattering vector $\vec{Q}$ coincides with a reciprocal lattice vector $\vec{G}$,

$$\vec{Q} = \vec{G} = h \cdot \vec{g}_1 + k \cdot \vec{g}_2 + l \cdot \vec{g}_3, \tag{4.6}$$

which is the Laue condition [42].

Although Bragg's law and the Laue condition arise from different viewpoints – interplanar interference versus scattering from a periodic atomic array – they describe the same physical requirement for constructive interference. Bragg's law is simply the one-dimensional, plane-normal projection of the more general Laue condition. Both formulations therefore provide equivalent criteria for predicting the angular positions of diffraction peaks in crystalline materials [93].

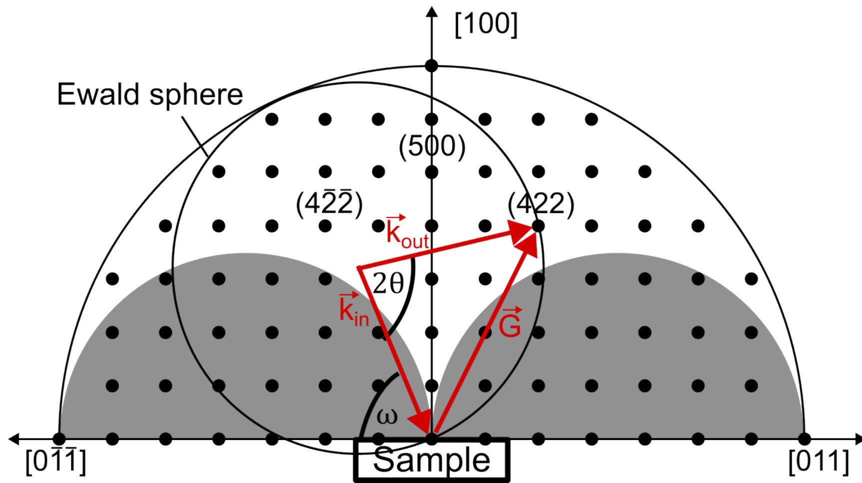

FIGURE 4.8: Ewald construction for a (422) reflection. The reciprocal lattice of a (100)-oriented cubic crystal is mapped by the incident wavevector $\vec{k}_{in}$ drawn from the origin. Diffraction occurs when a reciprocal lattice point lies on the surface of the Ewald sphere of radius $|\vec{k}| = 2\pi/\lambda$, here fulfilled for the (422) point by $\vec{k}_{out}$. The shaded regions indicate non-accessible peaks. Adapted from [42].

The Laue condition elegantly expresses diffraction in terms of the reciprocal lattice: a Bragg peak is observed whenever the difference between the incident and outgoing wave vectors matches a reciprocal lattice vector. A useful geometric construction to visualize this relationship is the Ewald construction.

Figure 4.8 depicts the construction for a sample with surface orientation (100) and incidence of the X-ray beam along the [011] crystallographic direction for the (422) reflection. The incident wavevector $\vec{k}_{in}$ is drawn with its tip at the origin of reciprocal space, and an Ewald sphere of radius $|\vec{k}|$ is constructed around this point. The Laue condition is satisfied if the scattered wavevector $\vec{k}_{out}$, having the same magnitude as $\vec{k}_{in}$, points to a reciprocal lattice point on the sphere. In this case diffraction occurs and $\vec{Q} = \vec{k}_{out} - \vec{k}_{in} = \vec{G}$. [42].

While these conditions determine the angles at which diffraction occurs, they do not predict the intensities of the diffracted beams. The intensity depends on the distribution of scattering centers within the unit cell and is described by the structure factor

$$F = \sum_{n=1}^{N} f_n \exp\left(i\vec{Q} \cdot \vec{r}_n\right), \tag{4.7}$$

which is the sum over all N atoms in the unit cell [91]. f_n is the atomic scattering factor of the nth atom and is determined by the inner atomic charge distribution and $\vec{r}_n$ its position in the unit cell. The measured intensity is proportional to the squared modulus of the structure factor

$$I_{hkl} \propto |F|^2. \tag{4.8}$$

A real crystal consists of more than one unit cell, and the thus resulting intensity is due to the contribution of all unit cells illuminated by the X-ray beam. The total scattered amplitude A is given by $A = F \cdot L$, where

$$L = \sum_{T} \exp\left(i\vec{Q} \cdot \vec{T}\right) \tag{4.9}$$

is the contribution of these unit cells, and $\vec{T}$ is a set of vectors pointing to all illuminated unit cells [91]. For a simple cubic lattice with N_i illuminated cells along the ith crystallographic direction,

$$L = \sum_{n_1=1}^{N_1} \sum_{n_2=1}^{N_2} \sum_{n_3=1}^{N_3} \exp\left[i\left(Q_1 n_1 a_1 + Q_2 n_2 a_2 + Q_3 n_3 a_3\right)\right]. \tag{4.10}$$

The intensity contribution due to L is again given by its absolute value squared and can be calculated by writing the individual sums as geometric series, yielding the *Laue interference function* [91, 94, 95]

$$I \propto \prod_{i=1}^{3} \frac{\sin^2\left(\frac{1}{2} N_i Q_i a_i\right)}{\sin^2\left(\frac{1}{2} Q_i a_i\right)}. \tag{4.11}$$

In between the sharp Bragg peaks, Laue oscillations arise, which will be discussed in detail in Section 4.3.2. In real crystals, the diffraction pattern is further influenced by strain, mosaicity, and defects, which broaden or attenuate the diffraction peaks. HRXRD is therefore highly sensitive to crystal quality [42, 91].

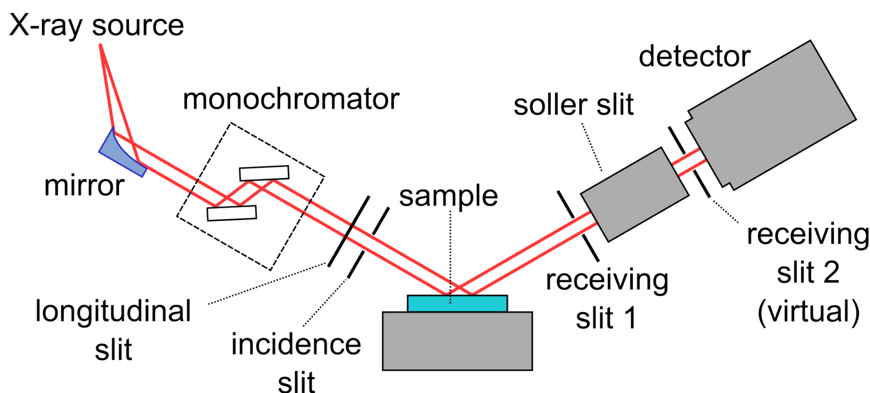

FIGURE 4.9: Schematic of the parallel-beam optics configuration used for the HRXRD measurements performed in this work.

High-resolution X-ray diffraction (HRXRD) measurements presented in this thesis were performed using a *Rigaku SmartLab* diffractometer, which allows for independent control of the incidence angle ω and the detector angle 2θ. All measurements were carried out using a parallel-beam optics configuration, schematically illustrated in Figure 4.9.

X-rays were generated by a rotating-anode source operated at an accelerating voltage of 45 kV and a current of 200 mA. The emitted radiation was first conditioned by a parabolic multilayer mirror to produce a highly parallel beam and subsequently monochromatized using a Ge(400)×2 monochromator. Downstream of the monochromator, the beam footprint on the sample surface was defined by a replaceable longitudinal slit controlling the beam width, followed by an adjustable incidence slit that determines the vertical beam divergence.

After diffraction at the sample, the scattered X-rays passed through a receiving slit, which served to suppress background radiation. A 2.5° Soller slit was placed downstream to limit beam divergence in the direction perpendicular to the plane in Figure 4.9. The diffracted intensity was recorded using a HyPix-3000 detector, a two-dimensional semiconductor detector. During measurement the active area of the detector can be restricted, acting as a virtual second receiving slit. The detector offers a high maximum count rate of more than 1×10^6 counts/s/pixel and high spatial resolution, with a pixel size of $100\,\mu m^2$ [96].

4.3.1 Reciprocal space maps

Reciprocal space maps (RSMs) are obtained by recording the diffracted X-ray intensity over a two-dimensional range of incidence angles ω and detector angles 2θ in the vicinity of a reciprocal lattice point. Such maps provide information about the scattering distribution both parallel and perpendicular to the sample surface, which enables the investigation of film parameters like lattice mismatch, relaxation, and tilt in epitaxial layers.

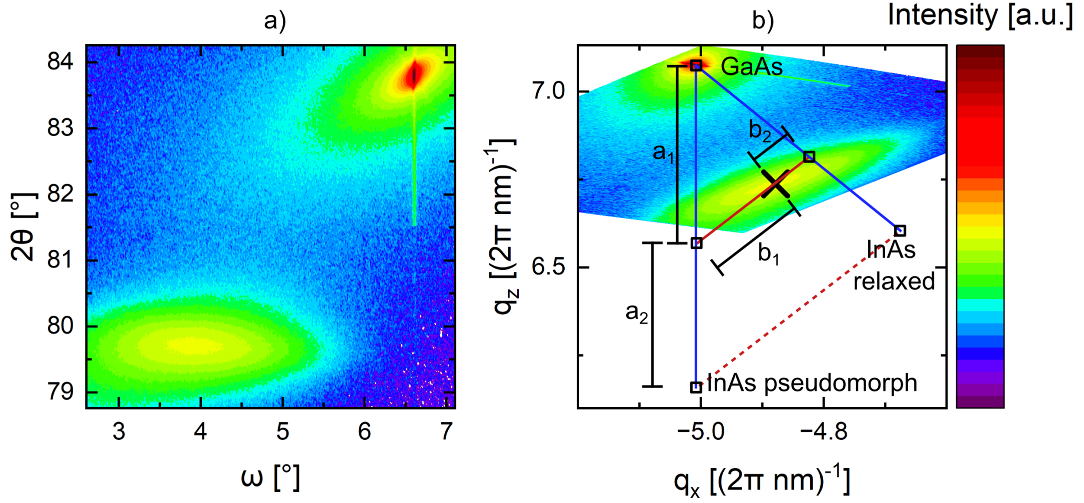

FIGURE 4.10: Angular space map a) transformed via coordinate transformation into a RSM b). The measurement was performed at the $(4\bar{2}\bar{2})$ Bragg peaks of an $In_xAl_{1-x}As$ layer grown on GaAs (100). The geometric construction in the RSM can be used to deduce composition x and the degree of relaxation of the $In_xAl_{1-x}As$ layer.

Figure 4.10 a) shows a typical angular-space measurement of an approximately 50 nm thick $In_xAl_{1-x}As$ layer grown on GaAs (100), recorded around the $(4\bar{2}\bar{2})$ reflection of the substrate. To interpret the measurement in crystallographic terms, the recorded intensity distribution is transformed into reciprocal coordinates using

$$q_x = \pm\frac{1}{\lambda}\left[\cos\left(\Delta\omega\right) - \cos\left(2\theta - \Delta\omega\right)\right] \tag{4.12}$$

$$q_z = \frac{1}{\lambda}\left[\sin\left(\Delta\omega\right) + \sin\left(2\theta - \Delta\omega\right)\right], \tag{4.13}$$

where $\lambda = 0.154\,\text{nm}$ is the wavelength of the Cu K_α radiation and the sign in Equation 4.12 is chosen positive for positive (hkl) indices and negative for negative $(h\bar{k}\bar{l})$ indices [93]. The *Rigaku SmartLab* software includes a built-in tool that performs this transformation automatically. The resulting RSM is shown in Figure 4.10 b).

To evaluate an RSM, the expected reciprocal lattice points of all relevant materials must first be calculated. In the present example this includes GaAs for the substrate, and AlAs and InAs, which form the $In_xAl_{1-x}As$ alloy layer. The reciprocal coordinates of a reflection (hkl) are obtained through Equation 4.2,

$$q_x = \pm\frac{1}{a}\sqrt{k^2 + l^2} \tag{4.14}$$

$$q_z = \frac{1}{a}\sqrt{h^2}, \tag{4.15}$$

where a is the lattice constant of the material and the sign convention for q_x follows that of Equation 4.12.

For alloy layers, one must distinguish between the expected reciprocal-lattice positions of unstrained material and those of pseudomorphic layers. For a pseudomorphic film, the in-plane lattice constant is forced to match that of the substrate, a_S. In this case the lateral strain $\epsilon_{||}$ of the layer is equal to the misfit

$$\epsilon_{||} = f = \frac{a_S - a_L}{a_L}, \tag{4.16}$$

with the unstrained lattice constant of the film a_L.

The corresponding out-of-plane strain $\epsilon_{\perp}$ is determined by the elastic distortion of the unit cell and depends for growth on (100) substrates on the elastic constants C_{11} and C_{12}. The strained out-of-plane lattice constant $a_{\perp}$ is given by [42]

$$a_{\perp} = \left(2 \cdot \frac{C_{12}}{C_{11}} \cdot \epsilon_{||} + 1\right). \tag{4.17}$$

The strained and unstrained lattice constants yield distinct reciprocal-lattice positions and by comparing the measured layer peak to these theoretical points in the RSM, the alloy composition and the degree of strain relaxation can be directly determined. Table 4.1 lists the lattice constants and elastic stiffness coefficients for AlAs, GaAs, InAs, and InP, together with the corresponding theoretical reciprocal-lattice positions (q_x, q_z) for the (422) reflection. Values are shown for both relaxed and pseudomorphic layers grown on GaAs (100) and InP (100) substrates and the table's values can also be used for the $(4\bar{2}\bar{2})$ and (400) reflexes.

In practice, the calculated reciprocal-lattice positions are typically offset slightly from the experimentally measured ones due to small angular alignment inaccuracies. Therefore, when overlaying theoretical points onto an RSM, the entire set of calculated positions is shifted by the same offset determined from the relative distance between the measured and calculated substrate peak positions.

Including the calculated reciprocal-lattice points in the RSM, as illustrated in Figure 4.10 b) for an $In_xAl_{1-x}As$ layer grown on GaAs, enables the determination of the alloy composition x and its degree of relaxation R. The points for AlAs are omitted from this image, as they lie very close to the GaAs substrate peak (see Table 4.1). For a layer that is neither fully relaxed nor fully pseudomorphic, the measured layer peak falls between the lines connecting the relaxed and pseudomorphic reciprocal-lattice points of the binary constituents (blue lines). An additional line (red line) is then drawn through the measured peak, which is parallel to the line (dashed red line) connecting the InAs peaks. From this geometric construction, the alloy composition is obtained from the intersect of the red line with the vertical pseudomorphic line

TABLE 4.1: Lattice parameters a (nm), elastic stiffness coefficients C_{11}, C_{12} (GPa) [69], and calculated reciprocal lattice points q_x, q_z ($2\pi\,\mathrm{nm}^{-1}$) for GaAs, AlAs, InAs, and InP for the (422) reflex. For heteroepitaxial layers grown on GaAs and InP substrates, both relaxed and pseudomorphic values are listed.

(A) Lattice constants and stiffness coefficients

Material	a	C_{11}	C_{12}
InP	0.5867	1011	561
GaAs	0.5654	1221	566
AlAs	0.5661	1250	534
InAs	0.6058	833	453

(B) Growth on GaAs substrate

Material	$q_x^{(\text{relaxed})}$	$q_z^{(\text{relaxed})}$	$a^{(\text{pseudo})}$	$q_x^{(\text{pseudo})}$	$q_z^{(\text{pseudo})}$
GaAs	5.0027	7.0749			
AlAs	4.9963	7.0658	0.5667	5.0027	7.0580
InAs	4.6686	6.6024	0.6498	5.0027	6.1556

(C) Growth on InP substrate

Material	$q_x^{(\text{relaxed})}$	$q_z^{(\text{relaxed})}$	$a^{(\text{pseudo})}$	$q_x^{(\text{pseudo})}$	$q_z^{(\text{pseudo})}$
InP	4.8187	6.8147			
GaAs	5.0032	7.0756	0.5453	4.8187	7.3360
AlAs	4.9963	7.0658	0.5483	4.8187	7.2954
InAs	4.6686	6.6024	0.6263	4.8187	6.3862

$$x = \frac{a_1}{a_1 + a_2}, \tag{4.18}$$

while the degree of relaxation R is given by the distance of the layer peak towards the intersect with the diagonal relaxation line [93]

$$R = \frac{b_1}{b_1 + b_2}. \tag{4.19}$$

While asymmetric reflections such as (422) and $(4\bar{2}\bar{2})$ provide information on strain and composition, symmetric reflections can be used to detect tilt of the epitaxial layers [97]. Figure 4.11 a) shows a (400) scan of an $\mathrm{In}_y\mathrm{Ga}_{1-y}\mathrm{As}$ layer on GaAs, where the layer and substrate peaks lie on the same vertical line ($q_x = 0$), indicating that the layer is aligned with the substrate along the measured [011] direction.

In contrast Figure 4.11 b) depicts an (400) scan where the layer peaks are offset laterally, revealing a tilt relative to the substrate. Both tilted peaks are from a metamorphic buffer layer grown and supplied by Dr. Michael Jetter and colleagues from

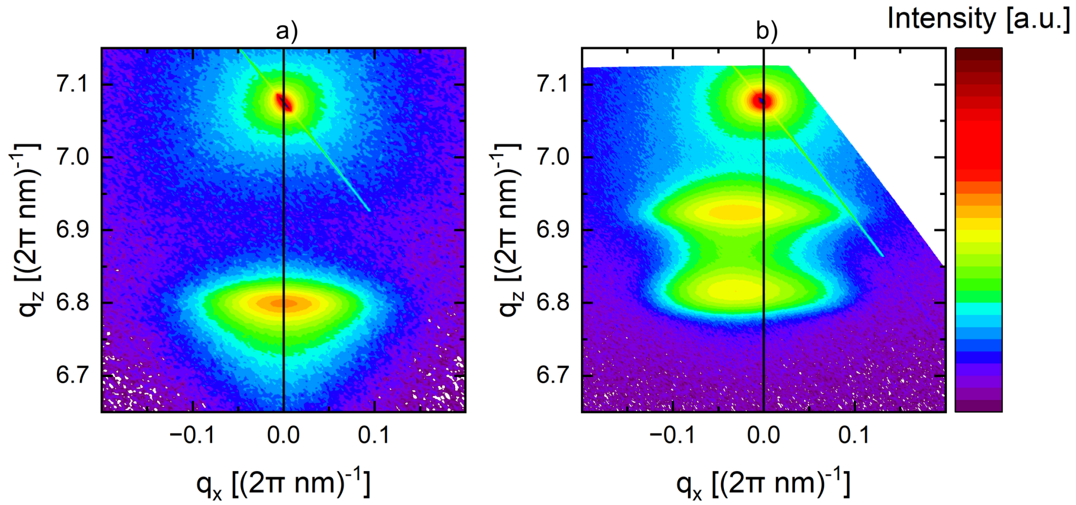

FIGURE 4.11: RSMs of a sample without a) and with b) layer tilt in relation to the GaAs (100) substrate. The RSMs were both measured at the (400) reflex, were a) shows an $In_yGa_{1-y}As/GaAs$ sample and b) a metamorphic buffer structure grown by Dr. Michael Jetter and colleagues from the University of Stuttgart.

the University of Stuttgart and will be discussed in more detail in chapter 6. The tilt angle α of the layer with respect to the substrate is given by

$$\alpha = \frac{\Delta q_x}{q_z}. \tag{4.20}$$

A complete determination of the tilt magnitude and direction requires two measurements with orthogonal in-plane scattering directions, for example along [011] and $[0\bar{1}1]$ [93].

4.3.2 ω-2θ-scans

In an $\omega 2\theta$-scan, the incidence angle ω and the detector angle 2θ are varied simultaneously while maintaining the condition $\omega = 2\theta/2$. For symmetric reflections such as (400), this scanning mode corresponds to probing the q_z component of the reciprocal lattice vector, while the in-plane component q_x remains fixed at zero.

Figure 4.12 shows an $\omega 2\theta$-scan of an $In_xAl_{1-x}As$ layer grown on InP, together with an RSM of the same reflection in the inset. The In concentration in the layer can be obtained from the angular separation between the substrate and layer peaks, where the layer peaks moves to the left of the InP peak for higher In concentrations.

For high-quality crystalline films, periodic Laue oscillations may be observed [95]. These oscillations arise from interference between X-rays scattered from the finite number N of coherently diffracting unit cells, as described in Eq. 4.11, which reads for the one dimensional case

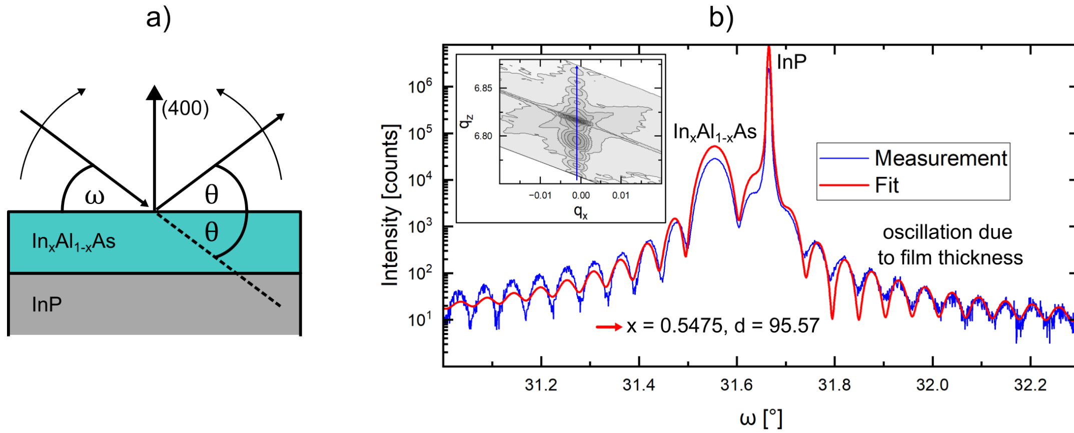

FIGURE 4.12: a) Schematic representation of an $\omega 2\theta$-scan on an $In_xAl_{1-x}As$/InP sample. b) Exemplary (400) $\omega 2\theta$-scan on such a sample with the measured data and the fitted function to discern its structure. The inset shows the RSM around the same (400) reflex of the same sample and the path that is traced through the RSM by the $\omega 2\theta$-scan.

$$I \propto \frac{\sin^2\left(\frac{N}{2}Qa\right)}{\sin^2\left(\frac{1}{2}Qa\right)} \tag{4.21}$$

At the positions for the Bragg condition $Qa = 2\pi n$ holds and $I \to N^2$, i.e. all unit cells interfere constructively. The periodicity of the Laue oscillation between the Bragg peaks is determined by the number of diffracting unit cells N and is given by $\Delta Q = 2\pi / Na$. As such the periodicity of the oscillation reduces with increasing N and the peak width decreases. Thus Laue oscillations are typically only visible for thin films and start to vanish at thicker layers. As the number of unit cells N can be extracted from the periodicity of the Laue oscillations this enables the determination the films thickness: The lattice constant of the ternary film can be calculated from its composition given by the relative peak positions. Once the lattice constant is known, N directly yields the film thickness [95].

To discern the sample structure from a given $\omega 2\theta$-scan the *Rigaku SmartLab* offers an invaluable evaluation and fitting tool. Here the user inputs the layer structure and a curve is fitted over the measured data, where composition and layer thickness are fit parameters. In Figure 4.12 b) the result of such an evaluation is shown, where the red line is the fit over the existing measurement data. $\omega 2\theta$-scans are highly advantageous for MBE cell calibration, as with the resulting parameters of composition and film thickness of tertiary semiconductors like $In_xAl_{1-x}As$ it is possible to accurately calculate the growth rate of both group-III cells. The film thickness d is given by the growth time t and the growth rate of the two cells G_{In} and G_{Al} with $d = t \cdot (G_{In} + G_{Al})$. The layer composition x is simply given by the ratio between the two growth rates $x = G_{In} / (G_{In} + G_{Al})$. As t is known this is a two dimensional system of equations with two unknowns, and the growth rates for both cells is given by

$$G_{In} = \frac{d \cdot x}{t} \quad \text{and} \quad G_{Al} = \frac{d \cdot (1-x)}{t}. \tag{4.22}$$

4.3.3 Rocking curve

Rocking curve (RC) or ω-scans are performed by fixing the detector angle 2θ at the Bragg condition of the investigated reflection, while the incident angle ω is varied. The theoretical framework of RC analysis assumes that a real crystal is composed of many slightly misoriented crystallites – often referred to as mosaic domains or sub-grains – that exhibit small angular deviations from one another and from the nominal substrate orientation [91]. Generally, such mosaic structures are present to some degree in nearly all crystalline materials, leading to angular broadening of the measured peaks.

In epitaxial film growth additional strain and deformations are introduced, leading to crystalline defects and dislocation networks, which in turn increase the mosaic spread. As such the extent of peak broadening in RC measurements – typically quantified by the full width at half maximum (FWHM) – is widely used as a figure of merit for crystalline quality: narrower peaks correspond to a lower degree of mosaicity and thus higher structural perfection [98].

The dislocation density ρ can be approximated as being proportional to the square of the RC peak width [98]. Following the expression originally derived by Dunn and Koch [99], it is given by

$$\rho = \frac{\beta^2}{2\pi \ln(2)\, b^2}, \tag{4.23}$$

where β denotes the FWHM and b the magnitude of the Burgers vector corresponding to the dislocation type.

4.4 Photoluminescence spectroscopy

Photoluminescence (PL) spectroscopy is a widely used, non-destructive technique for the optical characterization of semiconductor materials and nanostructures. Luminescence is defined as the emission of light resulting from radiative recombination processes involving excited electronic states. Due to the law of conservation of energy, a semiconductor must be driven out of thermal equilibrium in order to emit light, which is achieved by supplying energy through an excitation source. In photoluminescence, this excitation is achieved optically via photon absorption [100].

Upon optical excitation, an incident photon promotes an electron from the valence band into the conduction band, thereby simultaneously creating a hole in the valence band. The excited electron can subsequently relax back to the valence band if an unoccupied state is available. This relaxation can proceed either radiatively,

accompanied by the emission of a photon, or non-radiatively through the emission of phonons [101].

The optical excitation in PL spectroscopy is typically provided by a laser source. As the laser light propagates into the semiconductor, its intensity I decreases with penetration depth d according to the Beer-Lambert law,

$$I = I_0 \exp[-\alpha(\omega)\, d]\,, \tag{4.24}$$

where I_0 denotes the incident intensity and $\alpha(\omega)$ is the frequency-dependent absorption coefficient [102].

For above-band-gap excitation in semiconductors, penetration depths – defined as the distance over which the intensity of the non-reflected radiation is reduced to approximately $1/e^2 \approx 13\%$ of its initial value – are typically on the sub-micron scale for visible lasers [103]. For example, in $In_{0.52}Al_{0.48}As$, an absorption coefficient of approximately $\alpha \approx 0.003\,\mathrm{nm}^{-1}$ at a wavelength of 600 nm [101] results in a penetration depth of $\sim 670\,\mathrm{nm}$.

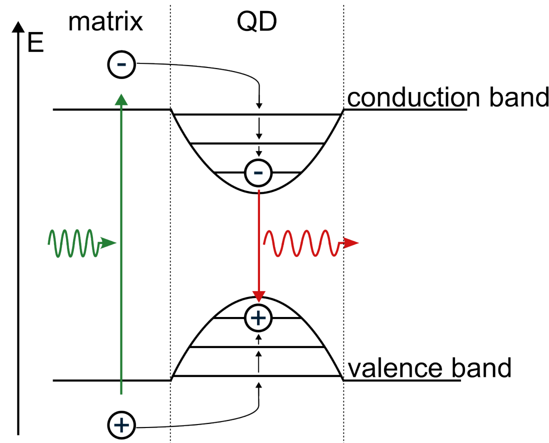

FIGURE 4.13: Schematic representation of non-resonant excitation and subsequent carrier relaxation and recombination in a quantum dot system.

In this work, PL spectroscopy was performed under non-resonant optical excitation, where a laser with photon energy above the band gap of the surrounding matrix material was used, as illustrated in Figure 4.13. The excitation creates free electron-hole pairs in the barrier (matrix) material. These carriers may subsequently diffuse toward nearby quantum dots (QDs), relax and can become captured into the discrete electronic states of individual QDs. Within a short timescale of typically a few hundred picoseconds, the captured carriers relax toward the lowest available states via phonon emission, followed by radiative recombination that gives rise to QD photoluminescence [21].

In addition to QD-related emission, radiative recombination can also occur in other regions of the heterostructure, such as the barrier material or a wetting layer, if present. A key advantage of the non-resonant excitation scheme is its experimental

simplicity, as the excitation laser does not need to be tuned to a specific transition energy and is spectrally well separated from the emitted QD luminescence [21].

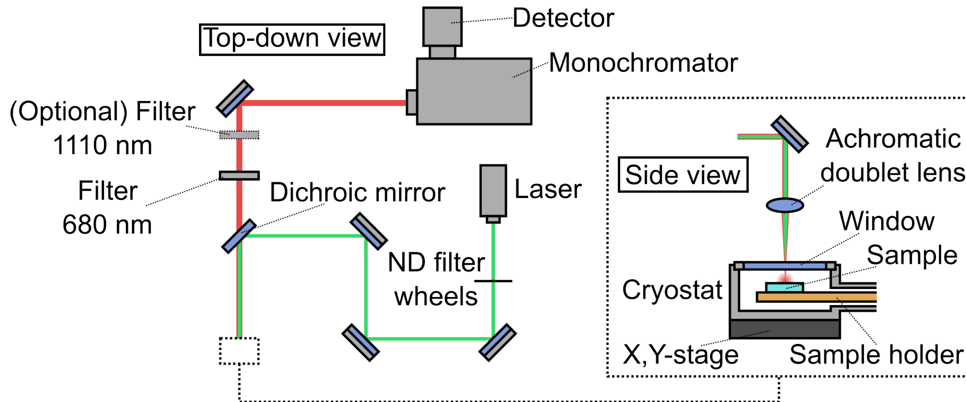

FIGURE 4.14: Schematic sketch of the PL spectroscopy setup employed in this work. The excitation beam path is shown in green, while the luminescence collection path is indicated in red.

A schematic of the PL spectroscopy setup used in this work is shown in Figure 4.14. Optical excitation was provided by one of two continuous-wave diode lasers: a green laser operating at 532 nm (2.33 eV, Thorlabs) and a red laser operating at 635 nm (1.95 eV, Edmund Optics), each with an output power of 4.5 mW. At a temperature of 14 K, the band gap of $In_{0.52}Al_{0.48}As$ is approximately 1.53 eV [69], enabling above-band-gap excitation with both laser sources.

The beam was then directed by a series of mirrors and focused onto the sample surface using an achromatic doublet lens with an anti-reflection coating optimized for the spectral range from 1050 nm to 1700 nm. Samples were glued onto a copper sample holder inside a windowed continuous-flow cryostat (*MicrostatHe*, Oxford Instruments), which was mounted onto an X,Y-stage, enabling lateral movement of the cryostat.

Thermal contact between the sample holder and the cryostat's heat exchanger enabled cooling by liquid helium or liquid nitrogen supplied from an external storage vessel. All samples investigated in this work were cooled using liquid helium, allowing a minimum temperature of 14 K to be reached. To improve thermal insulation, the cryostat was evacuated, with typical pressures in the order of $\sim 1 \times 10^{-5}$ mbar achieved during operation.

The emitted photoluminescence was collected by the same achromatic lens and guided via mirrors into the detection path. To suppress backscattered excitation light, a dichroic mirror and a long-pass filter with a cutoff wavelength of 680 nm were placed before the detector. An additional long-pass filter with a cutoff at 1110 nm was routinely used to prevent the detection of second-order diffraction peaks at wavelengths above 1300 nm. Spectral analysis was performed using a *Shamrock 500i* spectrograph (Andor Technology) equipped with a linear InGaAs photodiode array detector (*iDus DU490A-1.7*, Andor Technology), which was operated at a temperature of $-60\,^{\circ}$C.

Chapter 5

Local droplet etching on $In_{0.52}Al_{0.48}As$

This chapter presents the experimental results obtained during the adaptation of the local droplet etching (LDE) process to the $InP/In_xAl_{1-x}As/In_yGa_{1-y}As$ material system. Most of the results discussed here have been reported previously, and the corresponding publications are cited in the relevant sections.

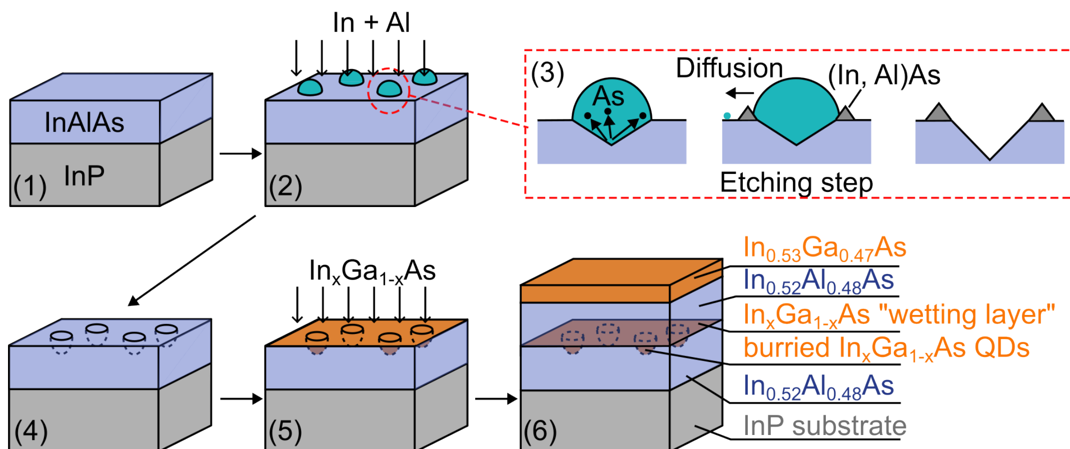

FIGURE 5.1: Schematic overview of the fabrication process for LDE QDs on InP. (1) Growth of lattice matched $In_{0.52}Al_{0.48}As$ at a substrate temperature of $T_{sub} = 505\,°C$ with As_2 BEP of $p_{As2} = 2.00 \times 10^{-5}$ mbar. (2) Reduction of the As_2 pressure by a factor of 10–100 and deposition of group-III material at the substrate temperature T_{etch} used for the LDE process. The group-III material forms droplets on the surface and (3) during the etching step material is removed from the semiconductor layer locally at the position of the droplets. (4) This results in the formation of nanoholes and surrounding ring structure on the layer surface. (5) $In_xGa_{1-x}As$ is deposited, which diffuses into the nanoholes and infills them from the bottom up. (6) Finally, the infilled nanoholes are overgrown with an $In_{0.52}Al_{0.48}As$ layer for QD confinement and an oxidation protection $In_{0.53}Ga_{0.47}As$ layer.

The chapter is organized in such a way, that the presented results follow chronologically the epitaxial steps of fabricating a complete LDE QD sample, as depicted in Figure 5.1.

It begins with the preparation and characterization of lattice-matched $In_{0.52}Al_{0.48}As$

and $In_{0.53}Ga_{0.47}As$ layers, grown on InP substrates. These layers serve as the templates for subsequent droplet-etching experiments. The following sections then describe the LDE experiments that were performed on $In_{0.52}Al_{0.48}As$ layers, where a wide range of etching parameters and their effect on the generated nanoholes were tested, with an emphasis on producing high-quality templates for further QD fabrication. These results are then followed by a discussion of results of LDE experiments performed on $In_{0.53}Ga_{0.47}As$ layers. Next, the infilling of etched nanoholes on $In_{0.52}Al_{0.48}As$ layers with $In_xGa_{1-x}As$ deposition is presented. The chapter concludes with the overgrowth of the infilled nanoholes, yielding buried $In_xGa_{1-x}As$ quantum dots embedded in an $In_{0.52}Al_{0.48}As$ matrix.

5.1 Film growth on InP (100)

All InP wafers used in this thesis were semi-insulating (100)-oriented 3-inch wafers supplied by *AXT, Inc*. Prior to epitaxial growth, the native oxide layer was removed in the MBE main chamber by heating each wafer to 540 °C for 10 min under an As_2 background pressure of 2.00×10^{-5} mbar. It is well established that during this deoxidation procedure an exchange between phosphorus and arsenic takes place, resulting in the formation of a thin InAs layer of approximately 2–3 ML on top of the InP substrate [104]. Despite this exchange process the method is widely used, even showing improved device performances compared to deoxidation under P atmosphere in some cases [105].

For subsequent overgrowth of the InP substrate with $In_{0.52}Al_{0.48}As$, scanning tunneling electron microscopy has demonstrated that the crystal structure is preserved between substrate and film across the artificially formed InAs interlayer [106]. PL measurements further confirm the presence of the resulting quantum well-like InP/InAs/$In_{0.52}Al_{0.48}As$ structure [104], however the corresponding emission wavelengths typically fall in the range of 0.97–1.35 eV [106], and are therefore well separated from the targeted 1.55 µm emission at approximately 0.8 eV.

After oxide desorption, the substrate temperature was lowered to the growth temperature, which for $In_{0.52}Al_{0.48}As$ and $In_{0.53}Ga_{0.47}As$ layers was typically 505 °C, measured by band-edge thermometry. The exact compositions of these layers were subsequently verified by HRXRD measurements, as described in Section 4.3.

Figure 5.2 a) shows the $\omega 2\theta$-scan of an $In_{0.523}Al_{0.477}As$ layer grown on InP. Clear thickness fringes arising from Laue oscillations are visible even at lattice match, enabling an accurate determination of the layer thickness. In practice, tuning the In concentration in $In_xAl_{1-x}As$ is delicate: a composition change of approximately 0.5 % corresponds to a shift of about 1 °C in the In cell temperature at growth rates of $\sim 1\,\text{Å}\,\text{s}^{-1}$. Achieving the correct composition can therefore be a time-consuming process that requires several calibration steps and considerable user experience. In this work, a tolerance of ±0.5 % around the nominal $In_{0.52}Al_{0.48}As$ and $In_{0.53}Ga_{0.47}As$ compositions was considered acceptable.

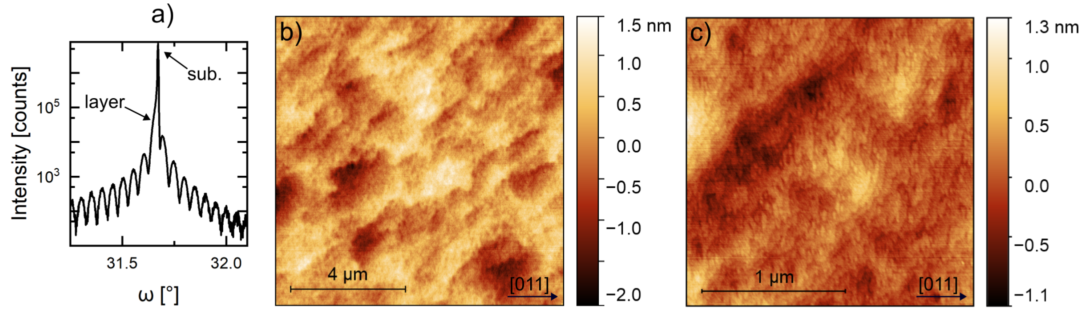

FIGURE 5.2: a) HRXRD $\omega 2\theta$-scan of a lattice-matched $In_xAl_{1-x}As$ layer grown on InP. b), c) AFM images of the same sample.

Following MBE maintenance and refilling of the effusion cells, further calibration steps were required. The Ga and Al fluxes were first coarsely adjusted using beam equivalent pressure (BEP) measurements. More accurate growth-rate calibration was then performed using GaAs and AlAs layers grown on GaAs substrates and monitored via RHEED oscillations. The In cell was initially adjusted using BEP measurements and then calibrated more precisely by growing InGaAs layers on GaAs substrates and analyzing them by HRXRD.

Figure 5.2 b) shows a typical AFM image of a 100 nm thick $In_{0.52}Al_{0.48}As$ surface grown at 505 °C and an As_2 flux of 2.00×10^{-5} mbar. These growth conditions consistently yielded smooth surfaces for both $In_{0.52}Al_{0.48}As$ and $In_{0.53}Ga_{0.47}As$ layers and the RMS in this image shows a value of $\sigma_{RMS} = 0.45$ nm. Figure 5.2 c) shows the same sample with higher magnification and resolution. Here an RMS roughness of $\sigma_{RMS} = 0.26$ nm is revealed. The steps that are visible in this image show heights of 200–300 pm, indicating ML sized $In_{0.52}Al_{0.48}As$ steps.

While the layer composition is a key parameter, the substrate temperature and arsenic flux also play critical roles in achieving optimal film quality. The growth temperature determines the diffusion length of adatoms [42]; higher temperatures increase the probability that adatoms encounter vacant lattice sites, thereby improving surface smoothness. Consequently, elevated growth temperatures have been shown to enhance the crystalline quality of $In_{0.52}Al_{0.48}As$ layers grown on InP (100) [107].

However, the maximum growth temperature is limited by the comparatively lower activation energy for desorption of In adatoms compared to Ga and Al on $In_xAl_{1-x}As$ and $In_yGa_{1-y}As$ surfaces [108, 109]. The literature contains varying reports regarding the onset of significant In desorption: pit formation on lattice-matched $In_{0.52}Al_{0.48}As$ has been observed above 505 °C when measured by pyrometry [110]. In another study, desorption effects became pronounced only above 545 °C [111]. A surface-reconstruction change attributed to desorption in $In_xAl_{1-x}As$/GaAs layers has also been reported at 515 °C, measured by thermocouple [112].

The As flux – more precisely, the V/III-ratio – is equally important for optimized film growth. An unbalanced ratio, either too low or too high, has been shown to significantly deteriorate the surface morphology of $In_{0.52}Al_{0.48}As$ and $In_{0.53}Ga_{0.47}As$

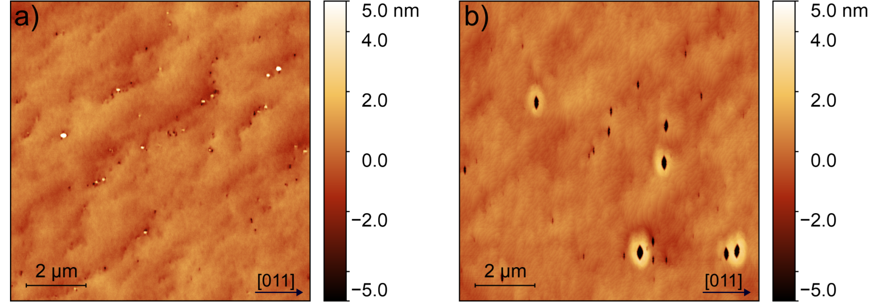

FIGURE 5.3: AFM images of a) $In_{0.52}Al_{0.48}As$ and b) $In_{0.53}Ga_{0.47}As$ layers grown lattice matched on InP at 505 °C under too much As_2 BEP, leading to the formation of surface defects.

and may introduce crystalline defects [113, 114]. Figure 5.3 a) shows the surface morphology of a 100 nm $In_{0.52}Al_{0.48}As$ layer grown at a V/III ratio of ~ 22 at 505 °C. The surface displays pits up to 5 nm deep and island-like features reaching heights of 13 nm. Under identical conditions, an $In_{0.53}Ga_{0.47}As$ layer also exhibits poor morphology, with pits up to 40 nm deep and elongated along the $[0\bar{1}1]$ direction, as shown in Figure 5.3 b).

When the growth temperature was increased to 515 °C, while keeping the same V/III ratio, $In_{0.52}Al_{0.48}As$ layers exhibited smooth surfaces with an RMS roughness of $\sigma_{RMS} = 0.56$ nm measured over 10×10 µm^2. This reflects the narrow process window for achieving optimal surface quality. The precise growth conditions for $In_{0.52}Al_{0.48}As$ and $In_{0.53}Ga_{0.47}As$ depend heavily on how temperature and flux are measured and therefore must be optimized individually for each MBE system [114].

In this work, all lattice-matched $In_{0.52}Al_{0.48}As$ and $In_{0.53}Ga_{0.47}As$ layers grown on InP (100) were deposited using the following parameters:

- InAs growth rate: 1.04 Å s^{-1}; In BEP: 1.40×10^{-6} mbar
- AlAs growth rate: 0.96 Å s^{-1}; Al BEP: 4.1×10^{-7} mbar
- GaAs growth rate: 0.92 Å s^{-1}; Ga BEP: 5.2×10^{-7} mbar
- As_2 BEP: 2.00×10^{-5} mbar
- Growth temperature: 505 °C (measured by band-edge thermometry, *BandiT*)

Having established conditions for the growth of smooth $In_xAl_{1-x}As$ layers, next the dislocation densities ρ of these films were investigated by rocking-curve analysis at the (400) Bragg reflection. Figure 5.4 a) shows the ω-scans measured on a 100 nm thick $In_{0.55}Al_{0.45}As$ layer for azimuthal orientations of $\varphi = 0°$ and $\varphi = 90°$. For this composition, which is slightly lattice-mismatched to InP, the (400) Bragg reflection of the layer is well separated from that of the substrate, and no peak overlap occurs.

Table 5.1 summarizes the measured FWHM (β) values for $\varphi = 0$, 90, 180, and 270° for both the $In_{0.55}Al_{0.45}As$ layer and the InP substrate. Dislocation densities were calculated using Equation 4.23. For $In_xAl_{1-x}As$ and $In_yGa_{1-y}As$ layers grown on InP (100), misfit dislocations are predominantly of the 60° type and glide along $\{111\}$ planes with Burgers vectors of the form $a/2\langle 110\rangle$ [115]. 60° type dislocations

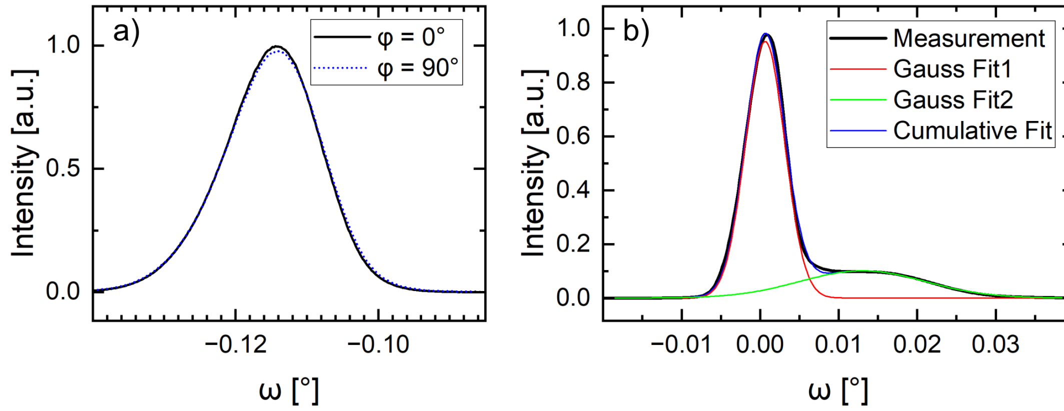

FIGURE 5.4: HRXRD rocking curves showing the (400) Bragg peak of an $In_{0.55}Al_{0.45}As$ layer measured along the [011]- and $[0\bar{1}1]$-directions. The peak is well separated from the (400) InP substrate peak (not shown), allowing for the straightforward measurement of the FWHM β. b) Single rocking curve at the (400) Bragg peak of $In_{0.52}Al_{0.48}As$. Two Gauss peaks were fitted through the measurement with the peak analysis tool of *OriginPro*.

TABLE 5.1: Summary of FWHMs and derived dislocation densities ρ for the $In_{0.55}Al_{0.45}As$ layer and the InP substrate. The HRXRD measurements were acquired with an angular step size of $\Delta\omega = 0.0002°$. For the averaged values for ρ, uncertainties correspond to the standard deviation over the four measurement orientations.

φ (°)	$In_{0.55}Al_{0.45}As$ β (°)	InP β (°)
0	0.0155	0.0060
90	0.0159	0.0076
180	0.0155	0.0065
270	0.0149	0.0067
Average ρ (cm^{-2})	$(9.7 \pm 0.4) \times 10^6$	$(1.8 \pm 0.3) \times 10^6$

are typically dominating in bulk InP substrates, as well [116]. Therefore, a Burgers-vector magnitude of 4.15 Å was used in the calculations of the dislocation densities. Compared with the InP substrate, the $In_{0.55}Al_{0.45}As$ layer exhibits dislocation densities roughly one order of magnitude higher.

Figure 5.4 b) shows a similar scan of a lattice-matched $In_{0.52}Al_{0.48}As$ layer. Two Gaussian peaks were fitted to separate substrate and layer contributions. From these fits, $\beta = (0.019 \pm 0.001)°$ for the layer was obtained, corresponding to a dislocation density of $\rho = (1.5 \pm 0.2) \times 10^7\ cm^{-2}$ for this measurement direction.

These values agree with those determined for the $In_{0.55}Al_{0.45}As$ layer, indicating that the slight lattice mismatch is not the main source of peak broadening compared with the substrate. This increase might originates from the InP/$In_xAl_{1-x}As$ interface. As discussed earlier, deoxidation of the InP substrate under an arsenic flux leads to the formation of a thin InAs layer due to As-P exchange. This interfacial

layer may promote the formation of misfit dislocations, thereby increasing the dislocation density in the overlying film.

Thus, while the employed growth conditions led to smooth $In_{0.52}Al_{0.48}As$ layers on InP – ensuring optimal conditions for reproducible droplet formation, nanohole etching and infilling – further optimization of the growth conditions and the deoxidation step may help to reduce the dislocation densities in the resulting layers.

5.2 Influence of etching parameters

Following the growth of lattice-matched $In_{0.52}Al_{0.48}As$ layers, the LDE process could be applied to these templates. As discussed in Section 3.5, a wide parameter space governs droplet formation and the resulting nanohole morphology, including

- droplet material,
- droplet deposition amount,
- droplet deposition flux,
- substrate temperature during deposition,
- substrate temperature during etching,
- residual As pressure,
- etching time,
- post-etching overgrowth,

with the last point representing an additional parameter that will be examined in Section 5.2.3. During the adaptation of LDE to $In_{0.52}Al_{0.48}As$, all these parameters were systematically varied with the goal of controlling and improving the nanohole morphology so that the resulting structures could serve as optimized templates for quantum dot fabrication. The influence of each parameter will be discussed in detail in the following sections.

Before addressing the etching behavior itself, an initial experiment will be presented, which was performed to capture droplet formation prior to the onset of etching. After growth of a 100 nm $In_{0.52}Al_{0.48}As$ layer, the substrate temperature was lowered to $T = 435\,°C$. Although the etching temperatures can in principle be varied after the deposition step, the substrate temperature was always kept constant throughout the LDE process for all experiments performed. In the remainder of this thesis, this temperature is referred to as the etching temperature T_{etch}.

To preserve the droplets and prevent their consumption, the residual As pressure must be minimized (see Section 3.5). Under standard growth conditions, however, the lowest achievable As_2 pressure was $p_{As2} \approx 1 \times 10^{-7}$ mbar, as will be discussed in Section 5.2.4. Lower As pressures were only obtainable by decreasing the reservoir temperature of the As cell, which must be done slowly ($1\,°C\,min^{-1}$) to avoid condensation within the cells valve region. For the present experiment, the As cell reservoir temperature was reduced by 50 °C over 50 min after the sample had

reached $T_{etch} = 435\,°C$, resulting in an As_2 BEP of $p_{As2} = 1 \times 10^{-8}$ mbar, measured post-growth.

Once the As cell temperature ramp was finished, $\theta_{InAl} = 4.1$ ML of $In_{0.52}Al_{0.48}$ (abbreviated to InAl for the rest of this work) were deposited over 6 s at $T_{etch} = 435\,°C$. The deposition time corresponds to the time required to deposit 4.1 ML under standard $In_{0.52}Al_{0.48}As$ growth conditions. Immediately after deposition, the substrate temperature was rapidly reduced at a rate of $30\,°C\,s^{-1}$ to 250 °C, after which the sample was removed from the system for ex-situ analysis.

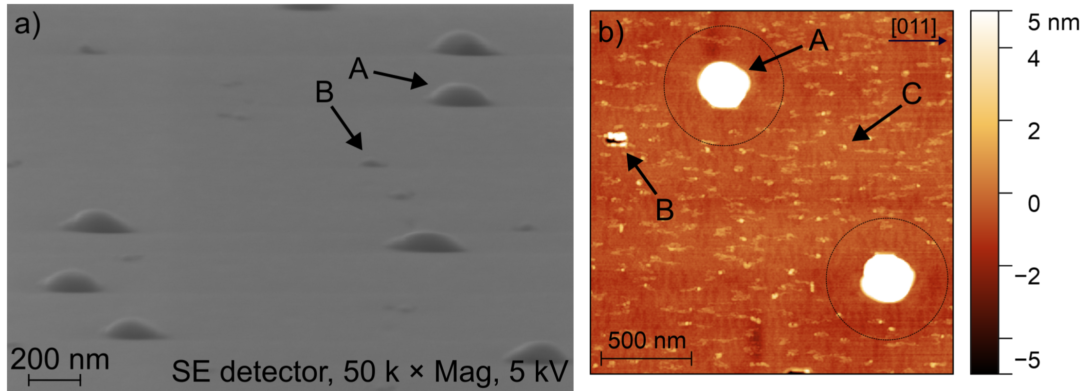

FIGURE 5.5: a) SEM image taken at a tilt angle of 10°, showing large droplets (A) and smaller nanoholes (B) formed under conditions intended to preserve the droplets during deposition. The image was taken by Dr. Viktoryia Zolatanosha. b) AFM image of the same sample, revealing additional surface features.

Figure 5.5 a) shows an SEM image of the resulting surface. Two characteristic feature types are visible: large droplets (A) and smaller structures (B). The AFM image in Figure 5.5 b) reveals that the B-type structures are asymmetric nanoholes. This indicates that, under the chosen parameters, a bimodal distribution formed during droplet deposition – a behavior commonly observed for particular combinations of T_{etch}, θ_{InAl}, and p_{As2} [77].

In addition, the AFM data shows extra features labeled C on the surface. These features are absent in the immediate vicinity of the larger droplets, as highlighted by the circles in Figure 5.5 b). Their occurrence is attributed to residual InAl from the end of the deposition step that nucleated into small clusters instead of aggregating into the larger droplets.

Figure 5.6 a) presents an AFM image of a single droplet. Although droplets are expected to be rotationally symmetric, the shape is partially distorted, indicating the onset of crystallization. The symmetry is broken in the upper region, where the first signs of ring formation appear – evidence of the LDE process in these larger droplets despite the low As flux and rapid cooling.

Figure 5.6 b) shows line profiles along the [011] and $[0\bar{1}\bar{1}]$ directions, together with an overlayed circle and a reference line at $z = 0$. From the [011] profile (black curve), it is evident that ring formation appears to begin at the triple line of droplet, vacuum, and substrate, consistent with observations in the $Al_xGa_{1-x}As$ system [80].

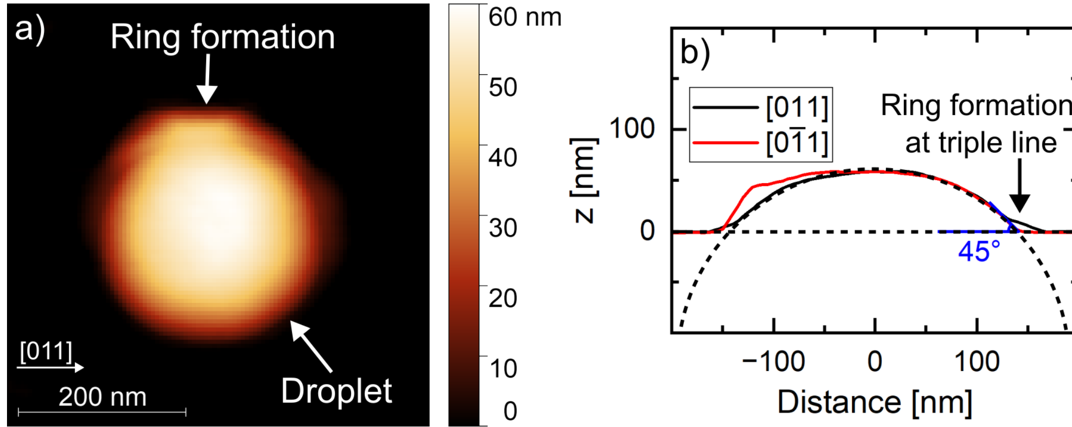

FIGURE 5.6: a) AFM image of an individual droplet. The upper part shows an onset of crystallization and wall formation typical for the initial stage of LDE. b) Corresponding height profiles along the [011] and [0$\bar{1}\bar{1}$] directions. A fitted circle and the reference line at $z = 0$ are shown for determining the contact angle Θ.

Contact angles Θ were measured for five individual droplets, yielding an average value of $\Theta = (44 \pm 1)^\circ$.

As the droplets resemble spherical caps, their volume V can be approximated accordingly. The droplets analyzed here exhibit an average diameter of $d = (315 \pm 9)$ nm and a height of $h = (55 \pm 2)$ nm, corresponding to a spherical-cap volume of $V_{\text{sphere}} = (2.2 \pm 0.2) \times 10^{-15}\,\text{cm}^3$. Using the growth parameters, the expected droplet volume can be estimated from Equation 3.14. The total deposition amount was $\theta = 4.1$ ML, with $\theta_w = 0.3$ ML assumed to be consumed by surface wetting, based on deposition-amount tests discussed in Section 5.2.4. The droplet density was measured to be $n = 2.4 \times 10^7\,\text{cm}^{-2}$.

The nanoholes (B) are expected to have much smaller initial droplet material volumes compared to the large droplets (A), while only exhibiting a slightly higher density of $n = 6.1 \times 10^7\,\text{cm}^{-2}$. As such only the larger droplets will be considered for this comparison.

Following the procedure of Heyn et al. [77], the surface site density was determined as $N_0 = 5.8 \times 10^{14}\,\text{cm}^{-2}$, corresponding to two atoms per (100) surface site of the $In_{0.52}Al_{0.48}As$ unit cell. The molar volume of InAl, $V_m = 1.3\,\text{cm}^3\,\text{mol}^{-1}$, was calculated as a statistical average of the values of the elemental constituents [117].

Substitution of these parameters into Eq. 3.14 yields an expected droplet volume of $V \approx 2.0 \times 10^{-15}\,\text{cm}^3$, showing good agreement with the measured spherical-cap value $V_{\text{sphere}} = (2.2 \pm 0.2) \times 10^{-15}\,\text{cm}^3$ and confirming that the model is applicable under the presented growth conditions.

5.2.1 Nanohole degradation under As_2 flux

During the etching experiments on $In_{0.52}Al_{0.48}As$, different droplet materials were tested to generate nanoholes, i.e. In, Al, and InAl. It was observed that, under certain process conditions, the resulting nanoholes were not stable. In particular,

nanoholes formed with In and InAl droplets disappeared when the As_2 flux was increased again after the etching step.

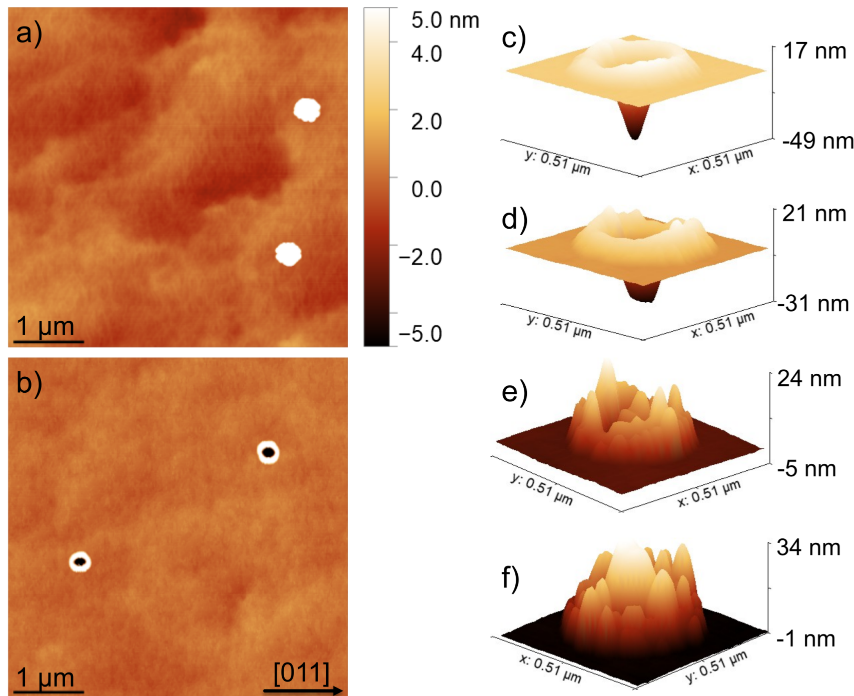

FIGURE 5.7: AFM images of samples produced by In droplet etching with (a) and without (b) resuming the As flux to $p_{As2} = 2.00 \times 10^{-5}$ mbar after the etching step. Additional samples exposed to As_2 for (c) 0, (d) 1, (e) 3, and (f) 5 min reveal progressive nanohole degradation under As_2 exposure. All etching was performed at $p_{As2} = 2 \times 10^{-7}$ mbar with $\theta = 1.4$ ML and $T_{etch} = 435$ °C. Published in [118].

Figure 5.7 a) shows an AFM image of an $In_{0.52}Al_{0.48}As$ layer after LDE performed with In droplets. A total of 1.4 ML of In was deposited over 4 s at $T_{etch} = 435$ °C under a residual As_2 flux of $p_{As2} = 2 \times 10^{-7}$ mbar. After a 3 min etching step, the As_2 flux was increased to its standard growth value of $p_{As2} = 2.00 \times 10^{-5}$ mbar to terminate the etching, followed by cooling to 300 °C. The AFM image reveals a smooth surface with island-like features, suggesting that droplets had formed during deposition, but the etching process had not taken place.

In contrast, Figure 5.7 b) shows the result when the As_2 flux was *not* increased after the 3 min etching step and remained at 2×10^{-7} mbar during cooling. In this case, the expected nanoholes and surrounding rings are clearly visible. Since etching worked under these conditions, the appearance of islands in Figure 5.7 a) must have been caused by the increase in As_2 flux.

To further investigate this behavior, a series of samples was grown with varying exposure times to the increased As_2 flux before cooling. Figures 5.7 c-f) show 3D AFM projections of selected nanoholes after exposure to $p_{As2} = 2.00 \times 10^{-5}$ mbar for 0, 1, 3, and 5 min, respectively. After the chosen exposure time, the flux was reduced back to 2×10^{-7} mbar and the samples cooled to 250 °C. At 0 min exposure, well-formed cone-shaped nanoholes with surrounding rings were observed. After 1 min, the nanoholes were still visible, but their tips became flatter, indicating partial

refilling. After 3 min, the nanoholes had vanished entirely, leaving only rings with small island-like structures. After 5 min, a larger island had formed within the ring, and the original nanohole-ring morphology was no longer present.

These results clearly demonstrate that nanoholes degrade when exposed to an elevated As_2 flux. Initially they decrease in depth and then subsequently, the nanoholes are completely refilled and replaced by droplet-like structures that grow with increasing As_2 exposure time, with a dominant island forming at the center. This behavior has not been reported for droplet etching in the well-established GaAs system. Moreover, degradation was only observed when In was involved in the etching process: nanoholes formed using Al droplets did *not* refill under increased As_2 flux. Thus, a fundamental difference exists between In- and Al-based droplet etching on the $In_{0.52}Al_{0.48}As$ system, with the observed tendency that increased In content in the etching material is correlated with stronger susceptibility to nanohole refilling.

It is hypothesized that surface material surrounding the nanoholes diffuses back into them – but only when In is present in the droplet material – which appears to be enabled by resuming the As_2 flux after the etching process. Such behavior is problematic for further QD fabrication because capping of the nanoholes requires an increase in As flux to ensure smooth $In_{0.52}Al_{0.48}As$ overgrowth (Section 5.1). However, a method was identified that successfully preserves the nanoholes under resumed As flux.

Nanohole preservation was achieved by overgrowing the etched surface with a thin $In_{0.52}Al_{0.48}As$ layer immediately after resuming the As_2 flux. The influence of this thin overgrowth was studied using samples etched with In, InAl, or Al droplets, followed by different amounts of $In_{0.52}Al_{0.48}As$ deposition at $T_{etch} = 435\,°C$. Afterward, the samples were heated to 505 °C before cooling. As this is the same temperature for further infilling and overgrowth of the nanohole templates, this step ensured that the nanoholes characterized by AFM correspond to those that would be present during subsequent processing.

Example line scans from these samples are displayed in Figure 5.8. All samples were grown using the same process parameters ($T_{etch} = 435\,°C$, $p_{As2} = 2 \times 10^{-7}$ mbar, $\theta = 1.4$ ML; InAl deposition over 2 s, In and Al over 4 s).

For In droplets, a clear improvement of nanohole geometry was observed for up to 4 ML of overgrowth. Without any overgrowth the process resulted in a complete collapse of the nanoholes, producing droplets with average heights of (64.9 ± 2.6) nm and diameters of (396 ± 9) nm along [011] and (389 ± 46) nm along $[0\bar{1}1]$ (Figure 5.8 a). With 2 ML overgrowth, shallow nanoholes were preserved with average depths of (12.2 ± 2.2) nm and diameters of (186 ± 10) nm along [011] and (179 ± 6) nm along $[0\bar{1}1]$ (Figure 5.8 b). Increasing the overgrowth to 4 ML led to significant improvement of the nanohole morphology, with much deeper nanoholes ((46.6 ± 5.3) nm), and diameters of (157 ± 13) nm along [011] and (131 ± 11) nm along $[0\bar{1}1]$ (Figure 5.8 c).

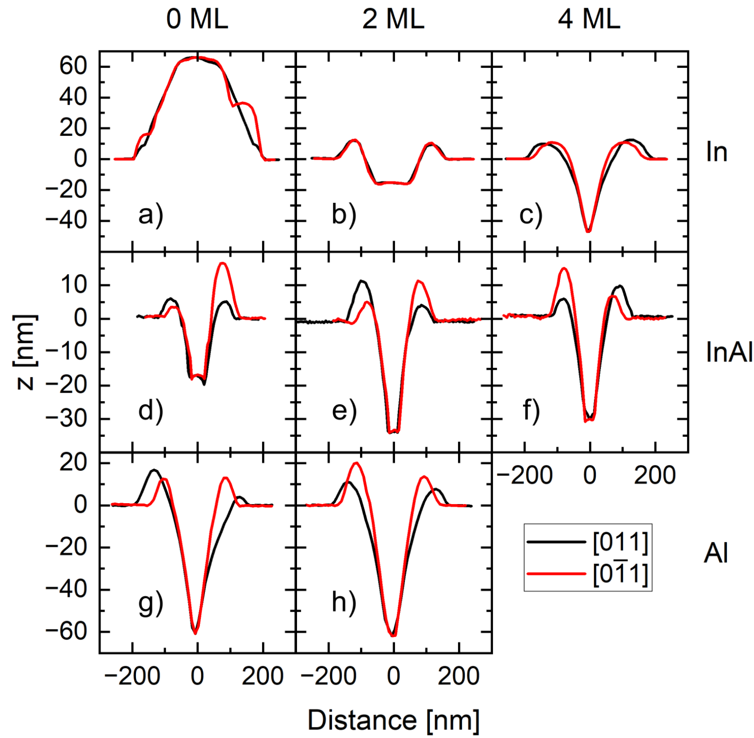

FIGURE 5.8: Line scans of nanoholes from samples overgrown with different amounts of $In_{0.52}Al_{0.48}As$ immediately after reopening the As valve. (a-c) In-droplet etching with 0, 2, and 4 ML overgrowth. (d-f) InAl-droplet etching with 0, 2, and 4 ML overgrowth. (g-h) Al-droplet etching with 0 and 2 ML overgrowth. Etching was performed at $p_{As2} = 2 \times 10^{-7}$ mbar, $\theta = 1.4$ ML, and $T_{etch} = 435\,°C$. Published in [118].

For InAl droplets, similar behavior was found: Compared to no overgrowth (Figure 5.8 d), 2 ML of $In_{0.52}Al_{0.48}As$ overgrowth significantly increased the depth of the nanoholes that were found on the sample (Figure 5.8 e). However, further increasing to 4 ML led to no further changes in the measured nanohole geometries (Figure 5.8 f)).

In contrast to the observations for In and InAl as etching material, the nanohole morphology did not depend on the post-annealing overgrowth when etching with Al droplets. At 0 ML (Figure 5.8 g)) the nanoholes showed no significant difference in shapes to the ones with 2 ML of post etching $In_{0.52}Al_{0.48}As$ overgrowth (Figure 5.8 h)).

These results show that thin $In_{0.52}Al_{0.48}As$ overgrowth effectively prevents degradation of nanoholes after increasing the As_2 flux at the end of the LDE process. The refilling observed for In and InAl droplets without overgrowth is thus avoided, enabling the nanoholes to be used for further processing. Although the exact mechanism remains unclear, it appears that the thin $In_{0.52}Al_{0.48}As$ layer suppresses back-diffusion of surface material once the As_2 flux is increased. Refilling might be primarily due to In adatoms, which bind more weakly to the $In_{0.52}Al_{0.48}As$ surface [108], progressively infilling the nanoholes.

This section is based on material previously published in [118].

5.2.2 Etching temperature

Among all LDE parameters, the substrate temperature during the etching process is arguably the most influential. The temperature during droplet deposition controls the adatom diffusion length and thus affects island formation in this stage. During the etching itself, the temperature governs the diffusion of material from the semiconductor layer into the droplet and from the droplet onto the surface.

Although all LDE parameters jointly determine the final nanohole morphology, the etching temperature T_{etch} represents a natural starting point for understanding their combined influence. While droplet deposition and etching can, in principle, be carried out at different temperatures, both steps were performed at the same temperature T_{etch} in this work.

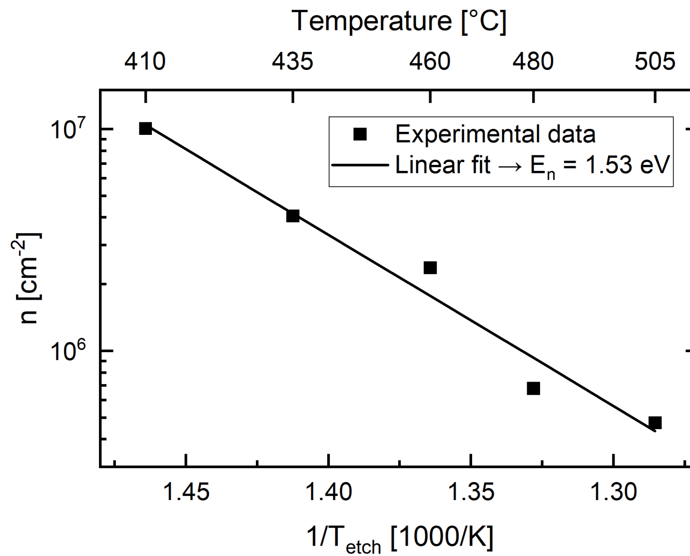

FIGURE 5.9: a) Logarithmic nanohole density n as a function of the inverse temperature for the samples described in the text. The solid line represents a linear fit from which the activation energy E_n was extracted. Published in [119].

Figure 5.9 shows the nanohole surface density as a function of $1/T_{\text{etch}}$ in an Arrhenius-type plot. For this series, InAl droplets were deposited for 6 s on a 100 nm $In_{0.52}Al_{0.48}As$ layer, corresponding to a total deposition of $\theta = 4.1$ ML. The etching temperature was varied between 410 and 505 °C. An As_2 flux of 2×10^{-6} mbar was used, and the etching step lasted 3 min before the As_2 flux was increased to 2.00×10^{-5} mbar. The nanoholes were directly overgrown with 1 ML of $In_{0.52}Al_{0.48}As$, then heated to 505 °C and cooled to 250 °C for removal. The nanohole densities were determined by SEM at 2000× magnification, evaluating at least 40 nanoholes per sample.

The temperature dependence of the nanohole density follows an exponential behavior consistent with nucleation theory [75], discussed earlier in Section 3.5:

$$n \propto \exp\left(\frac{E_n}{k_\mathrm{B} T_\mathrm{etch}}\right). \tag{5.1}$$

From the slope of the Arrhenius plot in Figure 5.9, a characteristic energy of $E_n = (1.53 \pm 0.16)$ eV was extracted. The obtained value is comparable in scale to activation energies previously reported for droplet etching in the AlGaAs system: 0.40 eV for Ga droplets on GaAs [73], 0.54 eV for Ga droplets on $Al_{0.35}Ga_{0.65}As$ [120], 0.46 eV for In droplets on GaAs [73], and 2.46 eV for Al droplets on $Al_{0.35}Ga_{0.65}As$ [77].

Nanohole densities in the $In_{0.52}Al_{0.48}As$ system ranged from $1.0 \times 10^7\,\mathrm{cm}^{-2}$ at $T_\mathrm{etch} = 410\,°\mathrm{C}$ to $5 \times 10^5\,\mathrm{cm}^{-2}$ at $T_\mathrm{etch} = 505\,°\mathrm{C}$, which is comparable to values reported for LDE on GaAs etched between 560 °C and 680 °C [77].

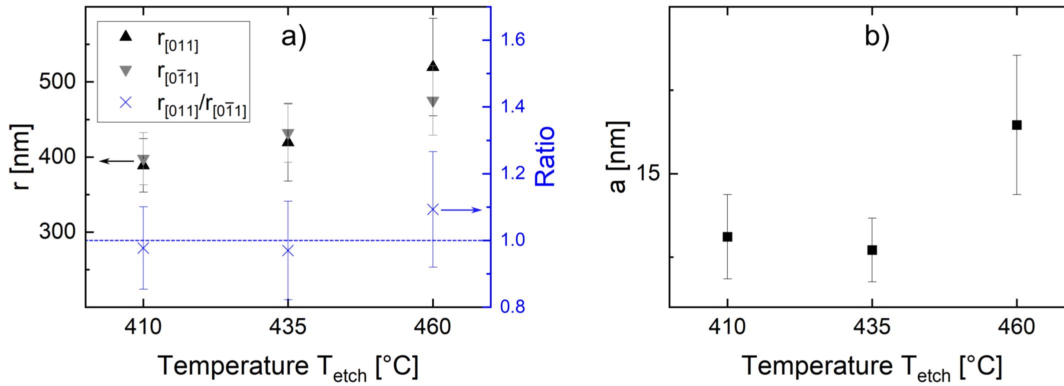

FIGURE 5.10: a) Average ring-hole diameter r and b) ring height a as functions of T_etch, determined from 20 nanoholes per sample.

While the nanohole density decreased with increasing T_etch, the lateral size of the full ring-hole structure increased. Figure 5.10 a) shows the average diameters $r_{[011]}$ and $r_{[0\bar{1}1]}$ and their ratio $r_{[011]}/r_{[0\bar{1}1]}$ as functions of temperature. A clear increase in r with rising T_etch was observed in all etching experiments conducted in this work. Moreover, the ring-hole structures tend to elongate along the [011] direction at higher temperatures.

The morphology of the ring surrounding the nanohole is assumed to originate primarily from the initial droplet geometry formed during the deposition step of the LDE process. Nucleation theory predicts that the droplet volume V scales with temperature [75]:

$$V \propto T_\mathrm{etch}. \tag{5.2}$$

Thus, with increasing T_etch the ring diameter increases as shown in Figure 5.10 a) and the ring height increases as shown in Figure 5.10 b). The observed elongation along [011] for $T_\mathrm{etch} = 460\,°\mathrm{C}$ suggests that this anisotropy was present in the initial droplet geometry, likely caused by asymmetric agglomeration during the droplet

formation, either due to an imbalance of diffusion or atomistic incorporation along the [011] and [0$\bar{1}$1]-directions activated by an increase in temperature [121].

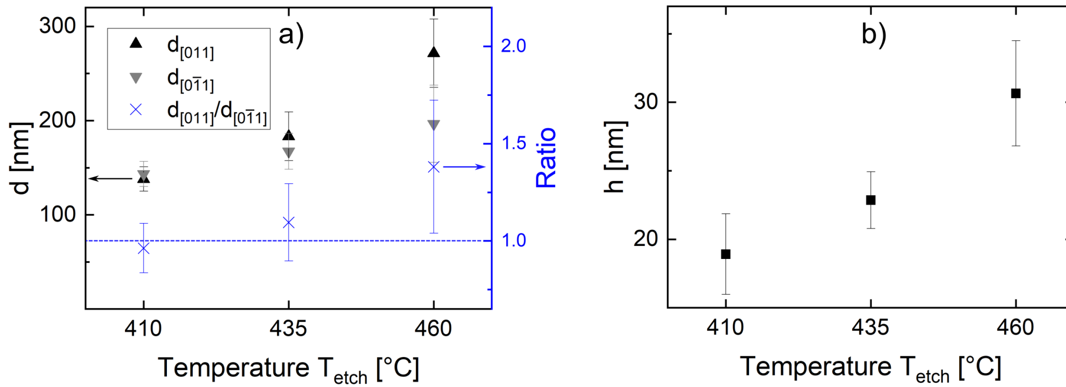

FIGURE 5.11: a) Average nanohole diameter d and b) nanohole depth h as functions of T_{etch}, determined from 20 nanoholes per sample.

Beyond the overall ring-hole size, the nanohole geometry itself is of particular relevance for QD fabrication. Figure 5.11 a) shows the opening diameter d measured along [011] and [0$\bar{1}$1] as well as the ratio $d_{[011]}/d_{[0\bar{1}1]}$. Similar to the ring-hole diameter r, the nanohole opening d increased with temperature. Since d depends strongly on the initial droplet diameter [122], this trend is expected. The increasing ratio $d_{[011]}/d_{[0\bar{1}1]}$ again indicates a temperature-dependent elongation along [011].

Figure 5.11 b) shows the nanohole depth h as a function of T_{etch}. The depth increased monotonically with temperature. Together with the nanohole symmetry, the depth is among the most critical parameters for QD engineering, since vertical confinement directly influences the emission wavelength of the resulting QDs.

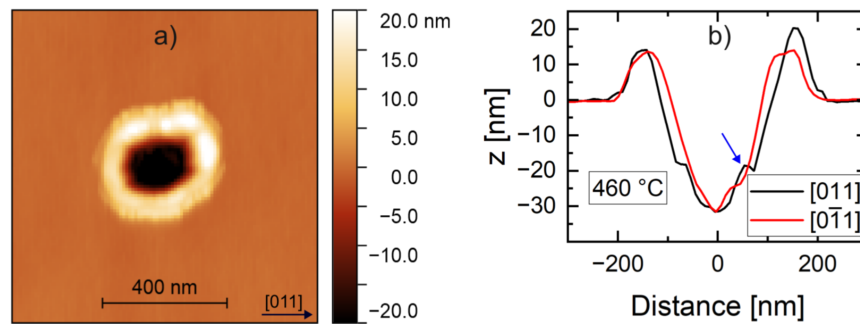

FIGURE 5.12: a) AFM image of a representative nanohole etched at $T_{etch} = 460\,°C$ and b) corresponding line scans along the main crystalline directions.

Figure 5.12 a shows an AFM image of a nanohole produced at $T_{etch} = 460\,°C$, together with the corresponding line scans along the main crystalline directions in Figure 5.12 b). An elongation along [011] is clearly visible. The blue arrow marks the source of the general asymmetry among all the nanoholes produced in this series, which is attributed to partial material refilling after resuming the As flux, as discussed in Section 5.2.1. Although 1 ML of $In_{0.52}Al_{0.48}As$ was overgrown, this thickness might have been insufficient to fully suppress refilling. The influence of T_{etch}

on nanohole morphology will be revisited in a later section using more optimized parameters, where it will be shown that the general temperature trends observed here remain valid.

This section is based on material previously published in [119].

5.2.3 $In_{0.52}Al_{0.48}As$ overgrowth

While a moderate post-etching overgrowth with $In_{0.52}Al_{0.48}As$ under As_2 flux can preserve the nanoholes for subsequent fabrication steps, it was found that growing even thicker layers on top of the etched nanoholes does not infill them significantly, as one might initially expect. This observation proved to be of particular interest and was investigated further by depositing various amounts of $In_{0.52}Al_{0.48}As$ after the etching stage. These experiments revealed that the overgrowth not only preserves the nanoholes but can also be used to modify their in-plane symmetry and the size of the surrounding ring structure.

T_{etch}	410 °C			
$d_{overgrowth}$	0 nm	50 nm	100 nm	150 nm
h [nm]	18.9 ± 3.0	17.5 ± 2.7	16.8 ± 2.2	14.6 ± 1.9
a [nm]	13.1 ± 1.3	5.0 ± 0.8	1.6 ± 0.5	0.2 ± 0.3
$d_{[011]}$ [nm]	138 ± 13	137 ± 29	170 ± 22	185 ± 25
$d_{[0\bar{1}1]}$ [nm]	143 ± 13	149 ± 14	225 ± 14	352 ± 42

T_{etch}	435 °C			460 °C	
$d_{overgrowth}$	0 nm	50 nm	150 nm	0 nm	50 nm
h [nm]	22.9 ± 2.1	25.2 ± 2.3	17.6 ± 3.4	30.7 ± 3.8	33.1 ± 4.5
a [nm]	12.7 ± 1.0	7.2 ± 0.6	0.7 ± 0.4	16.5 ± 2.1	11.0 ± 1.6
$d_{[011]}$ [nm]	183 ± 26	193 ± 31	208 ± 34	272 ± 36	276 ± 23
$d_{[0\bar{1}1]}$ [nm]	167 ± 19	183 ± 23	299 ± 78	197 ± 41	226 ± 44

TABLE 5.2: Average nanohole depth h, ring height a, and nanohole diameters $d_{[011]}$ and $d_{[0\bar{1}1]}$ for different overgrowth thicknesses and etching temperatures.

Table 5.2 summarizes the geometric properties of the nanoholes as a function of etching temperature and $In_{0.52}Al_{0.48}As$ overgrowth thickness. The values for the 0 nm samples correspond to the series discussed in the previous section, where a 1 ML conservation layer had been applied. For the thicker overgrowth layers (50 nm, 100 nm, and 150 nm), the 1 ML conservation layers were applied at T_{etch} as well and the additional $In_{0.52}Al_{0.48}As$ films were deposited after increasing the substrate temperature to $T = 505\,°C$.

For $T_{etch} = 410\,°C$, overgrowth thicknesses of 50, 100, and 150 nm were investigated. Although the nanohole depth decreased slightly with increasing overgrowth, the nanoholes did not disappear, even after 150 nm of material had been deposited. In contrast, the ring height a decreased significantly with overgrowth and essentially vanished at large overgrowth thicknesses, as shown in Figures 5.13 a,b). The nanohole diameter increased with overgrowth, especially along the $[0\bar{1}1]$ direction.

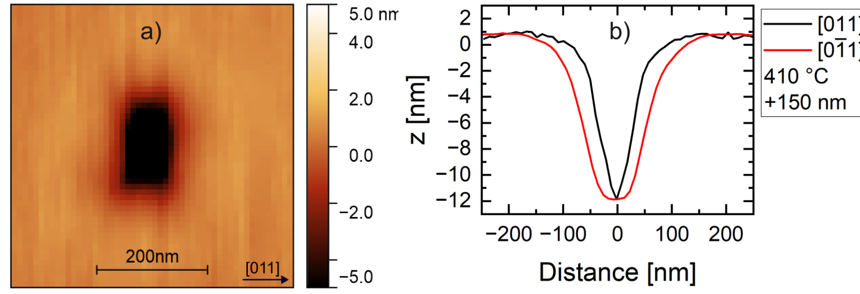

FIGURE 5.13: a) AFM image and b) line scans of a nanohole overgrown with 150 nm of $In_{0.52}Al_{0.48}As$ at $T_{etch} = 410\,°C$.

This indicates that the in-plane asymmetry shifted toward elongation along $[0\bar{1}1]$, becoming more pronounced for larger overgrowth thicknesses. Strongly asymmetric nanoholes were observed for the 150 nm overgrowth case at $T_{etch} = 410\,°C$.

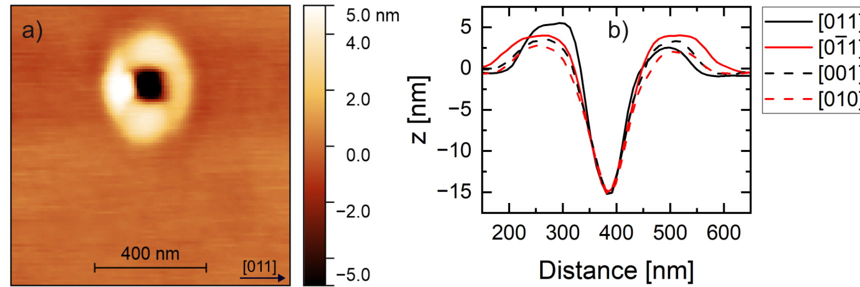

FIGURE 5.14: a) AFM image and b) line scans of a nanohole overgrown with 30 nm of $In_{0.52}Al_{0.48}As$ followed by an 18 nm digital alloy consisting of alternating $In_{0.53}Ga_{0.47}As$ and $In_{0.52}Al_{0.48}As$ layers.

The stability of nanoholes under controlled overgrowth also suggests a route for modifying the matrix material of the final QD structures. By overgrowing the nanoholes with lattice-matched $In_xGa_yAl_{1-y-x}As$, infilling with QD material and then using the same alloy to cap the infilled nanoholes, it would in principle be possible to tune the surrounding bandgap. Since growing true quaternary $In_xAl_yGa_{1-x-y}As$ is experimentally challenging, a digital alloy approach was tested. In this method, alternating nanometer-thin layers of $In_{0.52}Al_{0.48}As$ and $In_{0.53}Ga_{0.47}As$ are deposited so that the average composition mimics that of a quaternary alloy.

Figure 5.14 shows the resulting nanohole morphology after 30 nm of $In_{0.52}Al_{0.48}As$ overgrowth at 505 °C, followed by an 18 nm digital alloy consisting of six repetitions of 2 nm $In_{0.53}Ga_{0.47}As$ and 1 nm $In_{0.52}Al_{0.48}As$. The line scans in Figure 5.14 b) show that the nanohole retains its typical shape with good symmetry, particularly in the depth range from $z = -5$ nm to $z = -15$ nm.

Returning to Table 5.2, it is evident that the trends observed at $T_{etch} = 410\,°C$ also persist at higher etching temperatures ($T_{etch} = 435\,°C$ and 460 °C). With increasing overgrowth, the nanohole diameters expand, with $d_{[0\bar{1}1]}$ increasing more strongly than $d_{[011]}$. At 50 nm overgrowth, an increase in nanohole depth h was observed for both temperatures, possibly due to incomplete conservation with only 1 ML of

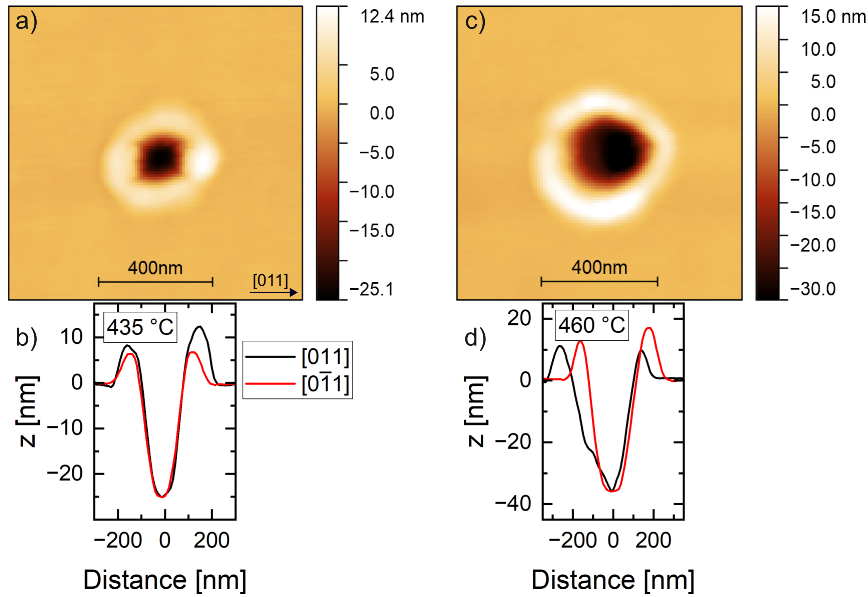

FIGURE 5.15: a,b) AFM image and line scan of a nanohole etched at $T_{etch} = 435\,°C$ with 50 nm overgrowth. c,d) Same for $T_{etch} = 460\,°C$.

post-etching $In_{0.52}Al_{0.48}As$. For thicker overgrowth layers, h decreased again, as illustrated by the 150 nm overgrowth case at $T_{etch} = 435\,°C$.

Overall, nanoholes etched at $T_{etch} = 410\,°C$ and 435 °C combined with 50 nm overgrowth provided promising templates for subsequent QD fabrication. Figures 5.15 a,b) show an exemplary nanohole for $T_{etch} = 435\,°C$ with 50 nm overgrowth and corresponding line scans.

At $T_{etch} = 460\,°C$, the nanohole diameters were already relatively large at 50 nm overgrowth, and further overgrowth was not pursued; an example is shown in Figures 5.15 c,d).

Although the nanoholes produced at $T_{etch} = 410\,°C$ and 435 °C already provided suitable templates for QD fabrication – and were used as such (see Section 5.5) – additional parameter optimization was carried out to produce deeper nanoholes with smaller diameters and, ideally, to eliminate the need for the 50 nm overgrowth step at 505 °C.

This section is based on material previously published in [119].

5.2.4 As flux and etching material amount

The next parameters investigated for their influence on nanohole formation were the residual As flux during etching and the deposited amount of etching material. As discussed in Section 3.5, the As flux plays a critical role throughout the LDE process. A sufficiently low As flux is required during droplet formation to allow liquid droplets to form. During the etching step the As flux regulates diffusion of material between droplet and layer surface, as it controls crystallization of etching material on the surface, which traps it there and prevents the diffusion back into the droplet. If the As pressure is too low, material from the layer surface diffuses back

into the droplet, suppressing etching; if it is too high, premature crystallization stops the etching process.

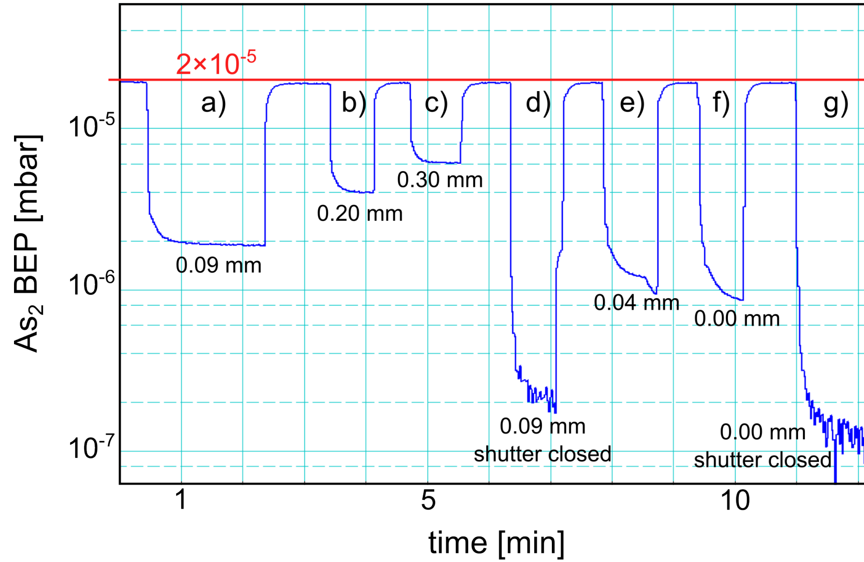

FIGURE 5.16: Beam equivalent pressures (BEPs) of the As_2 flux measured with the beam flux monitor (BFM) for various As-valve configurations. The red line indicates the BEP used for layer growth, corresponding to a valve opening of 1.89 mm during this experiment.

The residual As_2 flux during the LDE process was controlled by the opening position of the valve of the valved As cracker source (VACS) and by the state of the shutter in front of the cell. The valve opening is adjusted by a motorized control unit and can be set between 0.00 mm and 7.99 mm with a resolution of 0.01 mm. During recipe-based growth via the control program Epicad the lowest possible valve opening is 0.09 mm and lower valve openings must be set manually outside of the automatic recipe-based growth.

Figure 5.16 shows the BEP measured over time for different valve and shutter configurations at a cracker temperature of 900 °C. Reducing the valve opening from 1.89 mm to 0.09 mm lowered the BEP from 2.00×10^{-5} mbar to 2.0×10^{-6} mbar after 30 s. Even lower pressures were achieved by also closing the shutter: Figure 5.16 d) shows a BEP of 2×10^{-7} mbar measured 30 s after reducing the valve opening to 0.09 mm and closing the shutter. Closing the valve completely (Figure 5.16 g)) yielded only a further reduction by a factor of two.

Reaching the low 10^{-8} mbar range would have required decreasing the reservoir temperature itself (see Section 5.2), which can only be done at a rate of 1 °C min^{-1} to avoid condensation in the valve region of the As cell. Additionally, due to the relatively large volume of the As reservoir proper flux stabilization can take up multiple hours. As this would significantly complicate growth of nanohole structure and their further infilling and overgrowth, the experiments on As-flux dependence were restricted to BEPs of $p_{As2} = 2 \times 10^{-7}$ mbar and above.

For this series, 100 nm of lattice-matched $In_{0.52}Al_{0.48}As$ was first grown on InP at 505 °C. The temperature was then lowered to $T_{etch} = 435$ °C, chosen because it had

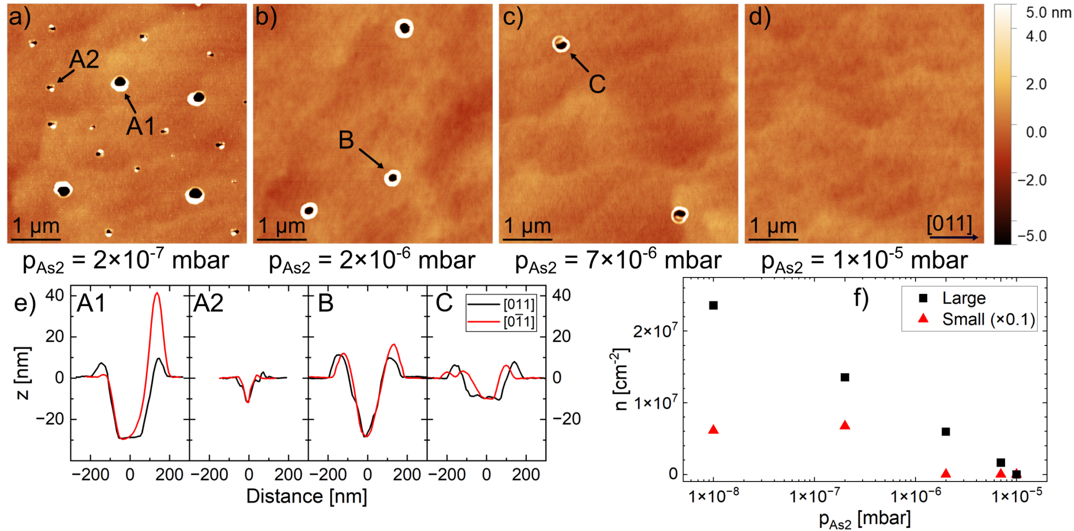

FIGURE 5.17: a-d) AFM images of samples etched using different As_2 fluxes as indicated. All samples were grown with $\theta_{\text{InAl}} = 4.1\,\text{ML}$, $T_{\text{etch}} = 435\,°\text{C}$, and $t_{\text{overgrowth}} = 2\,\text{ML}$. e) Line scans for selected nanoholes marked in the AFM images. f) Nanohole densities n as a function of residual As_2 flux p_{As2}. Values for the smaller nanohole species were multiplied by a factor of 0.1 for clarity. The nanohole densities were determined by SEM, evaluating at least 100 nanoholes per sample. Published in [118].

produced relatively deep nanoholes ($\sim 25\,\text{nm}$) with favorable in-plane symmetry in the previous experiments. After reaching T_{etch}, the As_2 flux was adjusted via the As valve opening and shutter state as described above and the following As_2 pressures were tested: $p_{\text{As2}} = 2 \times 10^{-7}$, 2.0×10^{-6}, 7.0×10^{-6}, and $1.00 \times 10^{-5}\,\text{mbar}$. The InAl deposition amount of $\theta_{\text{InAl}} = 4.1\,\text{ML}$ over 6 s and the subsequent 3 min etching time were kept identical to earlier experiments. To ensure sufficient nanohole conservation, the post-etching overgrowth at T_{etch} was increased to 2 ML. Afterward, the samples were heated to 505 °C and then cooled for removal. No additional overgrowth at 505 °C was performed.

Figure 5.17 a) shows the surface morphology for $p_{\text{As2}} = 2 \times 10^{-7}\,\text{mbar}$, where a bimodal nanohole distribution was observed. Larger nanoholes exhibited an average depth of $(28.9 \pm 1.6)\,\text{nm}$ and a density of $1.3 \times 10^7\,\text{cm}^{-2}$, while smaller nanoholes appeared at a much higher density of $6.7 \times 10^7\,\text{cm}^{-2}$. As discussed previously, bimodal distributions are known from the GaAs system [83, 84] and arise for particular combinations of T_{etch}, θ_{InAl}, and p_{As2}, and might be associated with changes in surface reconstruction [77] or with the group-III and As adatom ratio on the surface during droplet formation [83].

Increasing the As pressure ten-fold to $p_{\text{As2}} = 2.0 \times 10^{-6}\,\text{mbar}$ (Figure 5.17 b)) produced a uniform nanohole distribution. The nanohole depth remained unchanged, but the density dropped to $6.0 \times 10^6\,\text{cm}^{-2}$ and the small nanohole population had disappeared.

Further increasing the As flux to $p_{\text{As2}} = 7.0 \times 10^{-6}\,\text{mbar}$ resulted in nanoholes that showed signs of incomplete etching (Figure 5.17 c). The higher As flux likely

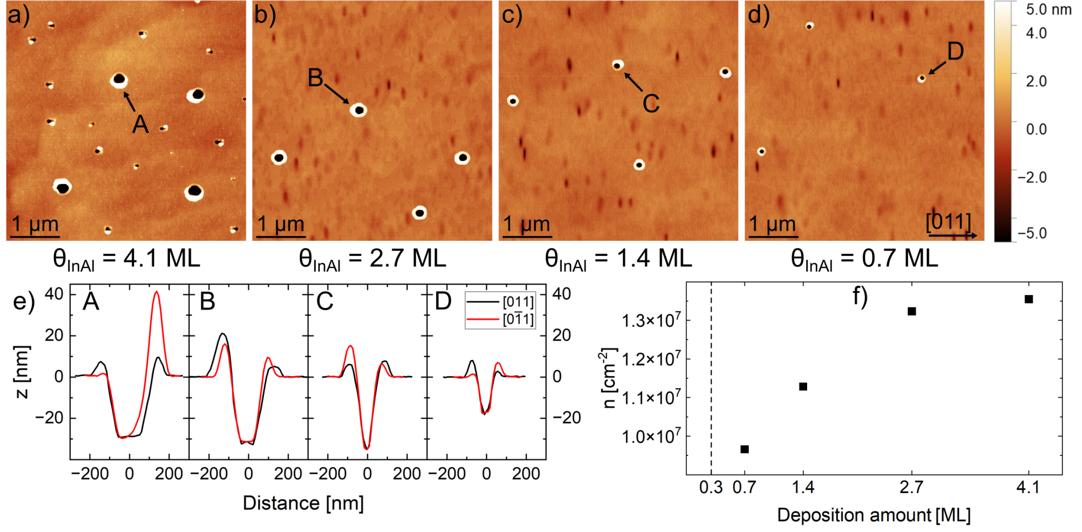

FIGURE 5.18: a-d) AFM images of samples grown with fixed $p_{As2} = 2 \times 10^{-7}$ mbar, $T_{etch} = 435\,°C$, and $t_{overgrowth} = 2$ ML while varying the InAl amount θ_{InAl} as indicated. e) Line scans along the two high-symmetry directions for selected nanoholes. f) Nanohole density n plotted as a function of θ_{InAl}. No nanoholes were found for $\theta_{InAl} = 0.3$ ML (indicated by the dashed line). The nanohole densities were determined by SEM, evaluating at least 200 nanoholes per sample. Published in [118].

caused premature crystallization of etching material, which terminated the etching process. The density also decreased to $1.6 \times 10^6\,cm^{-2}$.

At $p_{As2} = 1.00 \times 10^{-5}$ mbar no nanoholes formed (Figure 5.17 d). At this pressure, sufficient As was available to react with all supplied In and Al, resulting in formation of a 4.1 ML $In_{0.52}Al_{0.48}As$ layer rather than droplets – thus preventing droplet etching entirely.

Figure 5.17 f) shows the measured nanohole densities plotted as a function of the logarithmic BEP. The data points corresponding to $p_{As2} = 1 \times 10^{-8}$ mbar originate from the earlier experiment in which the As reservoir temperature was reduced in order to capture the droplet state (see Section 5.2). The density of the larger nanoholes exhibits a clear dependence on the As_2 flux, which may be attributed to an effective reduction of the group-III material deposition rate F caused by the crystallization of adsorbed adatoms upon interaction with arsenic on the surface. A similar trend has been reported for local droplet etching on $Al_{0.36}Ga_{0.64}As$ layers, where reduced arsenic background pressures likewise resulted in increased nanohole densities [80]. These observations highlight that the As flux is a critical parameter that must be controlled with high accuracy to ensure the reproducible formation of nanoholes.

To eliminate the bimodal nanohole distribution observed at this parameter combination and to reduce the relatively large nanohole diameters, the etching process was further optimized by investigating the influence of the InAl deposition amount θ_{InAl}. This series of samples was grown in the same manner as the previous one, with the only difference being a fixed As flux of $p_{As2} = 2 \times 10^{-7}$ mbar and a variation in θ_{InAl}. Deposition amounts of $\theta_{InAl} = 4.1, 2.7, 1.4, 0.7,$ and 0.3 ML were tested

by adjusting the deposition times to 6, 4, 2, 1, and 0.5 s, respectively.

Figure 5.18 a) shows again the sample obtained with $p_{As2} = 2 \times 10^{-7}$ mbar and $\theta_{InAl} = 4.1$ ML, exhibiting a bimodal nanohole distribution. Reducing the InAl amount resulted in a uniform nanohole distribution (Figure 5.18 b). The average nanohole diameters decreased from (254 ± 18) nm along [011] and (205 ± 7) nm along $[0\bar{1}1]$ for $\theta_{InAl} = 4.1$ ML to (174 ± 9) nm and (145 ± 10) nm, respectively, for $\theta_{InAl} = 2.7$ ML. This reduction can be attributed to the smaller droplet volumes expected for lower material deposition, as $V \propto \theta$ (see Equation 3.14). Interestingly, the nanohole depth remained nearly unchanged: the average depths were (28.9 ± 1.6) nm and (27.3 ± 3.6) nm for $\theta_{InAl} = 4.1$ ML and 2.7 ML, respectively.

Further reduction of the etching material to $\theta_{InAl} = 1.4$ ML (Figure 5.18 c)) decreased the nanohole diameters to (113 ± 10) nm along [011] and (100 ± 7) nm along $[0\bar{1}1]$. Somewhat surprisingly, the average depth increased slightly to (33.2 ± 2.5) nm. However, when θ_{InAl} was further reduced to 0.7 ML (Figure 5.18 d), both the nanohole diameters ((82 ± 3) nm along [011] and (77 ± 3) nm along $[0\bar{1}1]$) and the average depth ((17.6 ± 1.4) nm) decreased. A deposition amount of $\theta_{InAl} = 0.3$ ML resulted in a nanohole-free surface, indicating that all supplied adatoms bound to the arsenic terminated surface, leading to no droplet formation. Thus, the threshold for droplet formation at $T_{etch} = 435$ °C and $p_{As2} = 2 \times 10^{-7}$ mbar lies between $\theta_w = 0.3$ ML and 0.7 ML. This range agrees well with reports from LDE studies on $Al_{0.35}Ga_{0.65}As$ at $\sim 1 \times 10^{-7}$ mbar As BEP, where threshold values of $\theta_w = 0.2$ ML for Al droplets [77] and $\theta_w = 1.0$ ML for Ga droplets [120] were observed.

Figure 5.18 f) shows that the nanohole density decreased by approximately 30 % across the tested range as θ_{InAl} was reduced. However, this variation is small and may be attributed to statistical fluctuations. Heyn *et al.* reported no dependence of the density on the etching-material amount for Al droplet etching on $Al_xGa_{1-x}As$, establishing a coverage parameter of $z = 1$ in Equation 3.11 ($n \propto \theta^{1-z}$) [77]. Their reported densities ranged from 1×10^7 cm^{-2} to 3×10^7 cm^{-2}, whereas the values observed here fall within the narrower range of 1.0×10^7 cm^{-2} to 1.4×10^7 cm^{-2}.

These results support the conclusion that $z = 1$ also applies in the present system. As such, most of the droplet nucleation happens early in the process and the nanohole density n is effectively independent of the deposition amount θ_{InAl}, as new adatoms agglomerate into the existing droplets. However, this changes after a certain deposition amount (here for θ_{InAl} between 2.7 to 4.1 ML), when a second population of droplets begin to nucleate. This process might be linked to a change in surface reconstruction when a deposition threshold is reached, leading to creation of additional nucleation centers [77, 123].

Regarding the in-plane symmetry of the nanoholes, a slight elongation toward the [011] direction was consistently observed for all deposition amounts. The magnitude of this elongation decreased with decreasing θ_{InAl}, from (24.9 ± 6.6) % at 4.1 ML to (21.3 ± 8.4) % at 2.7 ML, (12.8 ± 6.6) % at 1.4 ML, and (6.1 ± 5.5) % at 0.7 ML. At 0.7 ML, 6 out of 10 analyzed nanoholes exhibited elongations below 10 %.

Particularly good in-plane symmetry was also found for the slightly deeper nanoholes generated with $\theta_{\mathrm{InAl}} = 1.4\,\mathrm{ML}$. In this group, 4 out of 10 nanoholes showed diameter differences below 10 % between the two high-symmetry directions, including one nanohole with perfect symmetry. Moreover, for all nanoholes at this deposition amount, the line scans along [011] and [0$\bar{1}$1] overlapped closely across most of the depth profile, with deviations confined to only the upper 5–10 nm.

This section is based on material previously published in [118].

5.2.5 Droplet material type and etching temperature

In the following experimental series, the influence of etching temperature was reexamined using the optimized parameters identified earlier, and the study was extended to investigate how different droplet materials affect nanohole formation. For this purpose, $In_{0.52}Al_{0.48}As$ layers with thicknesses up to 200 nm were grown, as nanoholes were expected to reach depths exceeding 100 nm at higher etching temperatures. After growth of the underlying layer, the substrate temperature was adjusted to the chosen etching temperature T_{etch}. The temperatures investigated were $T_{\mathrm{etch}} = 410, 435, 460, 480,$ and $505\,^{\circ}\mathrm{C}$.

During droplet formation, the arsenic flux was reduced to $p_{\mathrm{As2}} = 2 \times 10^{-7}\,\mathrm{mbar}$, and a nominal coverage of $\theta = 1.4\,\mathrm{ML}$ of InAl, In, or Al was deposited. The deposition times were 2 s for InAl and 4 s for In and Al, leading to different effective deposition rates across the droplet types. After droplet formation, a standard 3 min etching step was performed at the same reduced As flux, after which the As_2 pressure was increased to $p_{\mathrm{As2}} = 2 \times 10^{-5}\,\mathrm{mbar}$ to terminate etching. Subsequently, 4 ML of $In_{0.52}Al_{0.48}As$ were deposited to stabilize the etched nanoholes. Finally, the substrate temperature was raised to 505 °C – the temperature used for nanohole infilling in QD fabrication – before cooling the samples to 200 °C for removal.

Figures 5.19 a-c) show the dependence of nanohole depth h, ring height a, and nanohole d and ring-hole r diameters along the [011] and [0$\bar{1}$1] directions as functions of T_{etch} for InAl droplets. All parameters increased with temperature, consistent with the behavior discussed previously in Section 5.2.2. The insets in Figures 5.19 b) and 5.19 c) display the ratios $d_{[011]}/d_{[0\bar{1}1]}$ and $r_{[011]}/r_{[0\bar{1}1]}$, respectively.

A general tendency towards elongation of the nanohole diameter d along [011] was observed in all samples. Elongation increased with temperature, similar to the earlier experiments where T_{etch} was varied, however here the progression was not strictly monotonic; a sharp increase occurred between $T_{\mathrm{etch}} = 435$ and 460 °C.

For the ring-hole structures at 410 °C, the ratio $r_{[011]}/r_{[0\bar{1}1]} = (0.98 \pm 0.03)$ confirmed the absence of a preferred adatom incorporation direction at lower temperatures for the chosen LDE parameters. However, increasing T_{etch} led to progressively elongated ring structures, showing a clear temperature dependence.

Figures 5.20 a-c) present analogous results for the In- and Al-droplet series. Overall, Al droplets produced the deepest nanoholes across most temperatures, except at 505 °C. The nanohole depth increased from $h = (31.5 \pm 3.2)\,\mathrm{nm}$ to $(110.2 \pm 12.0)\,\mathrm{nm}$

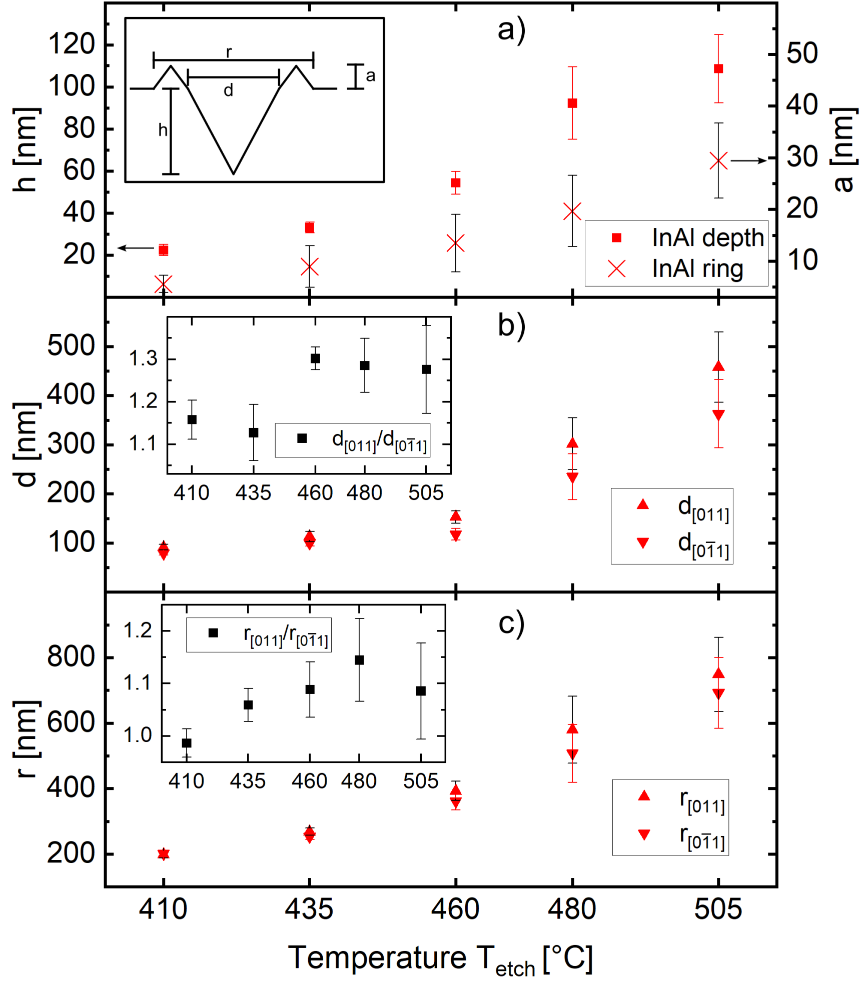

FIGURE 5.19: a) Average nanohole depth h, ring height a, b) nanohole diameter d and c) ring-hole diameter r plotted against T_{etch} for nanoholes etched into $In_{0.52}Al_{0.48}As$ layers with InAl droplets, as described in the text. Values were measured on 10 individual nanoholes on each sample.

for In droplets, and from $h = (33.1 \pm 9.0)$ nm to (107.0 ± 7.3) nm for Al droplets. The ability to generate ultra-deep nanoholes with controlled depths suggests promising applications for complex quantum architectures, such as vertically stacked QDs emitting in the O- and C-band telecommunications windows [124].

Increasing T_{etch} also enlarged the nanohole diameters. For all droplet materials, nanoholes were consistently wider along [011]. For In droplets, this elongation increased with temperature, whereas for Al droplets, it remained largely constant except for one outlier at 435 °C. Across the full temperature range, Al-etched samples exhibited the highest degree of nanohole diameter d elongation.

The generally observed elongation of the ring-hole diameter r suggests the idea that the initial droplet geometry might be causing the anisotropy in the nanohole diameters d. However, several nanoholes displayed rings with little or opposite elongation, while the nanoholes themselves remained elongated along [011]. This indicates that droplet shape alone cannot account for this observation.

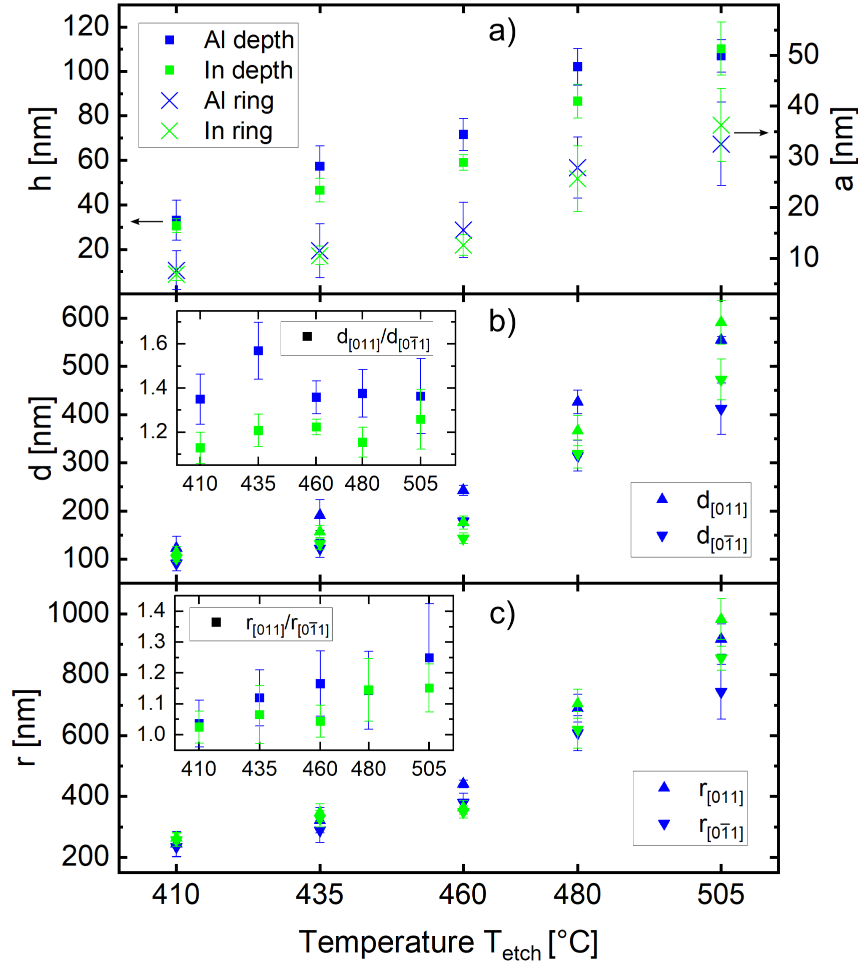

FIGURE 5.20: a) Average nanohole depth h, ring height a, b) nanohole diameter d and c) ring-hole diameter r plotted against T_{etch} for nanoholes etched into $In_{0.52}Al_{0.48}As$ layers with In or Al droplets, as described in the text. Values were measured on 10 individual nanoholes on each sample.

One plausible explanation for the observed elongation is anisotropic, facet dependent etching. Similar behavior has been reported for Al-droplet etching on AlGaAs layers and attributed to the polarity of the zincblende lattice. There, for (100)-oriented layers, the inner walls of the nanoholes were found to consist mainly of {111}, {211}, and {311} facets [82]. The {211} and {311} facets are stepped surfaces composed of {111} terraces separated by atomic steps. Because these facets can exhibit different terminations (A- vs. B-type) depending on their orientation, the local etch rate can differ between perpendicular crystallographic directions, leading to an elongated hole shape [82].

Further factors that may contribute are anisotropic mass transport in the droplet and anisotropic surface diffusion. In the $InP/In_{0.53}Ga_{0.47}As$ material system for example, surface diffusion of In adatoms has been shown to be larger along the [011] direction, with the degree of anisotropy increasing at higher substrate temperatures [125]. Taken together, these mechanisms might underlie the elongation of nanoholes observed in the $In_{0.52}Al_{0.48}As$ layers studied here.

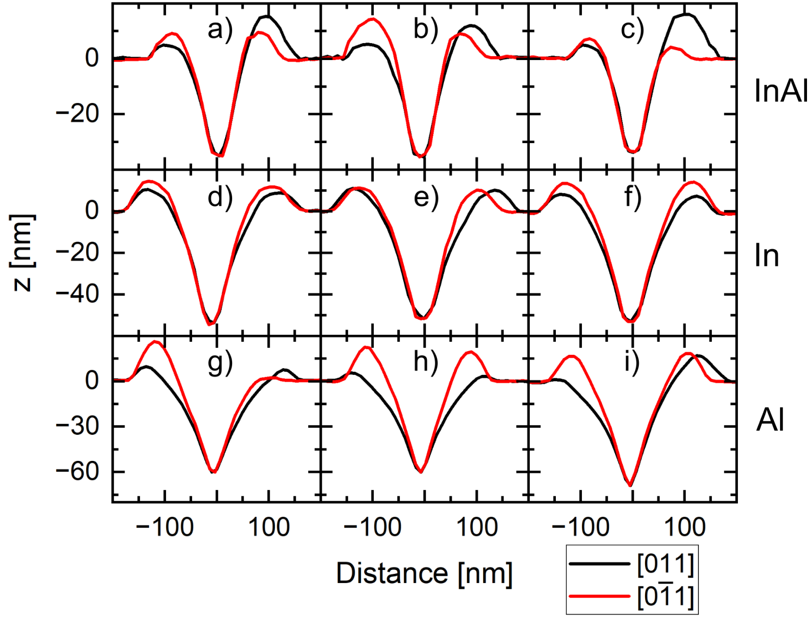

FIGURE 5.21: Selected line scans for nanoholes etched at $T_{\text{etch}} = 435\,°\text{C}$ using: a-c) InAl droplets, d-f) In droplets, and g-i) Al droplets.

Nanoholes etched with InAl droplets at $T_{\text{etch}} \leq 435\,°\text{C}$ exhibited the smallest difference between the [011] and [0$\bar{1}$1] diameters, consistent with earlier results. Interestingly, Al-etched nanoholes at 435 °C also displayed good symmetry within the lowest $\sim$ 30 nm of the depth, suggesting that symmetric QDs could be fabricated by infilling these holes only to this height. In-etched nanoholes at the same temperature exhibited reasonable symmetry in their lowest $\sim$ 30 nm, although these structures are less suitable for QD fabrication due to the presence of optically active In rings. Figures 5.21 a-i) display selected nanohole profiles from $T_{\text{etch}} = 435\,°\text{C}$ for all tested etching materials.

Overall, the results indicate that etching temperatures near $T_{\text{etch}} = 435\,°\text{C}$ yield nanoholes with the highest in-plane symmetry, independent of droplet material. This temperature window is therefore ideal for producing symmetric nanohole templates for well-defined QDs.

Figure 5.22 shows the nanohole densities n as a function of $1/T_{\text{etch}}$ in an Arrhenius-type plot. InAl droplets yielded the highest densities, whereas In and Al droplets produced significantly lower densities across all temperatures. This difference arises from the different deposition rates F used during droplet formation. According to Equation 3.11, the droplet density

$$n \propto F^p, \tag{5.3}$$

where θ is the total deposited material, and p the nucleation scaling exponent [75]. In the present series, InAl was deposited at 0.68 ML/s, approximately twice the deposition rate of In and Al (0.34 ML/s). Ratios of the measured nanohole densities

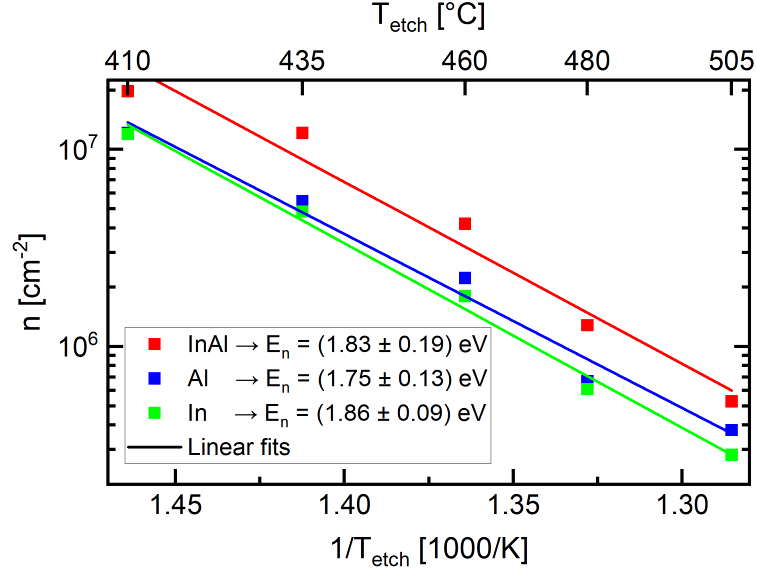

FIGURE 5.22: Logarithmic plot of nanohole densities n as a function of inverse temperature $1/T_{\text{etch}}$ for the samples described in the text. The nanohole densities were determined by SEM, evaluating at least 150 nanoholes per sample. Colored lines represent linear fits from which the activation energies E_n were extracted. Published in [118].

averaged over all temperatures yielded values of 1.8:1 (InAl:Al), 2.1:1 (InAl:In), and 1.2:1 (Al:In).

From deposition rate experiments that will be discussed in Section 5.2.6 a scaling exponent of $p_{460} = 0.88 \pm 0.05$ was found for InAl droplets at $T_{\text{etch}} = 460\,°\text{C}$. Assuming similar values of p for the In and Al droplets, puts the employed deposition rate ratios into a relatively good agreement with the ratios of the nanohole densities estimated from the data sets ($n/n = (0.68/0.34)^{0.88} = 1.84$).

The temperature dependence of nanohole density followed the exponential relation given by the characteristic activation energy E_n in Equation 3.11. Linear fits of the Arrhenius-type plots in Figure 5.22 yielded similar activation energies for the three droplet types of

- $E_n = (1.83 \pm 0.19)$ eV for InAl,
- $E_n = (1.75 \pm 0.13)$ eV for Al and
- $E_n = (1.86 \pm 0.09)$ eV for In.

Earlier experiments yielded a value of $E_n = (1.53 \pm 0.16)$ eV for InAl droplets etched at LDE parameters $p_{\text{As2}} = 2 \times 10^{-6}$ mbar and $\theta_{\text{InAl}} = 4.1$ ML (see Section 5.2.2).

Figure 5.23 shows the logarithmic nanohole density n for both InAl temperature series plotted against the inverse etching temperature $1/T_{\text{etch}}$. Samples etched at $p_{\text{As2}} = 2 \times 10^{-7}$ mbar generally exhibit a higher density at all temperatures except for $T_{\text{etch}} = 505\,°\text{C}$. As established earlier, θ_{InAl} has only a minor effect on the resulting density, while a clear dependence on p_{As2} was observed (see Section 5.2.4). Therefore, this difference in densities between the two series must originate from the employed residual arsenic pressure.

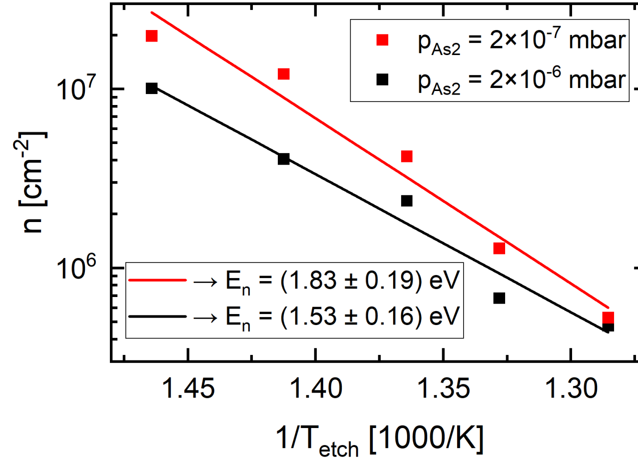

FIGURE 5.23: Logarithmic plot of nanohole densities n as a function of inverse temperature $1/T_{etch}$ for the two InAl temperature series: $p_{\mathrm{As2}} = 2 \times 10^{-6}$ mbar, $\theta_{\mathrm{InAl}} = 4.1$ ML and $p_{\mathrm{As2}} = 2 \times 10^{-7}$ mbar, $\theta_{\mathrm{InAl}} = 1.4$ ML. Solid lines represent linear fits from which the activation energies E_n were extracted.

Within the complete-condensation nucleation picture, the effective energy E_n contains contributions from the adatom diffusion barrier E_d and the nucleation energy E_i (see Equation 3.12) [75]. Changing the residual As background might modify surface reconstructions and/or influence cluster stability, modifying these energies. A lower As flux may therefore lead to a larger E_n, even if the overall droplet density increases due to a reduced competing combination of group-III adatoms with residual As.

This section is based on material previously published in [118].

5.2.6 Etching material deposition rate

The following experiment investigates how the deposition rate of the etching material during droplet formation influences the subsequent nanohole morphology. In this study, a nominal coverage of $\theta_{\mathrm{InAl}} = 1.4$ ML of InAl was deposited over time intervals of 20, 6.7, 2, and 1 s. These deposition times correspond to deposition rates ranging from $F = 0.2$ Å s^{-1} to $F = 4.0$ Å s^{-1}. The experiments were performed under an As_2 flux of $p_{\mathrm{As2}} = 2 \times 10^{-7}$ mbar at etching temperatures of $T_{\mathrm{etch}} = 350$ and 460 °C, respectively, followed by an etching duration of $t_{\mathrm{etch}} = 180$ s.

In this series, the arsenic background pressure was not increased after the etching step to terminate the process, as the conservation of the nanoholes with $In_{0.52}Al_{0.48}As$ deposition rates other than 2 Å s^{-1} has not been tested, and the same group-III effusion cells used for droplet formation would have been required for layer deposition. Consequently, all samples were cooled from the etching temperature to 200 °C at a rate of 30 °C min^{-1} under a constant As_2 flux of $p_{\mathrm{As2}} = 2 \times 10^{-7}$ mbar. It is likely that etching persisted to some extent during this cooldown phase, particularly for the samples processed at the higher temperature of $T_{\mathrm{etch}} = 460$ °C.

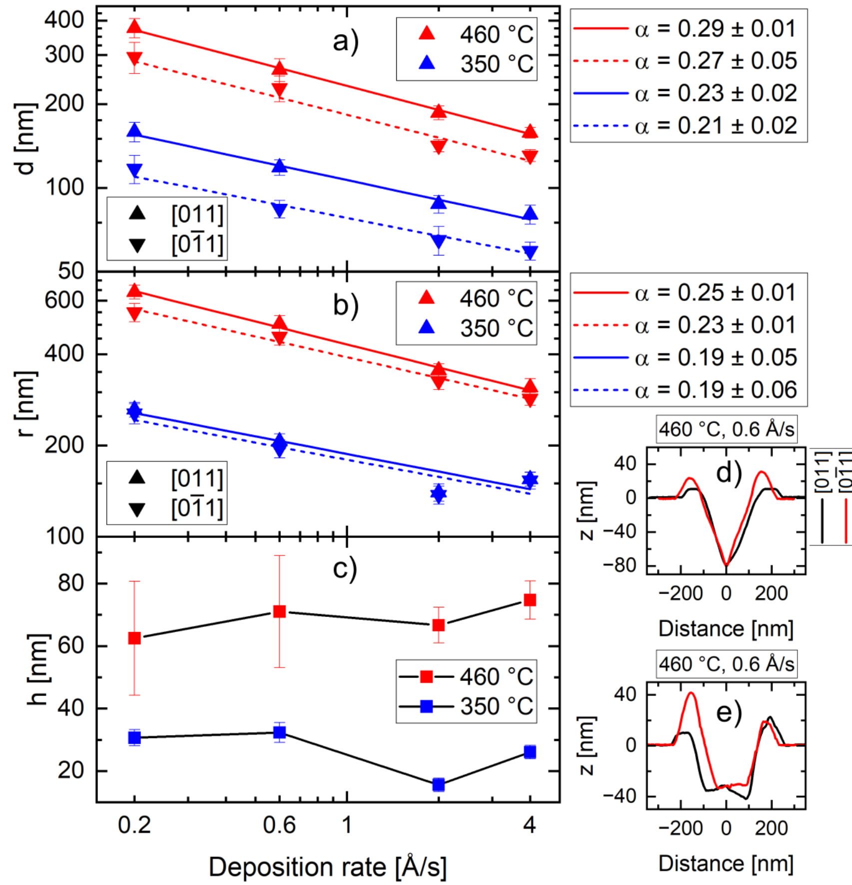

FIGURE 5.24: a) Double-logarithmic plot of the average nanohole diameter d and b) ring-hole diameter r as a function of the InAl deposition rate F during LDE. The colored lines represent linear fits with the slopes α. c) Nanohole depth h plotted against the logarithmic InAl deposition rate F. d), e) Exemplary line scans of the two types of nanoholes formed at $T_{etch} = 460\,°C$ and $F = 0.6\,Å\,s^{-1}$. Data originally published in [126].

The deposition rate of the etching material had a pronounced effect on both the in-plane dimensions of the resulting ring-hole structures and the nanohole diameters. Figure 5.24 a) presents the average nanohole diameters measured along the [011] and [0$\bar{1}$1] crystallographic directions as a function of the InAl deposition rate. For both investigated etching temperatures, a clear inverse correlation was observed: the nanohole diameter decreased with increasing deposition rate.

At $T_{etch} = 350\,°C$, the diameters amounted to $d_{[011]} = (159 \pm 13)$ nm and $d_{[0\bar{1}1]} = (117 \pm 14)$ nm for a deposition rate of $F = 0.2\,Å\,s^{-1}$. When the deposition rate was increased by an order of magnitude to $2.0\,Å\,s^{-1}$, the diameters approximately halved, yielding $d_{[011]} = (83 \pm 6)$ nm and $d_{[0\bar{1}1]} = (68 \pm 4)$ nm. A similar trend was found for the samples etched at $T_{etch} = 460\,°C$: the respective values decreased from $d_{[011]} = (376 \pm 30)$ nm and $d_{[0\bar{1}1]} = (295 \pm 38)$ nm at $F = 0.2\,Å\,s^{-1}$ to $d_{[011]} = (201 \pm 19)$ nm and $d_{[0\bar{1}1]} = (165 \pm 15)$ nm at $F = 2.0\,Å\,s^{-1}$.

A comparable dependence on deposition rate was also observed for the overall ring-hole structure. As shown in Figure 5.24 b), the average diameters r of the complete structures along the [011] and [0$\bar{1}$1] directions decreased systematically with

increasing deposition rate, consistent with the behavior of the nanohole diameters.

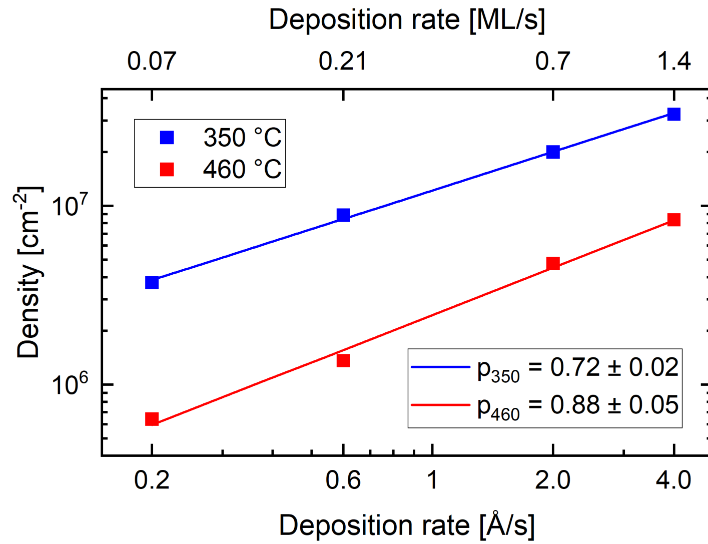

FIGURE 5.25: Nanohole density n as a function of the material deposition rate during LDE in a double logarithmic plot. Colored lines represent linear fits with slopes p. Measured by Normen Auler and originally published in [121].

This trend most likely reflects the behavior of the droplets formed during deposition: higher deposition rates lead to the formation of smaller droplets with higher areal densities. Figure 5.25 shows the nanohole density n as a function of the deposition rate F in a double-logarithmic plot. An increase in density with increasing deposition rate is clearly observed. According to classical scaling theory [75], the density n depends on the deposition rate F as described by Equation 5.3.

From the slopes of the linear fits shown in Figure 5.25, the nucleation scaling exponents p were determined for the two tested temperatures, resulting in $p_{350} = 0.72 \pm 0.02$ and $p_{460} = 0.88 \pm 0.05$ for $T_{\text{etch}} = 350\,^{\circ}\text{C}$ and $460\,^{\circ}\text{C}$, respectively [121].

As outlined in Section 3.5, the droplet volume depends on the total deposition amount θ, the droplet density n, and the portion of the material θ_w consumed in wetting the initially arsenic-terminated surface layer, as given by Equation 3.14 [127]. Consequently, the average droplet volume (and thus the droplet diameter) is expected to exhibit an inverse dependence on the deposition rate F,

$$V \propto F^{-p}. \tag{5.4}$$

The relationships summarized in Equations 5.3 and 5.4 are fully consistent with the experimental findings. Increasing the deposition rate results in an increase in the nanohole density on the surface, while the concurrent decrease in ring-hole diameter and nanohole diameter indicate the formation of smaller droplets. This interpretation is further supported by the measured ring heights a: for $T_{\text{etch}} = 460\,^{\circ}\text{C}$, the average height decreases from $a = (23 \pm 6)$ nm at $F = 0.2\,\text{Å}\,\text{s}^{-1}$ to $a = (11 \pm 6)$ nm at $F = 4.0\,\text{Å}\,\text{s}^{-1}$.

Under the assumption that the droplets maintain a constant contact angle over the investigated range of deposition rates, they can be approximated as spherical caps of constant aspect ratio. In this case, the droplet volume scales cubically with the base diameter according to $V \propto d^3_{\text{droplet}}$ [128]. Combining this relation with Equation 5.4 yields

$$d_{\text{droplet}} \propto V^{1/3} \propto F^{-p/3}. \tag{5.5}$$

The linear fits in the double-logarithmic plots of Figures 5.24 a) and b) show that the nanohole and ring-hole diameters follow power laws of the form $d \propto F^{-\alpha}$ (and analogously $r \propto F^{-\alpha}$). The values for α and for the nucleation scaling exponents p, determined independently from the density scaling, approximately exhibit the expected relationship of $p \approx 3\alpha$. Here, the ring-hole diameters r exhibit stronger deviations from the ideal proportionality case. This behavior suggests that r might not be proportional to droplet size alone, but includes an additional contribution from flux-independent lateral material transport during the etching process. The nanohole diameter scaling however shows a relatively good agreement with the model, indicating that d is directly proportional to the lateral size of the initial droplets.

In contrast to the dependence observed for the diameters, the nanohole depth did not scale monotonically with the deposition rate of the etching material. Figure 5.24 c) shows the average nanohole depth h as a function of the deposition rate for the two investigated etching temperatures. For both temperatures, a similar non-monotonic trend was observed: the average depth initially increased as the deposition rate rose from $F = 0.2\,\text{Å}\,\text{s}^{-1}$ to $0.6\,\text{Å}\,\text{s}^{-1}$, decreased at $F = 2.0\,\text{Å}\,\text{s}^{-1}$, and then increased again at $F = 4.0\,\text{Å}\,\text{s}^{-1}$. Such behavior is unexpected if the depth were governed solely by the droplet size at constant T_{etch}. Instead, both temperature series show qualitatively the same shape of the trend, offset by their etching temperature difference, with higher temperatures producing deeper nanoholes overall. The non-monotonic behavior cannot be attributed to statistical variation alone, as the spread in measured depths is small, particularly for $T_{\text{etch}} = 350\,°\text{C}$. At present, the underlying mechanism responsible for these variations remains unresolved.

For the series etched at $T_{\text{etch}} = 460\,°\text{C}$, two distinct nanohole morphologies were consistently observed at $F = 0.2\,\text{Å}\,\text{s}^{-1}$ and $F = 0.6\,\text{Å}\,\text{s}^{-1}$, which explains the larger deviation of the data points from the average trend. Figures 5.24 d) and e) display representative AFM images from the $T_{\text{etch}} = 460\,°\text{C}$, $F = 0.6\,\text{Å}\,\text{s}^{-1}$ sample, illustrating these two morphologies. The first type, shown in Figure 5.24 d), consists of deeper nanoholes with rounded bottoms, where the deepest point lies near the center. The second type, displayed in Figure 5.24 e), consists of slightly shallower holes with noticeably flat bottoms. Complementary SEM measurements confirmed that

these morphological differences are not caused by indium-aluminum phase separation, as this would have resulted in different material compositions of the surrounding ring, leading to visible contrast differences [129]. The shallower nanoholes resemble initial etching stages and may result from incomplete material removal due to an imbalance between etching duration and the available liquid etchant volume.

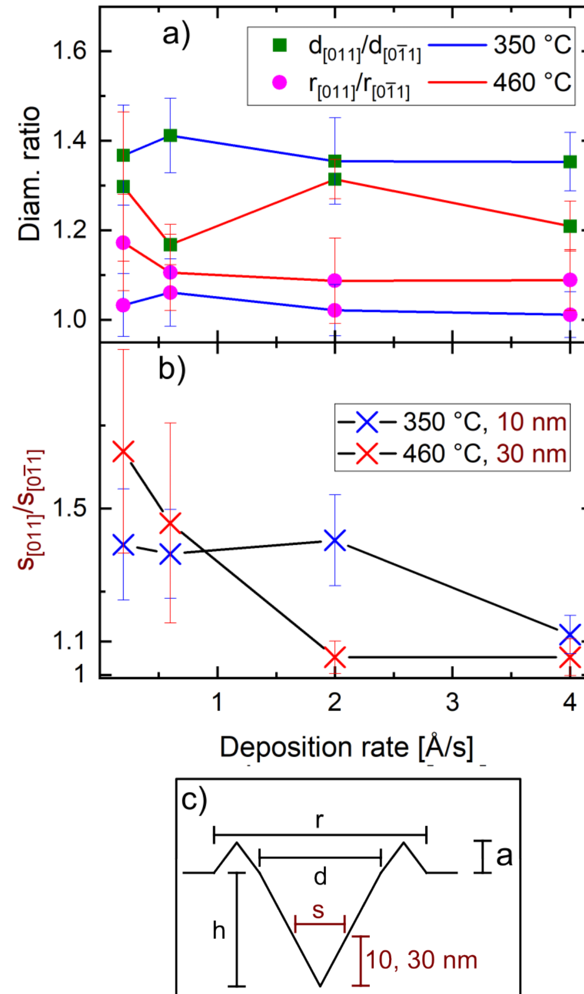

FIGURE 5.26: a) Ratios of ring-hole diameters $r_{[011]}/r_{[0\bar{1}1]}$ and nanohole diameters $d_{[011]}/d_{[0\bar{1}1]}$ plotted against the deposition rate. b) Nanohole diameter ratios at 10 nm above the nanohole for the $T_{\text{etch}} = 350\,°\text{C}$ series and at 30 nm above the nanohole for the $T_{\text{etch}} = 460\,°\text{C}$ series to discern their viability as templates for QD processing. c) Sketch of measured nanohole parameters.

To further analyze the symmetry properties of the etched nanostructures, the diameter ratios of the nanoholes and ring-hole structures were evaluated. Figure 5.26 a) presents the average diameter ratios of the nanoholes ($d_{[011]}/d_{[0\bar{1}1]}$) and of the entire ring-hole structures ($r_{[011]}/r_{[0\bar{1}1]}$) as a function of the deposition rate for both investigated etching temperatures.

For $T_{\text{etch}} = 350\,°\text{C}$, the sample grown at $F = 4\,\text{Å}\,\text{s}^{-1}$ exhibited the highest degree of symmetry. Here, the ring-hole structures showed an average ratio close to the

ideal value of unity, with $r_{[011]}/r_{[0\bar{1}1]} = 1.01 \pm 0.05$, and 12 out of 20 measured structures fell within the range (1.00 ± 0.03). Although the rings tended to be slightly elongated, no preferential crystallographic orientation was apparent at this temperature.

In contrast, increasing the etching temperature to $T_{\mathrm{etch}} = 460\,^{\circ}\mathrm{C}$ led to a pronounced change in structural anisotropy. At the same deposition rate of $F = 4\,\mathrm{Å\,s^{-1}}$, only 3 of the 20 analyzed structures lay within $r_{[011]}/r_{[0\bar{1}1]} = (1.00 \pm 0.03)$, while the remaining 17 were consistently elongated along the [011] direction. This fits well with earlier observations, were the ring-hole diameter r has shown significant elongation only for temperatures above $T_{\mathrm{etch}} = 410\,^{\circ}\mathrm{C}$ (see Sections 5.2.2 and 5.2.5).

Interestingly, an opposite trend was observed for the nanohole cavities themselves: the elongation ratio $d_{[011]}/d_{[0\bar{1}1]}$ decreased with increasing etching temperature. This behavior contrasts with earlier experiments, in which an increase in temperature was generally associated with enhanced elongation of the nanohole diameter.

At present, no definitive explanation for this discrepancy can be provided. The droplet etching process involves a complex interplay of several temperature dependent mechanisms, including facet-specific etching rates, material transport during etching, and possible changes in surface reconstruction around $T \approx 410\,^{\circ}\mathrm{C}$ [121]. The combined influence of these effects may give rise to the observed behavior. A conclusive interpretation, however, would require a detailed analysis of the nanohole faceting and its temperature dependence.

To assess the suitability of the etched nanoholes as templates for symmetric quantum dots, the nanohole diameters were analyzed at heights of 10 nm and 30 nm above the minimum depth for the $T_{\mathrm{etch}} = 350\,^{\circ}\mathrm{C}$ and $T_{\mathrm{etch}} = 460\,^{\circ}\mathrm{C}$ samples, respectively (see Figure 5.26 b)). At $T_{\mathrm{etch}} = 350\,^{\circ}\mathrm{C}$, the holes produced at deposition rates between 0.2 and $2\,\mathrm{Å\,s^{-1}}$ exhibited strong elongation, even when considering only a 10 nm infilling height. The morphology improved significantly for the $F = 4\,\mathrm{Å\,s^{-1}}$ sample, where the average ratio was (1.12 ± 0.06); however, 18 of the 20 analyzed nanoholes still displayed ratios greater than 1.05. Consequently, the parameters tested at $T_{\mathrm{etch}} = 350\,^{\circ}\mathrm{C}$ are not suitable for achieving high structural symmetry in quantum dot fabrication.

The situation improves markedly at higher etching temperatures. Samples etched at $T_{\mathrm{etch}} = 460\,^{\circ}\mathrm{C}$ with deposition rates of 2 and $4\,\mathrm{Å\,s^{-1}}$ exhibited highly favorable symmetry for potential nanohole infilling up to 30 nm. For both conditions, 12 out of 20 measured nanoholes showed diameter ratios below 1.05. The $F = 4\,\mathrm{Å\,s^{-1}}$ sample in particular demonstrated smaller overall diameters compared with the $F = 2\,\mathrm{Å\,s^{-1}}$ sample ($F = 2\,\mathrm{Å\,s^{-1}}$: $d_{[011],30\,\mathrm{nm}} = (66 \pm 6)\,\mathrm{nm}$, $d_{[0\bar{1}1],30\,\mathrm{nm}} = (64 \pm 6)\,\mathrm{nm}$; $F = 4\,\mathrm{Å\,s^{-1}}$: $d_{[011],30\,\mathrm{nm}} = (47 \pm 4)\,\mathrm{nm}$, $d_{[0\bar{1}1],30\,\mathrm{nm}} = (47 \pm 5)\,\mathrm{nm}$).

A representative line scan taken from the $T_{\mathrm{etch}} = 460\,^{\circ}\mathrm{C}$ sample at $F = 2\,\mathrm{Å\,s^{-1}}$ is shown in Figure 5.27. Since the in-plane symmetry and overall geometry of quantum dots have a direct impact on their optical properties [130, 131, 132], these results

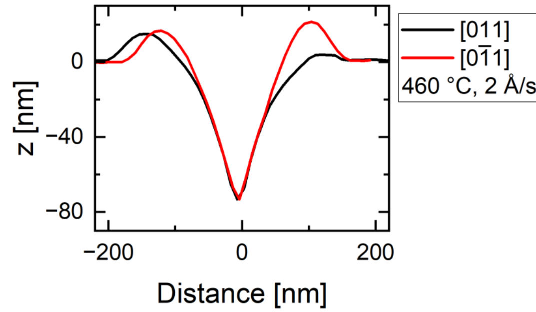

FIGURE 5.27: Exemplary line scan of a nanohole etched at $T_{etch} = 460\,°C$ with $F = 2\,Å\,s^{-1}$. Published in [126].

highlight the role of the material deposition rate during droplet deposition as a key parameter for controlling droplet size and the resulting nanohole morphology.

This section is based on material previously published in [126].

5.2.7 Etching time

In this final series of experiments conducted on $In_{0.52}Al_{0.48}As$ layers, the effect of the etching duration during the LDE process was investigated for InAl, In, and Al droplets. These experiments aimed to evaluate how prolonged or shortened etching influences the depth and morphology of the resulting nanoholes. The etching temperature was fixed at $T_{etch} = 435\,°C$ and a nominal coverage of $\theta = 1.4$ ML of InAl, In, or Al was deposited within 2 s for InAl and 4 s for pure In and Al, respectively. After droplet formation, the samples underwent an etching step under a reduced arsenic flux of $p_{As2} = 2 \times 10^{-7}$ mbar, for durations ranging from $t_{etch} = 30$ to 600 s. To terminate the etching process, the As_2 flux was increased to $p_{As2} = 2 \times 10^{-5}$ mbar, and 4 ML of $In_{0.52}Al_{0.48}As$ were deposited to preserve the etched nanoholes. Following this step, all samples were reheated to 505 °C – corresponding to the temperature typically used for nanohole infilling during QD fabrication – before being cooled to 200 °C.

Figures 5.28 a-c) show the dependence of the nanohole depth h on the etching time t_{etch} for samples processed with InAl, In, and Al droplets, respectively. In the InAl droplet series, h increased steadily between $t_{etch} = 30$ and 180 s, reaching a maximum depth of $h = (33.2 \pm 2.5)$ nm at $t_{etch} = 180$ s. For longer etching times, the depth decreased slightly and approached a plateau by $t_{etch} = 360$ s, showing no significant change relative to the longest investigated duration of $t_{etch} = 600$ s.

The series etched with In droplets exhibited a comparable overall behavior at longer etching times, with maximum depths of (49.1 ± 2.1) nm and (49.4 ± 4.0) nm reached between $t_{etch} = 270$ and 360 s, followed by a subsequent decrease at $t_{etch} = 600$ s. However, the early evolution of the nanoholes differed notably from the InAl case. For short etching durations ($t_{etch} = 30$ to 135 s), most nanoholes were

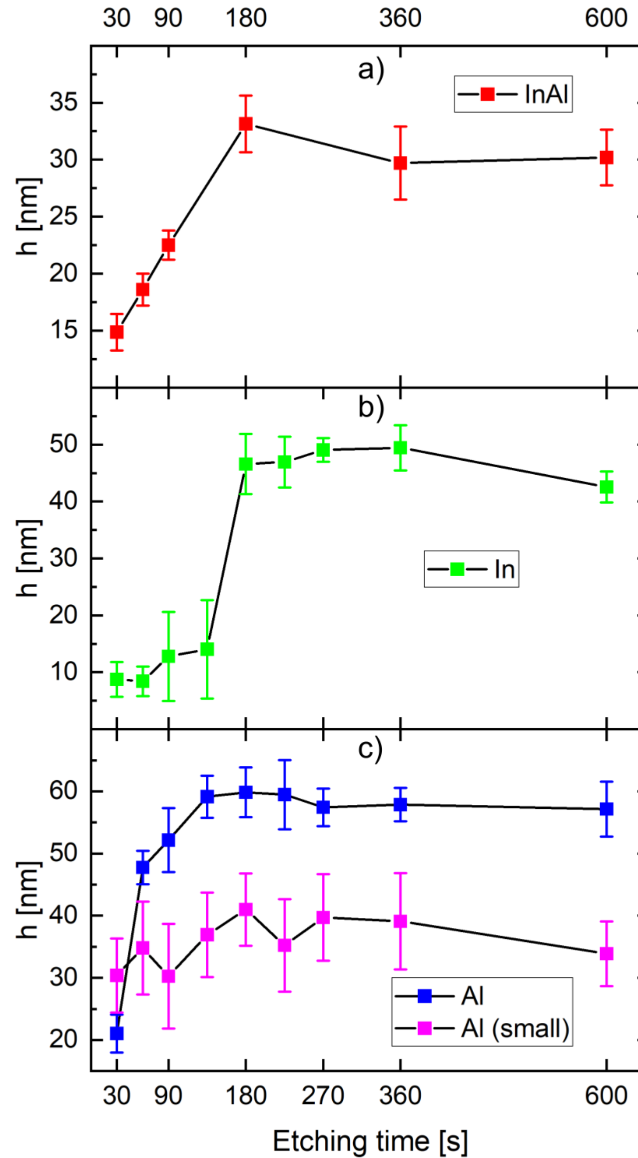

FIGURE 5.28: Average etching depth h for a) InAl, b) In and c) Al deposition during LDE plotted against the etching time t_{etch}. 20 individual nanoholes were measured for each sample. Published in [126].

shallow with predominantly flat bottoms. As t_{etch} increased, the fraction of well-developed nanoholes – defined here as those exhibiting a rounded bottom – gradually increased, which is reflected in the larger data scatter at $t_{\text{etch}} = 90$ and 135 s. Beyond this stage, h rose sharply at $t_{\text{etch}} = 180$ s and the shallow and flat nanoholes vanished. Afterward, etching progressed more slowly until $t_{\text{etch}} = 270$ s.

For the Al droplet series, two distinct types of nanoholes were observed under all tested conditions, as illustrated in the AFM image in Figure 5.29. The pronounced difference in feature size suggests the formation of droplets with a bimodal size distribution. Accordingly, the nanoholes were separated into two subsets based on the ring-hole diameter along the [011] direction: small structures with $r_{[011]} \leq 250$ nm and large ones with $r_{[011]} \geq 280$ nm. The large nanoholes occurred approximately twice as frequently as the smaller ones. Statistical analysis performed separately for

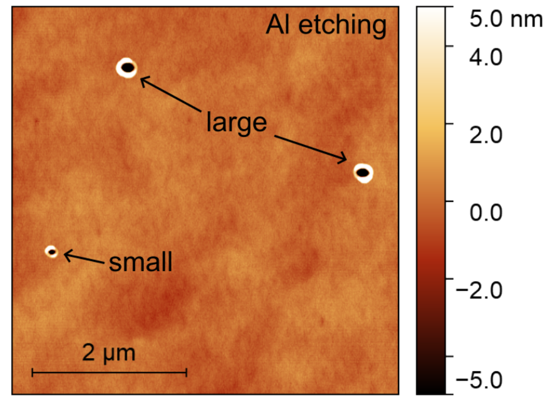

FIGURE 5.29: AFM image of the $t_{\text{etch}} = 30\,\text{s}$ Al deposition sample, showing the bimodal size of the generated nanoholes. Published in [126].

each group, as well as for the combined dataset, revealed consistent overall trends.

For the large nanohole subset, the depth h increased rapidly up to $t_{\text{etch}} = 60\,\text{s}$, followed by a slower increase until $t_{\text{etch}} = 135\,\text{s}$, reaching a plateau at $h = (59.1 \pm 3.4)\,\text{nm}$ that persisted up to $t_{\text{etch}} = 225\,\text{s}$ ($h = (59.5 \pm 5.6)\,\text{nm}$). Beyond this point, the depth gradually decreased with further etching, reaching a plateau by the longest investigated duration of $t_{\text{etch}} = 600\,\text{s}$, which mirrors the general behavior observed for In and InAl droplets.

For the subset of small Al nanoholes, the average depth at the shortest tested etching time of $t_{\text{etch}} = 30\,\text{s}$ was $h = (30.4 \pm 6.0)\,\text{nm}$, indicating a higher initial etching rate than observed for the larger nanoholes. However, as the etching proceeded, the depth increased only moderately, likely limited by the reduced initial droplet volume. The maximum depth was reached between $t_{\text{etch}} = 180$ and $360\,\text{s}$, followed by a decrease at $t_{\text{etch}} = 600\,\text{s}$.

Figures 5.30 a-c) present the average nanohole diameters along the $[011]$ and $[0\bar{1}1]$ crystallographic directions as a function of etching time t_{etch} for InAl, In, and Al droplets, respectively. In all cases, the nanoholes exhibited elongation along the $[011]$ direction, consistent with earlier observations. For InAl droplets, the diameter in both directions decreased steadily with increasing etching time, reaching a minimum at $t_{\text{etch}} = 360\,\text{s}$, followed by a slight increase for still longer etching durations. The In droplet series showed a qualitatively similar dependence: the average diameters decreased to a minimum at $t_{\text{etch}} = 225\,\text{s}$ and then slightly increased for longer etching times.

In contrast, nanoholes formed from Al droplets showed no statistically significant change in diameter across the entire range of investigated etching times ($t_{\text{etch}} = 30\text{–}600\,\text{s}$). Although small fluctuations between samples were observed, no systematic trend was apparent.

To interpret these results, the fundamental framework of LDE in III-V semiconductors is recalled, introduced in Section 3.5, and the process is divided into two distinct phases. In the first phase, the liquid group-III droplet actively dissolves the

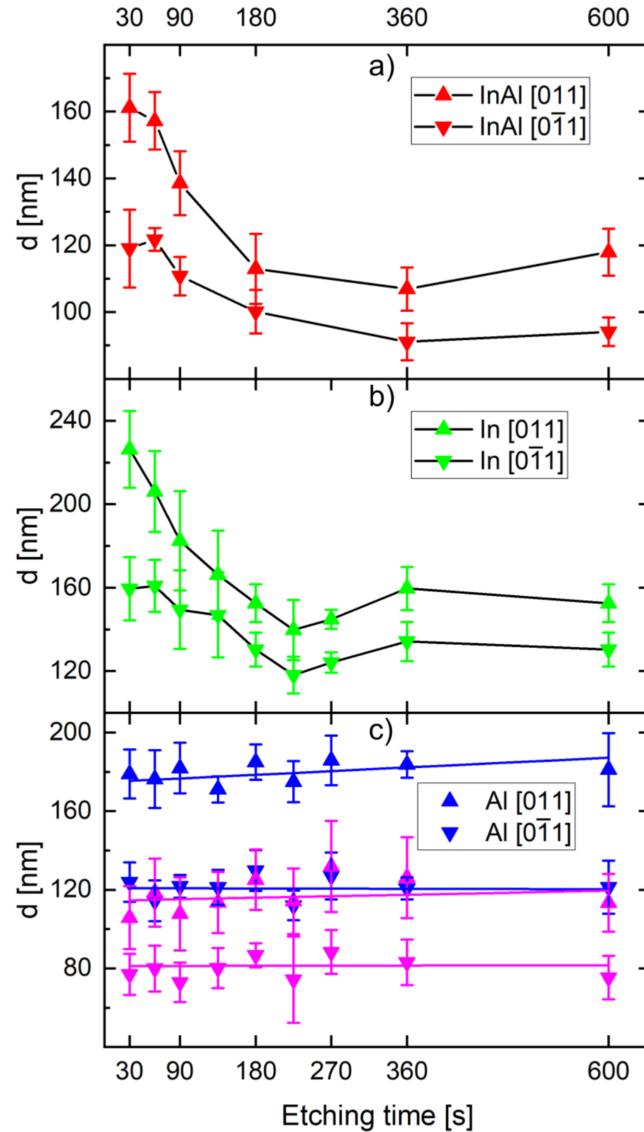

FIGURE 5.30: Average nanohole diameter d for a) InAl, b) In and c) Al deposition during LDE plotted against the etching time t_{etch}. 20 individual nanoholes were measured for each sample. Colored lines in c) represent linear fits. Published in [126].

underlying semiconductor, effectively drilling into the surface. Substrate atoms diffuse into the droplet due to the arsenic concentration gradient between the liquid droplet and the solid layer, causing local liquefaction beneath the droplet. Meanwhile, the outer shell of the droplet partially crystallizes with arsenic already present in the melt, forming the ring-like structure around the nanohole [78].

Simultaneously, group-III atoms from the droplet diffuse outward along the surface, while surface adatoms diffuse inward toward the droplet. The residual arsenic pressure controls this exchange because adsorbed arsenic atoms rapidly immobilize group-III species by promoting surface crystallization [74]. Phase I ends once the droplet is fully consumed, at which point the etching process ceases [81].

After the droplet has been completely removed, the nanohole reaches its maximum depth, and the outward diffusion of material from the hole stops. However, adatoms from the surrounding surface can still diffuse back into the nanohole, gradually refilling it over time [81]. This leads to a reduction in the measured depth for extended etching durations, a behavior consistently observed in all three droplet systems under the present conditions.

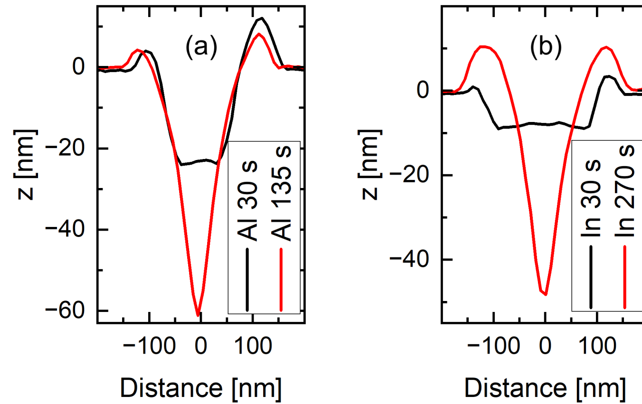

FIGURE 5.31: a,b) Line scans along [011] of selected nanoholes from Al and In etching, respectively. Chosen to represent the statistical average from their respective measurement set. Published in [126].

The early-stage evolution of nanoholes produced by Al droplets on $In_{0.52}Al_{0.48}As$ closely mirrors that reported for Ga droplets on GaAs [122]. As shown in Figure 5.31 a), the holes initially appear shallow with flat bottoms, later deepening and developing a rounded profile. The in-plane diameter remains essentially constant throughout the investigated range of t_{etch} (30–600 s), indicating a strong dependence on the initial droplet size and a negligible degree of lateral material redistribution during etching.

For holes originating from larger Al droplets (as classified earlier by ring diameter), rapid drilling occurs within the first 60 s, after which the process slows and effectively ceases around $t_{etch} = 135$ s. In contrast, smaller droplets produce holes that are already relatively deep at $t_{etch} = 30$ s ($h = (30.4 \pm 6.0)$ nm) and increase only modestly in depth, reaching $h = (41.0 \pm 5.8)$ nm at $t_{etch} = 180$ s. This observation suggests that, for Al droplets, most of the excavation occurs early in the etching process.

Nanoholes produced using In droplets exhibit a noticeably delayed onset of etching activity. Little change in depth is observed during the first 60 s, despite the presence of initially flat-bottomed features, as shown in Figure 5.31 b). Between $t_{etch} = 90$ s and 180 s, however, these cavities rapidly transform into deeper holes with rounded bottoms, indicating a sudden increase in the drilling rate. Beyond this point, the hole depth stabilizes, consistent with the transition into Phase II of the LDE process. Notably, a simultaneous reduction in in-plane diameter in both [011] and $[0\bar{1}1]$ directions was observed, accompanied by changes in the inner wall

morphology. InAl droplets exhibited similar trends in diameter reduction and wall evolution, consistent with their mixed In-Al composition.

The decrease in nanohole diameter observed for In- and InAl-based droplets suggests that, unlike in the Ga-on-GaAs system [74, 122], not all dissolved substrate material diffuses radially outward toward the surface. Instead, part of it appears to redeposit along the inner sidewalls, effectively narrowing the holes. The fact that this behavior occurs only when indium is present implies that it may be linked to differences in surface diffusion kinetics, binding energies, or facet-dependent reconstructions specific to In-containing alloys. These observations further suggest that the chemical composition of the nanohole sidewalls depends strongly on the etchant species employed.

For quantum dot fabrication, this would result in variations of confinement potential even if the overall nanohole geometries were matched between different etching materials. Recent studies have demonstrated that aluminum incorporation into nanohole sidewalls in $Al_yGa_{1-x}As$ systems can produce structural asymmetries that modify the excitonic fine-structure splitting [132]. Accordingly, a detailed analysis of sidewall composition in droplet-etched nanoholes on $In_{0.52}Al_{0.48}As$ layers will be essential both for optimizing QD emission near 1.55 µm and for developing a deeper understanding of the LDE process in $In_xAl_{1-x}As$ materials.

This section is based on material previously published in [126].

5.2.8 Droplet etching with Ga

In addition to In, Al, and InAl droplets, the use of Ga as etching material was also examined. For this purpose, 3.3 ML of Ga were deposited over 4 s onto a 100 nm thick $In_{0.52}Al_{0.48}As$ layer. The arsenic pressure during LDE was set to $p_{As2} = 2 \times 10^{-6}$ mbar, and the etching step lasted 3 min. After etching, the As flux was returned to $p_{As2} = 2 \times 10^{-5}$ mbar, and the substrate temperature was increased to 505 °C before cooling the sample for removal. Two samples were grown with etching temperatures of $T_{etch} = 435$ °C and 505 °C.

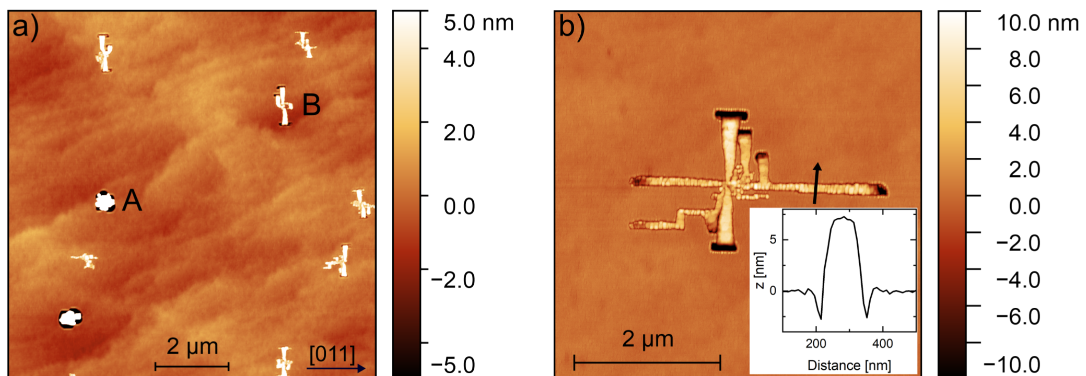

FIGURE 5.32: AFM images of LDE on $In_{0.52}Al_{0.48}As$ with Ga deposition at a) $T_{etch} = 435$ °C and b) 505 °C. The inset in b) shows the height profile along the arrow. Published in [118].

Figure 5.32 a) shows the sample etched at $T_{etch} = 435\,°C$. Two distinct types of structures were observed: droplet-like structures with surrounding trenches (A), and larger elongated structures (B). For the higher etching temperature of 505 °C, shown in Figure 5.32 b), type A structures were no longer present, and the elongated type B structures increased in size. The height profile in the inset highlights shallow trenches on either side of the elevated feature extending across the surface.

These observations suggest that Ga adatoms initially congregate into droplets, but that the droplets are unstable and tend to disintegrate or spread during the LDE process. The distribution of the structures in Figure 5.32 a) resembles surface distributions of the nanohole structures obtained for In, Al, and InAl droplets, but the resulting features differ fundamentally: type A objects lack a ring structure and instead form central protrusions surrounded by etch pits. For type B objects, etch pits surround the elevated features (Figure 5.32 b).

This behavior indicates that the etching mechanism for Ga on $In_{0.52}Al_{0.48}As$ is qualitatively different from that observed for the other droplet materials. Although droplets form initially, their instability leads to etching primarily at the droplet perimeter rather than beneath the droplet center. The instability seems to be temperature dependent, as at lower T_{etch} some structures still resemble droplet-like objects. Maybe, once the droplet size gets too large, its initial form is no longer favorable and it forms type B structures. At higher temperatures all droplets then transition to type B, due to their higher volume. The crystallization of the droplet appears to happen from the center of the droplet, resulting in a central structure and not a ring surrounding a nanohole.

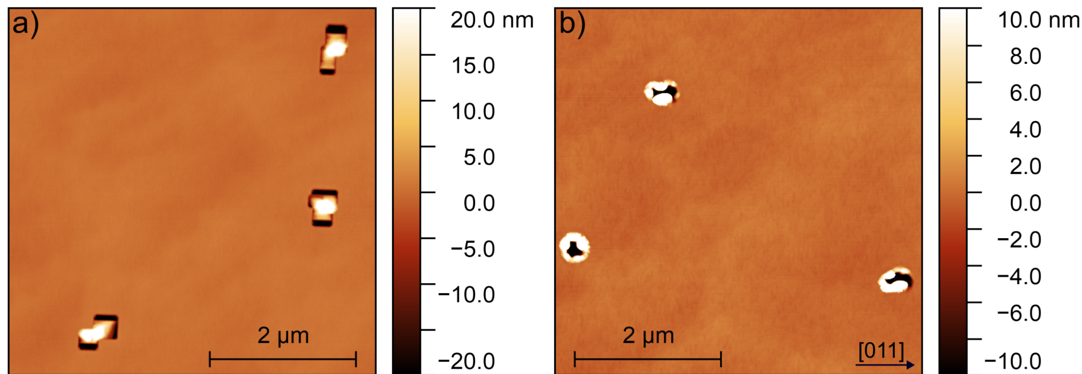

FIGURE 5.33: a) AFM image of LDE with Ga at $\theta_{Ga} = 1.4\,ML$, $p_{As2} = 2 \times 10^{-7}$ mbar, and $T_{etch} = 435\,°C$. b) AFM image of LDE with InGa at $\theta_{InGa} = 4.1\,ML$, $p_{As2} = 2 \times 10^{-6}$ mbar, and $T_{etch} = 435\,°C$. Published in [118].

Figure 5.33 a) shows a second Ga etching experiment, in which both the Ga deposition amount ($\theta_{Ga} = 1.4\,ML$) and the As_2 flux ($p_{As2} = 2 \times 10^{-7}$ mbar) were reduced at $T_{etch} = 435\,°C$. Under these conditions, the type B elongated structures disappeared. However, the etching still did not produce nanoholes of the typical ring-hole morphology. Instead, trenches surrounded a central elevated structure, again suggesting that crystallization initiated near the droplet center rather than the outer shell. The resulting etch pits also appeared rectangular in shape.

To explore whether combining Ga with In would improve the etching behavior, InGa ($In_{0.53}Ga_{0.47}$) droplets were tested, as well. Figure 5.33 b) shows the AFM image obtained after depositing $\theta_{\mathrm{InGa}} = 4.1$ ML InGa at $T_{\mathrm{etch}} = 435\,°\mathrm{C}$ and $p_{\mathrm{As2}} = 2 \times 10^{-6}$ mbar. The resulting structures appear to exhibit properties of typical nanohole etching from the In components and the atypical etching from the Ga components, as nanoholes with ring-like features were obtained, however, with pronounced asymmetry of the structures. The upper and right-hand structures in Figure 5.33 b) are strongly elongated, suggesting possible droplet motion during etching. Furthermore, for these two structures the ring is also not completely surrounding the nanohole, similar to what was observed for pure Ga.

Taken together, the results indicate that Ga does not produce proper nanoholes on $In_{0.52}Al_{0.48}As$ under any conditions. The etching mechanism appears to differ fundamentally from that observed for In or Al droplets: Ga droplets are unstable, etching occurs at the droplet perimeter rather than beneath the droplet center, and the resulting structures lack the well-defined ring-hole morphology.

This section is based on material previously published in [118].

5.3 Local droplet etching on $In_{0.53}Ga_{0.47}As$

Droplet etching was also tested on $In_{0.53}Ga_{0.47}As$ using In, Ga, and Al as etching materials. The parameters were chosen to match those that had proven effective for $In_{0.52}Al_{0.48}As$: $T_{\mathrm{etch}} = 435\,°\mathrm{C}$, $p_{\mathrm{As2}} = 2 \times 10^{-7}$ mbar, $\theta = 1.4$ ML, and an etching time of 3 min. After etching, the samples were cooled down at $30\,°\mathrm{C\,min}^{-1}$ for take-out, without increasing the As flux.

Figure 5.34 a) shows an AFM image of a sample where Ga was deposited onto a 200 nm thick $In_{0.53}Ga_{0.47}As$ layer. Similar to the observations for LDE of Ga on $In_{0.52}Al_{0.48}As$, no proper nanoholes or ring structures were formed. Instead, two types of features developed: island-like structures (A) and highly elongated structures (B). Again it appears that the droplets were not stable, running apart, or moving across the surface during LDE. However, in this system, type B structures were predominantly elongated along $[011]$. Lateral etching was nevertheless evident. Figure 5.34 b) shows a selected structure where the etch pit is clearly visible, exhibiting a quadratic structure with well-defined facets.

Measurement of the local slopes of the visible walls from the AFM topography revealed inclination angles relative to the (100) surface (Figure 5.34 c)) of $(55 \pm 1)°$. This would be consistent with the $\{111\}$ family of planes (54.7°), indicating that the etch pits formed with Ga on $In_{0.53}Ga_{0.47}As$ consist of four $\{111\}$ facets.

Figure 5.35 a) shows the corresponding experiment using Al droplets on a 100 nm thick $In_{0.53}Ga_{0.47}As$ layer. Surprisingly, this also did not produce typical nanoholes. Instead, rectangular etch pits formed, similar to those observed when using Ga. Figure 5.35 b) shows that the walls in the resulting structures were again parallel oriented along the $[011]$ and $[0\bar{1}1]$ directions. Measuring the inclination angles of the

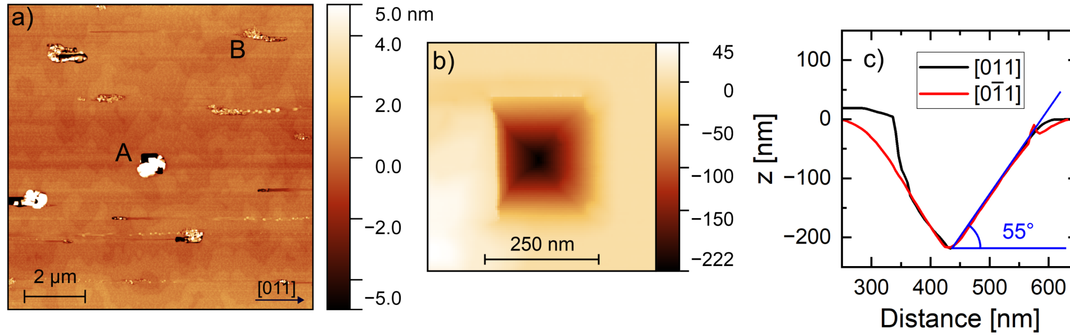

FIGURE 5.34: a) AFM image after LDE by Ga deposition on an $In_{0.53}Ga_{0.47}As$ layer. b) A nanohole from this sample with three free sidewalls, enabling the measurement of their angles relative to the $In_{0.53}Ga_{0.47}As$ surface via their line scans in c).

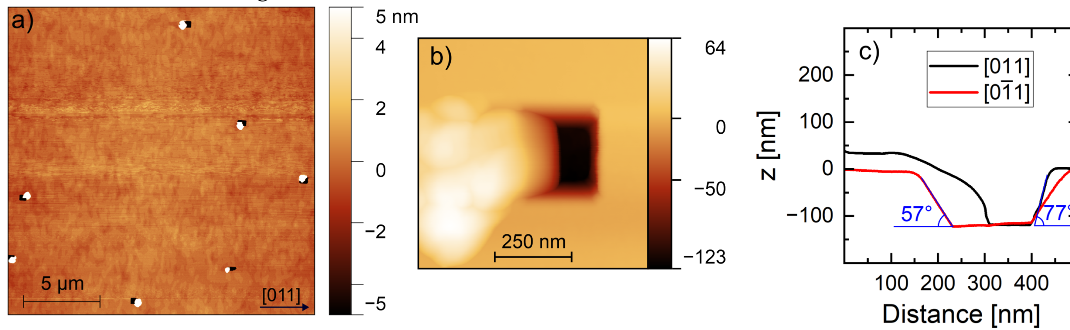

FIGURE 5.35: a) AFM image after LDE by Al deposition on an $In_{0.53}Ga_{0.47}As$ layer. b) A nanohole from this sample with three free sidewalls, enabling the measurement of their angles relative to the $In_{0.53}Ga_{0.47}As$ surface via their line scans in c).

slopes along the $[0\bar{1}1]$ direction yielded values of $(56 \pm 1)^\circ$ and $(57 \pm 1)^\circ$, which could again be attributed to $\{111\}$ facets. However, the facet perpendicular to this direction not covered by crystallized etching material exhibited a slope of 77°, consistent with several possible higher index planes such as (133) (76.7°).

In contrast, Figure 5.36 a) shows that In droplets produced proper nanoholes with surrounding rings on 100 nm of $In_{0.53}Ga_{0.47}As$. These nanoholes were extremely deep: some penetrated through the entire 100 nm $In_{0.53}Ga_{0.47}As$ layer and continued into the InP substrate. Two types of nanoholes were observed: (A) deep nanoholes with rounded bottoms (Figures 5.36 b,c)), and (B) shallower, strongly asymmetric nanoholes with flat bottoms (Figures 5.36 d,e)). Because LDE with In was the only approach that yielded recognizable nanoholes on $In_{0.53}Ga_{0.47}As$, the experiments were extended to lower etching temperatures of $T_{etch} = 400\,°C$ and $350\,°C$.

Figures 5.37 a) and 5.37 b) show the results for $T_{etch} = 400\,°C$ and $350\,°C$, respectively. Proper nanoholes were again formed, and their size decreased with decreasing temperature. The deepest nanohole observed at 400 °C was approximately 70 nm, and at 350 °C approximately 40 nm. All nanoholes were elongated along the $[0\bar{1}1]$ direction, which is noteworthy because nanoholes on $In_{0.52}Al_{0.48}As$ were typically elongated along the perpendicular direction. The inner walls of the nanoholes also appeared to be relatively rough-looking under AFM investigation and the addition of the possibly optically active In ring surrounding the nanoholes, renders In

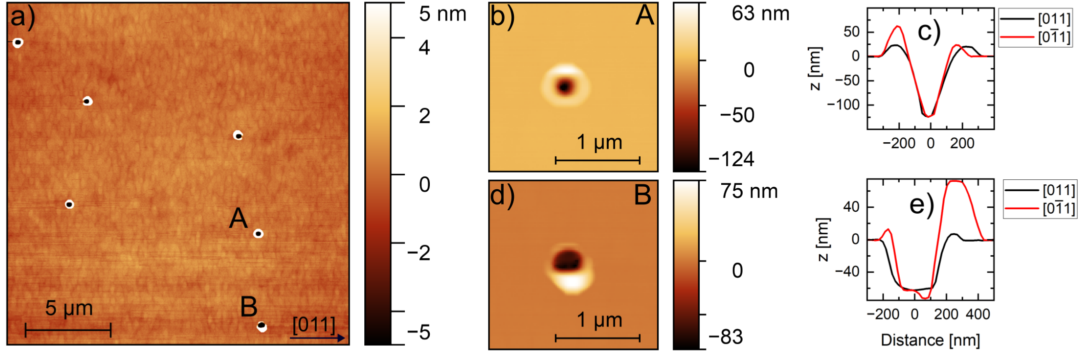

FIGURE 5.36: a) AFM image after LDE by In deposition on an $In_{0.53}Ga_{0.47}As$ layer at $T_{etch} = 435\,°C$. Two types of nanoholes were formed on this sample, depicted in the AFM images and corresponding line scans: b), c) Deep nanoholes with rounded bottoms and d), e) shallower ones exhibiting incomplete looking profiles.

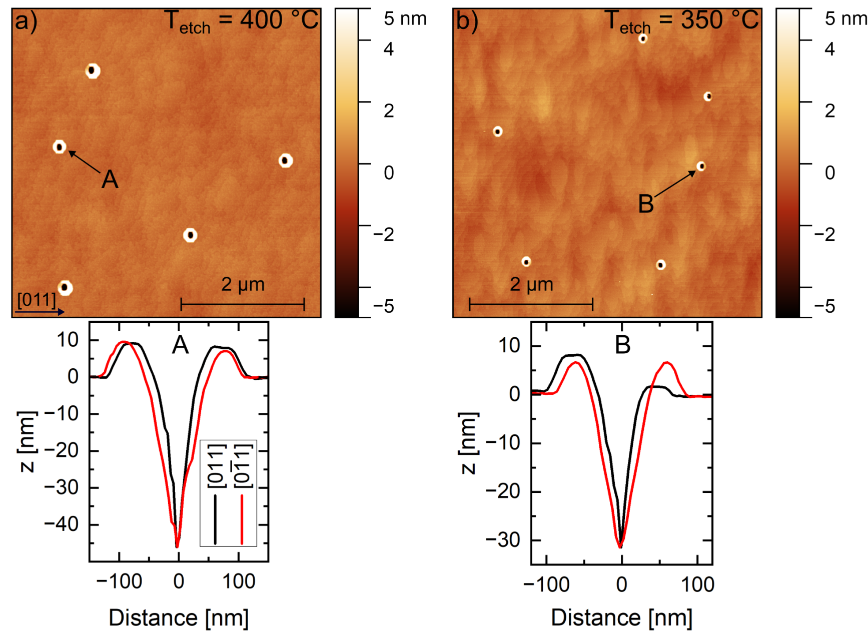

FIGURE 5.37: AFM images and selected line scans for In LDE on $In_{0.53}Ga_{0.47}As$ at a) $T_{etch} = 400\,°C$ and b) $T_{etch} = 350\,°C$.

etched nanoholes on $In_{0.53}Ga_{0.47}As$ unsuitable for QD fabrication.

In summary, these experiments revealed significant challenges when attempting LDE on $In_{0.53}Ga_{0.47}As$ using any of the tested droplet materials (Al, Ga, or In), as well as when using Ga droplets on $In_{0.52}Al_{0.48}As$. The etching process here differs fundamentally from what has been established on the $Al_xGa_{1-x}As$ material platform and the very comparable results that were achieved after the adaptation of LDE to $In_{0.52}Al_{0.48}As$. Direct droplet etching on $In_{0.53}Ga_{0.47}As$ therefore appears unsuitable for generating nanohole templates.

However, successful overgrowth of $In_{0.52}Al_{0.48}As$ has been demonstrated, including the use of digital $In_{0.52}Al_{0.48}As/In_{0.53}Ga_{0.47}As$ alloys. This suggests an alternative strategy: instead of attempting to etch nanoholes directly into $In_{0.53}Ga_{0.47}As$,

one could etch nanoholes into a suitable $In_xAl_{1-x}As$ layer and subsequently overgrow them with the desired barrier material.

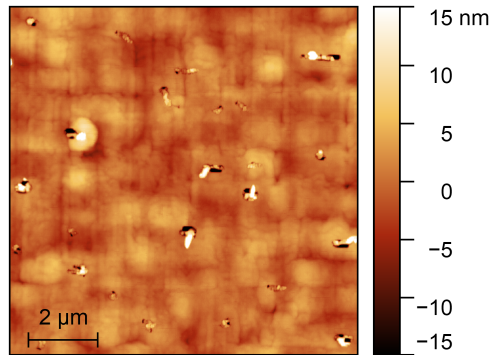

FIGURE 5.38: AFM image after LDE on an $In_{0.30}Ga_{0.70}As$-metamorphic buffer layer (MBL) using $In_{0.30}Al_{0.70}$ deposition. The MBL was grown in Stuttgart by Dr. Michael Jetter and colleagues. LDE was performed in Paderborn by Marvin Böing.

Such an experiment was conducted on metamorphic buffer layers supplied by Dr. Michael Jetter and colleagues from the University of Stuttgart. These samples contain a surface layer of $In_{0.30}Ga_{0.70}As$ and one proposed concept for QD fabrication in this material system is to combine LDE with SK growth: nanoholes would be etched into the $In_{0.30}Ga_{0.70}As$ surface, subsequently infilled with InAs, and finally embedded within an $In_{0.30}Ga_{0.70}As$ matrix. However, experiments performed by Marvin Böing showed that LDE did not produce proper nanoholes in the $In_{0.30}Ga_{0.70}As$ layer, consistent with the observations presented here for $In_{0.53}Ga_{0.47}As$.

Figure 5.38 shows a representative AFM image from one of these experiments. In this case, 100 nm of $In_{0.30}Ga_{0.70}As$ were grown on the metamorphic buffer layer supplied by Stuttgart, which will be discussed more detailed in Chapter 6. Etching was attempted by depositing 1.4 ML of $In_{0.30}Al_{0.70}$ at $T_{etch} = 435\,°C$ and $p_{As2} = 2 \times 10^{-7}$ mbar. After 3 min of etching and conservation with 4 ML of $In_{0.30}Ga_{0.70}As$, the AFM image revealed strongly asymmetric, elongated structures similar to those produced when Ga was used as the etchant on $In_{0.53}Ga_{0.47}As$, rather than proper nanoholes with surrounding rings.

As a workaround, 100 nm of $In_{0.30}Al_{0.70}As$ were deposited instead, and LDE was performed using $In_{0.30}Al_{0.70}$ droplets. Figure 5.39 a) shows that proper nanoholes with surrounding ring structures were successfully obtained under these conditions. In a subsequent step, 20 nm of $In_{0.30}Ga_{0.70}As$ were deposited at 310 °C, and Figure 5.39 b) demonstrates that the nanoholes were preserved during this overgrowth step, enabling further device fabrication. This approach therefore provides a viable means of incorporating alternative barrier materials even when direct nanohole etching is not feasible.

Further details on growth and etching on metamorphic buffer layers will be discussed in Chapter 6. In the next section, the focus will shift to the infilling of

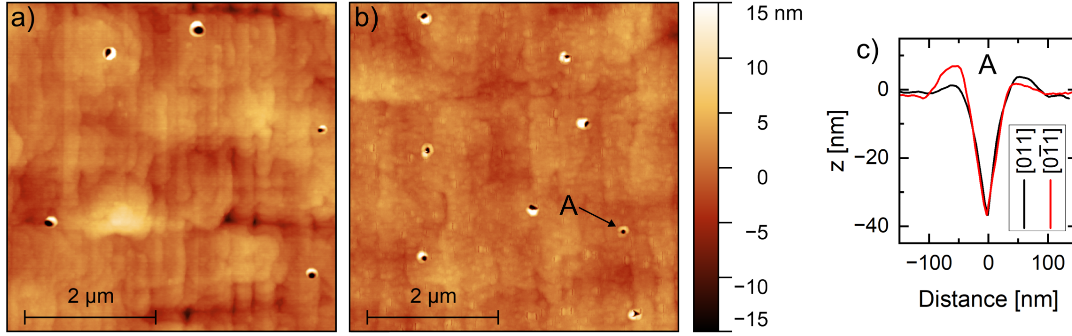

FIGURE 5.39: a) AFM image after LDE with $In_{0.30}Al_{0.70}$ deposition on an $In_{0.30}Al_{0.70}As$ layer grown on an $In_{0.30}Ga_{0.70}As$-metamorphic buffer layer (MBL). b) Same, but with 20 nm of $In_{0.30}Ga_{0.70}As$ overgrowth. c) Line scan of the nanohole indicated in b). The MBLs were grown in Stuttgart and further processed by Marvin Böing in Paderborn.

nanoholes etched into $In_{0.52}Al_{0.48}As$, their subsequent overgrowth for QD formation, and the optical spectroscopy of the resulting structures.

5.4 Infilling of droplet etched nanoholes

After the detailed analysis of nanohole etching, attention is now turned to the subsequent infilling step. For the initial experiments, nanoholes fabricated with $\theta_{\mathrm{InAl}} = 4.1$ ML, $T_{\mathrm{etch}} = 410\,°\mathrm{C}$, $p_{\mathrm{As2}} = 2 \times 10^{-6}$ mbar, and 50 nm of post-etching $In_{0.52}Al_{0.48}As$ overgrowth were selected. Following LDE, the substrate temperature was increased to 505 °C.

The As_2 flux was then reduced from 2.00×10^{-5} mbar to 1.5×10^{-5} mbar, and, after a short stabilization period, $In_{0.53}Ga_{0.47}As$ was deposited using a pulsed deposition mode. Here the shutters of the In and Ga cells were opened for 1 s and subsequently closed for 1 min, pausing the deposition. This was done to increase the adatom diffusion length and to improve diffusion into the nanoholes. The pulsed deposition step was then repeated until the desired amount of $In_{0.53}Ga_{0.47}As$ was deposited. In this first test, 1.0 nm (5× pulses) and 1.4 nm (7× pulses) were deposited. After deposition, the sample was cooled to 250 °C for take-out.

Figure 5.40 shows multiple line scans of the infilled nanoholes along both high-symmetry directions. Although infilling was observed, the difference between 1.0 nm and 1.4 nm deposition was marginal and difficult to quantify. This motivated the testing of an alternative approach using an As_4 environment.

For this second experiment, the sample was cooled after the LDE step and, once at 250 °C, the VACS cracker temperature was lowered from 900 °C to 450 °C, generating a predominantly As_4 flux. The As_4 pressure was adjusted to $p_{\mathrm{As4}} = 1.5 \times 10^{-5}$ mbar and the substrate temperature was again increased to 505 °C, and pulsed deposition of $In_{0.53}Ga_{0.47}As$ was performed as before. Afterwards, the sample was subsequently cooled and removed from the chamber.

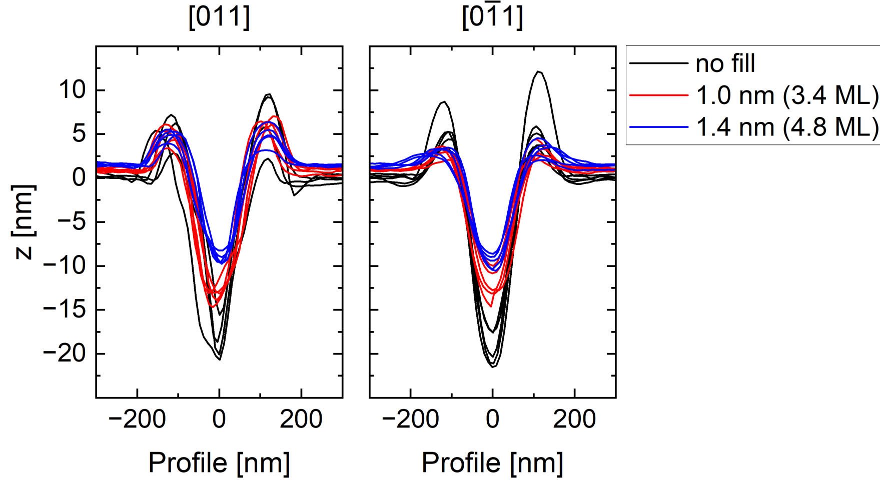

FIGURE 5.40: Overlayed line profiles of multiple nanoholes (5 per sample) with different amounts of $In_{0.53}Ga_{0.47}As$ deposition for infilling under As_2 environment. Nanoholes were etched with $\theta_{InAl} = 4.1$ ML, $T_{etch} = 410\,°C$, $p_{As2} = 2 \times 10^{-6}$ mbar and 50 nm post etching overgrowth with $In_{0.52}Al_{0.48}As$.

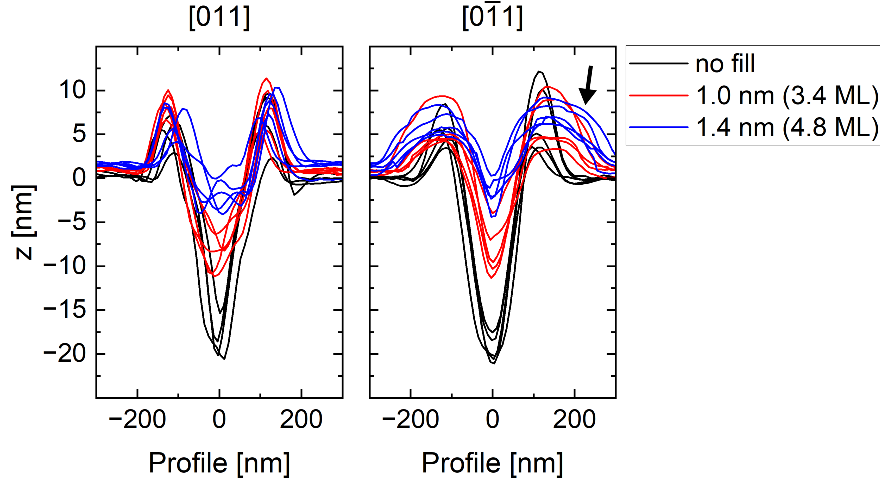

FIGURE 5.41: Overlayed line profiles of multiple nanoholes (5 per sample) with different amounts of $In_{0.53}Ga_{0.47}As$ deposition for infilling under As_4 environment.

Figure 5.41 demonstrates that nanohole infilling under an As_4 environment was significantly more effective. Here a deposition of only 1.4 nm of $In_{0.53}Ga_{0.47}As$ was sufficient to nearly infill the nanoholes entirely. This improvement is attributed to the reduced adatom mobility under As_2, which is more reactive than As_4 and limits the group-III adatom diffusion length. In contrast, As_4 requires cracking at the substrate surface before incorporation, thereby enhancing the diffusion length of In and Ga adatoms. Along the $[0\bar{1}1]$ direction, an accumulation of material at the outer ring edge was observed (indicated by an arrow in Figure 5.41), while this effect was not seen along the $[011]$ direction.

The same infilling procedure under As_4 was then applied to nanoholes fabricated with the improved etching parameters: $T_{etch} = 435\,°C$, $p_{As2} = 2 \times 10^{-7}$ mbar, $\theta_{InAl} = 1.4$ ML, and 4 ML of post-etching overgrowth. The substrate and cracker

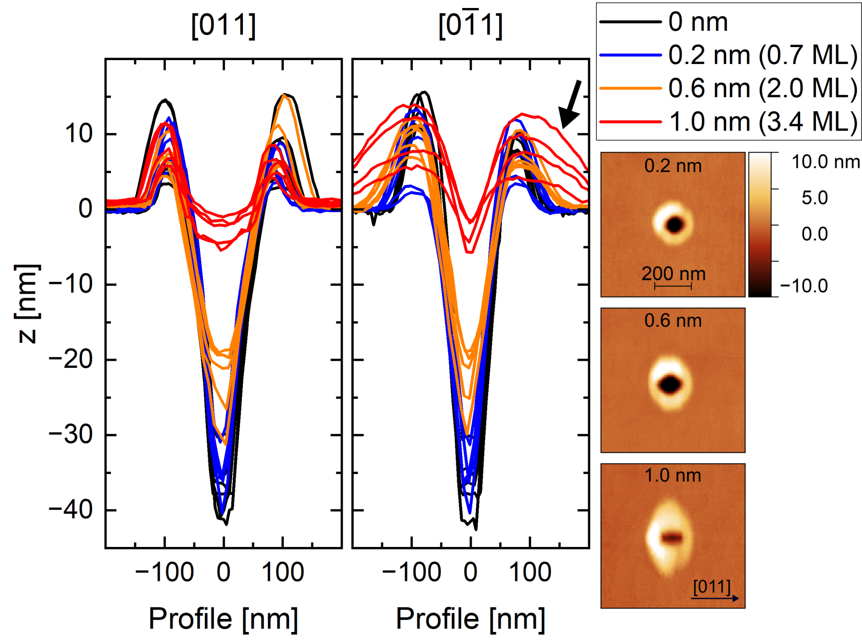

FIGURE 5.42: Overlayed line profiles of multiple nanoholes (5 per sample) with different amounts of $In_{0.53}Ga_{0.47}As$ deposition for infilling under As_4 environment. Nanoholes were etched with $\theta_{InAl} = 1.4\,ML$, $T_{etch} = 435\,°C$ and $p_{As2} = 2 \times 10^{-7}$ mbar.

temperature ramps were identical, and pulsed $In_{0.53}Ga_{0.47}As$ deposition was performed under $p_{As4} = 1.5 \times 10^{-5}$ mbar at 505 °C.

Figure 5.42 shows that the narrower, optimized nanoholes required significantly less material to reach similar infilling levels. Deposition of 0.2 nm (1× pulses), 0.6 nm (3× pulses), and 1.0 nm (5× pulses) was tested. As expected from their reduced volume, these nanoholes infilled more easily, yet the overall infilling behavior remained comparable to that observed previously and material accumulation was again observed at the ring edge along $[0\bar{1}1]$.

Infilling reduced the diameter at the infill level along the $[0\bar{1}1]$ direction, while the diameter along [011] remained unchanged, resulting in a V-shaped profile of the hole along $[0\bar{1}1]$. A similar behavior has been reported for nanoholes in $Al_{0.45}Ga_{0.55}As$ infilled with GaAs, where it was attributed to the preferential incorporation of group-III adatoms at B-type (As-terminated) step edges, which are oriented perpendicular to the $[0\bar{1}1]$ direction [133]. Likewise, this mechanism may also account for the preferential material accumulation at the outside of the ring along $[0\bar{1}1]$.

Finally, nanoholes etched with the optimized parameters were also infilled with InAs. For this, InAs was deposited in pulsed mode in amounts of 2.0 ML, 2.3 ML, 2.5 ML, 2.7 ML, 3.0 ML, and 3.5 ML.

Figure 5.43 a-d) show AFM images of selected nanostructures after deposition of 2.0 ML, 2.3 ML, 2.5 ML, and 3.0 ML of InAs, respectively. The onset of island-like formations was visible at 2.3 ML, which could indicate SK-like growth occurring within the nanoholes. Increasing the InAs deposition increased the infilling level, but the islands became highly asymmetric.

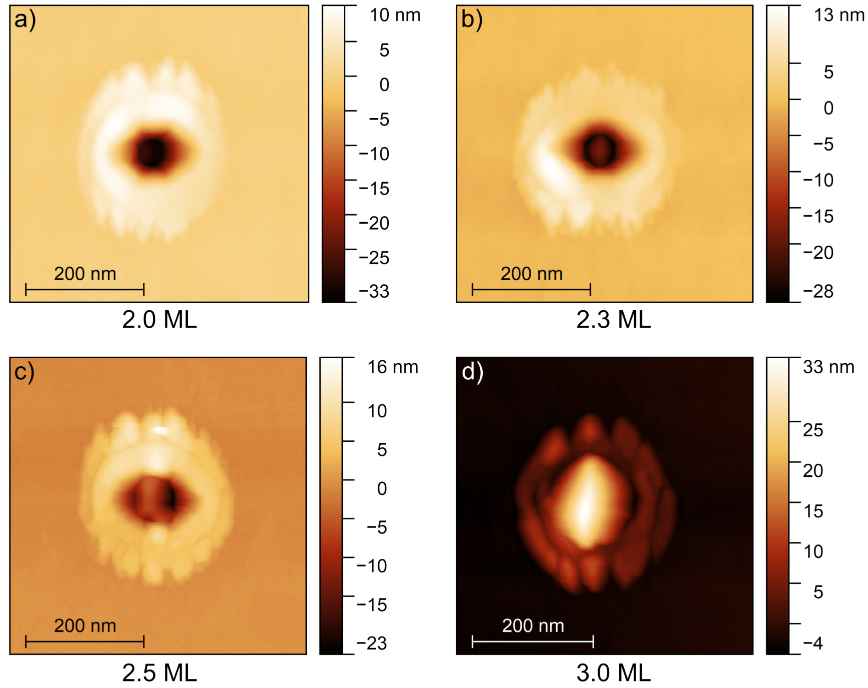

FIGURE 5.43: AFM images of nanoholes infilled by depositing InAs, whereas the deposition amounts are indicated under each image. Nanoholes were etched with $\theta_{\text{InAl}} = 1.4\,\text{ML}$, $T_{\text{etch}} = 435\,^\circ\text{C}$ and $p_{\text{As2}} = 2 \times 10^{-7}\,\text{mbar}$.

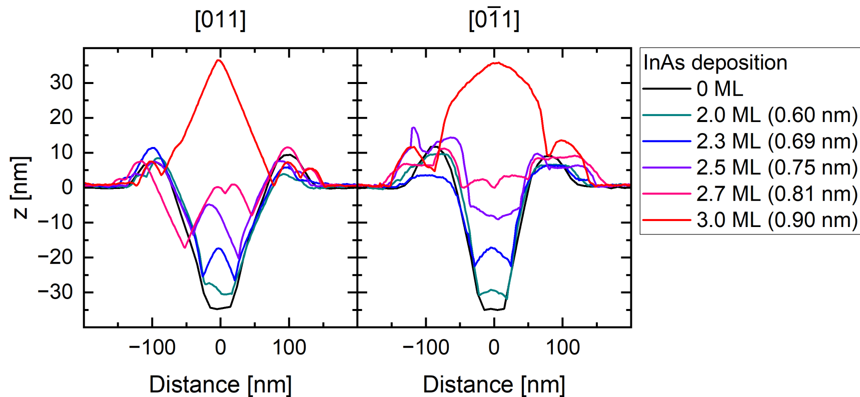

FIGURE 5.44: Selected line profiles for the InAs-infilled nanoholes shown in Figure 5.43, measured along the [011] and [0$\bar{1}$1] directions.

Figure 5.44 shows corresponding line scans. Again, the formation of islands at 2.3 ML is visible. The islands exhibited strong elongation along [0$\bar{1}$1], likely caused by strain anisotropy, a well-known effect in the $\text{In}_x\text{Al}_y\text{Ga}_{1-x-y}\text{As}$ [134] and InP [135] systems. On $\text{In}_x\text{Al}_y\text{Ga}_{1-x-y}\text{As}$ surfaces, unoptimized InAs deposition often leads to quantum wire like structures elongated along [0$\bar{1}$1] [134], consistent with the observations here, especially for the 3.0 ML deposition. No SK type dots were detected on the planar surface, even for 3.5 ML. The overfilling behavior in the nanoholes resembles the refilling process when exposing In etched nanoholes to increased As_2 BEPs, as discussed in Section 5.2.1.

Although no further InAs-infilling experiments were conducted, this short series

suggests that nanohole-confined growth of InAs QDs in $In_xAl_{1-x}As$ may be feasible in principle. Confinement inside an etched nanohole could provide improved symmetry compared to conventional SK growth. However, a comprehensive optimization effort would be required, which was beyond the scope of this work.

5.5 Quantum dot fabrication and spectroscopy

For QD fabrication, the infilled nanoholes were overgrown with an $In_{0.52}Al_{0.48}As$ layer. Because Al is highly reactive under atmospheric conditions, a final $In_{0.53}Ga_{0.47}As$ layer was added to protect the structure from oxidation. This additional cap layer proved problematic, as a sufficiently thick $In_{0.53}Ga_{0.47}As$ layer can emit photoluminescence (PL) close to 1500 nm.

For the first QD fabrication series, nanoholes were etched using $T_{\mathrm{etch}} = 410\,°\mathrm{C}$, $\theta_{\mathrm{InAl}} = 4.1\,\mathrm{ML}$, $p_{\mathrm{As2}} = 2 \times 10^{-6}\,\mathrm{mbar}$, an etching time of 3 min, and 50 nm of post-etching $In_{0.52}Al_{0.48}As$ overgrowth. The nanoholes were then infilled in pulsed deposition mode with 1.0 nm, 1.4 nm, and 1.8 nm of $In_{0.53}Ga_{0.47}As$ at 505 °C under an As_4 flux of $p_{\mathrm{As4}} = 1.5 \times 10^{-5}\,\mathrm{mbar}$.

After infilling, the substrate temperature was lowered, and the cracker temperature was increased from 450 °C to 900 °C to return to As_2 growth conditions ($p_{\mathrm{As2}} = 2.00 \times 10^{-5}\,\mathrm{mbar}$). Subsequently, 100 nm of $In_{0.52}Al_{0.48}As$ and either 10 nm (for the 1.0 nm and 1.4 nm fillings) or 5 nm (for the 1.8 nm infilling) of $In_{0.53}Ga_{0.47}As$ were deposited. The motivation for this reduced cap thickness will become evident from the PL results.

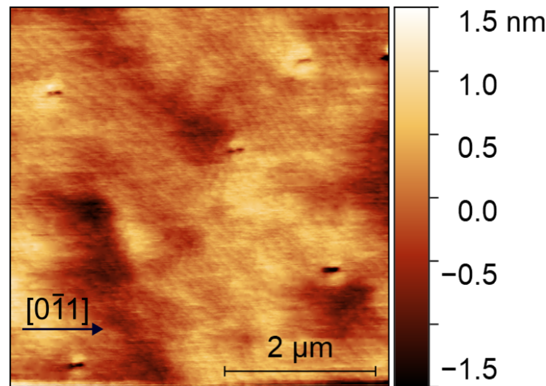

FIGURE 5.45: AFM image of a QD sample.

Figure 5.45 presents an AFM image of a representative sample after overgrowth of the infilled nanoholes. The surface appears smooth, with a RMS roughness of $\sigma_{\mathrm{RMS}} = 0.39\,\mathrm{nm}$ in the scanned area. Following overgrowth, the positions of the nanohole structures remain discernible as shallow depressions on the surface elongated along the $[0\bar{1}1]$ direction.

Figure 5.46 a) shows the PL spectra measured between 700 and 1600 nm, and the inset (Figure 5.46 b)) displays a magnification for the longer-wavelength region between 1200 to 1600 nm. The spectra are color-coded according to the $In_{0.53}Ga_{0.47}As$

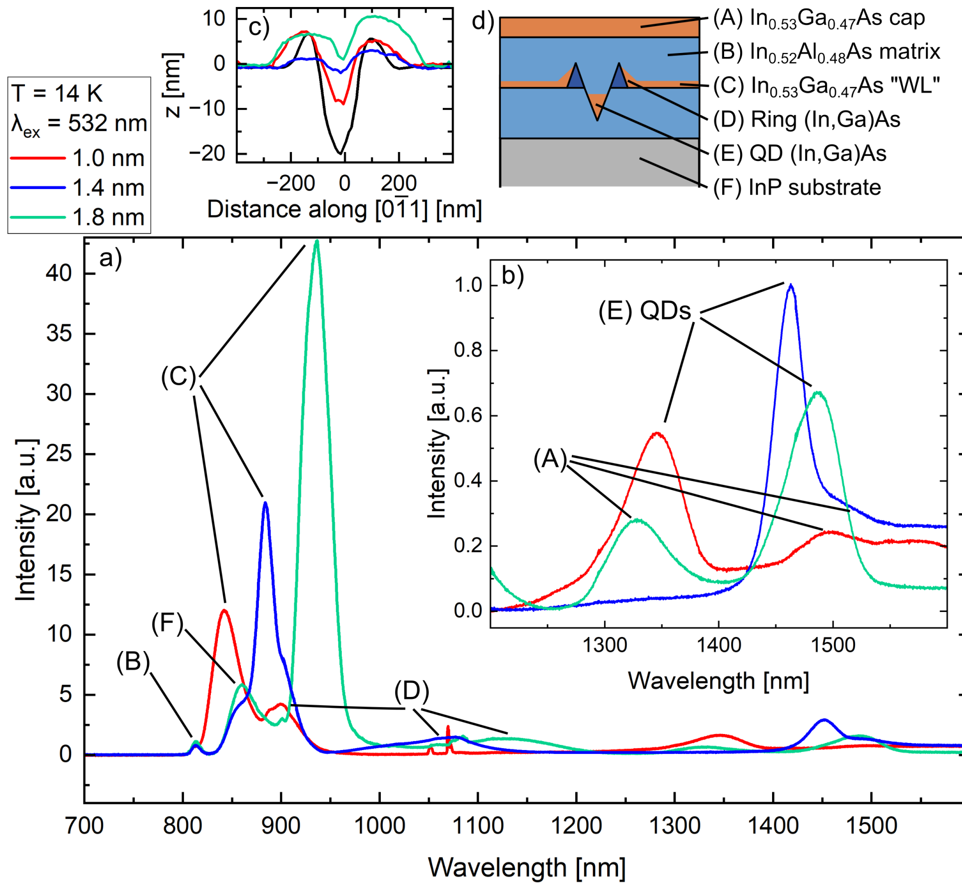

FIGURE 5.46: a,b) PL spectra of QDs fabricated from infilling by depositing different amounts of $In_{0.53}Ga_{0.47}As$ and overgrowing. The nanoholes were generated by droplet etching into $In_{0.52}Al_{0.48}As$ with $\theta_{InAl} = 4.1$ ML, $T_{etch} = 410\,°C$, $p_{As2} = 2 \times 10^{-6}$ mbar and 50 nm post etching overgrowth with $In_{0.52}Al_{0.48}As$. For the samples with 1.0 nm (red) and 1.4 nm (blue) of $In_{0.53}Ga_{0.47}As$ infilling the final $In_{0.53}Ga_{0.47}As$ on top for protection against oxidation was 10 nm thick, while this layer was only 5 nm thick for the 1.8 nm (green) sample. c) Shows the corresponding line profiles for samples with equivalent $In_{0.53}Ga_{0.47}As$ deposition amounts for infilling, but without overgrowth. d) Shows a sketch of the layer structure of the QD samples. a) and b) were published in [119].

infilling thickness, matching the uncapped line scans in Figure 5.46 c). As discussed in Section 4.4, PL measurements can provide an insight into the electronic structure of semiconductor heterostructures; however, this also complicates the analysis of novel heterostructure devices, since multiple layers can contribute to the overall emission spectrum. Figure 5.46 d) illustrates the different layers and structures in this sample and labels the corresponding possible PL sources (A-F).

The potential emission lines are associated with:

(A) the $In_{0.53}Ga_{0.47}As$ surface cap layer;
(B) the $In_{0.52}Al_{0.48}As$ bulk;
(C) the quasi-wetting layer formed during nanohole infilling;
(D) $In_xGa_{1-x}As$ material accumulated at the ring edges during infilling;
(E) the QDs formed inside the nanoholes;

(F) the InP substrate.

The band gap-energies at 14 K of the semiconductors in this structure and the corresponding band-to-band emission wavelengths were [69]:

- InP 1.421 eV, $\lambda = 873$ nm.
- $In_{0.52}Al_{0.48}As$ 1.529 eV, $\lambda = 811$ nm.
- $In_{0.53}Ga_{0.47}As$ 0.816 eV, $\lambda = 1520$ nm.

A small peak near 813 nm was observed in all spectra. This peak was visible in every PL spectra for LDE QD samples and as such it is straightforward to attribute this signal to band-to-band emission of the $In_{0.52}Al_{0.48}As$ layers (B).

For the green curve (1.8 nm) a peak at 861 nm was observed. The blue curve (1.4 nm), also shows a shoulder in the spectrum at the same wavelength. As this peak was also observed on many other LDE QD samples, it is attributed to band-to-band emission of the InP substrate (F). However, the wavelengths for this peak were always around 861 nm and as such slightly off from the estimated value based on literature data.

The intensive peaks between 800 and 1000 nm shift systematically with increasing $In_{0.53}Ga_{0.47}As$ deposition and are attributed to the quasi-wetting layers (C) (quantum wells) which were formed on the $In_{0.52}Al_{0.48}As$ layer during the nanohole infilling process. Their thicknesses should be as large as the $In_{0.53}Ga_{0.47}As$ deposition amount and as such their size much smaller than the QDs in the nanoholes or the material accumulated at the side of the rings, resulting in photon emission at higher energies.

The peaks in the 900–1200 nm spectral range also shift with increasing $In_{0.53}Ga_{0.47}As$ deposition during infilling. However, they appear significantly broader than the peaks attributed to the quasi-wetting layer. This observation suggests that the emission originates from the $In_xGa_{1-x}As$ accumulations at the ring edges (D). Their broad linewidths reflect the wide size distribution of these structures.

The remaining peaks – which lie in the 1200–1600 nm window – include contributions from both the cap layer (A) and the QDs (E). The $In_{0.53}Ga_{0.47}As$ cap layer forms a surface quantum well [136], confined on one side by the $In_{0.52}Al_{0.48}As$ layer and on the other side by surface oxide. $In_{0.53}Ga_{0.47}As$ surface quantum wells grown on InP have been shown to emit at wavelengths below that of bulk $In_{0.53}Ga_{0.47}As$, even when measured at room temperature. Luminescence of these surface quantum wells increases under liquid helium cooling, due to the freeze out of non-radiative surface recombination processes [137].

For the red sample (with 10 nm $In_{0.53}Ga_{0.47}As$ cap) a peak near 1495 nm was present. Similar, a shoulder can be seen in the blue sample (10 nm $In_{0.53}Ga_{0.47}As$ cap as well) at the same wavelength. This weaker peak shifts to 1325 nm for the green sample, where a cap layer of only 5 nm was present. Further tests confirmed, that this peak around 1325 nm is always present for 5 nm thick $In_{0.53}Ga_{0.47}As$ cap

layers, and as such these weaker peaks are attributed to emission from the cap layer (A) itself.

The remaining stronger peaks red-shift again with increasing $In_{0.53}Ga_{0.47}As$ deposition amount for infilling and are attributed to the QDs (E):

- 1.0 nm: $\lambda = 1346$ nm (0.921 eV, FWHM 0.037 eV).
- 1.4 nm: $\lambda = 1464$ nm, (0.847 eV, FWHM 0.024 eV).
- 1.8 nm: $\lambda = 1486$ nm (0.834 eV, FWHM 0.032 eV).

Overall, these peaks indicate that nanoholes with a lateral etching depth of only 20 nm are insufficient to shift the emission into the optical C-band. Additionally, the QD PL intensity was generally weak, likely due to their low density.

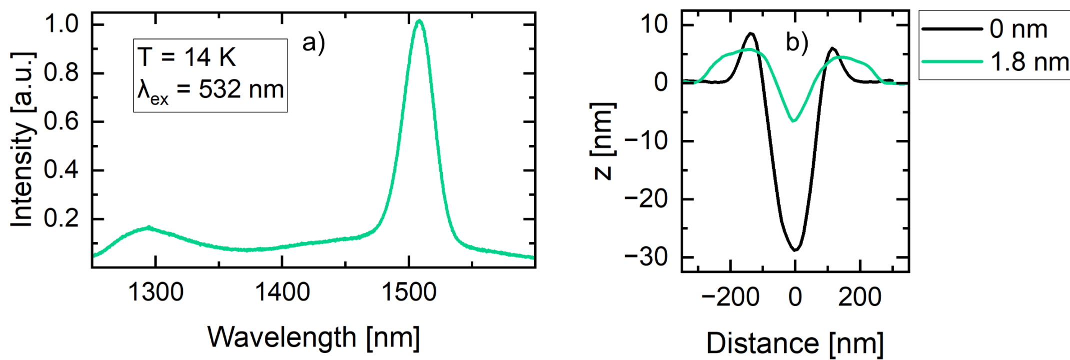

FIGURE 5.47: a) PL spectrum for nanoholes etched with with $\theta_{InAl} = 4.1$ ML, $T_{etch} = 410\,°C$, $p_{As2} = 2 \times 10^{-6}$ mbar and 50 nm post etching overgrowth with $In_{0.52}Al_{0.48}As$ and then infilled by depositing 1.8 nm of $In_{0.53}Ga_{0.47}As$ and subsequent overgrowth with 100 nm $In_{0.52}Al_{0.48}As$ and 5 nm $In_{0.53}Ga_{0.47}As$. b) Selected line profile for an equivalent uncapped sample.

Figure 5.47 a) shows the PL spectrum measured at 14 K for a sample were the nanoholes were generated with the same parameters as above, but the etching temperature was increased to $T_{etch} = 435\,°C$. The nanoholes were infilled by depositing 1.8 nm of $In_{0.53}Ga_{0.47}As$ and Figure 5.47 b) shows an exemplary line scan along the $[0\bar{1}1]$- direction for an empty and an infilled nanohole grown with these parameters. Based on the increased infilling height (approximately 25 nm compared to 20 nm previously), a further red-shift was anticipated.

The QD emission peak at $\lambda = 1508$ nm (0.822 eV, FWHM 0.016 eV) confirmed this expectation. The peak at 1295 nm corresponds to the 5 nm cap of $In_{0.53}Ga_{0.47}As$.

The μPL spectra in Figure 5.48 a,b) (measured by Christopher Buchholz from Prof. Dr. Klaus Jöns group at Paderborn University) show sharp emission lines typical of single QDs, and their wavelengths fall within the ensemble emission peaks. However, their intensities were several orders of magnitude too weak for further advanced characterizations.

Increasing the infilling amount to 2.4 nm and 3.0 nm was tested as well, but resulted in only minor peak shifts to 1512 nm and 1513 nm, respectively. Given the band gap energy of $In_{0.53}Ga_{0.47}As$ (0.816 eV, $\lambda = 1520$ nm [69]), it seems likely that

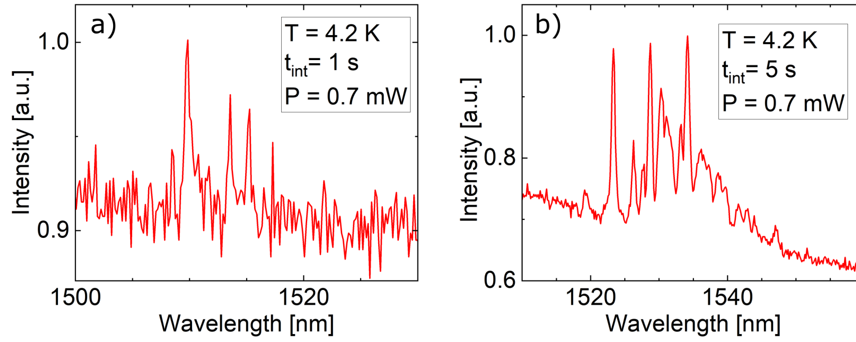

FIGURE 5.48: a) μPL spectrum from the sample in Figure 5.47. b) μPL spectrum from a QD sample with similar parameters as a) but $T_{\text{etch}} = 460\,°\text{C}$ and $In_{0.53}Ga_{0.47}As$ deposition of 2.8 nm for infilling. Both measurements performed by Christopher Buchholz.

lattice-matched $In_{0.53}Ga_{0.47}As$ infilling alone might not shift the emission well into the C-band, even with larger QDs.

To further shift the QD emission, the composition of the infilling material was varied. Nanoholes were etched with the optimized parameters ($T_{\text{etch}} = 435\,°\text{C}$, $p_{\text{As2}} = 2 \times 10^{-7}$ mbar, $\theta_{\text{InAl}} = 1.4$ ML, 4 ML overgrowth) and then infilled with 1.0 nm of $In_xGa_{1-x}As$ of varying composition.

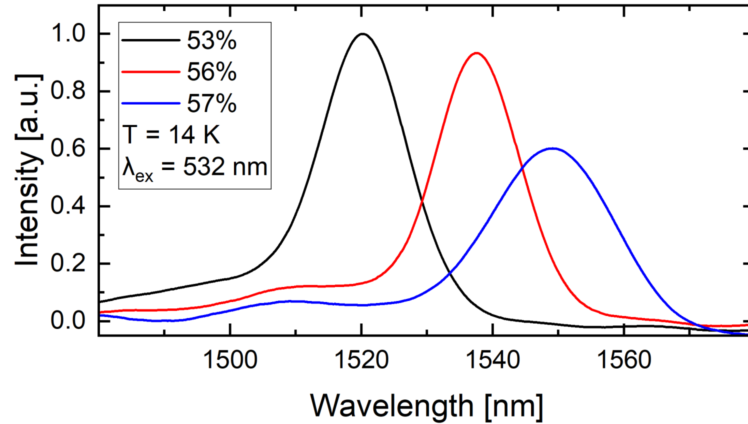

FIGURE 5.49: PL spectra for QD samples with 1.0 nm of $In_xGa_{1-x}As$ deposition for infilling, with different compositions x. The nanohole bases were etched into $In_{0.52}Al_{0.48}As$ layer with $T_{\text{etch}} = 435\,°\text{C}$, $p_{\text{As2}} = 2 \times 10^{-7}$ mbar, $\theta_{\text{InAl}} = 1.4$ ML and 4 ML of post-etching overgrowth. Published in [118].

Figure 5.49 shows the resulting PL spectra, corresponding to QDs with an approximate height of 30 nm (see Figure 5.42). By increasing the In content in the deposited $In_xGa_{1-x}As$ during infilling, a further red-shift of the QD emission was achieved, tuning the QD emission well into the telecom C-band:

- 53 %: $\lambda = 1520$ nm (0.816 eV, FWHM 0.009 eV).
- 56 %: $\lambda = 1538$ nm, (0.806 eV, FWHM 0.008 eV).
- 57 %: $\lambda = 1549$ nm (0.800 eV, FWHM 0.011 eV).

This section is based on material previously published in [118, 119].

Chapter 6

Local droplet etching on metamorphic buffer layers

One serious drawback of the InP/$In_xAl_{1-x}As$/$In_yGa_{1-y}As$ system is the limited availability of efficient distributed Bragg reflectors (DBRs). While DBRs can be grown on this platform, their fabrication is not straightforward: the low refractive-index contrast of materials lattice-matched to InP complicates both design and growth. For QD emission in the telecom C-band, InP/InAlGaAs DBRs can be used; however, this approach requires access to a phosphorus source, precise control over the quaternary InAlGaAs composition, and a larger number of DBR mirror pairs than in the simpler AlAs/GaAs system [138].

For these reasons, it is advantageous to shift the material platform from InP to GaAs. Using GaAs as a substrate still allows the incorporation of InAlAs or InGaAs layers through the use of metamorphic buffer layers (MBLs). The key idea is to gradually adjust the crystal lattice of the growing layer by incrementally increasing the indium concentration. This gradual change releases strain and generates dislocations within the MBL, which generally propagate laterally in these layers, rather than vertically towards the upper layers. In this way, the MBL acts as a virtual substrate and prevents strain-related dislocations from propagating into the active layers [139].

The metamorphic buffer structures examined in this work were provided by the collaborators Dr. Michael Jetter and colleagues from the University of Stuttgart. Detailed descriptions of these MBL designs can be found in [97]. The samples were grown via metalorganic vapor-phase epitaxy (MOVPE) on Si-doped 3-inch GaAs (100) wafers. Prior to the MBL, a 250 nm $Al_{0.92}Ga_{0.08}As$ layer was included as a potential etch-stop or sacrificial layer for subsequent processing. After an additional 50 nm GaAs layer, the metamorphic buffer was grown, consisting of a 30 nm $In_{0.26}Ga_{0.74}As$ abrupt change (jump) layer, a 130 nm $In_xGa_{1-x}As$ layer following a convex In grading from 26 % to 40 % In concentration, and lastly a 60 nm $In_{0.30}Ga_{0.70}As$ inverse layer for strain release.

6.1 Characterization of MBLs

Before introduction into the MBE system and further processing, the 3-inch wafers were cleaved into quarters and characterized by HRXRD and AFM measurements.

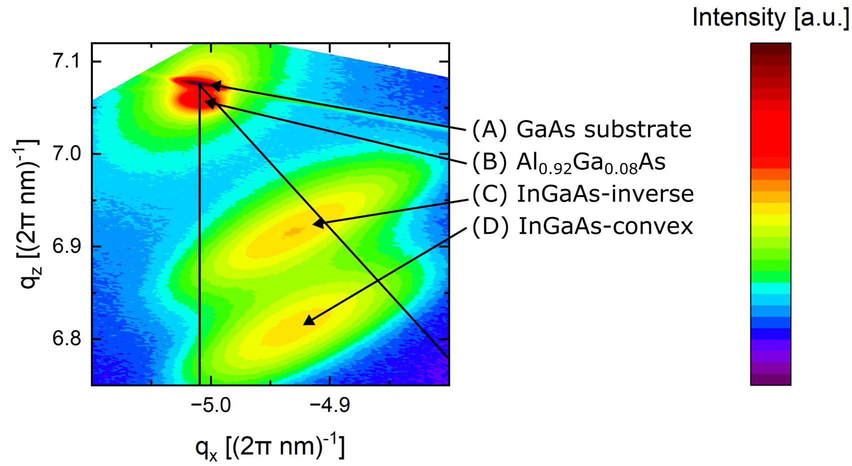

FIGURE 6.1: HRXRD RSM around the $(4\bar{2}\bar{2})$ Bragg peaks of an MBL sample received from Dr. Michael Jetter and colleagues (University of Stuttgart).

Figure 6.1 shows an exemplary HRXRD reciprocal space map (RSM) recorded around the asymmetric $(4\bar{2}\bar{2})$ GaAs reflection. The vertical and diagonal black lines indicate the pseudomorphic and relaxation lines, respectively, as described in Section 4.3.1. The most intense peak (A) originates from the GaAs substrate, while the peak directly below it (B) corresponds to the $Al_{0.92}Ga_{0.08}As$ layer. The remaining two peaks arise from the metamorphic buffer: peak (D) corresponds to the InGaAs-convex layer, and peak (C) originates from the topmost InGaAs-inverse layer.

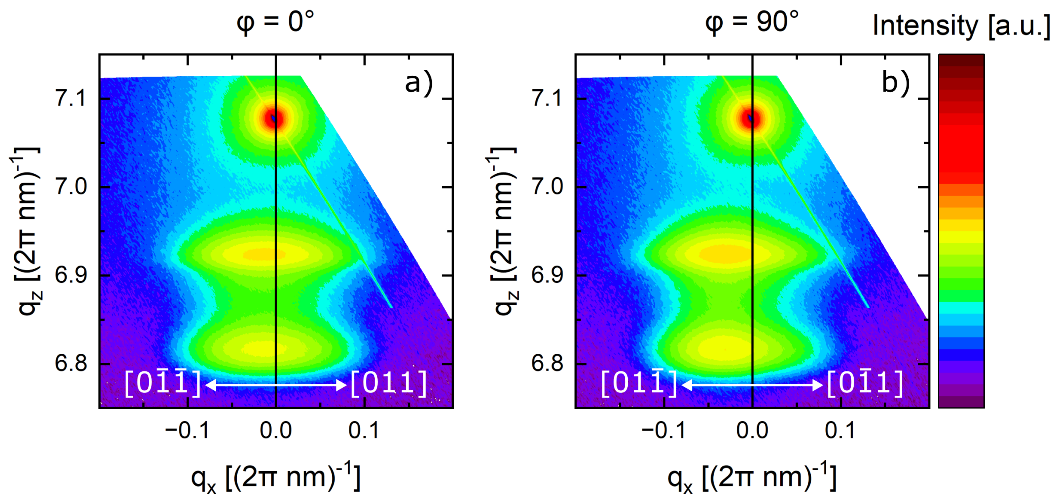

FIGURE 6.2: HRXRD RSM around the (400) Bragg peaks of an MBL sample measured for two perpindicular azimutal directions a) $\varphi = 0°$ and b) a) $\varphi = 90°$

To assess the structure of the MBLs in more detail, symmetric RSMs around the GaAs (400) reflection were also recorded. As shown in Figure 6.2, the MBL layers exhibit a distinct lattice tilt with respect to the GaAs substrate. Such a tilt is commonly

observed for strain-relaxed layers grown on lattice-mismatched substrates.

During growth of metamorphic buffers, strain relaxation predominantly occurs through the formation of 60° misfit dislocations on $\{111\}$ planes, with Burgers vectors of the form $a/2\langle 110\rangle$. Assuming a GaAs (100) substrate, each Burgers vector can be decomposed into in-plane $\langle 011\rangle$ edge and screw components – which provide strain relaxation and can cause twists about the interface, respectively – and an out-of-plane tilt component (along [100]), which creates a step on the layer surface [140, 141].

The sign of the tilt component can vary between [100] and $[\bar{1}00]$ and as such a sufficiently random distribution of the 60° misfit dislocations can cancel the tilt components out, resulting in no tilt of the layer. However, when the distribution is biased, the surface orientation of the layer can tilt away from the (100) orientation of the substrate. Generally, MBLs frequently exhibit spatially varying tilt across the wafer [141, 142]. Therefore, HRXRD analysis of these structures requires both symmetric and asymmetric RSMs recorded at the same sample position.

In Figure 6.2 a), the measurement was performed at $\varphi = 0°$, where the [011] direction points towards positive q_x (HRXRD detector side). In Figure 6.2 b), the azimuth was rotated to $\varphi = 90°$, such that $[0\bar{1}1]$ points toward positive q_x. In both orientations, the two MBL peaks are shifted along the q_x axis relative to the substrate peak, confirming the presence of a lattice tilt.

In symmetric scans, any deviation of the layer peak along q_x relative to the substrate arises exclusively from tilt. The projected tilt angle α can therefore be extracted using Equation 4.20. For the measurements shown in Figure 6.2, the tilt magnitudes for the InGaAs-inverse layer were

$$\alpha(\varphi = 0°) = -0.002\,\text{rad} = -0.09°,$$
$$\alpha(\varphi = 90°) = -0.004\,\text{rad} = -0.24°.$$

These values indicate that the InGaAs-inverse layer is overall tilted by

$$\alpha = \sqrt{\alpha_{0°}^2 + \alpha_{90°}^2} = 0.26°$$

relative to the GaAs substrate (100) surface. The in-plane direction of the tilt is given by $\gamma = \arctan(\alpha_{0°}/\alpha_{90°}) = 68.7°$, measured counterclockwise from $[0\bar{1}\bar{1}]$ toward $[01\bar{1}]$.

After determining the tilt, asymmetric RSMs can be used to determine the composition and relaxation of the InGaAs-inverse layer. Figures 6.3 a) and b) show $(4\bar{2}\bar{2})$ maps recorded at $\varphi = 0°$ and $\varphi = 90°$, respectively, for the same sample. A rotational correction must be applied to account for the tilt before extracting the reciprocal lattice coordinates of the layer. Using the small-angle rotation matrix

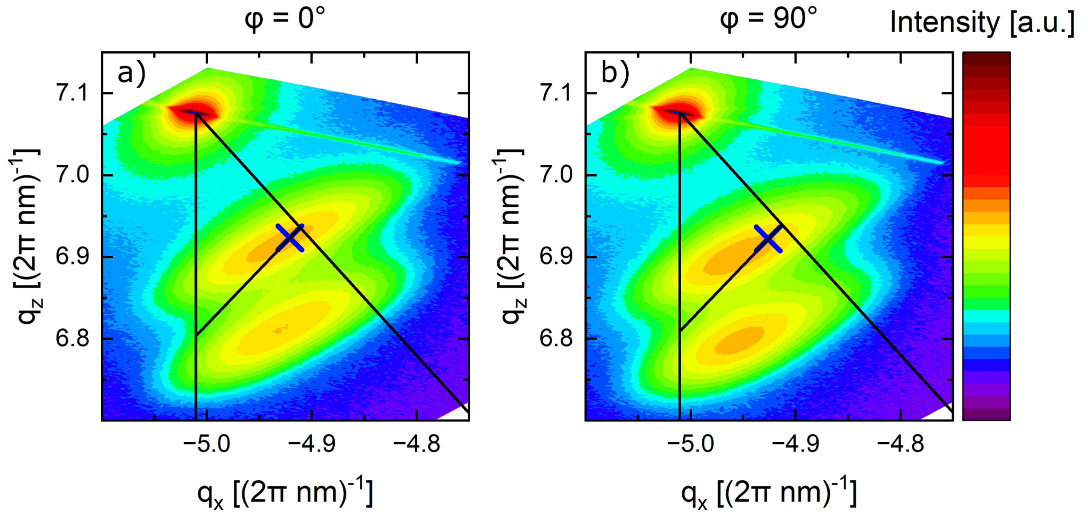

FIGURE 6.3: HRXRD RSM around the $(4\bar{2}\bar{2})$ Bragg peaks of an MBL sample measured for a) $\varphi = 0°$ and b) a) $\varphi = 90°$. The blue crosses mark the tilt corrected reciprocal space coordinates of the measured InGaAs-inverse layer.

$$\begin{pmatrix} q'_x \\ q'_z \end{pmatrix} = \begin{pmatrix} \cos(\alpha) & -\sin(\alpha) \\ \sin(\alpha) & \cos(\alpha) \end{pmatrix} \cdot \begin{pmatrix} q_x \\ q_z \end{pmatrix},$$

the corrected coordinates (q'_x, q'_z) are obtained as

$$q'_x = q_x \cdot \cos(\alpha) - q_z \cdot \sin(\alpha) \tag{6.1}$$

$$q'_z = q_x \cdot \sin(\alpha) + q_z \cdot \cos(\alpha), \tag{6.2}$$

where α is the tilt measured for the corresponding azimuth [143]. The corrected peak positions are marked as blue crosses in Figures 6.3 a,b). From these, In concentrations of 29.6 % and 29.0 % and relaxation degrees of 90 % and 87 % were extracted from the $\varphi_{0°}$ and $\varphi_{90°}$ maps, respectively.

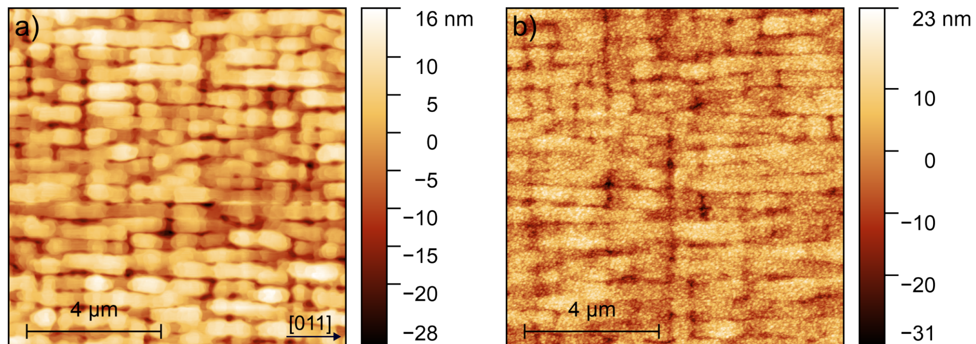

FIGURE 6.4: a) AFM image of an MBL surface as received. b) The same sample after attempting *thermal oxide removal* in the MBE main chamber and overgrowth with 110 nm $In_{0.33}Al_{0.67}As$ and 110 nm $In_{0.38}Al_{0.62}As$ at $T_{sub} = 310\,°C$.

Figure 6.4 a) shows an AFM image of an MBL surface as received, revealing a

pronounced cross-hatch pattern – a hallmark of metamorphic buffer layers [144]. These cross-hatch patterns are stemming from the plastic strain relaxation in the MBLs and it is generally assumed that this pattern is related to the underlying misfit dislocation grid [145]. The RMS roughness of the sample shown here was σ_{RMS} = 6.2 nm, measured over a $10 \times 10\ \mu m^2$ area.

6.2 $In_xAl_{1-x}As$ layer growth on MBLs

After pre-growth characterization, the MBL samples were introduced into the MBE system. Direct measurement of the substrate temperature using the bandiT system (band-edge thermometry) was not possible, since the optical absorption characteristics of the MBL samples were unknown. Therefore, the manipulator thermocouple readings were used instead. Prior to growth, a GaAs wafer supplied by the Stuttgart group was used to compare its bandiT and thermocouple temperatures, allowing an approximate calibration.

Because the MBL samples had been exposed to ambient conditions, removal of the surface oxide was required before epitaxial overgrowth. Thermal oxide desorption in the MBE main chamber was tested first, but these attempts were unsuccessful. Figure 6.4 b) shows the surface of the same sample as in Figure 6.4 a) after heating to T_{sub} = 500 °C for 10 min followed by deposition of 110 nm $In_{0.33}Al_{0.67}As$ and 110 nm $In_{0.38}Al_{0.62}As$ at T_{sub} = 310 °C. Although the RMS roughness increased only slightly to σ_{RMS} = 6.5 nm (from 6.2 nm), the surface exhibited the formation of small island-like features. Multiple combinations of oxide removal conditions and $In_xAl_{1-x}As$ growth parameters were tested, but these islands consistently reappeared. Furthermore, no discernible differences were observed between the HRXRD measurements recorded before and after overgrowth when thermal desorption was attempted.

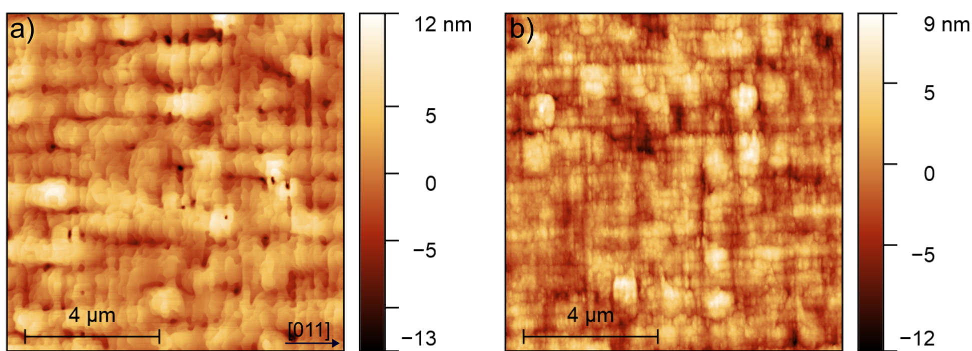

FIGURE 6.5: a) AFM image of an MBL surface as received. b) The same sample after *wet-chemical oxide removal* and overgrowth with 110 nm $In_{0.33}Al_{0.67}As$ and 110 nm $In_{0.38}Al_{0.62}As$ at T_{sub} = 310 °C.

Because thermal deoxidation was ineffective, a wet-chemical approach was adopted. Figure 6.5 a) shows the AFM image of the sample surface before the procedure. For GaAs (100), it has been shown that HCl-isopropanol (HCl-iPA) treatments effectively remove the native oxide while preserving surface morphology [146]. Therefore, an

analogous method was applied to the MBL sample: the wafer was immersed for 30 s in a 3:1 solution of HCl (31%) and iPA. The etching was stopped by transferring the wafer into pure iPA, after which it was blown dry by nitrogen and loaded into the MBE load-lock as quickly as possible.

After standard bake-out procedures, the sample was transferred into the growth chamber and heated to $T_{sub} = 520\,°C$ for 20 min. Take-out and surface inspection after this step confirmed that the morphology remained unchanged, with an RMS roughness of $\sigma_{RMS} = 2.8$ nm measured before and after the described processing steps.

The sample was then re-introduced to the MBE while performing the exact same preparation steps. Subsequently, it was overgrown with 110 nm $In_{0.33}Al_{0.67}As$ and 110 nm $In_{0.38}Al_{0.62}As$, the same as for the sample in Figure 6.4 b) with the thermal treatment. The resulting AFM image in Figure 6.5 b) exhibits a RMS of $\sigma_{RMS} = 2.6$ nm and shows that the previously observed islands are no longer present.

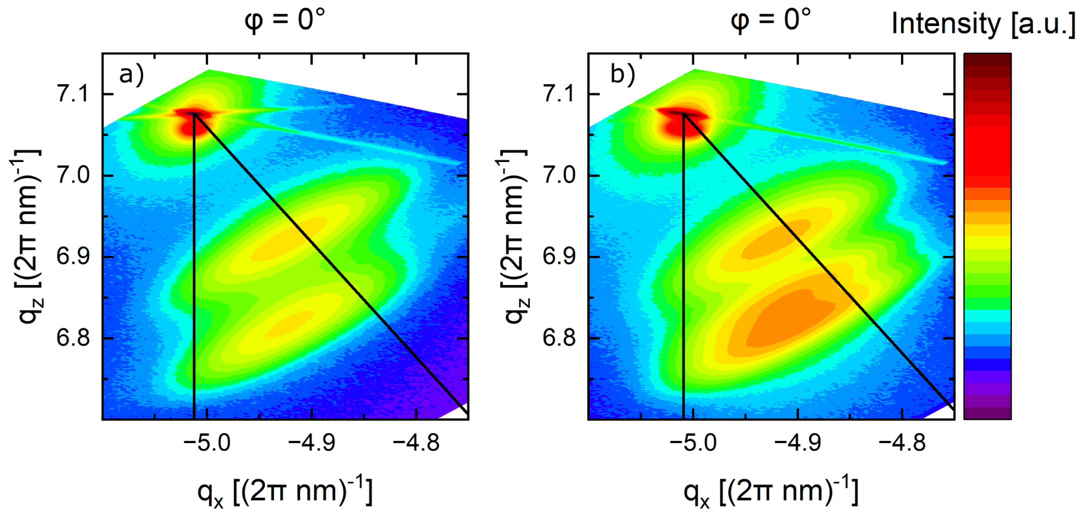

FIGURE 6.6: a) $(4\bar{2}\bar{2})$ RSM after attempted thermal deoxidation and overgrowth with 110 nm $In_{0.33}Al_{0.67}As$ and 110 nm $In_{0.38}Al_{0.62}As$. b) Same layer structure but following wet-chemical oxide removal.

HRXRD measurements also confirmed the improvement: Figure 6.6 a) shows the RSM of a sample that had only undergone thermal oxide removal. As in Figure 6.1, only the peaks corresponding to GaAs, $Al_{0.92}Ga_{0.08}As$, the InGaAs-convex layer, and the InGaAs-inverse layer are visible. Generally, no discernible changes were visible when comparing HRXRD measurements before and after overgrowing samples when only heating the samples before depositing the $In_xAl_{1-x}As$ layers. In contrast, Figure 6.6 b) shows a distinguishable change in the RSM for the wet-chemically treated sample, due to the additional $In_xAl_{1-x}As$ layers.

6.3 Droplet etching on $In_xAl_{1-x}As$ layers grown on MBLs

Droplet etching on the MBL/$In_{0.33}Al_{0.67}As$/$In_{0.38}Al_{0.62}As$ structures was tested by depositing 1.4 ML of $In_{0.38}Al_{0.62}$ over 2.6 s at a substrate temperature of T_{etch} = 435 °C, measured by thermocouple. At this temperature, a bare GaAs reference wafer displayed a bandiT reading of 445 °C. The residual As_2 pressure was set to $p_{As2} = 2 \times 10^{-7}$ mbar, and the etching time was 3 min. Etching was terminated by increasing the As_2 flux to $p_{As2} = 2 \times 10^{-5}$ mbar, followed by overgrowth with 4 ML of $In_{0.38}Al_{0.62}As$. The sample was then cooled and removed for characterization.

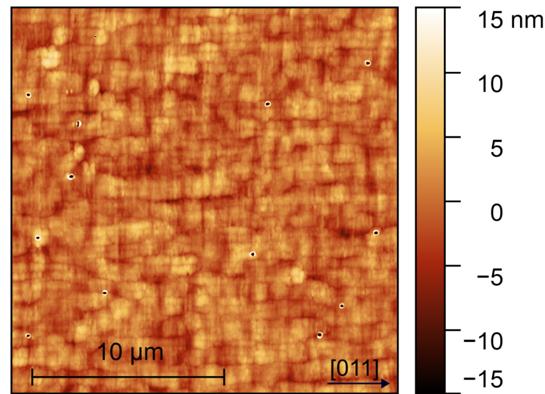

FIGURE 6.7: AFM image of an MBL sample with $In_{0.33}Al_{0.67}As$ and $In_{0.38}Al_{0.62}As$ overgrowth, after LDE with $In_{0.38}Al_{0.62}$ deposition at T_{etch} = 435 °C.

Figure 6.7 shows an AFM image of the resulting surface. The cross-hatch pattern originating from the MBL remains visible beneath the $In_{0.38}Al_{0.62}As$ overlayer. Nanoholes with surrounding ring structures were observed, with an overall nanohole density of $n = 3 \times 10^6$ cm^{-2}. However, a considerable spread in nanohole sizes was found, which typical etching depths of 50–70 nm, but also some much smaller ones with only $\sim$ 25 nm. Additionally, their shapes were generally less symmetric than those produced on $In_{0.52}Al_{0.48}As$ grown on InP.

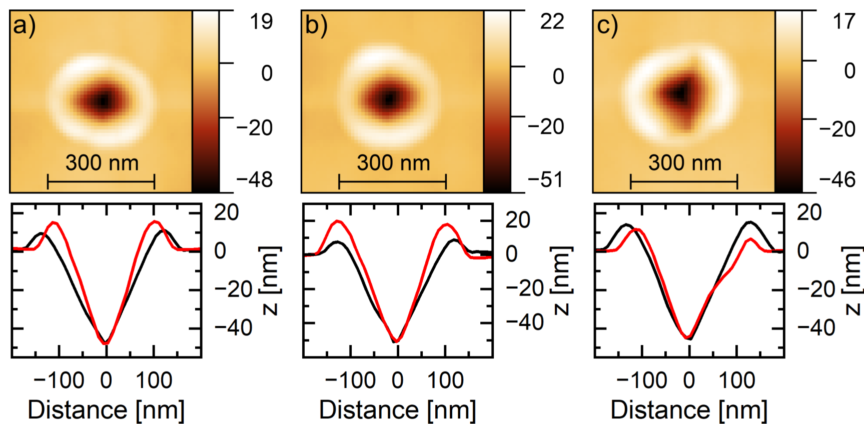

FIGURE 6.8: Selected nanoholes and corresponding line scans from an MBL sample with $In_{0.33}Al_{0.67}As$ / $In_{0.38}Al_{0.62}As$ overgrowth and LDE using $In_{0.38}Al_{0.62}$ droplets at T_{etch} = 435 °C.

Figures 6.8 a-c) shows examples of individual nanoholes from this sample. Consistent with earlier observations, the nanoholes tended to be elongated along the [011] direction, as can be seen for Figures 6.8 a) and b). Some nanoholes were strongly deformed, as illustrated in Figure 6.8 c). These observations might stem from an increased anisotropy in mass transport, due to the presence strain in the layers. Additionally, the increased surface roughness stemming from the cross-hatch pattern could favor the formation of asymmetric droplets during the deposition stage. Consequently, future improvements in the layer quality should lead to an improved nanohole formation, resulting in better quantum dot templates.

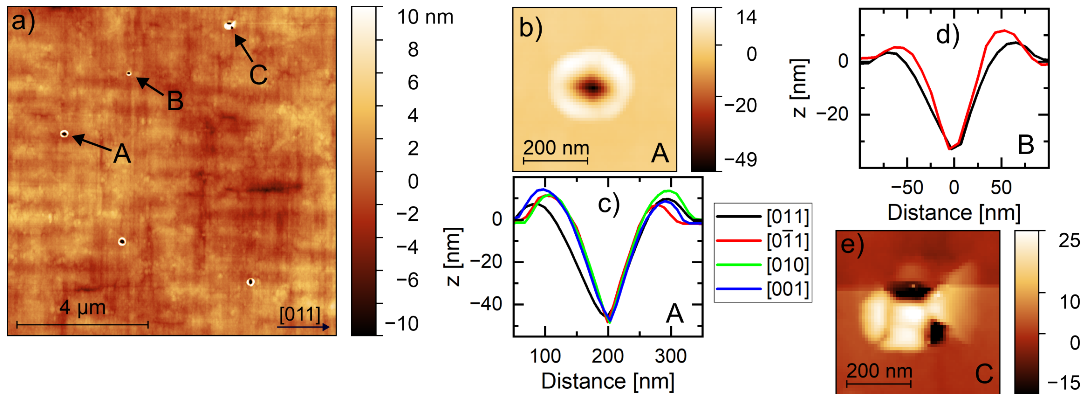

FIGURE 6.9: a) AFM image of an MBL/$In_{0.33}Al_{0.67}As$/$In_{0.38}Al_{0.62}As$ sample after LDE with $In_{0.38}Al_{0.62}$ at $T_{etch} = 415\,°C$. b-e) AFM images and line scans from the structures indicated in a).

In a second experiment, the etching temperature was reduced to $T_{etch} = 415\,°C$, corresponding to a bandiT temperature of approximately 420 °C for a GaAs reference wafer. As expected the nanohole density increased, resulting in a value of $n = 5 \times 10^6\,cm^{-2}$. Figure 6.9 a) shows an AFM image of the sample, which again exhibited a wider distribution of nanohole sizes, than those generated by the LDE experiments on $In_{0.52}Al_{0.48}As$ grown on InP. The image reveals a clear differences in ring-hole diameters between some of these structures (A: larger, B: smaller), reflecting different droplet sizes formed during the deposition stage. Malformed nanoholes (C) are also present. Figure 6.9 c) shows a line scan of a representative nanohole along four crystalline directions, demonstrating again the typical elongation along [011].

In a next step, the thickness of the $In_xAl_{1-x}As$ layer stack was increased, to enable higher In compositions in the final layer. Five successive 110 nm $In_xAl_{1-x}As$ layers were grown, starting with $In_{0.35}Al_{0.65}As$ and ending with $In_{0.55}Al_{0.45}As$. This was done to enable later infilling with lattice matched $In_{0.56}Ga_{0.44}As$ to generate QDs emitting in the telecom C-band and to spectrally separate the QD signal from eventual band-to-band emission of the MBL.

Figures 6.10 a) and b) show an AFM scan of the sample before and after this overgrowth, respectively. The resulting surface exhibited an RMS roughness of

σ_{RMS} = 2.4 nm, similar to the 2.3 nm measured prior to overgrowth, comparable to the results after overgrowth with the thinner $In_{0.33}Al_{0.67}As$/ $In_{0.38}Al_{0.62}As$ stack.

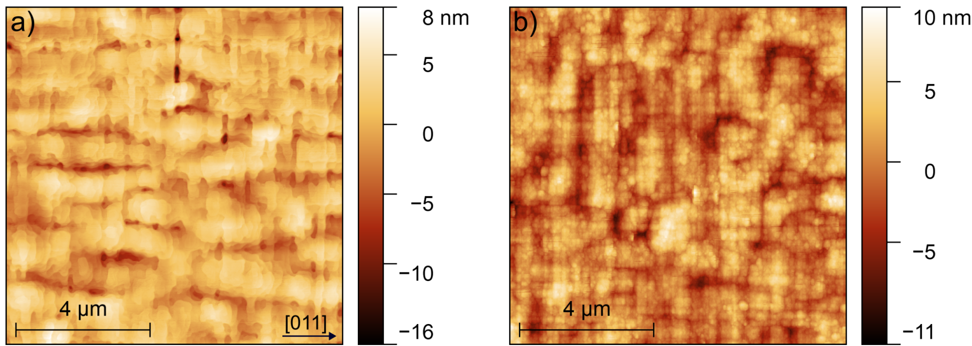

FIGURE 6.10: AFM images of an MBL sample a) before and b) after overgrowth with five 110 nm $In_xAl_{1-x}As$ layers, where x was increased in steps of 0.05 from $In_{0.35}Al_{0.65}As$ to $In_{0.55}Al_{0.45}As$.

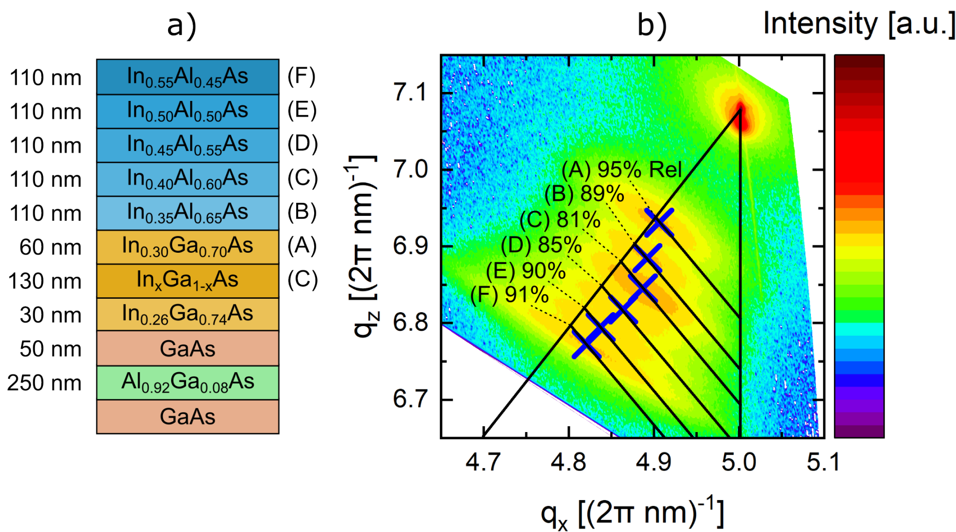

FIGURE 6.11: a) Layer structure of the sample discussed in the text. The MBL was grown in Stuttgart and its In content is graded by a 30 nm $In_{0.26}Ga_{0.74}As$ abrupt change (jump) layer, a 130 nm $In_xGa_{1-x}As$ layer following a convex design with final In concentration of 40 % and at the top a 60 nm $In_{0.30}Ga_{0.70}As$ inverse layer for strain release. Details can be found in Reference [97]. The MBL was overgrown in Paderborn with five 110 nm $In_xAl_{1-x}As$ layers, where x was increased in steps of 0.05 from $In_{0.35}Al_{0.65}As$ to $In_{0.55}Al_{0.45}As$. b) (422) RSM of such a sample, the blue crosses mark the tilt corrected reciprocal space coordinates for the measured layer peaks. The peaks are labeled with their calculated relaxation degrees.

Figures 6.11 a) and b) present a sketch of the sample structure and the (422) reciprocal space map (RSM) with tilt-corrected reciprocal-space coordinates for the six measured layer peaks, measured on the sample with nanoholes shown in Figure 6.12 a). The peaks were labeled according to their presumed origin within the layer sequence, based on the In concentrations extracted from the measurements. Since the $In_xGa_{1-x}As$-convex layer terminates at an In content of 40 %, its diffraction signal is located close to that of the $In_{0.40}Al_{0.60}As$ layer. Consequently, peak (C) could not be unambiguously assigned to either layer.

For this proof-of-concept structure, a decrease in the degree of relaxation from 95 % for the InGaAs-inverse layer to 91 % for the topmost $In_{0.55}Al_{0.45}As$ layer was determined. Corresponding rocking-curve measurements of the (400) Bragg reflection at $\varphi = 0°$ and $\varphi = 90°$ yielded average dislocation densities of $\rho = 1.8 \times 10^{10}\,cm^{-2}$ ($\beta = 0.65°$) for the InGaAs-inverse layer and $\rho = 3.5 \times 10^{10}\,cm^{-2}$ ($\beta = 0.89°$) for the $In_{0.55}Al_{0.45}As$ layer.

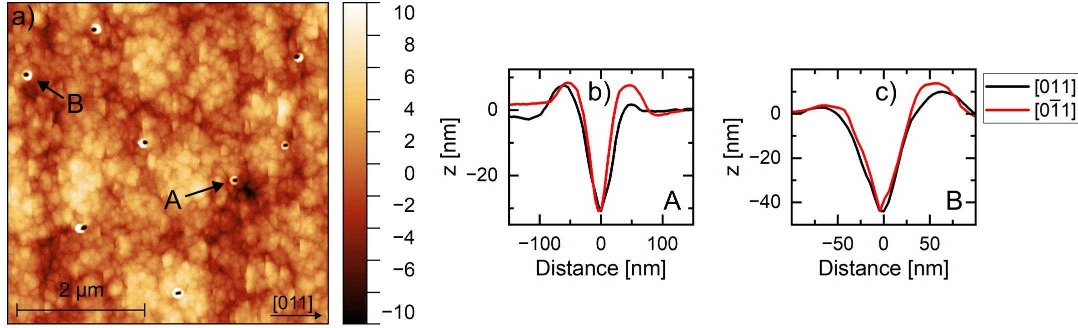

FIGURE 6.12: a) AFM image after performing LDE with $In_{0.55}Al_{0.45}$ at T_{etch} = 415 °C on an $In_{0.35}Al_{0.65}As \cdots In_{0.55}Al_{0.45}As$ layer stack. b,c) Line scans of the nanoholes indicated in a).

Droplet etching was then repeated on the final $In_{0.55}Al_{0.45}As$ layer surface using 1.4 ML of $In_{0.55}Al_{0.45}$ deposited over 2.0 s at T_{etch} = 415 °C. As shown in Figure 6.12 a), well-defined nanoholes again formed, with a significantly higher density of $n = 2 \times 10^7\,cm^{-2}$. This value lies in the same range as earlier experiments with comparable LDE parameters on $In_{0.52}Al_{0.48}As$/InP, where densities of $2 \times 10^7\,cm^{-2}$ and $1 \times 10^7\,cm^{-2}$ were found at T_{etch} = 410 °C and 435 °C, respectively (see Figure 5.22).

The increased nanohole density on $In_{0.55}Al_{0.45}As$ compared to $In_{0.35}Al_{0.67}As$ is attributed mainly to the higher material deposition rate: on $In_{0.35}Al_{0.67}As$, 1.4 ML was deposited over 2.6 s (0.54 ML s^{-1}), whereas here the same amount was deposited over 2.0 s (0.70 ML s^{-1}), consistent with the deposition rate dependence discussed in Section 5.2.6. A statistical analysis of 20 nanoholes on the $In_{0.55}Al_{0.45}As$ sample yielded average depths of $h = (34.4 \pm 6.2)$ nm and average diameters of $d_{[011]} = (82 \pm 14)$ nm and $d_{[0\bar{1}1]} = (62 \pm 7)$ nm. The depth is comparable to earlier results on $In_{0.52}Al_{0.48}As$/InP at T_{etch} = 435 °C, where $h = (33.2 \pm 2.5)$ nm was observed. However, the size distribution here was much broader, and many nanoholes exhibited irregular shapes, similar to those shown in Figures 6.8 and 6.9. Representative line scans are shown in Figures 6.12 b) and 6.12 c).

6.4 Nanohole infilling and overgrowth

For the infilling of nanoholes, $In_{0.56}Ga_{0.44}As$ was deposited in a pulsed deposition mode, using 1 s deposition intervals followed by 1 min pauses under an As_4 flux of $p_{As4} = 1.5 \times 10^{-5}$ mbar. Deposition amounts of 0.6 nm and 1.0 nm were tested, consistent with the earlier infilling studies shown in Figure 5.42. The deposition

temperature was set to $T_{sub} = 500\,°C$, measured by thermocouple, at which a bare GaAs reference wafer also showed $T_{banditT} = 500\,°C$.

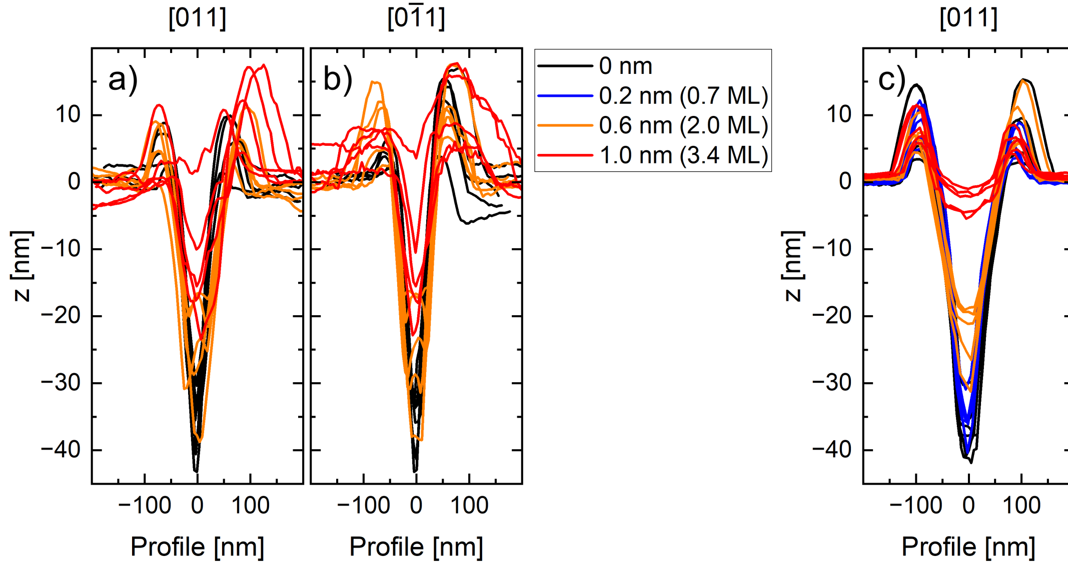

FIGURE 6.13: a,b) Overlayed line scans of nanoholes etched into an $In_{0.35}Al_{0.65}As \cdots In_{0.55}Al_{0.45}As$ layer stack, after deposition of the indicated $In_{0.56}Ga_{0.44}As$ amounts for infilling. c) Comparison to nanoholes etched into $In_{0.52}Al_{0.48}As$ grown lattice-matched on InP and infilled with $In_{0.53}Ga_{0.47}As$ under similar parameters (copied from Figure 5.42).

Figures 6.13 a) and b) show overlayed line profiles of the nanoholes along the [011] and [0$\bar{1}$1] directions, respectively, for samples without infilling (black), with 0.6 nm infilling (orange), and with 1.0 nm infilling (red). Figure 6.13 c) shows corresponding line scans from nanoholes etched into $In_{0.52}Al_{0.48}As$ with similar parameters ($T_{etch} = 435\,°C$, $p_{As2} = 2 \times 10^{-7}$ mbar, $\theta_{InAl} = 1.4$ ML and 4 ML of post-etching overgrowth) and infilled with $In_{0.53}Ga_{0.47}As$.

Interpretation of the profiles on the $In_{0.55}Al_{0.45}As$-MBL stack is complicated by the higher surface roughness, which prevents precise alignment of the depth profiles at a common zero-height z reference. Additionally, the infilling levels exhibit larger variation than those in Figure 6.13 c). For instance, for 1.0 nm of deposition, the nanohole infilling heights span from $z = 25$ nm unfilled to almost completely infilled, whereas the InP-based samples showed a variation of only about ~ 5 nm. Nevertheless, the profiles in Figures 6.13 a) and b) demonstrate that pulsed $In_{0.56}Ga_{0.44}As$ deposition under As_4 conditions successfully fills these nanoholes.

In the next step, nanoholes infilled with 1.0 nm of $In_{0.56}Ga_{0.44}As$ were overgrown with 100 nm of $In_{0.55}Al_{0.45}As$ and 3 nm of $In_{0.56}Ga_{0.44}As$, which served as a protection layer against oxidation. These layers were deposited at $T_{sub} = 310\,°C$ under an As_2 flux of $p_{As2} = 2.00 \times 10^{-5}$ mbar.

Figures 6.14 a) and b) show the PL spectra of three samples: a bare MBL, an MBL overgrown with the $In_xAl_{1-x}As$ layer stack, and an infilled-nanohole QD sample. Figure 6.14 a) (800–1200 nm, logarithmic scale) reveals three peaks (A), (B), and (C) originating from the MBL, which are present in all samples. After overgrowth, an

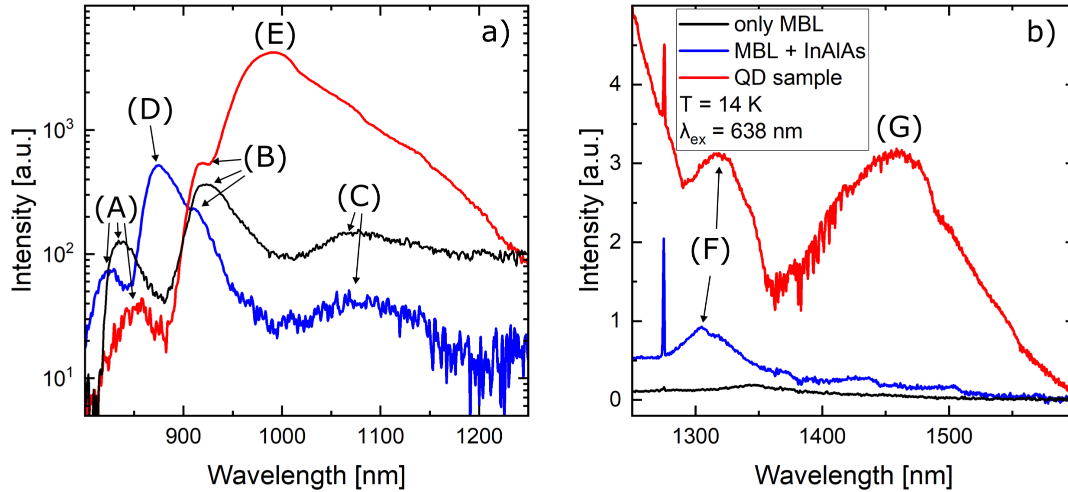

FIGURE 6.14: PL spectra of different MBL samples: bare MBL (black), MBL with $In_{0.35}Al_{0.65}As \cdots In_{0.55}Al_{0.45}As$ overgrowth (blue), and QD sample with infilled nanoholes and $In_{0.55}Al_{0.45}As$ / $In_{0.56}Ga_{0.44}As$ overgrowth (red).

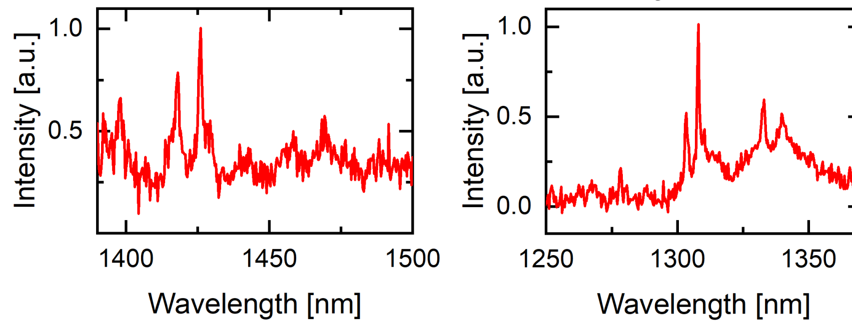

FIGURE 6.15: μPL spectra of the QD-MBL sample, measured by Dr. Michael Jetter and colleagues (University of Stuttgart).

additional peak (D) appears, which likely stems from the multilayer stack but disappears in the QD sample. Due to the complexity of the MBL structure and the presence of partial strain relaxation, an unambiguous assignment of these peaks is challenging.

A prominent, broad peak (E) appears around 1000 nm for the QD sample. This peak is attributed to the quasi-wetting layer formed by the $In_{0.56}Ga_{0.44}As$ deposition for infilling. Its breadth is consistent with the increased surface roughness compared to the smoother InP-based samples (see Figure 5.46).

Figure 6.14 b) (1250–1600 nm) shows peaks at approximately 1310 nm (F) in both the stack-only and QD samples. The origin of these peaks remains unclear. A distinct peak at 1460 nm (G) appears only in the QD sample and is attributed to emission from the infilled and overgrown nanoholes. The wavelength peak is a bit shorter than anticipated, but it is in an expected range for a proof of concept experiment and it reflects the broad size distribution of nanoholes and infilling amounts.

Figure 6.15 shows μPL spectra measured on the QD sample. Similar to the $In_{0.53}Ga_{0.47}As/In_{0.52}Al_{0.48}As$ QDs (Figure 5.48), sharp emission lines were observed, but their intensities were too low for advanced characterization in absence of a DBR.

Chapter 7

Summary and Outlook

This dissertation presented the first successful adaptation of the local droplet etching (LDE) process to the InP/$In_{0.52}Al_{0.48}As$ material platform. However, this was not straightforward, due to the need for the accurate control of the composition of the ternary alloys $In_xAl_{1-x}As$ and $In_yGa_{1-y}As$. Further it was found that nanoholes etched using In droplets degraded after the LDE process upon returning the arsenic flux to the BEP required for layer growth. To overcome this challenge, a practical approach was developed in which a thin layer of a few monolayers of $In_{0.52}Al_{0.48}As$ was deposited immediately after increasing the As flux. This overgrowth step effectively preserved the nanoholes and prevented their collapse during subsequent processing steps.

LDE offers a wide parameter space, and the present work systematically examined the influence of several critical parameters on nanohole formation: substrate temperature T_{etch}, residual arsenic pressure p_{As} during etching, composition of the droplet material (In, Al, InAl, or Ga), material deposition amount θ, deposition rate F, etching time t_{etch} and post-etching overgrowth. The main objective of these experiments was to establish growth conditions that yield nanoholes suitable as templates for quantum dot (QD) fabrication.

It was found that the combination of $T_{\mathrm{etch}} = 435\,^{\circ}\mathrm{C}$, $p_{\mathrm{As2}} = 2 \times 10^{-7}\,\mathrm{mbar}$, $\theta_{\mathrm{InAl}} = 1.4\,\mathrm{ML}$, $F = 0.68\,\mathrm{ML/s}$ and a post-etch overgrowth of 4 ML produced nanoholes approximately (33 ± 2) nm deep with favorable in-plane symmetry. The same parameters – albeit with $F = 0.34\,\mathrm{ML/s}$ – were also effective for Al- and In-based droplets, which formed promising, but deeper, templates for infilling. These yielded average depths of (57 ± 9) nm for Al and (47 ± 5) nm for In, showing slightly stronger elongation. Nevertheless, limited infilling of only 30–40 nm is expected to still produce QDs with good in-plane symmetry.

Arrhenius-type plots of the nanohole density as a function of inverse etching temperature $1/T_{\mathrm{etch}}$ yielded comparable activation energies for all three droplet types, namely $E_n = (1.83 \pm 0.19)$ eV for InAl, $E_n = (1.75 \pm 0.13)$ eV for Al, and $E_n = (1.86 \pm 0.09)$ eV for In. The etching parameters were identical for all droplet materials, except for the deposition rate F, which was higher for InAl droplets, which resulted in higher nanohole densities. In contrast, In and Al droplets produced significantly lower densities across all temperatures, in agreement with expectations

from classical nucleation theory [75]. Additional experiments varying the deposition rate for InAl droplets revealed an increase in nanohole density and a decrease in the ring-hole diameter with increasing F, indicating the formation of more but smaller droplets at higher deposition rates.

In contrast, the total deposited amount θ_{InAl} showed no significant influence on nanohole density for InAl droplets etched at $p_{\mathrm{As}_2} = 2 \times 10^{-7}$ mbar and $T_{\mathrm{etch}} = 435\,^{\circ}\mathrm{C}$. This observation was consistent with previous studies on Al droplet etching on $\mathrm{Al}_x\mathrm{Ga}_{1-x}\mathrm{As}$, which also reported no clear dependence of nanohole density on the deposited amount [77]. Nevertheless, the resulting nanohole morphology was found to depend strongly on θ_{InAl}. Moreover, a minimum coverage of at least $\theta_w = 0.3$ ML was identified as a prerequisite for droplet formation.

Similarly, the residual As_2 background pressure was shown to also exert a strong influence on nanohole formation. At $\theta_{\mathrm{InAl}} = 4.1$ ML and $T_{\mathrm{etch}} = 435\,^{\circ}\mathrm{C}$, no droplets formed at $p_{\mathrm{As}_2} = 1 \times 10^{-5}$ mbar, whereas bimodal nanohole size distributions were observed at 2×10^{-7} mbar. The residual arsenic pressure also had a measurable impact on nanohole density.

It was also observed that a post-etching overgrowth with $\mathrm{In}_{0.52}\mathrm{Al}_{0.48}\mathrm{As}$ under As_2 flux not only preserves the nanoholes but can also be used to modify their in-plane symmetry and the size of the surrounding ring structure. This also enables the overgrowth of the nanoholes with another semiconductor materials, e.g. $\mathrm{In}_{0.53}\mathrm{Ga}_{0.47}\mathrm{As}$.

Experiments varying the etching duration t_{etch} for InAl, Al, and In droplets revealed a partial refilling of the nanoholes during the LDE process, similar to behavior previously reported for the GaAs system [81]. Moreover, these studies indicated fundamental differences in the etching mechanisms between In and Al droplets, highlighting the need for further investigations to fully understand the physics governing droplet etching into $\mathrm{In}_{0.52}\mathrm{Al}_{0.48}\mathrm{As}$ layers. Interestingly, only droplets containing In and Al – or their mixtures – produced well-defined nanoholes on $\mathrm{In}_{0.52}\mathrm{Al}_{0.48}\mathrm{As}$, whereas Ga droplets failed to form nanohole structures.

As an exploratory test, droplet etching was also applied to $\mathrm{In}_{0.53}\mathrm{Ga}_{0.47}\mathrm{As}$, where Ga and Al droplets did etch pits into the surface, but this did not result in the typical round shaped nanoholes with a surrounding ring structure. Only the In droplets produced proper nanholes in $\mathrm{In}_{0.53}\mathrm{Ga}_{0.47}\mathrm{As}$ layers. Furthermore, in contrast to $\mathrm{In}_{0.52}\mathrm{Al}_{0.48}\mathrm{As}$, where nanoholes consistently elongated along the $[011]$-direction, In droplets on $\mathrm{In}_{0.53}\mathrm{Ga}_{0.47}\mathrm{As}$ produced nanoholes elongated along the $[0\bar{1}1]$-direction. These results hint at a fundamental difference in etching behavior between these two semiconductor alloys.

Nanoholes in $\mathrm{In}_{0.52}\mathrm{Al}_{0.48}\mathrm{As}$ were successfully infilled using pulsed deposition of $\mathrm{In}_{0.53}\mathrm{Ga}_{0.47}\mathrm{As}$ and infilling proved to be significantly more efficient under an As_4 flux environment than under As_2. QDs consisting of $\mathrm{In}_{0.53}\mathrm{Ga}_{0.47}\mathrm{As}$ embedded in an

$In_{0.52}Al_{0.48}As$ matrix were fabricated and characterized by ensemble photoluminescence (PL) spectroscopy. Preliminary μPL measurements, performed in collaboration with the group of Prof. Dr. Klaus Jöns (Paderborn University), revealed sharp emission lines from individual QDs, but the overall intensity was too low for detailed characterization. The emission exhibited a red-shift with increased infilling, but remained below the telecom C-band. Thus slightly higher indium concentrations than the nominal lattice-matched composition were tested and for QDs with a height of $\sim$ 30 nm a increase of only 3–4 % from the latticed matched $In_{0.53}Ga_{0.47}As$ composition was sufficient to shift the ensemble QD emission into the C-band.

To explore the combination of $In_xAl_{1-x}As/In_yGa_{1-y}As$ structures with the technological advantages of GaAs-based systems – such as easier integration with distributed Bragg reflectors (DBRs) – metamorphic buffer layer samples were provided by Dr. Michael Jetter and colleagues from the University of Stuttgart. These buffers featured a topmost $In_{0.30}Ga_{0.70}As$ layer, over which additional $In_xAl_{1-x}As$ layers up to 110 nm thick were grown, increasing the indium content by approximately 5 % per layer, up to $In_{0.55}Al_{0.45}As$. Nanohole etching in these metamorphic $In_{0.55}Al_{0.45}As$ layers, performed under the previously optimized conditions, produced less homogeneous results than those obtained on $In_{0.52}Al_{0.48}As$ grown on InP, but the holes could still be infilled and overgrown to form embedded $In_{0.56}Ga_{0.44}As$ QDs in an $In_{0.55}Al_{0.45}As$ matrix. Ensemble PL spectra from these samples were complex due to the intricate layer structure, making it difficult to identify individual contributions; nonetheless, μPL measurements performed in Stuttgart showed sharp emission lines, albeit not within the C-band and with too low intensity for detailed optical characterization in the absence of a DBR.

This work demonstrates the first adaptation of the LDE process to $In_{0.52}Al_{0.48}As$ layers lattice matched to InP and provides an initial proof of concept for combining this approach with the GaAs system via metamorphic buffer layers. The results establish a foundation for producing LDE $In_yGa_{1-y}As$-based QDs designed for telecom-wavelength emission. Future research should focus on further optimizing droplet etching on $In_{0.52}Al_{0.48}As$, exploring the underlying material physics of In- and Al-driven etching processes, and extending optical characterization. Achieving reliable emission within the C-band, along with efficient photon extraction through DBR or photonic-cavity integration, remains an important goal toward developing deterministic telecom-wavelength quantum light sources.

Appendix A

Sample number reference catalog

Figure 5.2. Lattice-matched $In_xAl_{1-x}As$ layer grown on InP: A2731.
Figure 5.3. a) $In_{0.52}Al_{0.48}As$ (A3069) and b) $In_{0.53}Ga_{0.47}As$ (A3076) layers grown under too much As_2 BEP.
Figure 5.4. (400) Bragg peaks of $In_xAl_{1-x}As$. a) A3356 and b) A2371.
Figure 5.5 and 5.6. Droplet formation: A2817.

TABLE A.1: Figure 5.7. Nanohole degradation under increased As_2 flux.

a)	b)	c)	d)	e)	f)
A2992	A2998	A3139	A3140	A3154	A3155

TABLE A.2: Figure 5.8. Conservation of nanoholes with $In_{0.52}Al_{0.48}As$ overgrowth.

Material	0 ML	2 ML	4 ML
In	A2992	A2898	A2998
InAl	A2971	A2875	A2975
Al	A2977	A2901	-

TABLE A.3: Figure 5.9. Nanohole density as a function of inverse etching temperature.

T_{etch}	505 °C	480 °C	460 °C	435 °C	410 °C	390 °C
	A2625	A2621	A2512	A2508	A2560	A2620

TABLE A.4: Figure 5.10 and Figure 5.11. Geometric properties of nanoholes as a function of the etching temperature.

T_{etch}	410 °C	435 °C	460 °C
	A2560	A2508	A2512

Figure 5.12. AFM image of a nanohole etched at $T_{\text{etch}} = 460\,°C$: A2512.
Figure 5.13. AFM image a nanohole overgrown with 150 nm of $In_{0.52}Al_{0.48}As$ at $T_{etch} = 410\,°C$: A2573.
Figure 5.14. Nanohole overgrown with digital alloy: A2447.
Figure 5.15. Nanohole etched at $T_{etch} = 435\,°C$ (A2477) and $T_{etch} = 460\,°C$ (A2494).

TABLE A.5: Table 5.2. Geometric properties of nanoholes for different overgrowth thicknesses and etching temperatures.

T_{etch}	410 °C			
$d_{overgrowth}$	0 nm	50 nm	100 nm	150 nm
	A2560	A2364	A2572	A2573

T_{etch}	435 °C			460 °C	
$d_{overgrowth}$	0 nm	50 nm	150 nm	0 nm	50 nm
	A2509	A2477	A2578	A2512	A2494

TABLE A.6: Figure 5.17. Influence of residual As_2 pressure.

p_{As2}(mbar)	1×10^{-8}	2×10^{-7}	2×10^{-6}	7×10^{-6}	1×10^{-5}
	A2817	A2789	A2786	A2796	A2797

TABLE A.7: Figure 5.18. Influence of deposition amount.

θ_{InAl}	4.1 ML	2.7 ML	1.4 ML	0.7 ML	0.3 ML
	A2789	A2874	A2875	A2876	A2884

TABLE A.8: Figure 5.19. Geometric properties of nanoholes as a function of the etching temperature. InAl droplets, $\theta = 1.4$ ML and $p_{As2} = 2 \times 10^{-7}$ mbar.

T_{etch}	410 °C	435 °C	460 °C	480 °C	505 °C
	A3002	A2875	A2882	A3008	A3018

TABLE A.9: Figure 5.20. Geometric properties of nanoholes as a function of the etching temperature. In and Al droplets, $\theta = 1.4$ ML and $p_{As2} = 2 \times 10^{-7}$ mbar.

T_{etch}	410 °C	435 °C	460 °C	480 °C	505 °C
In	A3003	A2998	A3004	A3009	A3019
Al	A2993	A2977	A2997	A3010	A3020

Figure 5.21. Selected line scans for InAl (A2875), In (A2998) and Al (A2977).

Figure 5.22. Nanohole density as a function of the inverse temperature: See Table A.8 and A.9.

TABLE A.10: Figure 5.23. Nanohole density as a function of the inverse temperature for $p_{As2} = 2 \times 10^{-6}$ mbar and $p_{As2} = 2 \times 10^{-7}$ mbar.

T_{etch}	410 °C	435 °C	460 °C	480 °C	505 °C
$p_{As2} = 2 \times 10^{-6}$ mbar	A2560	A2508	A2512	A2621	A2625
$p_{As2} = 2 \times 10^{-7}$ mbar	A3002	A2875	A2882	A3008	A3018

Figure 5.27. Exemplary line scan: A3559.

Figure 5.29. AFM image for Al deposition with $t_{etch} = 30$ s: A3300.

Figure 5.30. Nanohole diameter as a function of the etching time: See Table A.12.

Figure 5.31. Selected line scans. Etching with Al: $t_{etch} = 30$ s (A3300) and $t_{etch} = 135$ s (A3321). Etching with In: $t_{etch} = 30$ s (A3308) and $t_{etch} = 270$ s (A3311)

TABLE A.11: Figure 5.24, 5.25 and 5.26. Geometric properties of nanoholes as a function of the material flux for $T_{etch} = 350\,°C$ and $T_{etch} = 460\,°C$.

Droplet rate	0.2 Å s^{-1}	0.6 Å s^{-1}	2.0 Å s^{-1}	4.0 Å s^{-1}
$T_{etch} = 350\,°C$	A3485	A3484	A3558	A3493
$T_{etch} = 460\,°C$	A3480	A3479	A3559	A3492

TABLE A.12: Figure 5.28. Nanohole depth as a function of the etching time.

t_{etch}	30 s	60 s	90 s	135 s	180 s	225 s	270 s	360 s	600 s
InAl	A2915	A2916	A2917	-	A2875	-	-	A2969	A3373
In	A3308	A3309	A3310	A3323	A2998	A3324	A3311	A3312	A3313
Al	A3300	A3301	A3302	A3321	A2977	A3322	A3305	A3306	A3307

Figure 5.32. AFM images after LDE with Ga on $In_{0.52}Al_{0.48}As$: a) A2813, b) A2814.
Figure 5.33. AFM images after LDE with Ga or InGa on $In_{0.52}Al_{0.48}As$: a) A2902, b) A2807.
Figure 5.34. AFM image after LDE with Ga on $In_{0.53}Ga_{0.47}As$: A3483.
Figure 5.35. AFM image after LDE with Al on $In_{0.53}Ga_{0.47}As$: A3482.
Figure 5.36. AFM image after LDE with In on $In_{0.53}Ga_{0.47}As$: A3481.
Figure 5.37. AFM images after LDE with In on $In_{0.53}Ga_{0.47}As$: a) A3527, b) A3502.
Figure 5.38. AFM image after $In_{0.30}Al_{0.70}$ LDE on an $In_{0.30}Ga_{0.70}As$ MBL: W02673-B.
Figure 5.39. AFM image after LDE with $In_{0.30}Al_{0.70}$ on an $In_{0.30}Al_{0.70}As$ layer grown on a MBL a) W02673-C, and after $In_{0.30}Ga_{0.70}As$ overgrowth b) W02853-D.

TABLE A.13: Figure 5.40 and 5.41. Line profiles for various infilling amounts with $In_{0.53}Ga_{0.47}As$ under As_2 and As_4 environment.

$In_{0.53}Ga_{0.47}As$	no fill	3.4 ML	4.8 ML
As_2	A2364	A2606	A2610
As_4	A2364	A2397	A2365

TABLE A.14: Figure 5.42. Line profiles for various infilling amounts with $In_{0.53}Ga_{0.47}As$ under As_4 environment.

$In_{0.53}Ga_{0.47}As$	no fill	0.7 ML	2.0 ML	3.4 ML
	A2875	A2896	A2894	A2893

TABLE A.15: Figure 5.43 and 5.44. AFM images and line profiles for various infilling amounts with InAs under As_4 environment.

InAs	no fill	2.0 ML	2.3 ML	2.5 ML	2.7 ML	3.0 ML
	A3359	A3377	A3387	A3379	A3388	A3381

TABLE A.16: Figure 5.46. PL spectra of QDs fabricated from infilling by depositing different amounts of $In_{0.53}Ga_{0.47}As$ and overgrowing.

$In_{0.53}Ga_{0.47}As$	1.0 nm	1.4 nm	1.8 nm
	A2421	A2416	A2436

Figure 5.47. a) PL spectrum of infilled nanoholes: A2478. b) Nanohole line scans: A2477 (0 nm) and A2495 (1.8 nm).
Figure 5.48. μPL spectra: a) A2478 and b) A2498.

TABLE A.17: Figure 5.49. PL spectra for QD samples with 1.0 nm of $In_xGa_{1-x}As$ deposition for infilling, with different compositions x

x	53 %	56 %	57 %
	A2895	A2897	A3200

Figure 6.1. RSM around the $(4\bar{2}\bar{2})$ peaks of an MBL sample: W02672-A.
Figure 6.2 and 6.3. RSM around the (400) and $(4\bar{2}\bar{2})$ peaks of an MBL sample: W02676-A.
Figure 6.4. AFM image of an MBL surface before and after attempting thermal oxide removal and overgrowth: W02505-A.
Figure 6.5. AFM image of an MBL surface before and after attempting wet-chemical oxide removal and overgrowth: W02508-B.
Figure 6.6. $(4\bar{2}\bar{2})$ RSM after attempted thermal oxide removal and overgrowth (W02505-A) and wet-chemical oxide removal and overgrowth (W02508-B).
Figure 6.7 and 6.8. AFM measurements of an MBL sample with $In_{0.33}Al_{0.67}As$ and $In_{0.38}Al_{0.62}As$ overgrowth, after LDE with $In_{0.38}Al_{0.62}$ deposition at $T_{etch} = 435\,°C$: W02508-C.
Figure 6.9. AFM measurements of an MBL/$In_{0.33}Al_{0.67}As$/$In_{0.38}Al_{0.62}As$ sample after LDE with $In_{0.38}Al_{0.62}$ at $T_{etch} = 415\,°C$: W02606-D.
Figure 6.10. AFM images of an MBL sample a) before and b) after overgrowth with five 110 nm $In_xAl_{1-x}As$ layers: W02672-A.
Figure 6.12. AFM image after performing LDE with $In_{0.55}Al_{0.45}$ at $T_{etch} = 415\,°C$ on an $In_{0.35}Al_{0.65}As \cdots In_{0.55}Al_{0.45}As$ layer stack: W02672-B.

TABLE A.18: Figure 6.13. Overlayed line scans of nanoholes etched into an $In_{0.35}Al_{0.65}As \cdots In_{0.55}Al_{0.45}As$ layer stack, after deposition of the indicated $In_{0.56}Ga_{0.44}As$ amounts for infilling.

$In_{0.56}Ga_{0.44}As$	no fill	2.0 ML	3.4 ML
	W02672-B	W02672-C	W02672-D

Figure 6.14. PL spectra of different MBL samples. Bare MBL measurement taken on a broken off piece of the W02505 wafer. With InAlAs stack: W02672-A. With QDs: W02672-D
Figure 6.15. μPL spectra of the QD-MBL sample: W02672-D.

Scientific contributions

The following scientific publications and conference submissions were contributed during research for this dissertation:

Scientific publications

- D. Deutsch, C. Buchholz, V. Zolatanosha, K. D. Jöns, and D. Reuter. “Telecom C-band photon emission from (In,Ga)As quantum dots generated by filling nanoholes in In0.52Al0.48As layers”. In: *AIP Advances* 13.5 (May 1, 2023), p. 055009. ISSN: 2158-3226. DOI: 10.1063/5.0147281.

- T. Henksmeier, P. Mahler, A. Wolff, D. Deutsch, M. Voigt, L. Ruhm, A. M. Sanchez, D. J. As, G. Grundmeier, and D. Reuter. “Low-Temperature Fabrication of Amorphous Carbon Films as a Universal Template for Remote Epitaxy”. In: *Communications Materials* 5.1 (Dec. 20, 2024), p. 276. ISSN: 2662-4443. DOI: 10.1038/s43246-024-00718-7.

- N. Auler, D. Deutsch, and D. Reuter. “Statistical Analysis of the Spatial Distribution of InAl Droplet-Etched Nanoholes in In0.52Al0.48As Layers”. In: *Crystals* 15.9 (Aug. 29, 2025), p. 770. ISSN: 2073-4352. DOI: 10.3390/cryst15090770.

- D. Deutsch, V. Zolatanosha, and D. Reuter. “Local Droplet Etching with In, Al and InAl in In0.52Al0.48As Layers for Generation of Quantum Dots Emitting in the Optical C-band”. In: *Journal of Crystal Growth* 668 (Oct. 2025), p. 128247. ISSN: 00220248. DOI: 10.1016/j.jcrysgro.2025.128247.

- D. Deutsch and D. Reuter. “Influence of the Etching Material Deposition Rate and Annealing Time on Nanohole Morphology Etched into InP/In0.52Al0.48As Layers via Local Droplet Epitaxy”. In: *Crystals* 15.11 (Oct. 23, 2025), p. 913. ISSN: 2073-4352. DOI: 10.3390/cryst15110913.

- (**under review**) C. Buchholz, J. N. C. Rodríguez, D. Deutsch, D. Reuter, K. D. Jöns. “Review on Telecom Quantum Dots: Challenges and Perspectives”. Submitted to: *Applied Physics Reviews*.

Conference submissions

- D. Deutsch, C. Buchholz, V. Zolatanosha, K. D. Jöns, D. Reuter. “Telecom C-band photon emission from (In,Ga)As Quantum Dots generated by filling nanoholes in In0.52Al0.48As layers” (Talk). DPG Spring Meeting of the Condensed Matter Section. Dresden, Germany. 26.03. - 31.03.2023.

- D. Deutsch, C. Buchholz, V. Zolatanosha, K. D. Jöns, D. Reuter. “Local Droplet Etching and Filling Behavior of Nanoholes in In0.52Al0.48As Layers” (Poster).

North American Conference on Molecular Beam Epitaxy. Madison, USA. 17.09. - 20.09.2023.

- D. Deutsch, C. Buchholz, V. Zolatanosha, K. D. Jöns, D. Reuter. "Telecom C-band emission from droplet etched quantum dots in the InP/InyAl1-yAs/InxGa1-xAs system" (Poster). Engineering of Quantum Emitter Properties. Paderborn, Germany. 07.10. - 08.10.2023.

- D. Deutsch, C. Buchholz, V. Zolatanosha, K. D. Jöns, D. Reuter. "Influence of droplet material, deposition amount and residual As pressure on nanohole formation by local droplet etching on In0.52Al0.48As layers" (Talk). DGKK & DEMBE workshop. Stuttgart, Germany. 27.11. - 29.11.2023.

- D. Deutsch, C. Buchholz, V. Zolatanosha, K. D. Jöns, D. Reuter. "Influence of InAl deposition amount and annealing time on nanohole formation by local droplet etching on In0.52Al0.48As layers" (Talk). DPG Spring Meeting of the Condensed Matter Section. Berlin, Germany. 17.03. - 22.03.2024.

- D. Deutsch, J. N. C. Rodríguez, C. Buchholz, V. Zolatanosha, K. D. Jöns, D. Reuter. "Droplet etched quantum dots embedded in an optical cavity for photon generation in the telecom C-band" (Poster). Quantum Photonics Spotlight. Paderborn, Germany. 08.10 - 10.10.2024.

- D. Deutsch, V. Zolatanosha, D. Reuter. "Degradation and conservation of droplet etched nanoholes on In0.52Al0.48As layers fabricated under As2 environment" (Poster). DGKK & DEMBE workshop. Berlin, Germany. 11.12 - 13.12.2024.

- D. Deutsch, C. Buchholz, V. Zolatanosha, K. D. Jöns, D. Reuter. "Droplet etched InxGa1-xAs quantum dots embedded in In0.52Al0.48As for optical C-band emission" (Talk). Euro MBE workshop. Auron, France. 09.03 - 13.03.2025.

Bibliography

[1] P. W. Shor. "Algorithms for Quantum Computation: Discrete Logarithms and Factoring". In: *Proceedings 35th Annual Symposium on Foundations of Computer Science*. 35th Annual Symposium on Foundations of Computer Science. Nov. 1994, pp. 124–134. DOI: 10.1109/SFCS.1994.365700.

[2] J. Carolan et al. "Universal Linear Optics". In: *Science* 349.6249 (Aug. 14, 2015), pp. 711–716. ISSN: 0036-8075, 1095-9203. DOI: 10.1126/science.aab3642.

[3] A. D. King et al. *Beyond-Classical Computation in Quantum Simulation*. Version 2. 2024. DOI: 10.48550/ARXIV.2403.00910. URL: https://arxiv.org/abs/2403.00910 (visited on 11/04/2025). Pre-published.

[4] L. S. Madsen et al. "Quantum Computational Advantage with a Programmable Photonic Processor". In: *Nature* 606.7912 (June 2, 2022), pp. 75–81. ISSN: 0028-0836, 1476-4687. DOI: 10.1038/s41586-022-04725-x.

[5] R. L. Rivest, A. Shamir, and L. Adleman. "A Method for Obtaining Digital Signatures and Public-Key Cryptosystems". In: *Communications of the ACM* 21.2 (Feb. 1978), pp. 120–126. ISSN: 0001-0782, 1557-7317. DOI: 10.1145/359340.359342.

[6] J. Sevilla and C. J. Riedel. *Forecasting Timelines of Quantum Computing*. Dec. 9, 2020. DOI: 10.48550/arXiv.2009.05045. arXiv: 2009.05045. Pre-published.

[7] C. H. Bennett and G. Brassard. "Quantum Cryptography: Public Key Distribution and Coin Tossing". In: *Theoretical Computer Science*. Theoretical Aspects of Quantum Cryptography – Celebrating 30 Years of BB84 560 (Dec. 4, 2014), pp. 7–11. ISSN: 0304-3975. DOI: 10.1016/j.tcs.2014.05.025.

[8] A. K. Ekert. "Quantum Cryptography Based on Bell's Theorem". In: *Physical Review Letters* 67.6 (Aug. 5, 1991), pp. 661–663. DOI: 10.1103/PhysRevLett.67.661.

[9] W. K. Wootters and W. H. Zurek. "A Single Quantum Cannot Be Cloned". In: *Nature* 299 (Oct. 1, 1982), pp. 802–803. ISSN: 0028-0836. DOI: 10.1038/299802a0.

[10] K. Azuma et al. "Quantum Repeaters: From Quantum Networks to the Quantum Internet". In: *Reviews of Modern Physics* 95.4 (Dec. 20, 2023), p. 045006. ISSN: 0034-6861, 1539-0756. DOI: 10.1103/RevModPhys.95.045006.

[11] X.-L. Wang et al. "Experimental Ten-Photon Entanglement". In: *Physical Review Letters* 117.21 (Nov. 15, 2016), p. 210502. ISSN: 0031-9007, 1079-7114. DOI: 10.1103/PhysRevLett.117.210502.

[12] D. Llewellyn et al. "Chip-to-Chip Quantum Teleportation and Multi-Photon Entanglement in Silicon". In: *Nature Physics* 16.2 (Feb. 2, 2020), pp. 148–153. ISSN: 1745-2473, 1745-2481. DOI: 10.1038/s41567-019-0727-x.

[13] J. Liu et al. “A Solid-State Source of Strongly Entangled Photon Pairs with High Brightness and Indistinguishability”. In: *Nature Nanotechnology* 14.6 (June 2019), pp. 586–593. ISSN: 1748-3387, 1748-3395. DOI: 10.1038/s41565-019-0435-9.

[14] N. Somaschi et al. “Near-Optimal Single-Photon Sources in the Solid State”. In: *Nature Photonics* 10.5 (May 2016), pp. 340–345. ISSN: 1749-4885, 1749-4893. DOI: 10.1038/nphoton.2016.23.

[15] L. Schweickert et al. “On-Demand Generation of Background-Free Single Photons from a Solid-State Source”. In: *Applied Physics Letters* 112.9 (Feb. 26, 2018), p. 093106. ISSN: 0003-6951, 1077-3118. DOI: 10.1063/1.5020038.

[16] F. Liu et al. “High Purcell Factor Generation of Indistinguishable On-Chip Single Photons”. In: *Nature Nanotechnology* 13.9 (Sept. 2018), pp. 835–840. ISSN: 1748-3387, 1748-3395. DOI: 10.1038/s41565-018-0188-x.

[17] N. Tomm et al. “A Bright and Fast Source of Coherent Single Photons”. In: *Nature Nanotechnology* 16.4 (Apr. 2021), pp. 399–403. ISSN: 1748-3387, 1748-3395. DOI: 10.1038/s41565-020-00831-x.

[18] A. Orieux et al. “Semiconductor Devices for Entangled Photon Pair Generation: A Review”. In: *Reports on Progress in Physics* 80.7 (July 1, 2017), p. 076001. ISSN: 0034-4885, 1361-6633. DOI: 10.1088/1361-6633/aa6955.

[19] C. Heyn et al. “Highly Uniform and Strain-Free GaAs Quantum Dots Fabricated by Filling of Self-Assembled Nanoholes”. In: *Applied Physics Letters* 94.18 (May 4, 2009), p. 183113. ISSN: 0003-6951, 1077-3118. DOI: 10.1063/1.3133338.

[20] D. Huber et al. “Highly Indistinguishable and Strongly Entangled Photons from Symmetric GaAs Quantum Dots”. In: *Nature Communications* 8.1 (May 26, 2017), p. 15506. ISSN: 2041-1723. DOI: 10.1038/ncomms15506.

[21] P. Michler. *Semiconductor Quantum Light Sources: Fundamentals, Technologies and Devices*. 1st ed. De Gruyter Textbook Series. Berlin/Boston: Walter de Gruyter GmbH, 2024. 1 p. ISBN: 978-3-11-070341-2.

[22] Y. H. Huo, A. Rastelli, and O. G. Schmidt. “Ultra-Small Excitonic Fine Structure Splitting in Highly Symmetric Quantum Dots on GaAs (001) Substrate”. In: *Applied Physics Letters* 102.15 (Apr. 16, 2013), p. 152105. ISSN: 0003-6951. DOI: 10.1063/1.4802088.

[23] L. Zhai et al. “Quantum Interference of Identical Photons from Remote GaAs Quantum Dots”. In: *Nature Nanotechnology* 17.8 (Aug. 2022), pp. 829–833. ISSN: 1748-3387, 1748-3395. DOI: 10.1038/s41565-022-01131-2.

[24] A. V. Kuhlmann et al. “Transform-Limited Single Photons from a Single Quantum Dot”. In: *Nature Communications* 6.1 (Sept. 8, 2015), p. 8204. ISSN: 2041-1723. DOI: 10.1038/ncomms9204.

[25] R. B. Patel et al. “Two-Photon Interference of the Emission from Electrically Tunable Remote Quantum Dots”. In: *Nature Photonics* 4.9 (Sept. 2010), pp. 632–635. ISSN: 1749-4885, 1749-4893. DOI: 10.1038/nphoton.2010.161.

[26] D. Bauch et al. *On-Demand Indistinguishable and Entangled Photons Using Tailored Cavity Designs*. Version 2. 2023. DOI: 10.48550/ARXIV.2303.13871. URL: https://arxiv.org/abs/2303.13871 (visited on 11/23/2025). Prepublished.

[27] E. Schöll et al. “Crux of Using the Cascaded Emission of a Three-Level Quantum Ladder System to Generate Indistinguishable Photons”. In: *Physical Review Letters* 125.23 (Dec. 1, 2020), p. 233605. ISSN: 0031-9007, 1079-7114. DOI: 10.1103/PhysRevLett.125.233605.

[28] K. Intonti et al. “The Second Quantum Revolution: Unexplored Facts and Latest News”. In: *Encyclopedia* 4.2 (Mar. 29, 2024), pp. 630–671. ISSN: 2673-8392. DOI: 10.3390/encyclopedia4020040.

[29] A. Einstein, B. Podolsky, and N. Rosen. “Can Quantum-Mechanical Description of Physical Reality Be Considered Complete?” In: *Physical Review* 47.10 (May 15, 1935), pp. 777–780. ISSN: 0031-899X. DOI: 10.1103/PhysRev.47.777.

[30] J. Schlienz and G. Mahler. “Description of Entanglement”. In: *Physical Review A* 52.6 (Dec. 1, 1995), pp. 4396–4404. ISSN: 1050-2947, 1094-1622. DOI: 10.1103/PhysRevA.52.4396.

[31] C. H. Bennett, G. Brassard, and N. D. Mermin. “Quantum Cryptography without Bell’s Theorem”. In: *Physical Review Letters* 68.5 (Feb. 3, 1992), pp. 557–559. ISSN: 0031-9007. DOI: 10.1103/PhysRevLett.68.557.

[32] M. Mubashir Khan, M. Murphy, and A. Beige. “High Error-Rate Quantum Key Distribution for Long-Distance Communication”. In: *New Journal of Physics* 11.6 (June 22, 2009), p. 063043. ISSN: 1367-2630. DOI: 10.1088/1367-2630/11/6/063043.

[33] A. Streltsov. *Quantum Correlations Beyond Entanglement: And Their Role in Quantum Information Theory*. SpringerBriefs in Physics. Cham: Springer International Publishing, 2015. ISBN: 978-3-319-09656-8. DOI: 10.1007/978-3-319-09656-8.

[34] D. F. V. James et al. “Measurement of Qubits”. In: *Physical Review A* 64.5 (Oct. 16, 2001), p. 052312. ISSN: 1050-2947, 1094-1622. DOI: 10.1103/PhysRevA.64.052312.

[35] R. Hafenbrak et al. “Triggered Polarization-Entangled Photon Pairs from a Single Quantum Dot up to 30 K”. In: *New Journal of Physics* 9.9 (Sept. 10, 2007), pp. 315–315. ISSN: 1367-2630. DOI: 10.1088/1367-2630/9/9/315.

[36] W. K. Wootters. “Entanglement of Formation and Concurrence”. In: *Quantum Information and Computation* 1.1 (July 2001), pp. 27–44. ISSN: 15337146, 15337146. DOI: 10.26421/QIC1.1-3.

[37] K. Berrada et al. “A COMPARATIVE STUDY OF NEGATIVITY AND CONCURRENCE BASED ON SPIN COHERENT STATES”. In: *International Journal of Modern Physics C* 21.03 (Mar. 2010), pp. 291–305. ISSN: 0129-1831, 1793-6586. DOI: 10.1142/S0129183110015129.

[38] R. J. Young et al. “Improved Fidelity of Triggered Entangled Photons from Single Quantum Dots”. In: *New Journal of Physics* 8.2 (Feb. 23, 2006), pp. 29–29. ISSN: 1367-2630. DOI: 10.1088/1367-2630/8/2/029.

[39] S. M. Girvin and K. Yang. *Modern Condensed Matter Physics*. Cambridge New York: Cambridge university press, 2019. ISBN: 978-1-107-13739-4.

[40] C. Kittel. *Introduction to Solid State Physics*. 8th ed. Hoboken, NJ: Wiley, 2005. 680 pp. ISBN: 978-0-471-41526-8.

[41] M. Grundmann. *The Physics of Semiconductors: An Introduction Including Nanophysics and Applications*. Graduate Texts in Physics. Cham: Springer International Publishing, 2016. ISBN: 978-3-319-23880-7. DOI: 10.1007/978-3-319-23880-7.

[42] U. W. Pohl. *Epitaxy of Semiconductors: Introduction to Physical Principles*. Graduate Texts in Physics. Berlin, Heidelberg: Springer Berlin Heidelberg, 2013. ISBN: 978-3-642-32970-8. DOI: 10.1007/978-3-642-32970-8.

[43] S. M. Sze, Yiming Li, and Kwok Kwok Ng. *Physics of Semiconductor Devices*. Fourth edition. Hoboken, NJ Chichester, West Sussex: Wiley, 2021. 931 pp. ISBN: 978-1-119-42913-5.

[44] V. Fock. "Bemerkung zur Quantelung des harmonischen Oszillators im Magnetfeld". In: *Zeitschrift für Physik* 47.5 (May 1, 1928), pp. 446–448. ISSN: 0044-3328. DOI: 10.1007/BF01390750.

[45] C. G. Darwin. "The Diamagnetism of the Free Electron". In: *Mathematical Proceedings of the Cambridge Philosophical Society* 27.1 (Jan. 1931), pp. 86–90. ISSN: 1469-8064, 0305-0041. DOI: 10.1017/S0305004100009373.

[46] M. Born and V. Fock. "Beweis des Adiabatensatzes". In: *Zeitschrift für Physik* 51.3–4 (Mar. 1928), pp. 165–180. ISSN: 1434-6001, 1434-601X. DOI: 10.1007/BF01343193.

[47] J. A. Vinasco et al. "Revisiting the Adiabatic Approximation for Bound States Calculation in Axisymmetric and Asymmetrical Quantum Structures". In: *Superlattices and Microstructures* 138 (Feb. 1, 2020), p. 106384. ISSN: 0749-6036. DOI: 10.1016/j.spmi.2019.106384.

[48] R. M. Roescu. "Wavefunctions and Carrier Carrier Interactions in InAs Quantum Dots Studied by Capacitance Voltage Spectroscopy". PhD thesis. Ruhr-Universität Bochum, Universitätsbibliothek, 2009.

[49] A. Wojs et al. "Electronic Structure and Magneto-Optics of Self-Assembled Quantum Dots". In: *Physical Review B* 54.8 (Aug. 15, 1996), pp. 5604–5608. ISSN: 0163-1829, 1095-3795. DOI: 10.1103/PhysRevB.54.5604.

[50] C. Heyn et al. "Cone-Shell Quantum Structures in Electric and Magnetic Fields as Switchable Traps for Photoexcited Charge Carriers". In: *Nanomaterials* 13.10 (May 22, 2023), p. 1696. ISSN: 2079-4991. DOI: 10.3390/nano13101696.

[51] C. Heyn et al. "Strong Electric Polarizability of Cone–Shell Quantum Structures for a Large Stark Shift, Tunable Long Exciton Lifetimes, and a Dot-to-Ring Transformation". In: *Nanomaterials* 13.5 (Feb. 25, 2023), p. 857. ISSN: 2079-4991. DOI: 10.3390/nano13050857.

[52] Y. H. Huo et al. *Semiconductor Quantum Dots with Light-Hole Exciton Ground State: Fabrication and Fine Structure*. Version 1. 2012. DOI: 10.48550/ARXIV.1208.6554. URL: https://arxiv.org/abs/1208.6554 (visited on 01/18/2026). Pre-published.

[53] J. Kim, C. Y. Wong, and G. D. Scholes. "Exciton Fine Structure and Spin Relaxation in Semiconductor Colloidal Quantum Dots". In: *Accounts of Chemical Research* 42.8 (Aug. 18, 2009), pp. 1037–1046. ISSN: 0001-4842. DOI: 10.1021/ar8002046.

[54] M. Bayer et al. “Fine Structure of Neutral and Charged Excitons in Self-Assembled In(Ga)As/(Al)GaAs Quantum Dots”. In: *Physical Review B* 65.19 (May 7, 2002), p. 195315. ISSN: 0163-1829, 1095-3795. DOI: 10.1103/PhysRevB.65.195315.

[55] P. Michler, ed. *Quantum Dots for Quantum Information Technologies*. Nano-Optics and Nanophotonics. Cham: Springer, 2017. 448 pp. ISBN: 978-3-319-56378-7. DOI: 10.1007/978-3-319-56378-7.

[56] M. A. Nielsen and Isaac L. Chuang. *Quantum Computation and Quantum Information*. 10. printing. Cambridge: Cambridge Univ. Press, 2009. 676 pp. ISBN: 978-0-521-63503-5.

[57] Peter Michler. *Single Semiconductor Quantum Dots*. NanoScience and Technology Ser. Berlin, Heidelberg: Springer, 2009. 1 p. ISBN: 978-3-540-87446-1.

[58] R. M. Stevenson et al. “Evolution of Entanglement Between Distinguishable Light States”. In: *Physical Review Letters* 101.17 (Oct. 20, 2008), p. 170501. DOI: 10.1103/PhysRevLett.101.170501.

[59] M. B. Ward et al. “Coherent Dynamics of a Telecom-Wavelength Entangled Photon Source”. In: *Nature Communications* 5.1 (Feb. 19, 2014), p. 3316. ISSN: 2041-1723. DOI: 10.1038/ncomms4316.

[60] D. Huber et al. “Semiconductor Quantum Dots as an Ideal Source of Polarization-Entangled Photon Pairs on-Demand: A Review”. In: *Journal of Optics* 20.7 (July 1, 2018), p. 073002. ISSN: 2040-8978, 2040-8986. DOI: 10.1088/2040-8986/aac4c4.

[61] A. Carmele et al. “Formation Dynamics of an Entangled Photon Pair: A Temperature-Dependent Analysis”. In: *Physical Review B* 81.19 (May 26, 2010), p. 195319. ISSN: 1098-0121, 1550-235X. DOI: 10.1103/PhysRevB.81.195319.

[62] N. Akopian et al. “Entangled Photon Pairs from Semiconductor Quantum Dots”. In: *Physical Review Letters* 96.13 (Apr. 6, 2006), p. 130501. ISSN: 0031-9007, 1079-7114. DOI: 10.1103/PhysRevLett.96.130501.

[63] A. Y. Cho and J. R. Arthur. “Molecular Beam Epitaxy”. In: *Progress in Solid State Chemistry* 10 (Jan. 1975), pp. 157–191. ISSN: 00796786. DOI: 10.1016/0079-6786(75)90005-9.

[64] J. R. Arthur. “Molecular Beam Epitaxy”. In: *Surface Science* 500.1–3 (Mar. 2002), pp. 189–217. ISSN: 00396028. DOI: 10.1016/S0039-6028(01)01525-4.

[65] M. A. Herman, Wolfgang Richter, and Helmut Sitter. *Epitaxy: Physical Principles and Technical Implementation*. Springer Series in Materials Science 62. Berlin ; New York: Springer, 2004. 522 pp. ISBN: 978-3-540-67821-2.

[66] D. Reuter, A. D. Wieck, and A. Fischer. “A Compact Electron Beam Evaporator for Carbon Doping in Solid Source Molecular Beam Epitaxy”. In: *Review of Scientific Instruments* 70.8 (Aug. 1, 1999), pp. 3435–3438. ISSN: 0034-6748, 1089-7623. DOI: 10.1063/1.1149933.

[67] T. Henksmeier. “Remote Heteroepitaxy of In(x)Ga(1-x)As on graphene covered GaAs-(001) substrates”. PhD thesis. Paderborn, 2021.

[68] J. W. Matthews and A. E. Blakeslee. “Defects in Epitaxial Multilayers”. In: *Journal of Crystal Growth* 27 (Dec. 1974), pp. 118–125. ISSN: 00220248. DOI: 10.1016/S0022-0248(74)80055-2.

[69] I. Vurgaftman, J. R. Meyer, and L. R. Ram-Mohan. “Band Parameters for III–V Compound Semiconductors and Their Alloys”. In: *Journal of Applied Physics* 89.11 (June 1, 2001), pp. 5815–5875. ISSN: 0021-8979, 1089-7550. DOI: 10.1063/1.1368156.

[70] N. Koguchi, S. Takahashi, and T. Chikyow. “New MBE Growth Method for InSb Quantum Well Boxes”. In: *Journal of Crystal Growth* 111.1–4 (May 1991), pp. 688–692. ISSN: 00220248. DOI: 10.1016/0022-0248(91)91064-H.

[71] N. Koguchi and K. Ishige. “Growth of GaAs Epitaxial Microcrystals on an S-Terminated GaAs Substrate by Successive Irradiation of Ga and As Molecular Beams”. In: *Japanese Journal of Applied Physics* 32 (5R May 1, 1993), p. 2052. ISSN: 0021-4922, 1347-4065. DOI: 10.1143/JJAP.32.2052.

[72] Z. M. Wang et al. “Self-assembly of GaAs Holed Nanostructures by Droplet Epitaxy”. In: *physica status solidi (a)* 202.8 (June 2005). ISSN: 1862-6300, 1862-6319. DOI: 10.1002/pssa.200510031.

[73] A. Stemmann et al. “Local Droplet Etching of Nanoholes and Rings on GaAs and AlGaAs Surfaces”. In: *Applied Physics Letters* 93.12 (Sept. 22, 2008), p. 123108. ISSN: 0003-6951, 1077-3118. DOI: 10.1063/1.2981517.

[74] C. Heyn et al. “Dynamics of Mass Transport during Nanohole Drilling by Local Droplet Etching”. In: *Nanoscale Research Letters* 10.1 (Dec. 2015), p. 67. ISSN: 1931-7573, 1556-276X. DOI: 10.1186/s11671-015-0779-5.

[75] J. A. Venables, G. D. T. Spiller, and M. Hanbucken. “Nucleation and Growth of Thin Films”. In: *Reports on Progress in Physics* 47.4 (Apr. 1, 1984), pp. 399–459. ISSN: 0034-4885, 1361-6633. DOI: 10.1088/0034-4885/47/4/002.

[76] H. Brune. “Microscopic View of Epitaxial Metal Growth: Nucleation and Aggregation”. In: *Surface Science Reports* 31.4–6 (Jan. 1998), pp. 125–229. ISSN: 01675729. DOI: 10.1016/S0167-5729(99)80001-6.

[77] C. Heyn, S. Schnüll, and W. Hansen. “Scaling of the Structural Characteristics of Nanoholes Created by Local Droplet Etching”. In: *Journal of Applied Physics* 115.2 (Jan. 14, 2014), p. 024309. ISSN: 0021-8979, 1089-7550. DOI: 10.1063/1.4861722.

[78] C. Heyn. “Kinetic Model of Local Droplet Etching”. In: *Physical Review B* 83.16 (Apr. 4, 2011), p. 165302. ISSN: 1098-0121, 1550-235X. DOI: 10.1103/PhysRevB.83.165302.

[79] C. D. Thurmond. “Phase Equilibria in the GaAs and the GaP Systems”. In: *Journal of Physics and Chemistry of Solids* 26.5 (May 1965), pp. 785–802. ISSN: 00223697. DOI: 10.1016/0022-3697(65)90254-4.

[80] C. Heyn et al. “Influence of Ga Coverage and As Pressure on Local Droplet Etching of Nanoholes and Quantum Rings”. In: *Journal of Applied Physics* 105.5 (Mar. 1, 2009), p. 054316. ISSN: 0021-8979, 1089-7550. DOI: 10.1063/1.3079789.

[81] D. Fuster, Y. González, and L. González. “Fundamental Role of Arsenic Flux in Nanohole Formation by Ga Droplet Etching on GaAs(001)”. In: *Nanoscale Research Letters* 9.1 (Dec. 2014), p. 309. ISSN: 1556-276X. DOI: 10.1186/1556-276X-9-309.

[82] V. Vonk et al. “Faceting of Local Droplet-Etched Nanoholes in AlGaAs”. In: *Physical Review Materials* 2.10 (Oct. 8, 2018), p. 106001. ISSN: 2475-9953. DOI: 10.1103/PhysRevMaterials.2.106001.

[83] C. Heyn et al. "Role of Arsenic During Aluminum Droplet Etching of Nanoholes in AlGaAs". In: *Nanoscale Research Letters* 11.1 (Dec. 2016), p. 428. ISSN: 1931-7573, 1556-276X. DOI: 10.1186/s11671-016-1648-6.

[84] A. Küster et al. "Droplet Etching of Deep Nanoholes for Filling with Self-Aligned Complex Quantum Structures". In: *Nanoscale Research Letters* 11.1 (June 3, 2016), p. 282. ISSN: 1556-276X. DOI: 10.1186/s11671-016-1495-5.

[85] G. Binnig, C. F. Quate, and Ch. Gerber. "Atomic Force Microscope". In: *Physical Review Letters* 56.9 (Mar. 3, 1986), pp. 930–933. ISSN: 0031-9007. DOI: 10.1103/PhysRevLett.56.930.

[86] P. J. Eaton and P. West. *Atomic Force Microscopy*. Oxford ; New York: Oxford University Press, 2010. 248 pp. ISBN: 978-0-19-957045-4.

[87] R. E. Smallman and A. H. W. Ngan. *Modern Physical Metallurgy*. 8th edition. Oxford Waltham, MA: Elsevier/Butterworth-Heinemann, 2014. ISBN: 978-0-08-098204-5.

[88] M. Von Ardenne. "Das Elektronen-Rastermikroskop: Theoretische Grundlagen". In: *Zeitschrift für Physik* 109.9–10 (Sept. 1938), pp. 553–572. ISSN: 0044-3328. DOI: 10.1007/BF01341584.

[89] A. Ul-Hamid. *A Beginners' Guide to Scanning Electron Microscopy*. Cham, Switzerland: Springer, 2018. ISBN: 978-3-319-98482-7.

[90] K. T. Arat et al. "Estimating Step Heights from Top-Down SEM Images". In: *Microscopy and Microanalysis* 25.4 (Aug. 2019), pp. 903–911. ISSN: 1431-9276, 1435-8115. DOI: 10.1017/S143192761900062X.

[91] M. Birkholz, P. F. Fewster, and C. Genzel. *Thin Film Analysis by X-ray Scattering*. Weinheim: Wiley-VCH, 2006. 356 pp. ISBN: 978-3-527-31052-4.

[92] W. H. Bragg and W. L. Bragg. "The Reflection of X-rays by Crystals". In: *Proceedings of the Royal Society of London. Series A, Containing Papers of a Mathematical and Physical Character* 88.605 (Jan. 1997), pp. 428–438. DOI: 10.1098/rspa.1913.0040.

[93] L. Spieß et al. *Moderne Röntgenbeugung: Röntgendiffraktometrie für Materialwissenschaftler, Physiker und Chemiker*. 3., überarbeitete Auflage. Springer eBooks Life Science and Basic Disciplines. Wiesbaden: Springer Spektrum, 2019. 1 p. ISBN: 978-3-8348-8232-5. DOI: 10.1007/978-3-8348-8232-5.

[94] E. Schierle. "Antiferromagnetism in Thin Films Studied by Resonant Magnetic Soft X-Ray Scattering". PhD thesis. Freie Universität Berlin, 2007. DOI: 10.17169/REFUBIUM-11239.

[95] A. M. Miller et al. "Extracting Information from X-ray Diffraction Patterns Containing Laue Oscillations". In: *Zeitschrift für Naturforschung B* 77.4–5 (May 25, 2022), pp. 313–322. ISSN: 0932-0776, 1865-7117. DOI: 10.1515/znb-2022-0020.

[96] P. Maj et al. "HyPix-3000 - a Large Area Single-Photon Counting Detector with Two Discriminator Thresholds". In: *2014 IEEE Nuclear Science Symposium and Medical Imaging Conference (NSS/MIC)*. 2014 IEEE Nuclear Science Symposium and Medical Imaging Conference (NSS/MIC). Seattle, WA, USA: IEEE, Nov. 2014, pp. 1–4. ISBN: 978-1-4799-6097-2. DOI: 10.1109/NSSMIC.2014.7431095.

[97] R. Sittig et al. "Thin-Film InGaAs Metamorphic Buffer for Telecom C-band InAs Quantum Dots and Optical Resonators on GaAs Platform". In: *Nanophotonics* 11.6 (Mar. 21, 2022), pp. 1109–1116. ISSN: 2192-8614. DOI: 10.1515/nanoph-2021-0552.

[98] S. Dolabella et al. "Lattice Strain and Defects Analysis in Nanostructured Semiconductor Materials and Devices by High-Resolution X-Ray Diffraction: Theoretical and Practical Aspects". In: *Small Methods* 6.2 (Feb. 2022), p. 2100932. ISSN: 2366-9608, 2366-9608. DOI: 10.1002/smtd.202100932.

[99] C. G. Dunn and E. F. Kogh. "Comparison of Dislocation Densities of Primary and Secondary Recrystallization Grains of Si-Fe". In: *Acta Metallurgica* 5.10 (Oct. 1957), pp. 548–554. ISSN: 00016160. DOI: 10.1016/0001-6160(57)90122-0.

[100] K. W. Böer and U. W. Pohl. *Semiconductor Physics*. Cham: Springer, 2018. ISBN: 978-3-319-69150-3.

[101] M. P. Lumb et al. "Characterization, Modeling and Analysis of InAlAsSb Schottky Barrier Solar Cells Grown on InP". In: *2014 IEEE 40th Photovoltaic Specialist Conference (PVSC)*. 2014 IEEE 40th Photovoltaic Specialists Conference (PVSC). Denver, CO, USA: IEEE, June 2014, pp. 0243–0246. ISBN: 978-1-4799-4398-2. DOI: 10.1109/PVSC.2014.6925668.

[102] C. F. Klingshirn. *Semiconductor Optics*. New York: Springer, 2012. ISBN: 978-3-642-28361-1.

[103] G. D. Gilliland. "Photoluminescence Spectroscopy of Crystalline Semiconductors". In: *Materials Science and Engineering: R: Reports* 18.3–6 (Mar. 1997), pp. 99–399. ISSN: 0927796X. DOI: 10.1016/S0927-796X(97)80003-4.

[104] D. Vignaud, X. Wallart, and F. Mollot. "InAlAs/InP Heterostructures: Influence of a Thin InAs Layer at the Interface". In: *Journal of Applied Physics* 76.4 (Aug. 15, 1994), pp. 2324–2329. ISSN: 0021-8979, 1089-7550. DOI: 10.1063/1.357604.

[105] Z.-L. Guo et al. "Correlation between MBE Deoxidation Conditions and InGaAs/InP APD Performance". In: *Journal of Infrared and Millimeter Waves* 43.1 (2024), p. 63. ISSN: 1001-9014. DOI: 10.11972/j.issn.1001-9014.2024.01.009.

[106] G. B. Galiev et al. "Structural and Electrical Properties of InAlAs/InGaAs/InAlAs HEMT Heterostructures on InP Substrates with InAs Inserts in Quantum Well". In: *Crystallography Reports* 59.6 (Nov. 2014), pp. 900–907. ISSN: 1063-7745, 1562-689X. DOI: 10.1134/S1063774514060108.

[107] F. Peiró et al. "Influence of the Desorption and Growth Temperatures on the Crystalline Quality of Molecular-Beam Epitaxy InAlAs Layers". In: *Journal of Vacuum Science & Technology B: Microelectronics and Nanometer Structures Processing, Measurement, and Phenomena* 10.5 (Sept. 1, 1992), pp. 2148–2152. ISSN: 1071-1023, 1520-8567. DOI: 10.1116/1.586181.

[108] J. Singh et al. "Role of Kinetics and Thermodynamics in Alloy Clustering and Surface Quality in InAlAs Grown by Molecular-Beam Epitaxy: Consequences for Optical and Transport Properties". In: *Journal of Applied Physics* 60.9 (Nov. 1, 1986), pp. 3167–3171. ISSN: 0021-8979, 1089-7550. DOI: 10.1063/1.337730.

[109] B. Goldstein and D. Szostak. “Preferential Evaporation of In from GaxIn1-xAs”. In: *Applied Physics Letters* 26.12 (June 15, 1975), pp. 685–687. ISSN: 0003-6951, 1077-3118. DOI: 10.1063/1.88035.

[110] D. V. Gulyaev et al. “Nature of the Pits on the Lattice-Matched InAlAs Layer Surface Grown on the (001) InP Substrate”. In: *Nanomaterials* 14.22 (Nov. 18, 2024), p. 1842. ISSN: 2079-4991. DOI: 10.3390/nano14221842.

[111] R. Houdré et al. “Characterization of InGaAs and InAlAs Layers on InP by Four-Crystal High Resolution X-ray Diffraction and Wedge Transmission Electron Microscopy”. In: *Journal of Crystal Growth* 111.1–4 (May 1991), pp. 456–460. ISSN: 00220248. DOI: 10.1016/0022-0248(91)91019-7.

[112] X. Zhou et al. “Surface Segregation of InGaAs Films by the Evolution of Reflection High-Energy Electron Diffraction Patterns”. In: *Chinese Physics B* 21.4 (Apr. 2012), p. 046103. ISSN: 1674-1056. DOI: 10.1088/1674-1056/21/4/046103.

[113] P. Gutowski et al. “MBE Growth of Strain-Compensated InGaAs/InAlAs/InP Quantum Cascade Lasers”. In: *Journal of Crystal Growth* 466 (May 2017), pp. 22–29. ISSN: 00220248. DOI: 10.1016/j.jcrysgro.2017.02.031.

[114] P. Gutowski et al. “Optimization of MBE Growth Conditions of In0.52Al0.48As Waveguide Layers for InGaAs/InAlAs/InP Quantum Cascade Lasers”. In: *Materials* 12.10 (May 17, 2019), p. 1621. ISSN: 1996-1944. DOI: 10.3390/ma12101621.

[115] P. Franzosi et al. “Misfit Dislocations in InGaAs/InP Mbe Single Heterostructures”. In: *Journal of Crystal Growth* 75.3 (June 1986), pp. 521–534. ISSN: 00220248. DOI: 10.1016/0022-0248(86)90098-9.

[116] G. Müller et al. “Types and Origin of Dislocations in Large GaAs and InP Bulk Crystals with Very Low Dislocation Densities”. In: *physica status solidi (a)* 202.15 (Dec. 2005), pp. 2870–2879. ISSN: 1862-6300, 1862-6319. DOI: 10.1002/pssa.200521179.

[117] C. N. Singman. “Atomic Volume and Allotropy of the Elements”. In: *Journal of Chemical Education* 61.2 (Feb. 1984), p. 137. ISSN: 0021-9584, 1938-1328. DOI: 10.1021/ed061p137.

[118] D. Deutsch, V. Zolatanosha, and D. Reuter. “Local Droplet Etching with In, Al and InAl in In0.52Al0.48As Layers for Generation of Quantum Dots Emitting in the Optical C-band”. In: *Journal of Crystal Growth* 668 (Oct. 2025), p. 128247. ISSN: 00220248. DOI: 10.1016/j.jcrysgro.2025.128247.

[119] D. Deutsch et al. “Telecom C-band Photon Emission from (In,Ga)As Quantum Dots Generated by Filling Nanoholes in In0.52Al0.48As Layers”. In: *AIP Advances* 13.5 (May 1, 2023), p. 055009. ISSN: 2158-3226. DOI: 10.1063/5.0147281.

[120] C. Heyn, A. Stemmann, and W. Hansen. “Dynamics of Self-Assembled Droplet Etching”. In: *Applied Physics Letters* 95.17 (Oct. 26, 2009), p. 173110. ISSN: 0003-6951, 1077-3118. DOI: 10.1063/1.3254216.

[121] N. Auler, D. Deutsch, and D. Reuter. “Statistical Analysis of the Spatial Distribution of InAl Droplet-Etched Nanoholes in In0.52Al0.48As Layers”. In: *Crystals* 15.9 (Aug. 29, 2025), p. 770. ISSN: 2073-4352. DOI: 10.3390/cryst15090770.

[122] X. Li et al. “Origin of Nanohole Formation by Etching Based on Droplet Epitaxy”. In: *Nanoscale* 6.5 (2014), p. 2675. ISSN: 2040-3364, 2040-3372. DOI: 10.1039/c3nr06064k.

[123] A. A. Lyamkina et al. "The Investigation of Intermediate Stage of Template Etching with Metal Droplets by Wetting Angle Analysis on (001) GaAs Surface". In: *Nanoscale Research Letters* 6.1 (Sept. 28, 2010), p. 42. ISSN: 1556-276X. DOI: 10.1007/s11671-010-9790-z.

[124] C. Heyn et al. "GaAs Quantum Dot Molecules Filled into Droplet Etched Nanoholes". In: *Journal of Crystal Growth* 477 (Nov. 2017), pp. 235–238. ISSN: 00220248. DOI: 10.1016/j.jcrysgro.2017.03.029.

[125] M. A. Stevens et al. "Surface Diffusion Measurements of In on InGaAs Enabled by Droplet Epitaxy". In: *Journal of Applied Physics* 121.19 (May 21, 2017), p. 195302. ISSN: 0021-8979, 1089-7550. DOI: 10.1063/1.4983257.

[126] D. Deutsch and D. Reuter. "Influence of the Etching Material Deposition Rate and Annealing Time on Nanohole Morphology Etched into InP/In0.52Al0.48As Layers via Local Droplet Epitaxy". In: *Crystals* 15.11 (Oct. 23, 2025), p. 913. ISSN: 2073-4352. DOI: 10.3390/cryst15110913.

[127] C. Heyn, D. Sonnenberg, and W. Hansen. "Local Droplet Etching: Self-Assembled Nanoholes for Quantum Dots and Nanopillars". In: *Nanodroplets*. Ed. by Z. M. Wang. Vol. 18. New York, NY: Springer New York, 2013, pp. 363–384. ISBN: 978-1-4614-9472-0. DOI: 10.1007/978-1-4614-9472-0_15.

[128] M. Iwamatsu. "A Generalized Young's Equation to Bridge a Gap between the Experimentally Measured and the Theoretically Calculated Line Tensions". In: *Journal of Adhesion Science and Technology* 32.21 (Nov. 2, 2018), pp. 2305–2319. ISSN: 0169-4243, 1568-5616. DOI: 10.1080/01694243.2018.1476036.

[129] X. Cao et al. "Local Droplet Etching on InAlAs/InP Surfaces with InAl Droplets". In: *AIP Advances* 12.5 (May 1, 2022), p. 055302. ISSN: 2158-3226. DOI: 10.1063/5.0088012.

[130] S. F. C. da Silva et al. "GaAs Quantum Dots Grown by Droplet Etching Epitaxy as Quantum Light Sources". In: *Applied Physics Letters* 119.12 (Sept. 24, 2021), p. 120502. ISSN: 0003-6951. DOI: 10.1063/5.0057070.

[131] Y. H. Huo et al. "A Light-Hole Exciton in a Quantum Dot". In: *Nature Physics* 10.1 (Jan. 2014), pp. 46–51. ISSN: 1745-2473, 1745-2481. DOI: 10.1038/nphys2799.

[132] Y. Zhang et al. "Unveiling the 3D Morphology of Epitaxial GaAs/AlGaAs Quantum Dots". In: *Nano Letters* 24.33 (Aug. 21, 2024), pp. 10106–10113. ISSN: 1530-6984, 1530-6992. DOI: 10.1021/acs.nanolett.4c02182.

[133] P. Atkinson, E. Zallo, and O. G. Schmidt. "Independent Wavelength and Density Control of Uniform GaAs/AlGaAs Quantum Dots Grown by Infilling Self-Assembled Nanoholes". In: *Journal of Applied Physics* 112.5 (Sept. 1, 2012), p. 054303. ISSN: 0021-8979, 1089-7550. DOI: 10.1063/1.4748183.

[134] R. Enzmann et al. "Design and Realization of Low Density InAs Quantum Dots on AlGaInAs Lattice Matched to InP(001)". In: *Journal of Crystal Growth* 312.16–17 (Aug. 2010), pp. 2300–2304. ISSN: 00220248. DOI: 10.1016/j.jcrysgro.2010.05.016.

[135] J. M. García et al. "InAs/InP(001) Quantum Wire Formation Due to Anisotropic Stress Relaxation: In Situ Stress Measurements". In: *Journal of Crystal Growth* 227–228 (July 2001), pp. 975–979. ISSN: 00220248. DOI: 10.1016/S0022-0248(01)00962-9.

[136] J. Dreybrodt, A. Forchel, and J. P. Reithmaier. "Optical Properties of Ga0.8In0.2As/GaAs Surface Quantum Wells". In: *Physical Review B* 48.19 (Nov. 15, 1993), pp. 14741–14744. ISSN: 0163-1829, 1095-3795. DOI: 10.1103/PhysRevB.48.14741.

[137] E. Yablonovitch, H. M. Cox, and T. J. Gmitter. "Nearly Ideal Electronic Surfaces on Naked In0.53Ga0.47As Quantum Wells". In: *Applied Physics Letters* 52.12 (Mar. 21, 1988), pp. 1002–1004. ISSN: 0003-6951, 1077-3118. DOI: 10.1063/1.99226.

[138] M. Benyoucef et al. "Telecom-Wavelength (1.5 µm) Single-Photon Emission from InP-based Quantum Dots". In: *Applied Physics Letters* 103.16 (Oct. 14, 2013), p. 162101. ISSN: 0003-6951, 1077-3118. DOI: 10.1063/1.4825106.

[139] I. Mathews et al. "InAlAs Solar Cell on a GaAs Substrate Employing a Graded InxGa1-xAs-InP Metamorphic Buffer Layer". In: *Applied Physics Letters* 102.3 (Jan. 21, 2013), p. 033906. ISSN: 0003-6951, 1077-3118. DOI: 10.1063/1.4789521.

[140] J. E. Ayers, S. K. Ghandhi, and L. J. Schowalter. "Crystallographic Tilting of Heteroepitaxial Layers". In: *Journal of Crystal Growth* 113.3–4 (Sept. 1991), pp. 430–440. ISSN: 00220248. DOI: 10.1016/0022-0248(91)90077-I.

[141] K. L. Schulte, M. T. Strand, and T. F. Kuech. "Evolution of Epilayer Tilt in Thick In Ga1-As Metamorphic Buffer Layers Grown by Hydride Vapor Phase Epitaxy". In: *Journal of Crystal Growth* 426 (Sept. 2015), pp. 283–286. ISSN: 00220248. DOI: 10.1016/j.jcrysgro.2015.05.009.

[142] M. Natali et al. "Lattice Curvature Generation in Graded In(x)Ga(1-x)As/GaAs Buffer Layers". In: *Physical Review B* 62.16 (Oct. 15, 2000), pp. 11054–11062. ISSN: 0163-1829, 1095-3795. DOI: 10.1103/PhysRevB.62.11054.

[143] A. Zhylik et al. "High-Resolution x-Ray Diffraction Investigation of Relaxation and Dislocations in SiGe Layers Grown on (001), (011), and (111) Si Substrates". In: *Journal of Applied Physics* 109.12 (June 15, 2011), p. 123714. ISSN: 0021-8979, 1089-7550. DOI: 10.1063/1.3597828.

[144] S. Saha, D. T. Cassidy, and D. A. Thompson. "Investigation of Cross-Hatch in In0.3Ga0.7As Pseudo-Substrates". In: *Journal of Applied Physics* 113.12 (Mar. 28, 2013), p. 124301. ISSN: 0021-8979, 1089-7550. DOI: 10.1063/1.4796104.

[145] R. Kumar et al. "Investigation of Cross-Hatch Surface and Study of Anisotropic Relaxation and Dislocation on InGaAs on GaAs (001)". In: *Electronic Materials Letters* 12.3 (May 2016), pp. 356–364. ISSN: 1738-8090, 2093-6788. DOI: 10.1007/s13391-016-5318-8.

[146] V. L. Alperovich et al. "Surface Passivation and Morphology of GaAs(1 0 0) Treated in HCl-isopropanol Solution". In: *Applied Surface Science* 235.3 (Aug. 2004), pp. 249–259. ISSN: 01694332. DOI: 10.1016/j.apsusc.2004.05.097.